UNIVERSITÀ DEGLI STUDI DI NAPOLI FEDERICO II

PH.D. THESIS
IN
INFORMATION TECHNOLOGY AND ELECTRICAL ENGINEERING

MATERIAL-INDEPENDENT MODES FOR THE ELECTROMAGNETIC SCATTERING FROM HOMOGENEOUS OBJECTS: FROM QUASISTATIC TO FULL-WAVE FORMULATIONS

MARIANO PASCALE

TUTOR: PROF. CARLO FORESTIERE

COORDINATOR: PROF. DANIELE RICCIO

XXXIII CICLO

SCUOLA POLITECNICA E DELLE SCIENZE DI BASE
DIPARTIMENTO DI INGEGNERIA ELETTRICA E TECNOLOGIE DELL'INFORMAZIONE

Alla mia famiglia

Abstract

The light manipulation at the nanoscale is the leitmotif of the research field of nanophotonics. Over the last decades, the classical limits imposed by diffraction have been largely surpassed by virtue of technological and theoretical breakthroughs in the field of light-matter interaction. Properly engineered metallic and dielectric nanostructures provide an unprecedented level of control over the electromagnetic radiation in subwavelength spatial regions. This is enabled by their resonant behavior at the optical frequencies. Thus, the development in this research field necessarily depends on an effective electromagnetic modeling of these resonances.

Hand in hand with the technological progress, there have been growing efforts in providing a complete and accurate framework for the description of resonances in metallic and dielectric nanostructures. The most powerful tools have certainly been represented by the spectral theories, in which the object electromagnetic behavior is characterized by its resonant modes. These modes are calculated as solutions of an auxiliary eigenvalue problem, i.e., the source-free Maxwell's equations. Several spectral theories have been developed, and in each of them the nanostructure geometric parameters, material, and resonant frequencies are intertwined in a different way, according to the choice of spectral parameter. For instance, the quasi-normal modes, widespread in the nanophotonics community, adopt, as the spectral parameter, the operating frequency, and hence the modes depend on both the nanostructure material and its shape.

In the recent years, a spectral method that uses the object relative permittivity as spectral parameter, has proved very useful in the modeling of the electromagnetic scattering from homogeneous isotropic nanostructures. This method relies on modes, called material-independent modes, that depend on the object geometry and the operating frequency, but not on the nanostructure dielectric permittivity.

The goal of this thesis is to develop the description of electromagnetic scattering by homogeneous objects in terms of material-independent modes. In particular,

In Chapter 1, we briefly review recent highlights in the modeling and applications of resonant metallic and dielectric nanostructures, and contextualize the spectral

theory of the material-independent modes.

In Chapter 2, we develop the formalism to describe the resonances in objects smaller than the incident wavelength. Specifically, we show that the resonances in metal and dielectric nanostructures of any shape are electro- and magneto-quasistatic in nature, respectively, and can be described through eigenfunctions (quasistatic modes) of compact and self-adjoint integral operators. Through means of a perturbative approach, we then provide an extension to the quasistatic analysis, and we link the radiation corrections to the frequency shift and radiation quality (Q) factor of the quasistatic modes, through closed-form expressions. In the derived expressions, the dependencies on the material and the size of the object are factorized.

In Chapter 3, we exploit the quasistatic mode framework introduced in the previous chapter for the calculation of the optimal current distribution supported by an object of dimension smaller than the wavelength, yelding the minimum Q factor. This part has been developed during my stay at the Photonics Initiative at the Advanced Science Research Center, in New York, under the supervision of Prof. Andrea Alù. The provided representation leads to analytical and closed form expressions of the electric and magnetic polarizability tensors of arbitrary shaped objects, whose eigenvalues are known to be linked to the minimum Q factor. Many examples are worked out, in three-dimensional, two-dimensional (surfaces), and translational invariant objects.

In Chapter 4, we introduce the full-wave material-independent modes for the description of the scattering from an arbitrary sized 3D object. As a case of study, we investigate the modes and resonances of the prototypical structure of a sphere. We show how the analysis of the object modes and eigenvalues provides a systematic classification of resonances and interference effects. In particular, in this framework, we are able to justify the differences in the power spectrum scattered by dielectric and metal nanoparticles.

In Chapter 5, we investigate the resonances and resonance modes in the electromagnetic scattering from metallic and dielectric sphere dimers in the full-wave regime, by using the material-independent modes. Along the lines of the well-known plasmon hybridization model, we see the dimer modes as the result of the hybridization of the modes of the two constituent spheres, whose importance is quantified by hybridization weights. In this way, as we vary the spheres arrangement, although the dimer modes change, they are still represented in terms of the same set of single-sphere modes, but with different hybridization weights. This study represents the first full-Maxwell theory of hybridization in dielectric dimers, and it also constitutes an extension of the plasmon-mode hybridization theory.

Contents

1 Introduction 1

1.1 Motivations for a modal analysis 2
1.2 Quasistatic modal decomposition 3
1.3 Quality factor of electrically small objects 5
1.4 Full-wave hybridization 7
1.5 Author's main contribution 8

2 Modes and resonances of electrically small objects 10

2.1 Three-dimensional objects 11
  2.1.1 Electroquasistatic modes and resonances 14
  2.1.2 Magnetoquasistatic modes and resonances 16
2.2 Radiation corrections 19
  2.2.1 3D Plasmonic Resonances 20
  2.2.2 Resonance frequency-shift and Q factor of plasmonic modes . 23
  2.2.3 3D Dielectric resonances 26
  2.2.4 Resonance frequency-shift and Q factor of dielectric modes . . 29
  2.2.5 Sphere 31
2.3 Translational Invariant (TI) objects 37
  2.3.1 TI Plasmonic Resonances 40
  2.3.2 Resonance frequency-shift and Q factor of plasmonic modes . 43
  2.3.3 TI Dielectric Resonances 45
  2.3.4 Resonance frequency-shift and Q factor of dielectric modes . . 47
  2.3.5 Cylinder 49
2.4 Two-dimensional objects (Surfaces) 55
2.5 Conclusions 59

3 Lower Bounds to Quality Factor of Small Radiators 61

3.1 Minimum Q factor of 3D radiators of the electric type 62
  3.1.1 Shapes supporting uniform electrostatic mode 67

3.1.2 Shapes with two reflection symmetries 68
3.1.3 Shapes with no symmetries 70
3.2 Minimum Q factor of 3D radiators of the magnetic type 70
3.2.1 Shapes supporting a MQS mode of the form $\hat{\mathbf{r}} \times \mathbf{c}$ 73
3.2.2 Shapes with two reflection symmetries 73
3.2.3 Shapes with no symmetries 76
3.3 Minimum Q factor of TI radiators of the electric type 77
3.3.1 Shape supporting a uniform EQS mode 78
3.3.2 Shape with reflection symmetry 78
3.4 Minimum Q factor of TI radiators of the magnetic type 80
3.4.1 Shapes supporting a single MQS mode 80
3.4.2 Shape with reflection symmetry 82
3.5 Conclusions 83

4 Material-independent modes 85
4.1 Full-wave modes and resonances 86
4.1.1 Resonance condition. Broad and narrow resonances 89
4.2 Material-independent modes of a sphere 91
4.3 Resonance properties of a sphere 95
4.3.1 Loci of the plasmonic modes 95
4.3.2 Loci of the dielectric modes 97
4.4 Scattering efficiency 101
4.5 Resonances and interferences in Ag spheres 103
4.6 Resonances and interferences in Si spheres 105
4.7 Conclusions 107

5 Full-wave electromagnetic modes and hybridization in nanoparticle dimers 109
5.1 Material-independent modes of a sphere dimer 109
5.2 Modes hybridization 112
5.2.1 Quasistatic hybridization 113
5.2.2 Full-wave hybridization 116
5.3 Resonance properties 122
5.4 Full wave hybridization in Ag and Si dimers 127
5.4.1 Transversely polarized Ag dimer 128
5.4.2 Longitudinally polarized Si dimer 131
5.5 Conclusions 137

A Multipoles **139**
A.1 Three-dimensional objects 139
A.2 Translational invariant objects 140

B Sphere **141**
B.1 Quasistatic regime 141
B.1.1 Solid sphere 141
B.1.2 Spherical shell 143
B.2 Full-wave regime 144
B.2.1 Material-independent modes 144
B.2.2 Scattering coefficients 146

C Quasistatic modes of some translational invariant structures **148**
C.1 Circular cylinder 148
C.2 Cylinder dimer 149

D Sphere dimer **152**
D.1 Methods 152
D.2 Scattering from an Ag dimer in the quasielectrostatic approximation . 157
D.3 Additional results on the homo-dimer with gap size $\Delta = R/4$ 159
D.3.1 Scattered electric field 159
D.3.2 Scattering efficiencies 160
D.4 Scattering from an homo-dimer with gap size $\Delta = R$ 161
D.4.1 Transversely polarized Ag homo-dimer 163
D.4.2 Longitudinally polarized Si homo-dimer 164

Bibliography **167**

Chapter 1

Introduction

Over the last decades, particular interest has been raised by the resonant electromagnetic scattering from metal and dielectric nanostructures.

Metal nanostructures can support coherent oscillations of their free electron plasma, known as localized surface plasmons, which generate a high electric field-enhancement [1, 2]. This property makes them particularly effective in light concentration into deep-subwavelength volumes, enabling the boosting of linear and nonlinear optical processes [3]. This fact stimulates a variety of potential applications, including high-sensitivity biosensors [4], nonlinear optics [5], and energy harvesting [6, 7]. Furthermore, due to their control capabilities of electromagnetic fields at the nanoscale, metals are largely employed in electromagnetic metamaterials, i.e., aggregates of elementary deep-subwavelength units arranged in repeating patterns to provide an unconventional electromagnetic response [8, 9, 10], for a plethora of applications, including cloaking devices [11, 12, 13], analog optical computing [14, 15, 16], super-resolution imaging [17, 18, 19, 20]. Nevertheless, the available metals for these applications, mostly noble metals (e.g., gold and silver), are plagued by high losses at the optical frequencies, which are inhibiting the development of practical devices [21].

Recently, dielectric resonators are gaining increasing attention in nanotechnology, and many researchers currently suggest that high-index dielectrics may be a feasible alternative to noble metals for many applications [22, 23, 24, 25, 26]. This interest has been prompted by the evidence that the enhancement of electric and magnetic fields in dielectric nanostructures is of the same order of magnitude of the one achievable in their metal counterpart. Dielectric objects of small dimensions compared to the free-space wavelength, in fact, may display a resonant behavior, provided their dielectric permittivity is sufficiently high [27, 28, 29]. This fact is well-known at radio frequencies, where low-loss dielectrics with high (≈ 100) relative dielectric permittivity are exploited in several applications, such as resonators and filters [30, 31, 32], while a series of perovskites has been measured at a relative permittivity larger than 1000 [33, 34, 35]. In the visible and near-infrared frequency ranges of the spectrum, resonances in high-index nanostructures, such as AlGaAs, Si, and Ge nanoparticles, have been experimentally observed, e.g., [36, 37, 25], and have been employed in various applications, e.g., [38, 39, 40, 41, 42, 43, 44]. In the nano-optics community, these resonances are known as “Mie resonances” [25].

The physics governing the scattering from high index dielectric nanoparticles is far richer than the physics behind the scattering from metal nanoparticles, due to the possibility of exciting magnetic modes [37, 36, 45, 46] and due to the presence of multimode interference, which may lead to the formation of Fano-resonances [47, 48].

1.1 Motivations for a modal analysis

The understanding of the resonant electromagnetic behavior of nanostructures is elemental for the analysis and engineering of the field-matter interaction. In this direction, the characterization of the scattering by nanostructures in terms of their resonant modes is enlightening. In fact, compared to the direct solution of the scattering problem, the description in terms of resonances and modes, which solely depend on the inherent properties of the nanostructure

- offers intuitive insights into the physics of the problem;
- enables the rigorous comprehension of interference phenomena, including Fano resonances, as the interplay among well-identified modes;
- suggests how to shape the excitation to achieve a prescribed tailoring of the scattering response.

In closed electromagnetic systems, the definition of resonances and modes is straightforward [49]. On the contrary, in open systems, where the electromagnetic field occupies an unbounded domain, this definition is challenging. In an oversimplified but widespread approach, the electromagnetic resonances of a body are found as the peaks of its scattered power spectrum when a frequency-tunable probe field illuminates it. The corresponding electromagnetic field distributions are denoted as “modes”. This approach is flawed for several reasons: it hides the modes that cannot be excited by the chosen incident field; it disregards the fact that a peak can be due to the interplay of two or more modes; it is not useful in the interpretation of the interference phenomena.

Several more rigorous approaches are possible, grounded in different choices of the modes. The quasi-normal modes are the most widely used ones for the investigation of the resonances of open systems [50, 51, 52, 53, 54].They are also known as resonant states [55]. They depend on both the material and the geometry of the scatterer. They are not orthogonal in the usual sense and diverge exponentially at large distances [56], thus they need to be normalized [57, 58, 59]. Another approach, increasingly used in nanophotonics, is represented by the characteristic modes [60, 61, 62, 63]. They are real and satisfy a weighted orthogonality. Moreover, they depend on the frequency, on the geometry, and on the material composition of the scatterer.

An alternative strategy, which we embrace throughout this work of thesis, is the material-independent mode decomposition [64, 65]. The material-independent modes allow separating the role of the geometry, material, and incident electromagnetic field; thus, they provide a very different perspective in the modeling of the resonant electromagnetic behavior of bodies than the aforementioned approaches. They are bi-orthogonal but, unlike the quasi-normal modes, they satisfy by construction the radiation conditions at infinity. Over the years, material-independent modes have been calculated in the quasi-static limit [66, 67, 68, 69, 70, 71, 72], in the long wavelength limit [64], and for the scalar Mie scattering [73]. They have been also derived within the quasi-static [74] and retarded [75] single dipole approximation.

More recently, the material-independent modes have been derived for the full-retarded vector scattering by a homogeneous sphere [65], by a coated sphere [76], by a flat slab [77], and by arbitrary shaped objects [78]. Furthermore, it has been also shown that the investigation of the eigenvalues associated to the material-independent modes unveils important structural properties of plasmonic and dielectric resonances [79]. These modes have also been proved effective in the design the permittivity of the object to pursue a prescribed tailoring of the scattered field, including the cancellation of the backscattering, the suppression of a given multipolar order, and the maximization of the scattered field in the near-field zone [80, 76]. They have been also employed in the modeling of complex lasing media [81].

1.2 Quasistatic modal decomposition

When the object is much smaller than the operating vacuum wavelength, its resonances and resonance modes are well described by the electro- and magneto-quasistatic approximations of the Maxwell's equations.

The electro-quasistatic approximation covers the (plasmon) resonance mechanism occurring in small metal nanoparticles with negative dielectric permittivity, arising from the interplay between the energy stored in the electric field and the kinetic energy of the metal free electrons. In this limit, there exist spectral theories modeling plasmon resonances. For instance, for a spherical nanoparticle of relative dielectric permittivity ε_R, and size much smaller than the incident wavelength, the Fröhlich condition [82], i.e., $\min_{\omega} |\varepsilon_R(\omega) + 2|$, predicts the resonant value of permittivity, and hence of the resonant frequency. Moreover, Mayergoyz et al. [70, 83] introduced a more general electro-quasistatic approach based on a surface integral equation. This approach is applicable to arbitrary shaped particles, whose resonances are associated with negative values of permittivity in correspondence of which source-free solutions exist [70, 84, 85, 86]. The applicability domain of these techniques has been extended through perturbation approaches to include first-order radiation corrections [70, 87].

For the modeling of metallic complex nanostructures, a very popular and useful approach is the plasmon hybridization model [88, 89]. The plasmon hybridization consists in the representation of the modes of a complex plasmonic nanostructure, i.e., "plasmonic molecule", in terms of the modes of its constituent parts, i.e. "plasmonic atoms". Thus, even if the mutual spatial arrangement of the atoms is changed, the modes of the plasmonic molecule are represented in terms of the same set of atomic modes, while only the atomic modes weights change. Many studies have demonstrated that very complex molecular modes arise from the hybridization of just few atomic modes [84, 90, 91, 92, 89].

Instead, dielectric resonators have been traditionally analyzed by using perfect magnetic wall boundary conditions (PMW) [33, 35, 31]. However, because electromagnetic fields do exist beyond the geometrical boundary of the cavity, this condition is unable to accurately predict resonances [93, 94, 95]. Many ad hoc corrections to the PMW conditions have been proposed, including the Cohn model [96], where an idealized waveguide with PMW walls is considered, and the Itoh-Rudokas model [97]. Instead, Van Bladel investigated these resonances without ad hoc assumptions, using an asymptotic expansion of the Maxwell's equation in differential form in terms of the inverse of the index of refraction [27]. Glisson et al. [98, 99] obtained the resonant frequencies of rotationally symmetric dielectric bodies by searching the frequencies at which the determinant of the impedance matrix is zero; they assembled the impedance matrix by discretizing a surface integral formulation of the full-Maxwell equation.

By using an integral formulation, the authors in [100] showed that the resonances of small objects with positive and high permittivity are described by the magneto-quasistatic approximation of the Maxwell's equations, and are due to the interplay between the polarization energy stored in the dielectric and the energy stored in the magnetic field. These resonances are associated with values of permittivity and frequency for which source-free solutions exist, in which the normal component of the displacement current density field vanishes on the surface of the particle.

Each quasistatic resonance also exhibits a radiation Q factor [101], which, in the limit of high Q and noninteracting modes, is equal to the inverse of the fractional bandwidth. In [101], the authors derived closed-form expressions for the frequency shift and radiation Q factor of objects of dimensions smaller than the incident wavelength in terms of the radiation corrections of the quasistatic modes. In the derived expressions, the dependencies on the material and the size of the object are factorized.

The aforementioned material-independent modes for the analysis of scattering from arbitrary sized objects are the full-wave extension of these quasistatic modes. In this framework, the investigation of the resonant modes in plasmonic and dielectric homogeneous nanoparticles of size smaller then the operating wavelength revealed that these resonances are electro- and magneto-quasistatic in nature [102, 100, 101].

For this reason, to provide a complete picture of the modeling of electromagnetic resonances in plasmonic and dielectric objects, we start this thesis with a description of their quasistatic modes, for different geometries. Later, we extend this analysis to the full-retarded scenario, by examining the an isolated sphere and a dimer.

1.3 Quality factor of electrically small objects

The technological advancement in the fabrication process has driven a reduction in the footprint of electromagnetic resonant devices, progressively scaled to fit subwavelength domains [103, 104, 105]. However, this generally comes at the cost of bandwidth (and therefore, e.g., operational speed). This fundamental trade-off between volume, peak field enhancement or scattering, and bandwidth has been investigated using various analytical and numerical methods [106, 107, 108, 109, 110], the most well-known of which is perhaps the Chu limit [111].

The Chu limit determines the minimum radiation quality factor (Q factor) of electrically small radiators, i.e., objects that fit inside a sphere of radius equal to the inverse of the field wave number [112]. This limit does apply to both self-resonant objects, and non self-resonant objects, provided that a convenient tuning network is used. The minimum Q factor is associated with an *optimal current*, which is the particular current density distribution supported by the radiator yielding the minimum Q .

The search for such lower bounds originated with the works of Chu [111], Wheeler [113], and Harrington [114], and several techniques were proposed over the years by many contributors including Collin and Rothschild [115], and McLean [116]. Thal [107] noticed that the previous approaches did not account for either the energy stored within the antenna or for any energy stored in the space between the actual antenna's physical boundary and the enclosing sphere (in cases where they are not the same), thus leading to loose bounds. By including these contributions, he arrived to more strict bounds compared to his predecessors. Then, in a series of contributions, starting in [106], Gustafsson and co-workers provided shape-dependent bounds on the minimum radiator's Q , linking it to the available volume in which the search of the optimal current is constrained. They also reduced the variational problem of finding the minimum Q of radiators to determining the largest eigenvalues of either electric or magnetic polarizability tensors. In the subsequent years, Gustafsson and co-workers refined and extended their original idea [117, 108], including also the very important contributions of Vandenbosch [118, 110]. Efficient numerical determination of optimal currents in terms of a mode expansions was also recently demonstrated [119, 120, 121].

Even though these limits have been originally conceived having small radio-frequency antennas in mind, they are also applicable to optical nanoantennas, which are often self-resonant, as in the case of plasmonic (metal) and dielectric resonators. In the long-wavelength limit, their resonances are well modeled by the quasistatic modes, and their Q factor.

Interestingly, the recent literature on Q factor bounds divides radiators into two categories (e.g., [118, 110, 122]), depending on the characteristics of the currents they support. Radiators of *electric-type* support currents with zero curl, i.e., *longitudinal* currents, while radiators of magnetic type support currents with zero divergence, i.e. *transverse* currents. This distinction naturally applies also to nanoantennas, since the plasmon resonances are driven by longitudinal currents, while the resonances in high-permittivity dielectric objects are driven by transverse currents.

In this work of thesis, we introduce a representation of the optimal current in terms of the quasistatic scattering resonance modes. This representation not only unveils the intimate connection between the optimal current yielding the minimum Q factor and the modes supported by plasmonic and high-permittivity resonators, but has several appealing advantages. A quasistatic mode expansion of the current density leads to analytical and closed form expressions of the electric and magnetic polarizability tensors of arbitrary shaped objects, whose eigenvalues have been linked by Gustafsson and coworkers to the minimum Q . This fact implies that the minimum Q and the corresponding optimal current can be directly determined from the knowledge of the eigenvalues and the dipole moments of quasistatic scattering modes.

1.4 Full-wave hybridization

Interacting nanoparticles, which can be either metallic or dielectric, constitute an example of composite open electromagnetic system. In particular, interacting metal nanoparticles have been extensively investigated [1]: they exhibit larger electric field enhancement with respect to their isolated constituents [3], they feature tunability of the resonance position [123, 124] and of the scattering directionality as the particle arrangement changes, and novel physical properties, such as Fano resonances [47, 125, 126].

As stated in the previous section, the plasmon hybridization theory has been a cornerstone for the modeling of such metal systems, within the electrostatic framework. As such, it is based on compact Hermitian operators and orthogonal electric field modes. This theory is only applicable to metal structures much smaller than the incident wavelength, because the magnetic interactions and radiation effects are not present. In other words, the plasmon resonators are treated as they effectively were *closed* resonators. For this reason, although its validity domain can be extended to include weak radiative contributions by using the aforementioned perturbation approaches [71] or by adding retardation to the Coulomb potential [127], it completely fails to describe dielectric resonators, which are dominated by magnetic interactions [37].

Dielectric particle dimers coupled in the near field zone may exhibit significant enhancement of both electric and magnetic fields [128, 129, 130, 131, 132, 133] with reduced heat conversion [134, 135], directional Fano-resonances [136], and strong directional scattering [137, 138]. A theory of hybridization in silicon (Si) dimers, although limited to electric and magnetic dipole-dipole interactions, has been theoretically proposed in [129] and experimentally validated in [131]. More recently, the hybridization in Si [45] and AlGaAs [139] dimers has been experimentally studied.

An important result of this thesis is the derivation of resonances and modes of a sphere dimer in the full-Maxwell regime [140]. In particular, we extended the scheme proposed by Bergman and Stroud [64], valid only in the long-wavelength limit, when all radii, as well as the interparticle distance, are small compared to the wavelength outside the scatterers. Along the lines of the plasmon hybridization model, we describe the dimer modes as the hybridization of the modes of the two constituent spheres: each dimer mode is expanded in terms of a complex weighted linear combination of a set of isolated-sphere modes. The method here proposed, permits the rigorous modeling of the resonant behavior of either palsmonic or dielectric homogeneous dimers, regardless of their size. This fact enables us to address, for the first time, the mode analysis and the hybridization in silicon dimers in the full-Maxwell regime, and to refine the understanding of plasmon-mode hybridization in a full-wave scenario.

1.5 Author's main contribution

I was the lead contributor to the

- formulation of the theory of hybridization, its numerical implementation, and interpretation of the results [140] (included in the fifth chapter of the present thesis),
- formulation of the spectral theory of a coated sphere, by using material-independent modes [76] (not included in the thesis).

During my stay at the Photonics Initiative at the Advanced Science Research Center, in New York, under the supervision of Prof. Andrea Alù, I developed

- an analysis of the Q factor of singular plasmonic nanoresonators (not included in the thesis),
- a method for the calculation of the minimum Q factor of electrically small radiators, through quasistatic scattering modes (described in the third chapter of the thesis),
- a formalism for the analysis of the resonances and the Q factor of translational invariant structures (included in the second and third chapter of the thesis).

The papers including these results are currently under preparation.

I also contributed to the following works:

- description of resonances in high-permittivity small dielectric objects through magneto-quasistatic scattering modes (included in the second chapter of the thesis) [100];
- description of modes and resonances in two-dimensional (surfaces) bodies (included in the second chapter of the thesis) [102];
- directional scattering cancellation for an electrically large dielectric sphere (not included in the thesis) [141];

- resonances in a long and narrow nanoribbon of finite length (not included in the thesis) [142];
- material-independent modes for the design and analysis of electromagnetic scattering [48, 80] (included in the third chapter of the thesis).

Chapter 2

Modes and resonances of electrically small objects

In the linear regime, a nonmagnetic, homogeneous object, assumed small compared to the incident wavelength in vacuum, may resonate through two mechanisms. The first one occurs in small particles with negative dielectric permittivities, e.g., metals at frequencies near their plasma frequency. For metals, it arises from the interplay between the energy stored in the electric field and the kinetic energy of the free electrons. When the object is very small compared to the wavelength in vacuum, these resonances are well described by the electro-quasistatic approximation of the Maxwell's equations and are associated with the negative values of the dielectric permittivity in correspondence of which source-free solutions exist [71, 143].

The second resonance mechanism occurs in small objects of high and positive dielectric permittivity, and it arises from the interplay between the polarization energy stored in the dielectric and the energy stored in the magnetic field. Manifestation of this kind of resonance can be found at microwave [144, 31] and optical [24, 145] frequencies. When the object is very small compared to the free-space wavelength, and the permittivity is very high, these resonances are well described by the magneto-quasistatic approximation of the Maxwell's equations, where the normal component of the displacement current density field vanishes on the surface of the particle [100].

Each quasistatic resonance mode may be characterized by a *radiation* quality factor (Q factor), which links the stored energy to the energy radiated toward infinity. In the limit of high Q and noninteracting modes, it is equal to the inverse of the fractional bandwidth.

In this chapter, we introduce the electro-quasistatic and magneto-quasistatic modes and resonances of linear, nonmagnetic, homogeneous and isotropic objects, using an integral formulation of the Maxwell's equations. We derive their radiation corrections through means of a perturbation approach, treating the size parameter of the object $x = k_0 \ell_c$, being k_0 the wave number and ℓ_c a characteristic length of the object, as a small parameter. Then, we provide closed-form expressions of the relative resonance frequency shift and the radiation Q factor of the quasistatic modes, as a function of their radiation corrections. We carry out this study for arbitrary shaped three-dimensional (3D) and translational-invariant (TI) objects, and surfaces (2D).

2.1 Three-dimensional objects

Let us consider a linear material occupying a domain Ω, bounded by a closed surface $\partial\Omega$ with normal $\hat{\mathbf{n}}$, sketched in Fig. 2.1. This material is assumed nonmagnetic, isotropic, homogeneous, nondispersive in space, time-dispersive, with relative dielectric permittivity ε_R, and it is surrounded by vacuum. The object is illuminated by a time-harmonic electromagnetic field incoming from infinity $\text{Re}\left\{\mathbf{E}_{\text{inc}}(\mathbf{r})e^{-i\omega t}\right\}$, where ω is the angular frequency. We characterize the electromagnetic scattering from an arbitrary shaped object in the quasistatic regime, starting from the full-wave description.

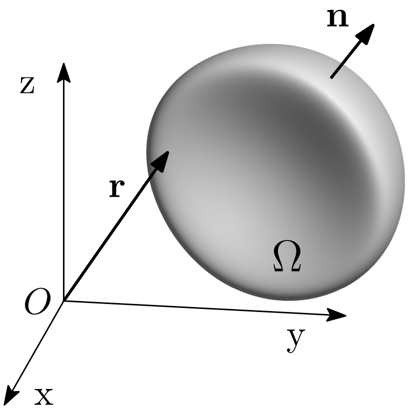

Figure 2.1 – A three-dimensional domain Ω, with normal $\hat{\mathbf{n}}$.

The scattering problem is formulated by considering as unknown the current density field $\mathbf{J}(\mathbf{r})$ induced in the object, which particularizes into: conduction current, in metals at frequencies below interband transitions; polarization current, in dielectrics; sum of conduction and polarization currents, in metals in frequency ranges where interband transitions occur.

We have $\mathbf{J}(\mathbf{r}) = -i\omega\varepsilon_0\chi\mathbf{E}(\mathbf{r})$, where $\mathbf{E}$ is the total electric field (induced and incident), ε_0 is the vacuum permittivity, and $\chi = (\varepsilon_R - 1)$ is the electric susceptibility. Both the vector fields $\mathbf{E}$ and $\mathbf{J}$ are divergence-free (div-free) in Ω due to the homogeneity and isotropy of the material. The current density $\mathbf{J}$ is governed by the full-wave volume integral equation [146, 147, 148]:

$$\frac{\mathbf{J}(\mathbf{r})}{\chi} + \nabla \oint_{\partial\Omega} \mathbf{J}(\mathbf{r}') \cdot \hat{\mathbf{n}}' G\left(\mathbf{r} - \mathbf{r}'\right) \, dS' - k_0^2 \int_{\Omega} \mathbf{J}(\mathbf{r}') G\left(\mathbf{r} - \mathbf{r}'\right) \, dV' \\ = -i\omega\varepsilon_0 \, \mathbf{E}_{\mathrm{inc}}(\mathbf{r}), \quad \forall \mathbf{r} \in \Omega, \quad (2.1)$$

where $k_0 = \omega/c_0$, being c_0 the speed of light in vacuum, and $G\left(\mathbf{r} - \mathbf{r}'\right) = e^{ik_0|\mathbf{r}-\mathbf{r}'|}/4\pi|\mathbf{r} - \mathbf{r}'|$ is the Green's function in vacuum.

The surface integral represents the contribution of the scalar potential to the induced electric field and the volume integral represents the contribution of the vector potential [146]. We introduce the dimensionless size parameter x defined as

$$x = \frac{\omega}{c_0} \ell_c, \quad (2.2)$$

being ℓ_c a characteristic linear length of the region Ω (e.g., the radius of the smallest sphere enclosing the object).

Then, Eq. (2.1) is recast as follows

$$\frac{\mathbf{J}(\mathbf{r})}{\chi} - \mathcal{L}\left\{\mathbf{J}\right\}(\mathbf{r}) = -i\omega\varepsilon_0 \, \mathbf{E}_{\mathrm{inc}}(\mathbf{r}), \quad \forall \mathbf{r} \in \Omega, \quad (2.3)$$

where the spatial coordinates have been normalized by ℓ_c, i.e., $\mathbf{r} \rightarrow \mathbf{r}/\ell_c$,

$$\mathcal{L}\left\{\mathbf{W}\right\}(\mathbf{r}) = -\nabla \oint_{\partial\Omega} \mathbf{W}(\mathbf{r}') \cdot \hat{\mathbf{n}}' g\left(\Delta r, x\right) \, dS' + x^2 \int_{\Omega} \mathbf{W}(\mathbf{r}') g\left(\Delta r, x\right) \, dV', \quad (2.4)$$

Ω is the corresponding scaled domain, ∇ is the scaled gradient operator, and $g\left(\Delta r, x\right)$ is the dimensionless scalar Green's function in vacuum

$$g\left(\Delta r, x\right) = \frac{e^{ix\Delta r}}{4\pi\Delta r}, \quad (2.5)$$

with $\Delta r = |\mathbf{r} - \mathbf{r}'|$.

We now study the solution of Eq. (2.3) in the quasistatic limit, namely for $x \rightarrow 0$. We introduce a complete basis for representing the unknown $\mathbf{J}$, which is obtained from the union of two orthogonal sets [100]. The first set $\{\mathbf{j}_h^{\|}\}$ is given by the solution of the eigenvalue problem

$$\mathcal{L}_e \left\{\mathbf{j}_h^{\|}\right\}(\mathbf{r}) = \frac{1}{\chi_h^{\|}} \mathbf{j}_h^{\|}(\mathbf{r}), \quad \forall \mathbf{r} \in \Omega, \quad (2.6)$$

where $\mathcal{L}_e$ is the *electrostatic integral operator* that gives the electrostatic field as a function of the surface charge density [143]:

$$\mathcal{L}_e\{\mathbf{W}\} = -\nabla \oint_{\partial\Omega} \mathbf{W}(\mathbf{r}') \cdot \hat{\mathbf{n}}' g_0\left(\Delta r\right)\, dS', \tag{2.7}$$

where

$$g_0\left(\Delta r\right) = \frac{1}{4\pi\Delta r} \tag{2.8}$$

is the dimensionless static Green's function in vacuum. The spectrum of $\mathcal{L}_e$ is countable infinite [143], and the eigenfunctions $\{\mathbf{j}_h^{\|}\}_{h\in\mathbb{N}}$ are *longitudinal* vector fields: they are both div-free and curl-free in Ω but have nonvanishing normal component to $\partial\Omega$ [71]. Moreover, $\mathcal{L}_e$ is self-adjoint and definite negative, therefore the eigenvalues $\chi_h^{\|}$ are real and negative, and the eigenfunctions are orthogonal according to the scalar product

$$\langle \mathbf{A}, \mathbf{B} \rangle_\Omega = \int_\Omega \mathbf{A} \cdot \mathbf{B}\, dV. \tag{2.9}$$

We then assume this set orthonormal, i.e.,

$$\langle \mathbf{j}_h^{\|}, \mathbf{j}_k^{\|} \rangle_\Omega = \delta_{h,k}, \tag{2.10}$$

where $\delta_{h,k}$ is the Kronecker delta function.

To complete the basis for the vector space of square integrable div-free functions in Ω, it is sufficient to add to $\{\mathbf{j}_h^{\|}\}$ a set of *transverse* vector fields $\{\mathbf{j}_h^{\perp}\}$, which are div-free in Ω, with vanishing normal component to $\partial\Omega$, i.e.

$$\mathbf{j}_h^{\perp} \cdot \hat{\mathbf{n}} \Big|_{\partial\Omega} = 0, \tag{2.11}$$

and are solutions of the eigenvalue problem in weak form

$$\mathcal{L}_m \left\{ \mathbf{j}_h^{\perp} \right\} (\mathbf{r}) = \frac{1}{\kappa_h^{\perp}} \mathbf{j}_h^{\perp}(\mathbf{r}), \quad \forall \mathbf{r} \in \Omega, \tag{2.12}$$

where $\mathcal{L}_m$ is the *magnetostatic integral operator*

$$\mathcal{L}_m\{\mathbf{W}\}(\mathbf{r}) = \int_\Omega \mathbf{W}(\mathbf{r}') g_0\left(\Delta r\right)\, dV'. \tag{2.13}$$

$\mathcal{L}_m$ has a countable infinite spectrum, and is self-adjoint and definite positive, therefore the eigenvalues $\{\kappa_h^{\perp}\}_{h\in\mathbb{N}}$ are real and positive, and the eigenfunctions $\{\mathbf{j}_h^{\perp}\}_{h\in\mathbb{N}}$

are orthogonal according to the scalar product (2.9), and assumed normalized, i.e.

$$\langle \mathbf{j}_h^{\perp}, \mathbf{j}_k^{\perp} \rangle_\Omega = \delta_{h,k}. \tag{2.14}$$

Furthermore, the eigenfunctions $\{\mathbf{j}_h^{\perp}\}$ are orthogonal to the eigenfunctions $\{\mathbf{j}_h^{\|}\}$. Both the sets of eigenvalues-eigenfunctions of the operators $\mathcal{L}_e$ and $\mathcal{L}_m$ are material independent, and do not depend on the size of the object, but only on its shape.

The union of the two sets $\{\mathbf{j}_h^{\|}\}$ and $\{\mathbf{j}_h^{\perp}\}$ is a complete basis for the vector space of square integrable div-free vector fields in Ω. Therefore, the current density $\mathbf{J}$ in the quasistatic regime ($x \rightarrow 0$) can be expressed as

$$\mathbf{J} = -i\omega\varepsilon_0\chi \sum_{h=1}^{\infty} \left[\frac{\chi_h^{\|}}{\chi_h^{\|} - \chi} \langle \mathbf{j}_h^{\|}, \mathbf{E}_{\text{inc}} \rangle_\Omega \, \mathbf{j}_h^{\|} + \frac{\kappa_h^{\perp}}{\kappa_h^{\perp} - x^2\chi} \langle \mathbf{j}_h^{\perp}, \mathbf{E}_{\text{inc}} \rangle_\Omega \, \mathbf{j}_h^{\perp} \right]. \tag{2.15}$$

This expansion disentangles the dependence on the material, in the form of polynomial functions of χ, from the dependence on the geometry, buried in the material independent eigenvalue-eigenfunction systems [64].

The expression of the current density $\mathbf{J}$ clearly highlights two distinct resonance conditions for χ, arising from different physical mechanisms: the first one is

$$\operatorname{Re}\{\chi\} = \chi_h^{\|}, \tag{2.16}$$

with the resonant excitation of the eigenfunction $\mathbf{j}_h^{\|}$; the second one is

$$\operatorname{Re}\{\chi\} = \frac{\kappa_h^{\perp}}{x^2}, \tag{2.17}$$

with the resonant excitation of the eigenfunction $\mathbf{j}_h^{\perp}$.

Thus, the sets $\{\mathbf{j}_h^{\|}\}$ and $\{\mathbf{j}_h^{\perp}\}$ can be interpreted as the *density current modes* of the body in the quasistatic limit, and $\{\chi_h^{\|}\}$ and $\{\kappa_h^{\perp}/x^2\}$ can be interpreted as the corresponding *eigen-susceptibilities.* The scalar products $\langle \mathbf{j}_h^{\|}, \mathbf{E}_{\text{inc}} \rangle$ and $\langle \mathbf{j}_h^{\perp}, \mathbf{E}_{\text{inc}} \rangle$ in Eq. (2.15) describe the coupling of the current modes with the external excitation.

2.1.1 Electroquasistatic modes and resonances

We now investigate in detail the electro-quasistatic resonances associated with the eigenvalues $\chi_h^{\|}$ and the eigenfunctions $\mathbf{j}_h^{\|}$ of the electrostatic integral operator $\mathcal{L}_e$ in Eq. (2.6). We call the eigenfunctions $\mathbf{j}_h^{\|}$ electroquasistatic (EQS) current modes, and the eigenvalues $\chi_h^{\|}$ EQS eigen-susceptibilities.

The EQS current modes $\mathbf{j}_h^{\|}$ are longitudinal vector fields: they are square integrable in Ω ($\mathbf{j}_h^{\|} \in \mathbf{L}^2(\Omega)$), and are both curl-free and div-free within the object, but have nonvanishing normal component to the object surface, i.e., $\mathbf{j}_h^{\|} \in \mathbf{L}_{\|}^2(\Omega)$,

$$\mathbf{L}_{\|}^2(\Omega) = \left\{ \mathbf{L}^2(\Omega) \,|\, \nabla \cdot \mathbf{j}^{\|} = 0, \nabla \times \mathbf{j}^{\|} = \mathbf{0} \text{ in } \Omega \setminus \partial\Omega \right\}. \tag{2.18}$$

The normal component of $\mathbf{j}_h^{\|}$ to the object's boundary is related to the induced surface charge density on $\partial\Omega$, and satisfies the *charge-neutrality* condition, namely

$$\oint_{\partial\Omega} \mathbf{j}_h^{\|} \cdot \hat{\mathbf{n}} \, dS = 0. \tag{2.19}$$

An important property of the spectrum of $\mathcal{L}_e$ is that the eigenvalues $\chi_h^{\|}$ accumulate at a finite value [71], specifically

$$\lim_{h \rightarrow +\infty} \chi_h^{\|} = -2, \tag{2.20}$$

independently from the shape of the object. For a time-dispersive metal described by the Drude model [1]

$$\chi = -\frac{\omega_p^2}{\omega(\omega + i\nu)}, \tag{2.21}$$

where ω_p and $\nu \ll \omega_p$ are the plasma and collision angular frequencies, the resonance frequencies corresponding to the eigen-susceptibilities $\chi_h^{\|}$ accumulate at $\omega_p/\sqrt{2}$, being ω_p the plasma frequency of the metal.
Under the normalization (2.10), i.e., $\left\| \mathbf{j}_h^{\|} \right\|_\Omega = 1$[1], the scaled [2] electrostatic energy of the h-th EQS current mode $\mathbf{j}_h^{\|}$ is

$$\mathcal{W}_e \left\{ \mathbf{j}_h^{\|} \right\} = -\frac{1}{2\varepsilon_0} \oint_{\partial\Omega} \oint_{\partial\Omega} g_0 \left(\Delta r\right) \sigma_h(\mathbf{r}) \sigma_h(\mathbf{r}') dS' dS = \frac{1}{2\varepsilon_0} \frac{1}{\left(-\chi_h^{\|}\right)}, \tag{2.22}$$

where $\sigma_h = \mathbf{j}_h^{\|} \cdot \hat{\mathbf{n}}$ is the surface charge density related to the h-th EQS current mode.

The electric dipole moment $\mathbf{P}_h$ of the EQS current mode $\mathbf{j}_h^{\|}$ is defined as [3]

$$\mathbf{P}_h = \int_\Omega \mathbf{j}_h^{\|} dV = \oint_{\partial\Omega} \mathbf{r} \left(\mathbf{j}_h^{\|} \cdot \hat{\mathbf{n}} \right) dS. \tag{2.23}$$

If the mode $\mathbf{j}_h^{\|}$ exhibits a vanishing electric dipole moment $\mathbf{P}_h$, it is called *dark*,

---

[1] $\left\| \cdot \right\|_\Omega$ is the norm induced by the scalar product in Eq. 2.9, namely $\left\| \mathbf{j}_h^{\|} \right\|_\Omega^2 = \langle \mathbf{j}_h^{\|}, \mathbf{j}_h^{\|} \rangle_\Omega$.

[2] To obtain the dimension of an energy, we have to multiply for $\frac{\ell_c^3}{\omega^2}$.

[3] With respect to the standard definitions of surface charge density and electric multipoles [149], the prefactor $1/(-i\omega)$ is omitted.

otherwise *bright*. When the object exhibits a density current mode that is spatially uniform in Ω, and directed along a given direction $\mathbf{c}$ (as it happens for instance for a sphere or a spheroid), the orthogonality condition (2.10) implies that all the remaining current modes exhibit a vanishing electric dipole moment along that specific direction, namely

$$\int_\Omega \mathbf{c} \cdot \mathbf{j}_k^{\parallel}\, dV = \mathbf{c} \cdot \mathbf{P}_k = 0. \tag{2.24}$$

Since the EQS operator $\mathcal{L}_e$ is definite negative, its eigen-susceptibilities are negative valued, therefore, according to the resonance condition (2.16), the corresponding current modes $\{\mathbf{j}_h^{\parallel}\}$ can be resonantly excited only in objects with negative dielectric permittivity, e.g., in metal nanoparticles at frequencies near their plasma frequency. For metals, they correspond to the resonant plasmon modes, deriving from the interplay between the energy stored in the electric field and the kinetic energy of the free electrons [143].

2.1.2 Magnetoquasistatic modes and resonances

We now investigate in detail the resonance mechanism associated with the eigenvalues $\kappa_h^{\perp}$ and the eigenfunctions $\mathbf{j}_h^{\perp}$ of the integral operator $\mathcal{L}_m$ in Eq. (2.13), which is magnetostatic in nature.

Indeed, we now briefly prove that the eigenfunctions $\mathbf{j}_h^{\perp}$ are source-free solutions of the Maxwell's equations in high-permittivity dielectric objects, in the limit $x \ll 1$ (small object), where x is the size parameter of the object, introduced in Eq. (2.2). Under these conditions, the electromagnetic field is primarily determined by the displacement current density field $\mathbf{J}$ induced inside the object itself [27]. Thus, we look for the values of the parameter $\beta = (x/\ell_c)^2\chi$ for which there exists a nontrivial solution of the source-free magnetoquasistatic (MQS) problem [150]

$$\nabla \times \mathbf{A} = \mu_0 \mathbf{H}, \tag{2.25a}$$

$$\nabla \times \mathbf{H} = \mathbf{J}, \tag{2.25b}$$

with the constitutive relation

$$\mathbf{J} = \frac{\beta}{\mu_0}\mathbf{A}\Pi_\Omega, \tag{2.26}$$

where $\chi = (\varepsilon_R - 1)$ is the electric susceptibility, Π_Ω is the characteristic function on the set Ω, i.e., $\Pi_\Omega = 1$ for $\mathbf{r} \in \Omega$ and 0 otherwise, μ_0 is the magnetic permeability in vacuum. The MQS vector potential $\mathbf{A}$ satisfies the Coulomb gauge ($\nabla \cdot \mathbf{A} = 0$) in Ω and $\mathrm{R}^3 \setminus \Omega$, and both $\mathbf{A}$ and the magnetic field $\mathbf{H}$ are regular at infinity. Equation

(2.26) disregards the effects of the displacement current density field in vacuum. Since the normal component of the current density field **J** at the boundary is equal to zero, the current density field **J** is div-free everywhere in R^3; on the contrary, the normal component of the vector potential at $\partial\Omega$ may be discontinuous. The fact that **J** has a vanishing normal component on $\partial\Omega$ implies also that the normal component of the polarization current density field is zero.

After scaling the spatial coordinates by the characteristic length ℓ_c ($\mathbf{r} \to \mathbf{r}/\ell_c$), problems (2.25) and (2.26) are solved by expressing the vector potential **A** in terms of the current density **J** as

$$\mathbf{A}(\mathbf{r}) = \mu_0 \ell_c^2 \mathcal{L}_m \left\{\mathbf{J}\right\}(\mathbf{r}), \tag{2.27}$$

where $\mathcal{L}_m$ is the MQS integral operator in Eq. (2.13), in which the presence of the static Green's function g_0 is due to having neglected the displacement current density in vacuum. By combining Eqs. (2.26) and (2.27), we obtain the linear eigenvalue problem

$$\mathcal{L}_m \left\{\mathbf{J}\right\}(\mathbf{r}) = \frac{1}{\kappa^\perp}\mathbf{J}(\mathbf{r}), \quad \forall \mathbf{r} \in \Omega, \tag{2.28}$$

with

$$\mathbf{J} \cdot \hat{\mathbf{n}}|_{\partial\Omega} = 0, \tag{2.29}$$

where $\kappa^\perp = x^2\chi$. We recognize the eigenvalue problem (2.12) with the constraint (2.11). Consequently, we call the eigenfunctions $\mathbf{j}_h^\perp$ MQS current modes, and $\kappa_h^\perp/x^2$ MQS eigen-susceptibilities. It is important to remind that Eq. (2.28) holds in the weak form in the functional space equipped with the inner product (2.9), and constituted by the *transverse* vector fields which are square integrable and div-free within Ω and have zero normal component to $\partial\Omega$ [100], i.e.

$$\mathbf{L}_\perp^2(\Omega) = \left\{ \mathbf{L}^2(\Omega) \,|\, \nabla \cdot \mathbf{j}^\parallel = 0, \text{ in } \Omega \setminus \partial\Omega \text{ and } \mathbf{j}^\perp \cdot \hat{\mathbf{n}} = \mathbf{0} \text{ on } \partial\Omega \right\}. \tag{2.30}$$

The integral operator $\mathcal{L}_m$ is compact, positive definite, and self-adjoint. Therefore, Eq. (2.12) admits a countable set of eigenvalues $\left\{\kappa_h^\perp\right\}_{h\in\mathbb{N}}$ real and positive, accumulating at infinity, namely

$$\lim_{h\to+\infty} \kappa_h^\perp = +\infty, \tag{2.31}$$

independently from the shape of the object. The integral operator $\mathcal{L}_m$, and hence its eigenvalues, depend on the chosen spatial coordinates normalization. Specifically, the eigenvalues $\kappa_h^\perp$ increase quadratically with ℓ_c.

The MQS current modes $\mathbf{j}_h^\perp$ are dark, i.e., have zero electric dipole moment according to the definition (2.23). Assuming the current modes to be unit vectors ($\left\|\mathbf{j}_h^\perp\right\|_\Omega = 1$), the scaled[4] magnetostatic energy of the h-th MQS current mode is

$$\mathcal{W}_m\{\mathbf{j}_h^\perp\} = \frac{1}{2}\int_\Omega \mathbf{j}_h^\perp \cdot \mathbf{A}\{\mathbf{j}_h^\perp\} dV = \frac{\mu_0}{8\pi}\int_\Omega \mathbf{j}_h^\perp(\mathbf{r}) \cdot \int_\Omega \frac{\mathbf{j}^\perp(\mathbf{r}')}{\Delta r} dV' dV = \frac{\mu_0}{2}\frac{1}{\kappa_h^\perp}. \quad (2.32)$$

The magnetic dipole moment $\mathbf{M}_h$ of the h-th MQS current mode $\mathbf{j}_h^\perp$ is defined as

$$\mathbf{M}_h = \frac{1}{2}\int_\Omega \mathbf{r} \times \mathbf{j}_h^\perp \, dV. \quad (2.33)$$

If the resonator supports a mode of the form $\mathbf{j}_h^\perp = \hat{\mathbf{r}} \times \mathbf{c}$, where $\mathbf{c}$ is a constant vector, the orthogonality condition (2.14) implies that the generic remaining current mode $\mathbf{j}_k^\perp$ has a vanishing magnetic dipole moment along $\mathbf{c}$, i.e.,

$$\frac{1}{2}\int_\Omega \mathbf{j}_k^\perp \cdot (\hat{\mathbf{r}} \times \mathbf{c}) \, dV = \mathbf{c} \cdot \mathbf{M}_k = 0. \quad (2.34)$$

Among the set of MQS current modes, there exists a subset of modes generating a transverse vector potential $\mathbf{A}\left\{\mathbf{j}_h^\perp\right\}$, i.e., with zero normal component to $\partial\Omega$:

$$\hat{\mathbf{n}} \cdot \mathbf{A}\left\{\mathbf{j}_h^\perp\right\}\Big|_{\partial\Omega} = 0. \quad (2.35)$$

We refer to a MQS mode belonging to this subset as $\mathbb{A}^\perp$-mode. The $\mathbb{A}^\perp$-modes are also solution of the problem (2.28) in a strong form (in the space of square integrable vector fields).

The resonance angular frequencies ω_h, given by

$$\omega_h = \frac{c_0}{\ell_c}\sqrt{\frac{\kappa_h^\perp}{\chi}}. \quad (2.36)$$

accumulate at infinity, in contrast to the EQS resonance frequencies which accumulate at a finite value ($\omega_p/\sqrt{2}$, if the object is filled with a Drude metal with plasma frequency ω_p). Moreover, the following bound on the eigenvalues hold:

$$\kappa_h^\perp \geq \frac{\sqrt{3}}{4\pi}\frac{1}{a^2}, \qquad \forall h \in \mathbb{N}, \quad (2.37)$$

where a is the radius of a sphere B_a having the same volume of Ω. The inequality

---

[4] To obtain the dimension of an energy, we have to multiply for ℓ_c^5.

(2.37) is obtained by multiplying both members of Eq. (2.28) by $\mathbf{j}_h^{\perp}$, assumed normalized according to Eq. (2.14), integrating over Ω and using the Cauchy-Schwarz inequality and the inequality [151]

$$\int_{\Omega} \frac{1}{\left|\mathbf{r}-\mathbf{r}'\right|^2} dV' \leq \int_{B_a} \frac{1}{\left|\mathbf{r}'\right|^2} dV' = 4\pi a, \qquad \forall \mathbf{r} \in \Omega. \tag{2.38}$$

Therefore, given the inequality in Eq. (2.37) and the resonance condition (2.17), the MQS current modes $\{\mathbf{j}_h^{\perp}\}$ can be resonantly excited in electrically small objects ($x \ll 1$) only with positive and high dielectric permittivities.

In the MQS resonances in dielectrics, the energy oscillates back and forth between the polarization energy of the dielectric and the magnetic energy. In fact, by combining Eqs. (2.32) and (2.36) we obtain

$$\frac{\ell_c^3}{\omega_h^2} \mathcal{W}_m\{\mathbf{j}_h^{\perp}\} = \frac{\ell_c^3}{2\varepsilon_0} \frac{\left\|\mathbf{j}_h^{\perp}\right\|_{\Omega}^2}{\omega_h^2 \chi}. \tag{2.39}$$

The left-hand side is the energy stored in the magnetic field associated with the current mode $\mathbf{j}_h^{\perp}$, while the right-hand side is the energy stored in the dielectric in the form of polarization energy at the resonance frequency ω_h.

2.2 Radiation corrections

Any resonant scattering mechanism in arbitrary sized object is associated with the solutions of the eigenvalue problem [65]

$$\mathcal{L}\{\mathbf{j}_h\} = \frac{1}{\gamma_h} \mathbf{j}_h, \tag{2.40}$$

where $\mathcal{L}$ is the full-retarded integral operator given Eq. (2.4), whose properties will be discussed in depth in Chapter 3. In the previous section, we show that in the quasistatic limit $x \rightarrow 0$, this eigenvalue problem splits into the EQS eigenvalue problem (2.6) and the MQS eigenvalue problem (2.13). Starting from this property, we introduce a classification of the eigenvalues of Eq. 2.40:

- The eigenfunctions of $\mathcal{L}$ that in the limit $x \rightarrow 0$ tend to the EQS modes are indicated with $\{\mathbf{u}_h\}$, and the corresponding eigenvalues are indicated with $\{\chi_h\}$. These eigenfunctions are called *plasmonic modes*.
- Dually, the set of eigenfunctions of $\mathcal{L}$ that in the limit $x \rightarrow 0$ tend to the MQS modes are indicated with $\{\mathbf{v}_h\}$, and the corresponding eigenvalues are indicated

with κ_h/x^2. Although in the limit $x \to 0$, the eigenvalues κ_h/x^2 diverge, the quantities κ_h remain constant. These eigenfunctions are called *dielectric modes.*

The union of the two sets $\{\mathbf{u}_h\}$ and $\{\mathbf{v}_h\}$ is a basis for the unknown current density field in Eq. (2.1). Its solution is expressed as

$$\mathbf{J} = -i\omega\varepsilon_0\chi \sum_{h=1}^{\infty} \left[\frac{\chi_h}{\chi_h - \chi} \langle \mathbf{u}_h, \mathbf{E}_{inc} \rangle_\Omega \, \mathbf{u}_h + \frac{\kappa_h}{\kappa_h - \chi x^2} \langle \mathbf{v}_h, \mathbf{E}_{inc} \rangle_\Omega \, \mathbf{v}_h \right] \tag{2.41}$$

where both the sets of modes $\{\mathbf{u}_h\}$ and $\{\mathbf{v}_h\}$ are normalized such that $\langle \mathbf{u}_h, \mathbf{u}_h \rangle_\Omega = 1$ and $\langle \mathbf{v}_h, \mathbf{v}_h \rangle_\Omega = 1 \ \forall h$. This equation tends to Eq. (2.15) in the quasistatic limit $x \to 0$.

We now introduce a perturbation technique to evaluate the plasmonic and dielectric resonances and resonance modes of an arbitrary shaped three- dimensional electrically having a dimension smaller than or almost equal to the operating wavelength, namely with size parameter $x < 1$, by starting from the corresponding resonances and resonance modes in the quasistatic regime. Moreover, we will iterate the procedure up to the first real and imaginary radiative corrections of the quasistatic eigenvalues, which we will demonstrate to be related to the frequency-shift and the radiation Q factor of the current modes, respectively. The full derivation of the procedure can be found in [101].

2.2.1 3D Plasmonic Resonances

To evaluate the plasmonic resonances of three-dimensional small particles, it is convenient to recast the eigenvalue problem (2.40) as

$$\mathbf{u}_h(\mathbf{r}) + \chi_h \left[\nabla \oint_{\partial\Omega} \mathbf{u}_h(\mathbf{r}') \cdot \hat{\mathbf{n}}' g\left(\Delta r, x\right) \, dS' - x^2 \int_\Omega \mathbf{u}_h(\mathbf{r}') g\left(\Delta r, x\right) dV' \right] = \mathbf{0}, \quad \forall \mathbf{r} \in \Omega. \tag{2.42}$$

When the free-space wavelength $\lambda = 2\pi c_0/\omega$ is large in comparison with the characteristic dimension ℓ_c, the size parameter x can be treated as a small parameter, and the Green function $g\left(\Delta r, x\right)$, the current mode $\mathbf{u}_h$, and the eigenvalue χ_h can all be expanded in terms of x in the neighborhood of the EQS resonance with eigenvalue

$\chi_h^{\parallel}$ and mode $\mathbf{j}_h^{\parallel}$:

$$\chi_h = \sum_{k=0}^{\infty} \chi_h^{(k)} x^k \,, \tag{2.43}$$

$$\mathbf{u}_h = \sum_{k=0}^{\infty} \mathbf{u}_h^{(k)} x^k \,, \tag{2.44}$$

$$g\left(\Delta r, x\right) = \frac{1}{4\pi} \sum_{k=0}^{\infty} i^k \frac{\Delta r^{k-1}}{k!} x^k \,, \tag{2.45}$$

where $\chi_h^{(0)} = \chi_h^{\parallel}$ and $\mathbf{u}_h^{(0)} = \mathbf{j}_h^{\parallel}$.
By using Eqs. (2.43-2.45), Eq. (2.42) becomes

$$\begin{aligned} 4\pi \sum_{k=0}^{\infty} \mathbf{u}_h^{(k)} x^k + \sum_{k=0}^{\infty} \chi_h^{(k)} x^k \Bigg[\nabla \oint_{\partial\Omega} \left(\sum_{k=0}^{\infty} i^k \frac{\Delta r^{k-1}}{k!} x^k \right) \left(\sum_{k=0}^{\infty} u_{n,h}^{(k)} x^k \right) dS' \\ - \int_{\Omega} \left(\sum_{k=0}^{\infty} i^k \frac{\Delta r^{k-1}}{k!} x^k \right) \left(\sum_{k=0}^{\infty} \mathbf{u}_h^{(k)} x^{k+2} \right) dV' \Bigg] = 0, \qquad \forall \mathbf{r} \in \Omega, \end{aligned} \tag{2.46}$$

where $u_{n,h}^{(k)} = \mathbf{u}_h^{(k)} \cdot \mathbf{n}\big|_{\partial\Omega}$ and $\chi_h^{(0)} = \chi_h^{\parallel}$.

Matching the first-order terms in Eq. (2.46), and applying the charge neutrality condition (2.19), the following integrodifferential equation is obtained:

$$\mathbf{u}_h^{(1)} + \frac{\chi_h^{\parallel}}{4\pi} \nabla \oint_{\partial\Omega} \frac{\mathbf{u}_h^{(1)}(\mathbf{r}') \cdot \hat{\mathbf{n}}'}{\Delta r} dS' = -\frac{\chi_h^{(1)}}{4\pi} \left(\nabla \oint_{\partial\Omega} \frac{j_{n,h}^{\parallel}(\mathbf{r}')}{\Delta r} dS' \right), \quad \forall \mathbf{r} \in \Omega, \tag{2.47}$$

where the scalar field $j_{n,h}^{\parallel} = \mathbf{j}_h^{\parallel} \cdot \hat{\mathbf{n}}\big|_{\partial\Omega}$ is defined on the object's surface $\partial\Omega$. Since $\chi_h^{\parallel}$ is an eigenvalue of the left-hand side of Eq. (2.47), a solution to (2.47) exists only under the condition that its right-hand side is orthogonal to the corresponding current mode $\mathbf{j}_h^{\parallel}$, according to the scalar product introduced in Eq. (2.9). This is the so-called *normal solvability condition* of Fredholm integral equations [152, 153]. Consequently,

$$\frac{\chi_h^{(1)}}{4\pi} \nabla \int_{\Omega} \mathbf{j}_h^{\parallel}(\mathbf{r}) \cdot \left(\int_{\partial\Omega} \frac{j_{n,h}^{\parallel}(\mathbf{r}')}{\Delta r} dS' \right) dV = \frac{\chi_h^{(1)}}{\chi_h^{\parallel}} \left\| \mathbf{j}_h^{\parallel} \right\|^2 = 0, \tag{2.48}$$

where Eq. (2.6) has been used. Thus Eq. (2.47) is only solvable if

$$\chi_h^{(1)} = 0. \tag{2.49}$$

Regardless of the object's shape, the first-order correction to EQS eigenvalues vanishes. As a result of (2.49), Eq. (2.47) only admits the trivial solution

$$\mathbf{u}_h^{(1)}(\mathbf{r}) = \mathbf{0} \qquad \forall \mathbf{r} \in \Omega. \tag{2.50}$$

Collecting the second-order terms in Eq. (2.46), and applying the normal solvability condition, the second-order correction $\chi_h^{(2)}$ is derived

$$\chi_h^{(2)} = -\frac{\left(\chi_h^{\parallel}\right)^2}{4\pi}\left[\oint_{\partial\Omega} j_{n,h}^{\parallel}(\mathbf{r}) \oint_{\partial\Omega} \frac{\Delta r}{2} j_{n,h}^{\parallel}(\mathbf{r}')dS'dS + \int_{\Omega} \mathbf{j}_h^{\parallel}(\mathbf{r}) \cdot \int_{\Omega} \frac{\mathbf{j}_h^{\parallel}(\mathbf{r}')}{\Delta r}\, dV'dV\right], \tag{2.51}$$

where the scalar field $j_{n,h}^{\parallel} = \mathbf{j}_h^{\parallel} \cdot \hat{\mathbf{n}}\big|_{\partial\Omega}$ is defined on the object's surface $\partial\Omega$. According to Eq. (2.51), $\chi_h^{(2)}$ is real. Moreover, the first term in parenthesis in Eq. (2.51) originates from the radiative self-interaction of the surface charge density associated with the EQS current mode through the scalar potential. The second term is instead proportional to the magnetostatic energy of the EQS current mode $\mathbf{j}_h^{\parallel}$. Eq. (2.51) is in agreement with the second-order correction to the EQS modes derived in [71] by expanding the Maxwell's equation in differential form. It will be demonstrated in Eq. (2.60) that $\chi_h^{(2)}$ is associated with the frequency-shift of the h-th plasmonic mode.

The second-order correction of the associated plasmonic mode $\mathbf{u}_h^{(2)}$ has both longitudinal and transverse components, denoted as $\mathbf{u}_h^{(2)\parallel}$ and $\mathbf{u}_h^{(2)\perp}$, respectively:

$$\mathbf{u}_h^{(2)} = \mathbf{u}_h^{(2)\parallel} + \mathbf{u}_h^{(2)\perp} = \sum_{\substack{k=1 \\ k\neq h}}^{\infty} \alpha_{h,k}^{(2)} \mathbf{j}_k^{\parallel} + \sum_{k=1}^{\infty} \beta_{h,k}^{(2)} \mathbf{j}_k^{\perp}, \tag{2.52}$$

where the longitudinal part $\mathbf{u}_h^{(2)\parallel}$ is represented in terms of the EQS mode basis $\left\{\mathbf{j}_k^{\parallel}\right\}_{k\in\mathbb{N}}$, and the transverse part $\mathbf{u}_h^{(2)\perp}$ in terms of the MQS mode basis $\left\{\mathbf{j}_k^{\perp}\right\}_{k\in\mathbb{N}}$. Assuming the eigenvalues nondegenerate, the expansion coefficients are:

$$\begin{aligned}\alpha_{h,k}^{(2)} = \frac{1}{4\pi}\frac{\chi_k^{\parallel}\chi_h^{\parallel}}{\chi_k^{\parallel}-\chi_h^{\parallel}}&\left[\oint_{\partial\Omega} j_{n,h}^{\parallel}(\mathbf{r}) \oint_{\partial\Omega} \frac{\Delta r}{2} j_{n,k}^{\parallel}(\mathbf{r}')dS'dS\right. \\ &\left.+\int_{\Omega} \mathbf{j}_h^{\parallel}(\mathbf{r}) \cdot \int_{\Omega} \frac{\mathbf{j}_k^{\parallel}(\mathbf{r}')}{\Delta r}\, dV'dV\right], \qquad \forall k \neq h \end{aligned} \tag{2.53}$$

$$\beta_{h,k}^{(2)} = \frac{\chi_h^{\parallel}}{4\pi}\int_{\Omega} \mathbf{j}_h^{\parallel}(\mathbf{r}) \cdot \int_{\Omega} \frac{\mathbf{j}_k^{\perp}(\mathbf{r}')}{\Delta r}\, dV'dV, \qquad \forall k \in \mathbb{N}. \tag{2.54}$$

Matching the third-order terms in Eq. (2.46), the third-order correction $\chi_h^{(3)}$ is obtained:

$$\chi_h^{(3)} = -i\frac{\left(\chi_h^{\parallel}\right)^2}{6\pi}|\mathbf{P}_h|^2, \tag{2.55}$$

which is purely imaginary and proportional to the squared magnitude of the electric dipole moment $\mathbf{P}_h$ of the h-th EQS mode, defined in Eq. (2.23). As it will be demonstrated in Eq. (2.62), $\chi_h^{(3)}$ determines the radiation Q factor of the h-th bright plasmonic mode. However, for dark plasmonic modes, $\chi_h^{(3)}$ vanishes, and a higher order perturbation, depending on a higher order multipole moment of the EQS current mode, has to be considered. Specifically, in this case it is mandatory to consider the fifth order perturbation $\chi_h^{(5)}$. For dark modes, it can be expressed in terms of the electric quadrupole tensor $\overleftrightarrow{\mathbf{Q}}_{\mathrm{E}|h}^{\parallel}$ of the EQS mode, and its components $Q_{\mathrm{E}|h|ij}$:

$$\chi_h^{(5)} = -i\frac{\left(\chi_h^{\parallel}\right)^2}{80\pi}\left[\sum_{i,j=1}^{3}\left(Q_{\mathrm{E}|h|ij}\right)^2 - \frac{1}{3}\mathrm{Tr}\left(\overleftrightarrow{\mathbf{Q}}_{\mathrm{E}|h}^{\parallel}\right)^2\right] \tag{2.56}$$

where Tr is the trace operator, and $\overleftrightarrow{\mathbf{Q}}_{\mathrm{E}|h}^{\parallel}$ is defined by Eq. (A.2) of the Appendix A. Thus, the fifth order correction is purely imaginary and proportional to the power radiated by a quadrupole.

The outlined procedure can be iteratively applied: if the fifth order correction vanishes, the next order correction that may give an imaginary contribution is the seventh, which can be calculated by matching the terms of the corresponding order in Eq. (2.46).

2.2.2 Resonance frequency-shift and Q factor of plasmonic modes

Let us now assume that the object is made of a time-dispersive metal, whose susceptibility χ is described by the Drude model in Eq. (2.21), with plasma frequency ω_p and collision frequency $\nu \ll \omega_p$. The EQS resonance frequency $\omega_h^{\parallel}$ of the h-th mode, is generally defined as the frequency at which the real part of the metal susceptibility $\mathrm{Re}\left\{\chi\left(\omega\right)\right\}$ matches the EQS eigenvalue $\chi_h^{\parallel}$; in the Drude case

$$\frac{x_h^{\parallel}}{x_p} = \frac{\omega_h^{\parallel}}{\omega_p} = \frac{1}{\sqrt{-\chi_h^{\parallel}}}, \tag{2.57}$$

where $x_h^{\parallel} = \omega_h^{\parallel}\ell_c/c_0$ and $x_p = \omega_p\ell_c/c_0$ are the size parameters at the EQS resonance frequency and at the plasma frequency, respectively.

In the full-wave scenario, by looking at the denominator in the first summation of Eq. (2.41), the value x_h of the size-parameter at the plasmonic resonance is the value of x at which the real part of the metal susceptibility $\chi(\omega)$ matches the real part of the corresponding eigenvalue $\chi_h(x_h)$ of Eq. (2.40). i.e.

$$\mathrm{Re}\left\{\chi_h\right\} = \mathrm{Re}\left\{\chi\left(\omega_h\right)\right\} \approx -\frac{\omega_p^2}{\omega_h^2} = -\frac{x_p^2}{x_h^2}, \tag{2.58}$$

where ω_h is the corresponding resonance frequency. Eq. (2.58) is the resonance condition of the plasmonic modes. For small particles $x_p \lessapprox 1$, by retaining only the real and imaginary nonzero corrections of the lowest order in Eq. (2.43), the plasmonic eigenvalue $\chi_h(x)$ is approximated as

$$\chi_h(x) \approx \chi_h^{\|} + \chi_h^{(2)} x^2 + \chi_h^{(n_i)} x^{n_i}, \tag{2.59}$$

where n_i is the order of the first nonzero imaginary correction $\chi_h^{(n_i)}$.
We define the frequency shift of the plasmonic resonance with respect to the EQS resonance as $\Delta\omega_h = \omega_h - \omega_h^{\|}$, and the shift in the resonance size parameter as $\Delta x_h = x_h - x_h^{\|}$. By plugging the Eq. (2.59) into the Eq. (2.58), for $\Delta\omega_h/\omega_h^{\|} \ll 1$, and in the small particle limit $x_h^{\|} \ll 1$, we find that

$$\frac{\Delta\omega_h}{\omega_h^{\|}} = \frac{\Delta x_h}{x_h^{\|}} \approx -\frac{1}{2}\frac{\chi_h^{(2)}}{\chi_h^{\|}}\left(x_h^{\|}\right)^2. \tag{2.60}$$

In conclusion, the relative frequency shift of any plasmonic mode is a quadratic function of $x_h^{\|}$, whose prefactor is one half the ratio between the second-order correction $\chi_h^{(2)}$ and the EQS eigenvalue $\chi_h^{\|}$.

The radiation Q factor $\mathrm{Q}_h^{\|}$ of the h-th EQS mode is obtained by considering the inverse of the full width at half maximum (FWHM) fractional bandwidth of the h-th addend of the first summation in Eq. (2.41), assuming negligible nonradiative losses $\mathrm{Im}\left\{\chi\right\} \approx 0$, and using the expansion (2.59):

$$\mathrm{Q}_h^{\|} = \left|\frac{\chi_h^{\|}}{\chi_h^{(n_i)}}\right| \left(\frac{1}{x_h}\right)^{n_i}. \tag{2.61}$$

The Q factor is an inverse power function of the size parameter at the resonance, whose exponent is the order n_i of the first nonvanishing imaginary correction, while the prefactor is the ratio between the EQS eigenvalue $\chi_h^{\|}$ and the correction $\chi_h^{(n_i)}$.

If the mode $\mathbf{j}^{\parallel}_h$ is bright, it follows that $\chi^{(3)}_h \neq 0$, $n_i = 3$, and the Q factor is obtained by combining Eqs. (2.55) and (2.61):

$$\mathrm{Q}^{\parallel}_h = \frac{6\pi}{(-\chi^{\parallel}_h)|\mathbf{P}_h|^2}\left(\frac{1}{x_h}\right)^3. \tag{2.62}$$

By expressing in Eq. (2.62) the EQS eigenvalue $\chi^{\parallel}_h$ in terms of the electrostatic energy $\mathcal{W}_e\left\{\mathbf{j}^{\parallel}_h\right\}$ of the mode $\mathbf{j}^{\parallel}_h$ (using Eq. (2.22)), $Q^{\parallel}_h$ is also found equal to 2π times the ratio of $\mathcal{W}_e\left\{\mathbf{j}^{\parallel}_h\right\}$ to the energy radiated in a period by the electric dipole $\mathbf{P}_h$ at the resonance frequency ω_h.

On the other hand, for a dark mode with nonvanishing electric quadrupole, it follows that $\chi^{(5)}_h \neq 0$, $n_i = 5$, and the Q factor is obtained by using Eqs. (2.56) and (2.61):

$$\mathrm{Q}^{\parallel}_h = \frac{80\pi}{\chi^{\parallel}_h\left[\sum_{ij}\left(Q_{\mathrm{E}|h|ij}\right)^2 - \frac{1}{3}\mathrm{Tr}\left(\overleftrightarrow{\mathbf{Q}}^{\parallel}_{\mathrm{E}|h}\right)^2\right]}\left(\frac{1}{x_h}\right)^5, \tag{2.63}$$

which is also equal to 2π times the ratio of the electrostatic energy of the h-th EQS mode to the energy radiated in a period by the electric quadrupole $\overleftrightarrow{\mathbf{Q}}^{\parallel}_{\mathrm{E}|h}$ at the resonance frequency ω_h. If the electric quadrupole moment is also vanishing, the outlined process can be iterated by considering higher order electric multipoles.

For the sake of completeness, we also consider the opposite regime, dominated by material losses. In this case, the dissipation Q factor $Q^{\parallel d}_h$ is obtained as the inverse of the fractional bandwidth of the h-th addend of the first summation in Eq. (2.41), assuming negligible radiation losses. For a Drude metal, we have

$$Q^{\parallel d}_h = \frac{\omega_h}{\nu}, \tag{2.64}$$

which was already shown by Wang and Shen in [84].

In an intermediate regime, the resulting resonance Q factor, indicated with Q_h, can be obtained through the parallel formula [154]

$$\frac{1}{Q_h} = \frac{1}{\mathrm{Q}^{\parallel}_h} + \frac{1}{Q^{\parallel d}}. \tag{2.65}$$

2.2.3 3D Dielectric resonances

To evaluate the dielectric resonances of three-dimensional small particles, it is convenient to recast the eigenvalue problem (2.40) as

$$x^2\mathbf{v}_h(\mathbf{r}) + \kappa_h \left[\nabla \oint_{\partial\Omega} \mathbf{v}_h(\mathbf{r}') \cdot \hat{\mathbf{n}}'\, g\left(\Delta r, x\right)\, dS' - x^2 \int_{\Omega} \mathbf{v}_h(\mathbf{r}') g\left(\Delta r, x\right) dV'\right] = \mathbf{0}, \qquad \forall \mathbf{r} \in \Omega. \quad (2.66)$$

As for the plasmonic case, the mode $\mathbf{v}_h$ and the corresponding eigenvalue κ_h are expanded at $x = 0$ in the neighborhood of MQS eigenvalue $\kappa_h^{\perp}$ and mode $\mathbf{j}_h^{\perp}$

$$\kappa_h = \sum_{k=1}^{\infty} \kappa_h^{(k)} x^k, \quad (2.67)$$

$$\mathbf{v}_h = \sum_{k=1}^{\infty} \mathbf{v}_h^{(k)} x^k. \quad (2.68)$$

By substituting Eqs. (2.67), (2.68), and (2.45) in Eq. 2.66

$$4\pi \sum_{k=0}^{\infty} \mathbf{v}_h^{(k)} x^{k+2} + \sum_{k=1}^{\infty} \kappa_h^{(k)} x^k \left[\nabla \oint_{\partial\Omega} \left(\sum_{k=1}^{\infty} i^k \frac{\Delta r^{k-1}}{k!} x^{k-2}\right) \left(\sum_{k=0}^{\infty} v_{h\,n}^{(k)} x^k\right) dS' - \int_{\Omega} \left(\sum_{k=1}^{\infty} i^k \frac{\Delta r^{k-1}}{k!} x^k\right) \left(\sum_{k=0}^{\infty} \mathbf{v}_h^{(k)} x^k\right) dV'\right] = 0 \quad \forall \mathbf{r} \in \Omega, \quad (2.69)$$

where $v_{h\,n}^{(k)} = \mathbf{v}_h^{(k)} \cdot \mathbf{n}\big|_{\partial\Omega}$, $\kappa_h^{(0)} = \kappa_h^{\perp}$ and $\mathbf{v}_h^{(0)} = \mathbf{j}_h^{\perp}$.

By matching the terms of the corresponding order in Eq. 2.69, it is possible to demonstrate that first-order corrections vanish regardless of the shape of the object:

$$\kappa_h^{(1)} = 0, \quad (2.70)$$

$$\mathbf{v}_h^{(1)}(\mathbf{r}) = 0, \qquad \forall \mathbf{r} \in \Omega. \quad (2.71)$$

The second-order correction $\kappa_h^{(2)}$ is a real quantity, namely

$$\kappa_h^{(2)} = \frac{\left(\kappa_h^{\perp}\right)^2}{8\pi} \left[\int_{\Omega} \mathbf{j}_h^{\perp}(\mathbf{r}) \cdot \int_{\Omega} \mathbf{j}_h^{\perp}(\mathbf{r}') \Delta r\, dV' dV + \sum_{k=1}^{\infty} \frac{\chi_k^{\parallel}}{4\mu_0} \left|\mathscr{W}_{m\mathrm{I}}\{\mathbf{j}_k^{\parallel}, \mathbf{j}_h^{\perp}\}\right|^2\right], \quad (2.72)$$

where $\mathscr{W}_{m\mathrm{I}}\{\mathbf{j}_k^{\parallel}, \mathbf{j}_h^{\perp}\}$ is the magnetostatic interaction energy between the MQS current mode $\mathbf{j}_h^{\perp}$ and the EQS current mode $\mathbf{j}_k^{\parallel}$, i.e.

$$\mathscr{W}_{m\mathrm{I}}\{\mathbf{j}_k^{\parallel},\mathbf{j}_h^{\perp}\}=\frac{\mu_0}{8\pi}\int_{\Omega}\mathbf{j}_k^{\parallel}(\mathbf{r})\cdot\int_{\Omega}\frac{\mathbf{j}_h^{\perp}(\mathbf{r}')}{\Delta r}\,dV'dV. \tag{2.73}$$

The first term in parentheses in Eq. 2.72 originates from the radiative self-interaction of the MQS mode $\mathbf{j}_h^{\perp}$ through the vector potential. The second term is a summation, whose addends are proportional to the ratio of the magnetostatic interaction energy between the MQS current mode $\mathbf{j}_h^{\perp}$ and the EQS current mode $\mathbf{j}_k^{\parallel}$, to the electrostatic energy of the EQS mode $\mathbf{j}_k^{\parallel}$ (using Eq. (2.22)).

The MQS current mode $\mathbf{j}_h^{\perp}$ may be an $\mathbb{A}^{\perp}$-mode, generating a transverse vector potential, according to the definition (2.35). In this case, since every EQS current mode is longitudinal, and transverse and longitudinal functions are orthogonal according to the scalar product (2.9), the energy $\mathscr{W}_{m\mathrm{I}}\{\mathbf{j}_k^{\parallel},\mathbf{j}_h^{\perp}\}$ vanishes $\forall k$, and Eq. (2.72) further simplifies:

$$\kappa_h^{(2)}=\frac{\left(\kappa_h^{\perp}\right)^2}{4\pi}\int_{\Omega}\mathbf{j}_h^{\perp}(\mathbf{r})\cdot\int_{\Omega}\frac{\Delta r}{2}\mathbf{j}_h^{\perp}(\mathbf{r}')dV'dV,\qquad\text{for }\mathbb{A}^{\perp}\text{-modes.} \tag{2.74}$$

As it will be demonstrated in Eq. (2.87), $\kappa_h^{(2)}$ is associated with the frequency-shift of dielectric modes.

The second-order correction $\mathbf{v}_h^{(2)}$ to the current density mode has both longitudinal and transverse components, denoted as $\mathbf{v}_h^{(2)\parallel}$ and $\mathbf{v}_h^{(2)\perp}$, which can be in turn expanded in terms of EQS and MQS current modes, respectively:

$$\mathbf{v}_h^{(2)}=\mathbf{v}_h^{(2)\parallel}+\mathbf{v}_h^{(2)\perp}=\sum_{k=1}^{\infty}\alpha_{h,k}^{(2)}\mathbf{j}_k^{\parallel}+\sum_{\substack{k=1\\k\neq h}}^{\infty}\beta_{h,k}^{(2)}\mathbf{j}_k^{\perp} \tag{2.75}$$

where, assuming the eigenvalues are nondegenerate, the expansion coefficients $\alpha_{h,k}^{(2)}$ and $\beta_{h,k}^{(2)}$ are

$$\alpha_{h,k}^{(2)}=-\frac{2\chi_k^{\parallel}}{\mu_0}\mathscr{W}_{m\mathrm{I}}\{\mathbf{j}_k^{\parallel},\mathbf{j}_h^{\perp}\},\qquad\forall k\in\mathbb{N}, \tag{2.76}$$

$$\beta_{h,k}^{(2)}=\frac{\kappa_k^{\perp}\kappa_h^{\perp}}{\kappa_h^{\perp}-\kappa_k^{\perp}}\frac{1}{4\pi}\left[\int_{\Omega}\mathbf{j}_k^{\perp}(\mathbf{r})\cdot\int_{\Omega}\frac{\Delta r}{2}\mathbf{j}_h^{\perp}(\mathbf{r}')dV'dV\right. \tag{2.77}$$

$$\left.-\sum_{s=1}^{\infty}\alpha_{h,s}^{(2)}\int_{\Omega}\mathbf{j}_s^{\parallel}(\mathbf{r}')\cdot\int_{\Omega}\frac{\mathbf{j}_k^{\perp}(\mathbf{r}')}{\Delta r}dV'dV\right],\qquad\forall k\neq h. \tag{2.78}$$

Although any magnetoquasistatic mode has a zero electric dipole moment, its second-order radiative correction $\mathbf{v}_h^{(2)}$ may exhibit a nonzero electric dipole moment $\mathbf{P}_h^{(2)}$, given by

$$\mathbf{P}_h^{(2)} = \sum_{k=1}^{\infty} \alpha_{h,k}^{(2)} \mathbf{P}_k, \tag{2.79}$$

where $\mathbf{P}_k$ is the electric dipole moment of the k-th EQS mode $\mathbf{j}_k^{\parallel}$. For $\mathbb{A}^{\perp}$-modes the longitudinal part of $\mathbf{v}_h^{(2)}$ vanishes, and they do not display electric dipole moment up to this order.

The third-order correction $\kappa_h^{(3)}$ is purely imaginary and depends on the magnetic dipole moment $\mathbf{M}_h$ of the mode $\mathbf{j}_h^{\perp}$:

$$\kappa_h^{(3)} = -i \frac{\left(\kappa_h^{\perp}\right)^2}{6\pi} |\mathbf{M}_h|^2, \tag{2.80}$$

where $\mathbf{M}_h$ is defined in Eq. 2.33. As it will be shown in (2.89), the correction $\kappa_h^{(3)}$, if nonvanishing, determines the radiative Q factor of the h-th dielectric mode. However, it vanishes when the corresponding magnetic dipole moment is zero. In this case, the next imaginary correction has order 5 and has the following expression:

$$\kappa_h^{(5)} = -i \frac{\left(\kappa_h^{\perp}\right)^2}{\pi} \left[\sum_{i,j=1}^{3} \frac{\left(Q_{\mathrm{M}|h|ij}^{\perp}\right)^2}{80} + \left| \mathbf{P}_{\mathrm{E2}|h}^{\perp} - \mathbf{P}_h^{(2)} \right|^2 \right] \tag{2.81}$$

where $\overleftrightarrow{\mathbf{Q}}_{\mathrm{M}|h}^{\perp}$ is the magnetic quadrupole tensor of the h-th MQS mode, defined in Eq. (A.5), $Q_{\mathrm{M}|h|ij}^{\perp}$ are its components, and $\mathbf{P}_{\mathrm{E2}|h}^{\perp}$ is the toroidal dipole, defined in Eq. (A.4), and $\mathbf{P}_h^{(2)}$ is the electric dipole moment of the second-order correction $\mathbf{v}_h^{(2)}$, introduced in Eq. (2.79). In conclusion, the fifth order correction is determined by two contributions: they account for the power radiated to infinity by the magnetic quadrupole $\overleftrightarrow{\mathbf{Q}}_{\mathrm{M}|h}^{\perp}$, and by an effective electric dipole resulting from the interference between the $\mathbf{P}_{\mathrm{E2}|h}^{\perp}$ and $\mathbf{P}_{\mathrm{E}|h}^{(2)}$.

For $\mathbb{A}^{\perp}$-modes, Eq. (2.81) further simplifies

$$\kappa_h^{(5)} = -i \frac{\left(\kappa_h^{\perp}\right)^2}{\pi} \left[\sum_{ij} \frac{\left(Q_{\mathrm{M}|h|ij}^{\perp}\right)^2}{80} + \left| \mathbf{P}_{\mathrm{E2}|h}^{\perp} \right|^2 \right]. \tag{2.82}$$

The outlined procedure can be iteratively applied. If the fifth order correction vanishes, the next order correction that may give an imaginary contribution is the seventh, which can be calculated by matching the terms of nine-th order in Eq. (2.69).

2.2.4 Resonance frequency-shift and Q factor of dielectric modes

It is now assumed that the object is made of a nondispersive dielectric material with positive susceptibility χ, with $\mathrm{Im}\left\{\chi\right\} \ll \mathrm{Re}\left\{\chi\right\}$. The size parameter $x_h^\perp$ at the resonance of the h-th MQS mode $\mathbf{j}_h^\perp$ is defined as the value of x at which the real part of the susceptibility χ matches the eigenvalue $\kappa_h^\perp/x^2$, namely:

$$x_h^\perp = \frac{\omega_h^\perp}{c_0}\ell_c = \sqrt{\frac{\kappa_h^\perp}{\mathrm{Re}\left\{\chi\right\}}}, \tag{2.83}$$

and $\omega_h^\perp$ is the corresponding MQS resonance frequency.

In the full-wave regime, the resonance of the dielectric mode $\mathbf{v}_h$ is defined by zeroing the real part of the denominator of the h-th addend of the second summation of Eq. (2.41). Thus, the value of size parameter $x_h = \omega_h \ell_c / c_0$ at the dielectric resonance is

$$\mathrm{Re}\left\{\kappa_h\right\} = \mathrm{Re}\left\{\chi\right\} x_h^2, \tag{2.84}$$

This is the resonance condition for dielectric modes, and ω_h is the dielectric resonance frequency. For small particles, $x_h \lessapprox 1$ and by keeping only the real and imaginary nonzero corrections of the lowest order in Eq. (2.67), the dielectric eigenvalue $\kappa_h\left(x\right)$ is approximated as

$$\kappa\left(x\right) \approx \kappa_h^\perp + \kappa_h^{(2)} x^2 + i\,\kappa_h^{(n_i)} x^{n_i}. \tag{2.85}$$

where n_i is the order of the first nonzero imaginary correction $\kappa_h^{(n_i)}$. By using Eq. (2.85) in (2.84), we find that

$$x_h = \frac{\omega_h}{c_0}\ell_c \approx \sqrt{\frac{\kappa_h^\perp}{\mathrm{Re}\left\{\chi\right\} - \kappa_h^{(2)}}} = \frac{x_h^\perp}{\sqrt{1 - \kappa_h^{(2)}/\mathrm{Re}\left\{\chi\right\}}}. \tag{2.86}$$

From this equation, for high-index dielectrics $\mathrm{Re}\left\{\chi\right\} \gg 1$, we obtain the relative frequency shift of the h-th dielectric resonance with respect to the MQS resonance frequency $\Delta\omega_h^\perp/\omega_h^\perp = (\omega_h - \omega_h^\perp)/\omega_h^\perp$, or the corresponding relative shift in the resonance size parameter, i.e., $\Delta x_h^\perp / x_h^\perp = (x_h - x_h^\perp)/x_h^\perp$

$$\frac{\Delta\omega_h}{\omega_h^\perp} = \frac{\Delta x_h}{x_h^\perp} \approx \frac{1}{2}\frac{\kappa_h^{(2)}}{\mathrm{Re}\left\{\chi\right\}} = \frac{1}{2}\frac{\kappa_h^{(2)}}{\kappa_h^\perp}\left(x_h^\perp\right)^2, \qquad \mathrm{Re}\left\{\chi\right\} \gg 1. \tag{2.87}$$

In conclusion, the relative frequency-shift of any dielectric mode is a quadratic function of $x_h^\perp$, whose prefactor is approximately half the ratio between the second-order correction $\kappa_h^{(2)}$ and the quasistatic eigenvalue $\kappa_h^{\perp}$.

The radiation Q factor $\mathrm{Q}_h^{\perp}$ of the h-th MQS mode is obtained by considering the inverse of the FWHM fractional bandwidth of the h-th addend of the second summation in Eq. (2.41), assuming negligible nonradiative losses $\mathrm{Im}\left\{\chi\right\} \approx 0$, and using the expansion (2.85):

$$\mathrm{Q}_h^{\perp} = \left|\frac{\kappa_h^{\perp}}{\kappa_h^{(n_i)}}\right| \left(\frac{1}{x_h}\right)^{n_i}. \tag{2.88}$$

The Q factor is an inverse power function of the size parameter at the resonance, whose exponent is the order n_i of the first nonvanishing imaginary correction, while the prefactor is the ratio between the MQS eigenvalue $\kappa_h^{\perp}$ and the correction $\kappa_h^{(n_i)}$. If the mode $\mathbf{j}_h^{\perp}$ exhibits nonvanishing magnetic dipole moment, the Q factor is obtained by combining Eqs. (2.80) and (2.88):

$$\mathrm{Q}_h^{\perp} = \frac{6\pi}{\kappa_h^{\perp} |\mathbf{M}_h|^2} \left(\frac{1}{x_h}\right)^{3}. \tag{2.89}$$

By expressing in Eq. (2.89) the MQS eigenvalue $\kappa_h^{\perp}$ in terms of the magnetostatic energy $\mathcal{W}_m\left\{\mathbf{j}_h^{\perp}\right\}$ of the mode $\mathbf{j}_h^{\perp}$ (using Eq. (2.32)), $Q_h^{\perp}$ is also found equal to 2π times the ratio of $\mathcal{W}_m\left\{\mathbf{j}_h^{\parallel}\right\}$ to the energy radiated in a period by the magnetic dipole $\mathbf{M}_h$ at the resonance frequency ω_h.

Furthermore, if the magnetic dipole vanishes, but at least one among the magnetic quadrupole moment $\overleftrightarrow{\mathbf{Q}}_{\mathrm{M}|h}^{\perp}$, and the effective dipole moment resulting from the interference between the toroidal dipole moment $\mathbf{P}_{\mathrm{E2}|h}^{\perp}$ and the dipole moment of the second-order mode correction $\mathbf{P}_{\mathrm{E}|h}^{(2)}$ is nonzero, the radiation Q factor has the following expression:

$$\mathrm{Q}_h^{\perp} = \frac{1}{\kappa_h^{\perp}\left[\frac{1}{80\pi}\sum_{ij}\left(Q_{\mathrm{M}|h|ij}^{\perp}\right)^2 + \frac{1}{6\pi}\left|\mathbf{P}_{\mathrm{E2}|h}^{\perp} - \mathbf{P}_h^{(2)}\right|^2\right]} \left(\frac{1}{x_h}\right)^{5}, \tag{2.90}$$

which is equal to 2π times the ratio of the magnetostatic energy of the h-th MQS mode to the sum of the energies radiated in a period by the magnetic quadrupole $\overleftrightarrow{\mathbf{Q}}_{\mathrm{M}|h}^{\perp}$ and by the effective dipole moment $\mathbf{P}_{\mathrm{E2}|h}^{\perp} - \mathbf{P}_h^{(2)}$, at the resonance frequency ω_h.

If they are all vanishing, the outlined process can be iterated by considering higher order magnetic multipoles.

In dielectric resonators, the opposite regime, dominated by material losses, is less common. Nevertheless, it is now considered for completeness. In this case, the dissipation Q factor $Q_h^{\perp d}$ is obtained as the inverse of the factional bandwidth of the h-th addend of the second summation in (2.41), assuming dominating nonradiative losses:

$$Q_h^{\perp d} = \frac{(\kappa_h^{\perp})^2}{\operatorname{Im}\{\chi\}} \frac{1}{x_h^2} \approx \frac{\operatorname{Re}\{\chi\}}{\operatorname{Im}\{\chi\}}. \tag{2.91}$$

In an intermediate regime, the total Q factor, indicated with Q_h is obtained as [154]

$$\frac{1}{Q_h} = \frac{1}{\mathrm{Q}_h^{\perp}} + \frac{1}{Q_h^{\| d}}. \tag{2.92}$$

2.2.5 Sphere

As a case of study, we consider the plasmonic and dielectric resonances of an electrically small sphere of radius R. The object characteristic length ℓ_c is assumed equal to the radius R, and hence the size parameter x is $x = \frac{\omega}{c_0} R$. The formulas of the radiation corrections here presented can be extrapolated by perturbing the denominators of the Mie coefficients in the neighborhood of their EQS and MQS resonances, and they can also be directly obtained from the Padè expansion of the Mie coefficients found by Tzarouchis and Sihvola in [155, 156].

In particular, the EQS eigenvalues of a sphere and their radiation corrections are:

$$\chi_n^{\|} = -\frac{2n+1}{n}, \tag{2.93a}$$

$$\chi_n^{(2)} = -\frac{2}{n^2} \frac{(n+1)(2n+1)}{(3+2n)(2n-1)}, \tag{2.93b}$$

$$\chi_n^{(2n+1)} = -i \, \frac{(n+1)}{[n(2n-1)!!]^2}, \tag{2.93c}$$

where $n \in \mathbb{N}$, and $(2n-1)!! = 1 \times 3 \times 5 \times \cdots \times (2n-1)$. The index n is the mode multipolar order: the modes with $n = 1$ are dipolar, $n = 2$ quadrupolar, and so on. Each eigenvalue $\chi_n^{\|}$ is associated with a set of $2n+1$ degenerate current modes $\mathbf{j}_{pmn}^{\|}$ with $m = 0, 1, 2, \ldots, n$, whose analytical expressions are given in Eq. (B.1) in Appendix B. The subscript p distinguishes between even (e) and odd (o) modes with respect to the azimuthal variable. The sphere EQS modes $\mathbf{j}_{e1n}^{\|}$ for $n = 1, 2, 3, 4$ are shown in Fig. 2.2.

The radiation Q factor of the plasmonic resonances is obtained by applying Eqs.

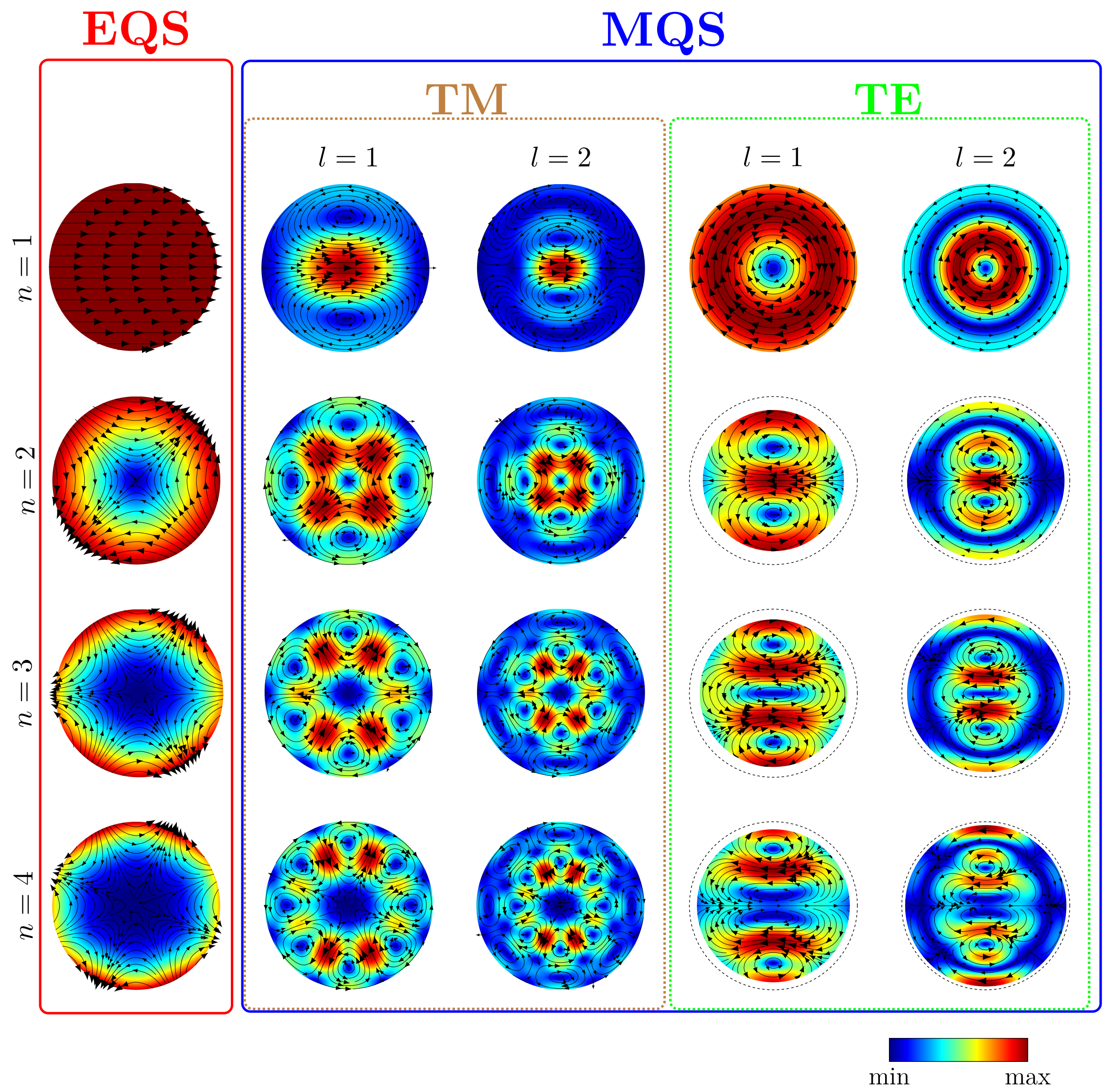

Figure 2.2 – Quasistatic modes of a sphere. Electroquasistatic modes $\mathbf{j}^{\parallel}_{e1n}$ with $n = 1, 2, 3, 4$. The magnetoquasistatic modes are divided into two subsets: the TM MQS mdoes $\mathbf{j}^{\perp\mathtt{TM}}_{e1nl}$, and the TE ($\mathbb{A}^{\perp}$) modes $\mathbf{j}^{\perp\mathtt{TE}}_{o1nl}$, with $n = 1, 2, 3, 4$ and $l = 1, 2$. Their projection on the $y = 0$ plane is shown, except for $\mathbf{j}^{\perp\mathtt{TE}}_{o121}$ ($y = 0.35R$ plane), $\mathbf{j}^{\perp\mathtt{TE}}_{o131}$ ($y = 0.3R$ plane), $\mathbf{j}^{\perp\mathtt{TE}}_{o141}$ ($y = 0.25R$ plane), and $\left.\mathbf{j}^{\perp\mathtt{TE}}_{o1n2}\right|_{n=2,3,4}$ ($y = 0.15R$ plane).

(2.93a) and (2.93c) in Eq. (2.61):

$$\mathrm{Q}^{\parallel}_{n} = \frac{n\left[(2n+1)!!\right]^{2}}{(n+1)(2n+1)}\frac{1}{x_{n}^{2n+1}}. \tag{2.94}$$

For instance, for the electric dipole, quadrupole, and octupole, we have $\mathrm{Q}^{\parallel}_{1} =$

$\frac{3}{2}\frac{1}{x_1^3}$, $\mathrm{Q}_2^{\|} = \frac{30}{x_2^5}$, $\mathrm{Q}_3^{\|} = \frac{1181}{x_3^7}$, respectively. Eq. (2.94) coincides with the formulas provided by G. Colas des Francs in [157].

The MQS modes are divided into two sets. The first set is composed by the current modes which have no radial component. Since the corresponding electric field has the same property, these modes are called *transverse electric* or TE modes. They also generate a vector potential, which has nonvanishing normal component to the particle-surface, so they are also $\mathbb{A}^{\perp}$-modes. Their eigenvalues and the corresponding corrections are [155, 156]:

$$\kappa_{nl}^{\perp\,\mathtt{TE}} = \left(z_{n-1,l}\right)^2, \tag{2.95a}$$

$$\kappa_{nl}^{\mathtt{TE}\,(2)} = -\frac{2n+1}{2n-1}, \tag{2.95b}$$

$$\kappa_{nl}^{\mathtt{TE}\,(2n+1)} = -i\frac{2}{\left[(2n-1)!!\right]^2}, \tag{2.95c}$$

where $z_{n,l}$ denotes the l-th zero of the spherical Bessel function j_n. Each eigenvalue $\kappa_{nl}^{\perp\,\mathtt{TE}}$ is associated with a set of $2n+1$ degenerate current modes $\mathbf{j}_{pmnl}^{\perp\,\mathtt{TE}}$, with $m = 0, 1, 2, \ldots, n$ and with even and odd parity, whose analytical expression is given in Eq. (B.3) in Appendix B. The odd MQS modes $\mathbf{j}_{o1nl}^{\perp\,\mathtt{TE}}$ with $n = 1, 2, 3, 4$, and $l = 1, 2, 3$ are shown in Fig. 2.2. The radiation Q factor of the TE MQS modes is obtained by combining Eq. (2.95) and (2.88):

$$\mathrm{Q}_{nl}^{\perp\,\mathtt{TE}} = \frac{\left[z_{n-1,l}\,(2n-1)!!\right]^2}{2}\left(\frac{1}{x_{nl}}\right)^{2n+1}. \tag{2.96}$$

For instance, for the magnetic dipole modes, we have

$$\mathrm{Q}_{1l}^{\perp\,\mathtt{TE}} = \frac{(l\pi)^2}{2}\frac{1}{x_{1l}^3}, \qquad \forall l \in \mathbb{N}. \tag{2.97}$$

The second set of current modes generate a magnetic field with vanishing radial component, so they are called TM modes. Their eigenvalues and the corresponding corrections are [155, 156]:

$$\kappa_{nl}^{\perp\,\mathtt{TM}} = \left(z_{n,l}\right)^2, \tag{2.98a}$$

$$\kappa_{nl}^{\mathtt{TM}\,(2)} = -\frac{n+2}{n}, \tag{2.98b}$$

$$\kappa_{nl}^{\mathtt{TM}\,(2n+3)} = +i\frac{2}{n^2\left[(2n-1)!!\right]^2}. \tag{2.98c}$$

Each eigenvalue $\kappa_{nl}^{\perp\mathtt{TM}}$ is associated with a set of $2n+1$ degenerate current modes $\mathbf{j}_{pmnl}^{\perp\mathtt{TM}}$, with $m = 0, 1, 2, \ldots, n$ and with even and odd parity whose analytic expression is given in Eq. (B.5) in Appendix B. The MQS modes $\mathbf{j}_{e1nl}^{\perp\mathtt{TM}}$ with $n = 1,\ 2,\ 3,\ 4$ and $l = 1,\ 2,\ 3$ are shown in Fig. 2.2. The radiation quality factor of the TE MQS modes is obtained by combining Eq. (2.98) and Eq. (2.88):

$$\mathrm{Q}_{nl}^{\perp\mathtt{TM}} = \frac{\left[n\, z_{n,l}\, (2n-1)!!\right]^2}{2} \left(\frac{1}{x_{nl}}\right)^{2n+3} \tag{2.99}$$

As an example, the toroidal electric dipole mode has radiation Q factor $\mathrm{Q}_{11}^{\perp\mathtt{TM}} = \dfrac{z_{11}^2}{2x_{11}^5}$.

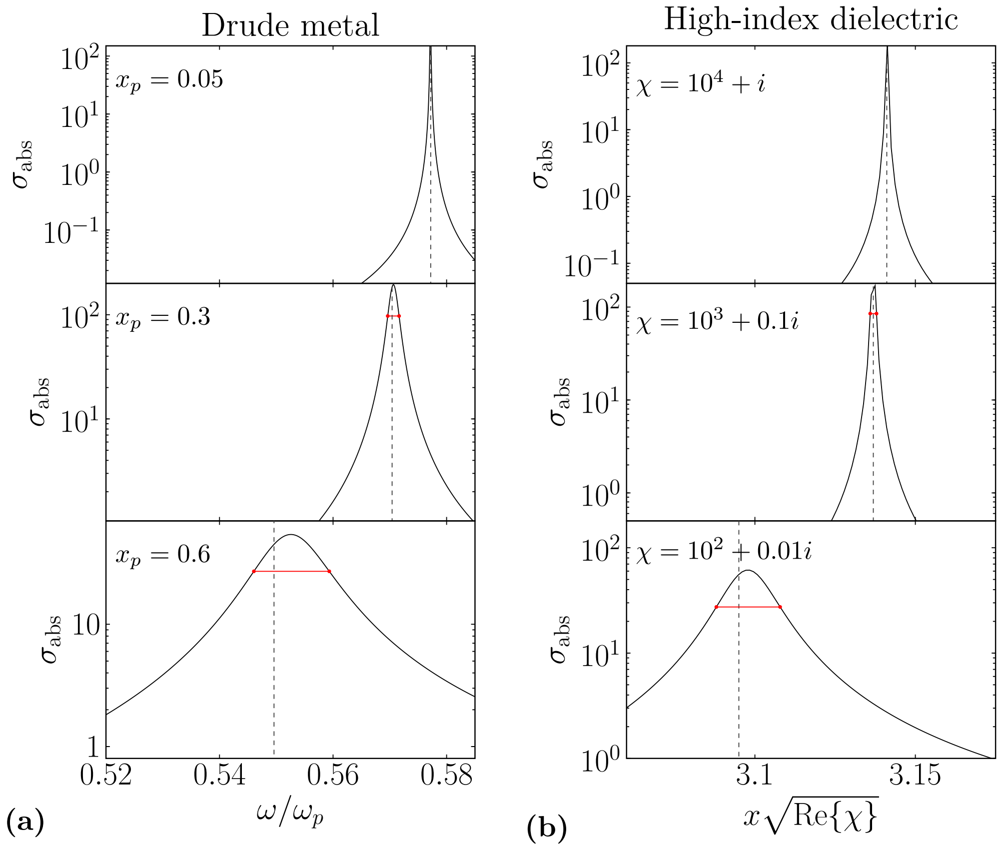

Figure 2.3 – (**a**) First peak of the absorption cross-section σ_{abs} of a Drude metal sphere with radius $R = \ell_c$ as a function of $\omega/\omega_p = x/x_p$, for $x_p = 0.05$ (top panel), $x_p = 0.3$ (middle panel), $x_p = 0.6$ (bottom panel). (**b**) First peak of the σ_{abs} of a dielectric sphere with susceptibility $\chi = 10^4 + i$ (top panel), $\chi = 10^3 + 0.1i$ (middle panel), $\chi = 10^2 + 0.01i$ (bottom panel), as a function of $x\sqrt{\mathrm{Re}\{\chi\}}$. The resonance position obtained by Eq. (2.60) (case (**a**)) and Eq. (2.87) (case (**b**)) are shown with vertical dashed lines. Horizontal lines show the peak `FWHM`.

With the aid of Fig. 2.3, we now briefly investigate the resonances of an electrically small sphere under plane-wave excitation, in two different scenarios: in the first one, the sphere is made of a Drude metal; in the second one, it is filled with a high-index dielectric ($\mathrm{Re}\{\chi\} \gg 1$). In both cases, low material losses are assumed ($\mathrm{Im}\{\chi\} \ll 1$): this hypothesis is essential for a fair comparison between the predicted radiation Q factor and the fractional bandwidth of the peaks, otherwise dominated by nonradiative (material) losses. As physical observable, we choose the absorption efficiency σ_{abs}, defined as

$$\sigma_{\text{abs}} = \frac{P_{\text{abs}}}{I_i\, \pi R^2} = \frac{x}{\pi} \mathrm{Im}\{\chi\} \int_{\Omega} \left| \frac{\mathbf{E}}{E_0} \right|^2 dV, \tag{2.100}$$

where P_{abs} is the absorbed power, $I_i = \varepsilon_0 c_0 / 2 E_0^2$ the incident irradiance, and E_0 the incident amplitude. It is calculated using the standard Mie theory [87]. The radiative shift of the first peak of σ_{abs} and its Q factor are investigated as the object size increases. In particular, the plasmonic and dielectric resonance frequencies are compared against the frequency at which the curve has the peak, denoted as ω_{res}. Similarly, the Q factor of the plasmonic and dielectric modes are validated against the corresponding heuristic Q factors, given by the inverse of the full-width at half maximum `FWHM` [158]. In the σ_{abs} spectra of Fig. 2.3, a segment joining the two ordinates at half maximum is also shown.

x_p	ω_1/ω_p	$\omega_{\text{res}}/\omega_p$	$Q^{\parallel d}$	$\mathrm{Q}_1^{\parallel}$	Q_1	$\texttt{FWHM}^{-1}$
0.05	0.577	0.577	5772	62416	5283	4641
0.3	0.570	0.570	5704	299	284	286
0.6	0.550	0.552	5496	42	42	42

Table 2.1 – Resonance frequency ω_1 and Q factors $Q^{\parallel d}$, $\mathrm{Q}_1^{\parallel}$, Q_1 of the first plasmonic mode of a Drude metal sphere ($\nu = 10^{-4}\omega_p$) with different values of x_p, and their heuristic estimates ω_{res} and $\texttt{FWHM}^{-1}$ at the peak of σ_{abs} in Fig. 2.3a.

In Fig. 2.3a, we plot the σ_{abs} for a sphere made of a low-loss Drude metal, with the dispersion relation given in Eq. (2.21), in which $\nu = 10^{-4}\omega_p$. We evaluate σ_{abs} for three different values of $x_p = 0.05,\ 0.3,\ 0.6$, which for a gold sphere ($\omega_p = 6.79\,\text{Prad/s}$ [159]) correspond to $R \approx 2\,\text{nm},\ 13\,\text{nm},\ 26\,\text{nm}$. The resonance position of the first excited plasmonic mode, which in the quasistatic limit tends to the dipolar EQS mode $\mathbf{j}_{e11}^{\parallel}$ (if the impinging plane wave is $\hat{\mathbf{x}}$-polarized), is obtained using Eq. (2.60), and is shown with a vertical dashed line. In Tab. 2.1, the resonance frequency ω_1 is compared against the corresponding peak position ω_{res}, and the resonant mode $\mathrm{Q}_1^{\parallel}$ against its heuristic counterpart $\texttt{FWHM}^{-1}$. The dissipation $Q^{\parallel d}$ and the total Q_1

factors, calculated using Eqs. (2.64) and (2.65), respectively, are also shown.

For $x_p = 0.05$ (top panel), the radius R is much smaller than the plasma wavelength λ_p, and hence the EQS approximation works very well: Eq. (2.57) exactly predicts the occurrence of the considered peak. In this case, the resonance is dominated by material losses, as confirmed by the values of the dissipation $Q^{\|d}$ and the inverse of the `FWHM` in Tab. 2.1.

Increasing x_p to $x_p = 0.3$ (middle panel) and $x_p = 0.6$ (bottom panel), the peak undergoes a broadening and a shift from its quasistatic position. Neverthless, the resonance position obtained through Eq. (2.60), which incorporates the radiation corrections, accurately predicts the occurrence of the peak. This time, the resonance is dominated by radiation losses, as confirmed by the good agreement between the mode $\mathrm{Q}_1^{\|}$ and $\mathtt{FWHM}^{-1}$ in Tab. 2.1.

χ	$x_{11}\sqrt{\mathrm{Re}\{\chi\}}$	$x_{\mathrm{res}}\sqrt{\mathrm{Re}\{\chi\}}$	$Q^{\perp d}$	$\mathrm{Q}_{11}^{\perp}$	Q_{11}	$\mathtt{FWHM}^{-1}$
$10^4 + i$	3.141	3.141	10^4	15920	9409	8955
$10^3 + 0.1i$	3.137	3.137	10^4	5048	3355	3181
$10^2 + 0.01i$	3.094	3.097	10^4	164	161	171

Table 2.2 – Resonance position $x_{11}\sqrt{\mathrm{Re}\{\chi\}}$ and Q factors $Q^{\perp d}$, $\mathrm{Q}_{11}^{\perp}$, Q_{11} of the first dielectric mode of a high-index dielectric sphere ($\mathrm{Re}\{\chi\} = 10^{-4}\mathrm{Im}\{\chi\}$) with different values of susceptibility χ, and their heuristic estimates $x_{\mathrm{res}}\sqrt{\mathrm{Re}\{\chi\}}$ and $\mathtt{FWHM}^{-1}$ at the peak of σ_{abs} in Fig. 2.3b.

In Fig. 2.3b, we investigate the first peak of the σ_{abs} of a sphere made of nondispersive high-index dielectric with low losses, as a function of the parameter $x\sqrt{\mathrm{Re}\{\chi\}}$. We consider three different values of susceptibility χ, namely $\chi = 10^4 + i$, $10^3 + 0.1i$, $10^2 + 0.01i$. In all cases, we have $\mathrm{Re}\{\chi\} = 10^4\mathrm{Im}\{\chi\}$, and hence the dissipation Q, calculated using Eq. (2.91), is $Q^{\perp d} = 10^4$. The resonance position of the dielectric mode that tends to the MQS dipolar mode $\mathbf{j}_{o111}^{\perp\mathtt{TE}}$ (if the impinging plane wave is $\hat{\mathbf{x}}$-polarized) is obtained by Eq. (2.87), and highlighted with a vertical dashed line. In Tab. 2.2, the resonance parameter x_{11} is compared against the corresponding peak position x_{res}, and the resonant mode $\mathrm{Q}_1^{\perp}$ against its heuristic counterpart $\mathtt{FWHM}^{-1}$. The dissipation $Q^{\perp d}$ and the total Q_{11}, calculated using Eq. (2.92), are also shown.

For $\chi = 10^4 + i$ (top panel), the size parameter $x \in [0.030, 0.032]$ is very small, and the MQS approximation works well: Eq. (2.83) exactly predicts the occurrence of the σ_{abs} peak. Here the resonance is dominated by material losses, as confirmed by the values of the dissipation $Q^{\perp d}$ and the inverse of the `FWHM` in Tab. 2.2.

Decreasing $\mathrm{Re}\left\{\chi\right\}$ to the cases $\chi = 10^3{+}0.1i$ (middle panel) and $\chi = 10^2{+}0.01i$ (bottom panel), the size parameter is increased to $x \in [0.096, 0.101]$ and $x \in [0.304, 0.320]$, respectively, and the σ_{abs} peak experiences a broadening and a red shift with respect to its quasistatic position. As confirmed by the third and fourth columns of Tab. 2.2, Eq. (2.87), which takes into account the radiation corrections, correctly estimates the occurrence of the peak. In the last case $\mathrm{Re}\left\{\chi\right\} = 10^2$, the resonance is dominated by radiation losses, and there is very good agreement between the mode $\mathrm{Q}_{11}^{\perp}$ and the $\mathtt{FWHM}^{-1}$.

2.3 Translational Invariant (TI) objects

We now investigate the scattering from a translational invariant (TI) object, using the methods developed so far. In this case, the domain of concern is the object cross-section, which we label Σ, with its boundary, which we label $\partial\Sigma$, as sketched in Fig 2.4. We denote with $\mathbf{r}$ the in-plane coordinates (x,y), and the operators such as divergence or gradient are assumed to only act on these coordinates. All the fields are assumed independent of z.

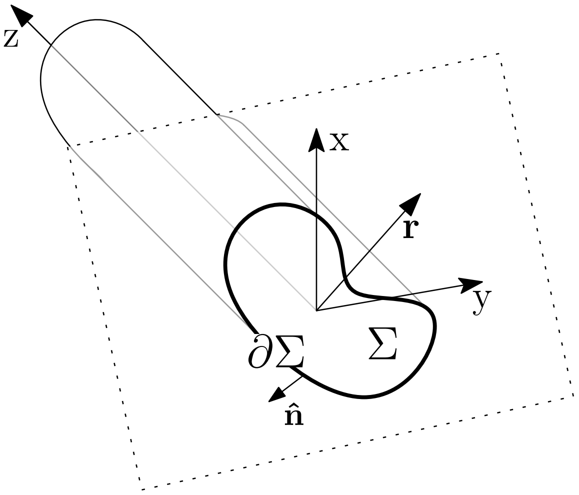

Figure 2.4 – A translational invariant object cross-section Σ, with boundary $\partial\Sigma$. $\hat{\mathbf{n}}$ is the in-plane outgoing normal to $\partial\Sigma$.

The object is made of a linear, isotropic, homogeneous, nonmagnetic material with relative dielectric permittivity ε_R and susceptibility χ, and it is surrounded by vacuum. It is illuminated by a time-harmonic electromagnetic field $\mathrm{Re}\left\{\mathbf{E}_{\mathrm{inc}}(\mathbf{r})e^{-i\omega t}\right\}$. As for the 3D case, we introduce the dimensionless size parameter $x = \dfrac{\omega}{c_0}\ell_c$, being ℓ_c a characteristic linear length of the region Σ, e.g., the radius of the smallest circle enclosing the object cross-section.

The current density field $\mathbf{J}$ induced in the object is governed by the full-wave two-dimensional integral equation

$$\frac{\mathbf{J}(\mathbf{r})}{\chi} - \mathcal{L}^{\mathtt{TI}}\{\mathbf{J}\}(\mathbf{r}) = -i\omega\varepsilon_0\,\mathbf{E}_{\text{inc}}(\mathbf{r}), \quad \forall \mathbf{r} \in \Sigma, \tag{2.101}$$

where the spatial coordinates have been normalized by ℓ_c ($\mathbf{r} \rightarrow \mathbf{r}/\ell_c$),

$$\mathcal{L}^{\mathtt{TI}}\{\mathbf{W}\}(\mathbf{r}) = \nabla \int_{\partial\Sigma} \mathbf{W}(\mathbf{r}') \cdot \hat{\mathbf{n}}' g^{2D}\left(\Delta r, x\right)\, dl' - x^2 \int_{\Sigma} \mathbf{W}(\mathbf{r}') g^{2D}\left(\Delta r, x\right)\, dS', \tag{2.102}$$

Σ is the scaled domain, ∇ is the scaled 2D gradient operator, $\hat{\mathbf{n}}$ is the outgoing in-plane normal to $\partial\Sigma$, and $g^{2D}\left(\Delta r, x\right)$ is the 2D Green's function in vacuum

$$g^{2D}\left(\Delta r, x\right) = -\frac{i}{4}\mathrm{H}_0^{(1)}(x\Delta r), \tag{2.103}$$

with $\Delta r = |\mathbf{r} - \mathbf{r}'|$, and $\mathrm{H}_0^{(1)}$ is the 0-order Hankel function of the first kind [160].

As for the 3D case, in order to represent the solution of Eq. (2.101) in the quasistatic limit ($x \rightarrow 0$), we build a complete basis joining two orthogonal sets. The first set $\{\mathbf{j}_h^{\parallel}\}$ is given by the solution of the eigenvalue problem

$$\mathcal{L}_e^{\mathtt{TI}}\{\mathbf{j}_h^{\parallel}\}(\mathbf{r}) = \frac{1}{\chi_h^{\parallel}}\mathbf{j}_h^{\parallel}(\mathbf{r}), \quad \forall \mathbf{r} \in \Sigma, \tag{2.104}$$

where $\mathcal{L}_e^{\mathtt{TI}}$ is the two dimensional electrostatic integral operator that gives the electrostatic field as a function of the linear boundary charge density [143]:

$$\mathcal{L}_e^{\mathtt{TI}}\{\mathbf{W}\} = \nabla \oint_{\partial\Sigma} \mathbf{W}(\mathbf{r}') \cdot \hat{\mathbf{n}}' g_0^{2D}\left(\Delta r\right)\, dl', \tag{2.105}$$

where

$$g_0^{2D}\left(\Delta r\right) = \frac{1}{2\pi}\log \Delta r \tag{2.106}$$

is the static Green's function in vacuum.

The spectrum of $\mathcal{L}_e^{\mathtt{TI}}$ is countable infinite [143], and the eigenfunctions $\{\mathbf{j}_h^{\parallel}\}_{h\in\mathbb{N}}$ are longitudinal vector fields: they are both div-free and curl-free in Σ but have nonvanishing normal component to $\partial\Sigma$. Moreover, $\mathcal{L}_e^{\mathtt{TI}}$ is self-adjoint and definite negative, therefore the eigenvalues $\chi_h^{\parallel}$ are real and negative, and the eigenfunctions are orthogonal according to the scalar product

$$\langle \mathbf{A}, \mathbf{B} \rangle_{\Sigma} = \int_{\Sigma} \mathbf{A} \cdot \mathbf{B}\, dS. \tag{2.107}$$

We then assume this set orthonormal, i.e., $\langle \mathbf{j}_h^{\parallel}, \mathbf{j}_k^{\parallel} \rangle_\Sigma = \delta_{h,k}$.

The second set is made up by transverse vector fields $\{\mathbf{j}_h^{\perp}\}$ orthogonal to the eigenfunctions $\{\mathbf{j}_h^{\parallel}\}$, which are div-free in Σ, with vanishing in-plane normal component to $\partial\Sigma$, and are solutions of the eigenvalue problem in weak form

$$\mathcal{L}_m^{\mathtt{TI}}\{\mathbf{j}_h^{\perp}\}(\mathbf{r}) = \frac{1}{\kappa_h^{\perp}} \mathbf{j}_h^{\perp}(\mathbf{r}), \quad \forall \mathbf{r} \in \Sigma, \tag{2.108}$$

where $\mathcal{L}_m^{\mathtt{TI}}$ is the two-dimensional magnetostatic integral operator

$$\mathcal{L}_m^{\mathtt{TI}}\{\mathbf{W}\}(\mathbf{r}) = -\int_\Sigma \mathbf{W}(\mathbf{r}') g_0^{2D}\left(\Delta r\right)\, dS'. \tag{2.109}$$

$\mathcal{L}_m^{\mathtt{TI}}$ has a countable infinite spectrum, and is self-adjoint and definite positive, therefore the eigenvalues $\{\kappa_h^{\perp}\}_{h\in\mathrm{N}}$ are real and positive, and the eigenfunctions $\{\mathbf{j}_h^{\perp}\}_{h\in\mathbb{N}}$ are orthogonal according to the scalar product (2.107), and assumed normalized, namely $\langle \mathbf{j}_h^{\perp}, \mathbf{j}_k^{\perp} \rangle_\Sigma = \delta_{h,k}$.

Eventually, as in the 3D case (see Eq. (2.15)), the current density $\mathbf{J}$ in the quasistatic regime ($x \to 0$) can be expressed in the form

$$\mathbf{J} = -i\omega\chi\varepsilon_0 \sum_{h=1}^{\infty} \left[\frac{\chi_h^{\parallel}}{\chi_h^{\parallel} - \chi} \langle \mathbf{j}_h^{\parallel}, \mathbf{E}_{\mathrm{inc}} \rangle_\Sigma \, \mathbf{j}_h^{\parallel} + \frac{\kappa_h^{\perp}}{\kappa_h^{\perp} - x^2\chi} \langle \mathbf{j}_h^{\perp}, \mathbf{E}_{\mathrm{inc}} \rangle_\Sigma \, \mathbf{j}_h^{\perp} \right], \tag{2.110}$$

and the resonance conditions for the eigenfunctions $\mathbf{j}_h^{\parallel}$ and $\mathbf{j}_h^{\perp}$ are $\mathrm{Re}\left\{\chi\right\} = \chi_h^{\parallel}$ and $\mathrm{Re}\left\{\chi\right\} = \kappa_h^{\perp}/x^2$, respectively. Thus, the sets $\{\mathbf{j}_h^{\parallel}\}_{h\in\mathbb{N}}$ and $\{\mathbf{j}_h^{\perp}\}_{\mathbb{N}}$ can be interpreted as the EQS and MQS current modes of the body, respectively, and $\{\chi_h^{\parallel}\}_{h\in\mathbb{N}}$, $\{\kappa_h^{\perp}/x^2\}_{h\in\mathbb{N}}$ their eigen-susceptibilities.

The 2D electrostatic and magnetostatic operators, as well as their eigenfunctions and eigenvalues, share the same properties of their 3D counterparts. All the quantities introduced for 3D objects modes, such as the dipole moments, are defined over the TI object cross-section (see Appendix A.2).

Maxwell's equations show that a two-dimensional field can be separated into a contribution from an H-wave (or TE), with the electric field lying in the cross-section Σ, and an E-wave (or TM), with the electric field directed along the z-direction [146]. The current density of H-waves lie in the cross-section Σ, and in the quasistatic limit are represented by both the sets $\{\mathbf{j}_h^{\parallel}\}$ and $\{\mathbf{j}_h^{\perp}\}$. On the contrary, the currents in an E-wave are directed along the z-direction, and in the quasistatic limit can be represented only by the set of modes solution of the MQS eigenvalue problem (2.108), but orthogonal to the cross-section Σ. This set of current modes are therefore independent from and orthogonal to the MQS current modes needed by the H-waves.

Any resonant scattering mechanism in 2D objects with arbitrary sized cross-section is associated with the solutions of the eigenvalue problem

$$\mathcal{L}^{\text{TI}}\{\mathbf{j}_h\} = \frac{1}{\gamma_h}\mathbf{j}_h, \tag{2.111}$$

where $\mathcal{L}^{2D}$ is the full-retarded operator in Eq. (2.102). The operator $\mathcal{L}^{2D}$ is compact, symmetric, but not self-adjoint. For any value of the size parameter x, its eigenvalues are complex with negative imaginary part. The eigenfunctions corresponding to two different eigenvalues are biorthogonal [64, 65]. This eigenvalue problem splits in the EQS eigenvalue problem (2.104) and in the MQS eigenvalue problem (2.108) in the quasistatic regime $x \to 0$. The eigenfunctions of $\mathcal{L}^{2D}$ that in the limit $x \to 0$ tend to the EQS modes are indicated with $\{\mathbf{u}_h\}$ and the corresponding eigenvalues are indicated with $\{\chi_h\}$. These eigenfunctions are called plasmonic modes. Dually, the set of eigenfunctions of $\mathcal{L}^{2D}$ that in the limit $x \to 0$ tend to the MQS modes are indicated with $\{\mathbf{v}_h\}$ and the corresponding eigenvalues are indicated with κ_h/x^2. Although in the limit $x \to 0$, the eigenvalues κ_h/x^2 diverge, the quantities κ_h remain constant. These eigenfunctions are called dielectric modes. The union of the two sets $\{\mathbf{u}_h\}$ and $\{\mathbf{v}_h\}$ is a basis for the unknown current density field in equation (2.111). Its solution is expressed as

$$\mathbf{J} = -i\omega\varepsilon_0\chi \sum_{h=1}^{\infty} \left[\frac{\chi_h}{\chi_h - \chi} \langle \mathbf{u}_h, \mathbf{E}_{inc} \rangle_\Sigma \, \mathbf{u}_h + \frac{\kappa_h}{\kappa_h - \chi x^2} \langle \mathbf{v}_h, \mathbf{E}_{inc} \rangle_\Sigma \, \mathbf{v}_h \right] \tag{2.112}$$

where both the set of modes $\{\mathbf{u}_h\}$ and $\{\mathbf{v}_h\}$ are normalized such that $\langle \mathbf{u}_h, \mathbf{u}_h \rangle_\Sigma = 1$ and $\langle \mathbf{v}_h, \mathbf{v}_h \rangle_\Sigma = 1$, $\forall h$. This equation tends to Eq. (2.110) in the quasistatic limit $x \to 0$.

We now apply the perturbation technique developed in Section 2.2 to TI objects, in order to evaluate the plasmonic and dielectric resonances of a TI object with arbitrary cross-section shape and size parameter $x < 1$, by starting from the corresponding modes in the quasistatic regime.

2.3.1 TI Plasmonic Resonances

To evaluate the plasmonic resonances of TI objects whose cross-section is smaller than or almost equal to the operating wavelength, it is convenient to recast the eigenvalue problem (2.111) as

$$\mathbf{u}_h(\mathbf{r}) + \chi_h \left[-\nabla \oint_{\partial\Sigma} \mathbf{u}_h(\mathbf{r}') \cdot \hat{\mathbf{n}}' g^{2D}\left(\Delta r, x\right)\, dl' + x^2 \int_{\Sigma} \mathbf{u}_h(\mathbf{r}') g^{2D}\left(\Delta r, x\right)\, dS' \right] = \mathbf{0}, \qquad \forall \mathbf{r} \in \Sigma. \quad (2.113)$$

We treat x as a small parameter, and expand the Green's function $g^{2D}\left(\Delta r, x\right)$, the current mode $\mathbf{u}_h$, and the eigenvalue χ_h in terms of x in the neighborhood of the EQS resonance associated with the eigenvalue $\chi_h^{\parallel}$ and mode $\mathbf{j}_h^{\parallel}$.
The 2D Green's function admits the following expansion [160]

$$g^{2D}\left(\Delta r, x\right) = -\frac{i}{4} + \frac{1}{2\pi} \sum_{k=1}^{\infty} \frac{(-1)^{k-1}}{(k!)^2} \left(\frac{\pi}{2} i + 1 + \frac{1}{2} + \dots + \frac{1}{k} \right) \left(\frac{x \Delta r}{2} \right)^{2k} + \frac{1}{2\pi} \sum_{k=0}^{\infty} \frac{(-1)^{k-1}}{(k!)^2} \left(\frac{x \Delta r}{2} \right)^{2k} \left(\log \frac{x \Delta r}{2} + \bar{\gamma} \right), \quad (2.114)$$

where $\bar{\gamma}$ is the Euler-Mascheroni constant. We assume the same expansion for $\mathbf{u}_h$ and χ_h, keeping only the terms tending to 0 for $x \to 0$, namely [5]

$$\chi_h = \sum_{k=0}^{\infty} \chi_h^{(2k)} x^{2k} + \sum_{k=1}^{\infty} \chi_h^{(2k|L)} x^{2k} \log x, \quad (2.115)$$

$$\mathbf{u}_h = \sum_{k=0}^{\infty} \mathbf{u}_h^{(2k)} x^{2k} + \sum_{k=1}^{\infty} \mathbf{u}_h^{(2k|L)} x^{2k} \log x, \quad (2.116)$$

where $\chi_h^{(0)} = \chi_h^{\parallel}$, and $\mathbf{u}_h^{(0)} = \mathbf{j}_h^{\parallel}$. We then plug the expansions (2.114-2.116) into the equation (2.113), and match in sequence the $(x^{2k} \log x)$- and (x^{2k})-terms.

Collecting the $(x^2 \log x)$-terms in Eq. (2.113), and applying the normal solvability condition of Fredholm integral equations [152, 153], the correction $\chi_h^{(2|L)}$ is derived

$$\chi_h^{(2|L)} = \frac{(\chi_h^{\parallel})^2}{4\pi} |\mathbf{P}_h^{\parallel}|^2 \quad (2.117)$$

which is real and proportional to the squared magnitude of the electric dipole moment $\mathbf{P}_h^{\parallel}$ of the h-th EQS mode, defined in Eq. (2.23), where the integration is now performed over the cross-section Σ.
The $(x^2 \log x)$-correction of the associated plasmonic mode is entirely longitudinal,

---

[5] It can be shown, through means of a proof by strong induction, that the odd-powers coefficients vanish.

and can be represented in terms of the EQS mode basis $\{\mathbf{j}_h^{\parallel}\}_{h\in\mathbb{N}}$:

$$\mathbf{u}_h^{(2|L)} = \sum_{\substack{k=1\\k\neq h}}^{\infty} \alpha_{h,k}^{(2|L)}\, \mathbf{j}_k^{\parallel}, \tag{2.118}$$

where the expansion coefficients $\alpha_{h,k}^{(2|L)}$ are

$$\alpha_{h,k}^{(2|L)} = \frac{\chi_h^{\parallel}\chi_k^{\parallel}}{\chi_h^{\parallel} - \chi_k^{\parallel}} \frac{\mathbf{P}_h^{\parallel} \cdot \mathbf{P}_k^{\parallel}}{4\pi}, \qquad \forall k \neq h. \tag{2.119}$$

Mathching the (x^2)-terms in Eq. (2.113), we obtain the real and imaginary parts of the correction coefficient $\chi_h^{(2)}$:

$$\begin{aligned}\operatorname{Re}\left\{\chi_h^{(2)}\right\} =&\left(\chi_h^{\parallel}\right)^2 \left[\frac{1+\bar{\gamma}-\log 2}{4\pi}|\mathbf{P}_h^{\parallel}|^2 + \frac{1}{8\pi}\oint_{\partial\Sigma} j_{n,h}^{\parallel}(\mathbf{r}) \oint_{\partial\Sigma} j_{n,h}^{\parallel}(\mathbf{r}')\Delta r^2 \log\Delta r dl'\, dl\right. \\ &\left. + \frac{1}{2\pi}\int_{\Sigma} \mathbf{j}_h^{\parallel}(\mathbf{r}) \cdot \int_{\Sigma} \mathbf{j}_h^{\parallel}(\mathbf{r}') \log\Delta r\, dS'\, dS\right], \end{aligned} \tag{2.120a}$$

$$\operatorname{Im}\left\{\chi_h^{(2)}\right\} = -\frac{\left(\chi_h^{\parallel}\right)^2}{8}|\mathbf{P}_h^{\parallel}|^2. \tag{2.120b}$$

where the scalar field $j_{n,h}^{\parallel} = \mathbf{j}_h^{\parallel} \cdot \hat{\mathbf{n}}\big|_{\partial\Sigma}$ is defined on the cross-section boundary $\partial\Sigma$. According to Eq. (2.120a), the real part of $\chi_h^{(2)}$ is split into three contributions: the one corresponding to the first term in parenthesis is proportional to the squared magnitude of the electric dipole moment $\mathbf{P}_h^{\parallel}$, and hence to its radiated power; the contribution corresponding to the second term originates from the radiative self-interaction of the boundary charge density associated with the EQS current mode through the scalar potential; the third contribution is instead proportional to the magnetostatic energy of the EQS current mode $\mathbf{j}_h^{\parallel}$, defined in Eq. (2.32) (the integral is now extended over the cross-section Σ). As for the $(x^2\log x)$-correction, according to Eq. (2.120b), the imaginary part of $\chi_h^{(2)}$ is entirely determined by the squared magnitude of the dipole moment $\mathbf{P}_h^{\parallel}$.

We will demonstrate in Eq. (2.127) that $\operatorname{Im}\left\{\chi_h^{(2)}\right\}$ determines the radiation Q-factor of the h-th bright EQS mode. Moreover, we will illustrate in Eq. (2.125) that the coefficients $\chi_h^{(2|L)}$ and $\chi_h^{(2)}$ are linked to the frequency-shift of the h-th plasmonic resonant mode.

If the mode $\mathbf{j}_h^{\parallel}$ is dark, i.e., $\mathbf{P}_h^{\parallel} = \mathbf{0}$, the expansion coefficient $\chi_h^{(2|L)}$ and the imaginary part of the expansion coefficient $\chi_h^{(2)}$ vanish. In this case, the first-order perturbation is the (x^2)-term, whose expansion coefficient $\chi_h^{(2)}$ is real, and is obtained by substituting $\mathbf{P}_h^{\|} = \mathbf{0}$ in Eqs. (2.120). Furthermore, the first imaginary contribution comes from the imaginary part of the (x^4)-term $\chi_h^{(4)}$, that, for dark modes, can be expressed in terms of the two-dimensional electric quadrupole tensor $\overleftrightarrow{\mathbf{Q}}_{\mathrm{E}|h}^{\|}$ of the h-th EQS mode, and its components $Q_{\mathrm{E}|h|ij}$:

$$\operatorname{Im}\left\{\chi_h^{(4)}\right\} = -\frac{\left(\chi_h^{\|}\right)^2}{64}\left[\sum_{i,j=1}^{2}\left(Q_{\mathrm{E}|h|ij}\right)^2 - \frac{1}{2}\operatorname{Tr}\left(\overleftrightarrow{\mathbf{Q}}_{\mathrm{E}|h}^{\|}\right)^2\right] \tag{2.121}$$

where $\overleftrightarrow{\mathbf{Q}}_{\mathrm{E}|h}^{\|}$ is defined in Eq. (A.7) in Appendix A. Thus the first imaginary correction for dark modes is proportional to the power radiated by a 2D quadrupole.

On the basis of low-order correction calculations, we infer that a zero imaginary part of the (x^n)-correction implies a zero imaginary part of the $(x^n \log x)$-correction, as well.

2.3.2 Resonance frequency-shift and Q factor of plasmonic modes

Assuming the object is filled with a Drude metal, whose susceptibility $\chi(\omega)$ is in Eq. (2.21), the EQS resonance frequency $\omega_h^{\|}$ of the h-th mode, is defined as the frequency at which the real part of the metal susceptibility $\operatorname{Re}\{\chi(\omega)\}$ matches the EQS eigenvalue $\chi_h^{\|}$, i.e.

$$\frac{x_h^{\|}}{x_p} = \frac{\omega_h^{\|}}{\omega_p} = \frac{1}{\sqrt{-\chi_h^{\|}}}, \tag{2.122}$$

where $x_h^{\|} = \omega_h^{\|}\ell_c/c_0$ and $x_p = \omega_p \ell_c/c_0$ are the size parameters at the EQS resonance frequency and at the metal plasma frequency, respectively.

In the full-wave regime, by looking at the denominator in the first summation of Eq. (2.112), the resonance condition of the plasmonic resonance is

$$\operatorname{Re}\{\chi_h\} = \operatorname{Re}\{\chi(\omega_h)\} \approx -\frac{\omega_p^2}{\omega_h^2} = -\frac{x_p^2}{x_h^2}, \tag{2.123}$$

where x_h and ω_h is the corresponding resonance size parameter and resonance frequency, respectively. For small particles $x_p \lessapprox 1$, by retaining only the real and imaginary nonzero corrections of the lowest order in Eq. (2.115), the plasmonic eigenvalue $\chi_h(x)$ is approximated as

$$\chi_h(x) \approx \chi_h^{\|} + x^2\left(\operatorname{Re}\left\{\chi_h^{(2)}\right\} + \chi_h^{(2|L)}\log x\right) + i\left(\operatorname{Im}\left\{\chi_h^{(n_i)}\right\}x^{n_i} + \operatorname{Im}\left\{\chi_h^{(n_{iL}|L)}\right\}x^{n_{iL}}\log x\right), \tag{2.124}$$

where n_{iL} and n_i are the orders of the first nonzero imaginary corrections $\text{Im}\left\{\chi_h^{(n_{iL}|L)}\right\}$ and $\text{Im}\left\{\chi_h^{(n_i)}\right\}$. From the considerations made in the previous section, $n_{iL} > n_i$. By plugging the Eq. (2.124) into the Eq. (2.123), we find that the relative frequency shift of the plasmonic resonance with respect to the EQS resonance $\Delta\omega_h/\omega_h^{\|} = (\omega_h - \omega_h^{\|})/\omega_h^{\|}$, or the relative shift in the resonance size parameter $\Delta x_h/x_h^{\|} = (x_h - x_h^{\|})/x_h^{\|}$, in the small cross-section limit $x_h^{\|} \ll 1$, and for $\Delta\omega_h/\omega_h^{\|} \ll 1$, can be approximated as

$$\frac{\Delta\omega_h}{\omega_h^{\|}} = \frac{\Delta x_h}{x_h^{\|}} \approx -\frac{1}{2\chi_h^{\|}}\left[\text{Re}\left\{\chi_h^{(2)}\right\}(x_h^{\|})^2 + \chi_h^{(2|L)}(x_h^{\|})^2 \log x_h^{\|}\right]. \tag{2.125}$$

Thus, the relative frequency shift of any 2D plasmonic mode is linked to the $(x^2 \log x)$-correction coefficient $\chi_h^{(2|L)}$ and to the real part of the (x^2) correction coefficient $\chi_h^{(2)}$.

The radiation Q factor $\text{Q}_h^{\|}$ of the h-th EQS mode is obtained by considering the inverse of the FWHM fractional bandwidth of the h-th addend of the first summation in Eq. (2.112), assuming negligible nonradiative losses $\text{Im}\{\chi\} \approx 0$, and using the expansion (2.124):

$$\text{Q}_h^{\|} = \frac{\chi_h^{\|}}{\text{Im}\left\{\chi_h^{(n_i)}\right\}}\left(\frac{1}{x_h}\right)^{n_i}. \tag{2.126}$$

If the mode $\mathbf{j}_h^{\|}$ is bright, the Q factor is obtained by combining Eqs. (2.120b) and (2.126):

$$\text{Q}_h^{\|} = \frac{8}{(-\chi_h^{\|})|\mathbf{P}_h|^2}\left(\frac{1}{x_h}\right)^2. \tag{2.127}$$

By expressing in Eq. (2.127) the EQS eigenvalue $\chi_h^{\|}$ in terms of the electrostatic energy $\mathcal{W}_e\left\{\mathbf{j}_h^{\|}\right\}$ of the mode $\mathbf{j}_h^{\|}$ (using Eq. (2.22), adapted for TI objects), $Q_h^{\|}$ is also found equal to 2π times the ratio of $\mathcal{W}_e\left\{\mathbf{j}_h^{\|}\right\}$ to the energy radiated in a period by the 2D electric dipole $\mathbf{P}_h$ at the resonance frequency ω_h.

On the other hand, for a dark mode with nonvanishing electric quadrupole, the Q factor is obtained by using Eqs. (2.121) and (2.126):

$$\text{Q}_h^{\|} = \frac{64}{\chi_h^{\|}\left[\sum_{ij}^2\left(Q_{\text{E}|h|ij}\right)^2 - \frac{1}{2}\text{Tr}\left(\overleftrightarrow{\mathbf{Q}}_{\text{E}|h}^{\|}\right)^2\right]}\left(\frac{1}{x_h}\right)^4, \tag{2.128}$$

which is also equal to 2π times the ratio of the electrostatic energy of the h-th EQS mode to the energy radiated in a period by the electric quadrupole $\overleftrightarrow{\mathbf{Q}}_{\text{E}|h}^{\|}$ at the resonance frequency ω_h. If the electric quadrupole moment is also vanishing, the outlined process can be iterated by considering higher order electric multipoles.

In the opposite regime, dominated by material losses, the dissipation Q factor $Q_h^{\|d}$ is obtained as in the 3D case, namely as the inverse of the fractional bandwidth of the h-th addend of the first summation in Eq. (2.110), and has the same expression as in Eq. (2.64). In the intermediate regime, where both the loss kinds are significant, the resulting resonance Q factor is obtained through Eq. (2.65).

2.3.3 TI Dielectric Resonances

To evaluate the dielectric resonances of 2D objects with small cross-section, it is convenient to recast the eigenvalue problem (2.111) as

$$x^2\mathbf{v}_h(\mathbf{r})+\kappa_h\left[-\nabla\oint_{\partial\Sigma}\mathbf{v}_h(\mathbf{r}')\cdot\hat{\mathbf{n}}'g^{2D}\left(\Delta r,x\right)\,dl'+x^2\int_{\Sigma}\mathbf{v}_h(\mathbf{r}')g^{2D}\left(\Delta r,x\right)\,dS'\right]=\mathbf{0},$$
$$\forall\mathbf{r}\in\Sigma. \quad (2.129)$$

As for the plasmonic modes, the mode $\mathbf{v}_h$ and the corresponding eigenvalue κ_h are expanded at $x=0$ in the neighborhood of MQS eigenvalue $\kappa_h^{\perp}$ and mode $\mathbf{j}_h^{\perp}$ in the form:

$$\kappa_h=\sum_{k=0}^{\infty}\kappa_h^{(2k)}x^{2k}+\sum_{k=1}^{\infty}\kappa_h^{(2k|L)}x^{2k}\log x, \quad (2.130)$$

$$\mathbf{v}_h=\sum_{k=0}^{\infty}\mathbf{v}_h^{(2k)}x^{2k}+\sum_{k=1}^{\infty}\mathbf{v}_h^{(2k|L)}x^{2k}\log x, \quad (2.131)$$

where $\kappa_h^{(0)}=\kappa_h^{\perp}$, and $\mathbf{v}_h^{(0)}=\mathbf{j}_h^{\perp}$. We then substitute Eqs. (2.130), (2.131), and (2.114) into the equation (2.129), match in sequence the $(x^{2k}\log x)$- and (x^{2k})-terms, and apply the normal solvability condition of Fredholm integral equations.

By matching the $(x^4\log x)$-terms in Eq. (2.129), we obtain:

$$\kappa_h^{(2|L)}=-\frac{\left(\kappa_h^{\perp}\right)^2}{2\pi}|\mathbf{M}_h^{\perp}|^2, \quad (2.132)$$

which is real and proportional to the squared magnitude of the magnetic dipole moment $\mathbf{M}_h^{\perp}$ of the h-th MQS mode, defined in Eq. (2.33), where the integration domain has to be replaced by the cross-section Σ.

The $(x^2\log x)$-correction of the associated dielectric mode is entirely transverse, and can be represented in terms of the MQS current mode basis $\{\mathbf{j}_h^\perp\}_{h\in\mathbb{N}}$:

$$\mathbf{v}_h^{(2|L)} = \sum_{\substack{k=1\\k\neq h}}^{\infty} \alpha_{h,k}^{(2|L)}\,\mathbf{j}_k^\perp, \tag{2.133}$$

where the expansion coefficients $\alpha_{h,k}^{(2|L)}$ are

$$\alpha_{h,k}^{(2|L)} = \frac{\kappa_k^\perp}{\kappa_h^\perp - \kappa_k^\perp}\frac{\mathbf{M}_h^\perp\cdot\mathbf{M}_k^\perp}{2\pi}, \qquad \forall k \neq h. \tag{2.134}$$

By matching the (x^4)-terms in Eq. (2.129), we obtain the real and imaginary parts of the correction coefficient $\kappa_h^{(2)}$:

$$\begin{aligned}\mathrm{Re}\left\{\kappa_h^{(2)}\right\} = \left(\kappa_h^\perp\right)^2 \Bigg[&\frac{\bar{\gamma} - 1 + \log 2}{2\pi}|\mathbf{M}_h^\perp|^2 \\ &-\frac{1}{8\pi}\int_\Sigma \mathbf{j}_h^\perp(\mathbf{r}')\cdot\int_\Sigma \mathbf{j}_h^\perp(\mathbf{r}')\Delta r^2\log\Delta r\,dS'\,dS\Bigg], \end{aligned}\tag{2.135a}$$

$$\mathrm{Im}\left\{\kappa_h^{(2)}\right\} = -\frac{\left(\kappa_h^\perp\right)^2}{4}|\mathbf{M}_h^\perp|^2. \tag{2.135b}$$

According to Eq. (2.135a), the real part of $\kappa_h^{(2)}$ is split into two contributions: the one corresponding to the first term in parenthesis is proportional to the squared magnitude of the magnetic dipole moment $\mathbf{M}_h^\perp$, and hence to its radiated power; the contribution corresponding to the second term originates from the radiative self-interaction of the MQS current mode through the vector potential. As for the ($x^2\log x$)-correction, according to Eq. (2.135b), the imaginary part of $\kappa_h^{(2)}$ is entirely determined by the squared magnitude of the dipole moment $\mathbf{M}_h^\perp$.

We will illustrate in Eq. (2.89) that $\mathrm{Im}\left\{\kappa_h^{(2)}\right\}$ determines the radiation Q-factor of the h-th MQS mode with nonvanishing magnetic dipole moment. Moreover, we will demonstrate in Eq. (2.125) that $\kappa_h^{(2|L)}$ and $\mathrm{Im}\left\{\kappa_h^{(2)}\right\}$ are associated with the frequency-shift of the resonant dielectric modes.

Nevertheless, if the mode $\mathbf{j}_h^\parallel$ has zero magnetic dipole moment, i.e., $\mathbf{M}_h^\perp = \mathbf{0}$, the expansion coefficient $\kappa_h^{(2|L)}$ and the imaginary part of the expansion coefficient $\kappa_h^{(2)}$ vanish. In this case, the first-order perturbation is the (x^2)-term, whose expansion coefficient $\kappa_h^{(2)}$ is real, and is obtained by substituting $\mathbf{M}_h^\perp = \mathbf{0}$ in Eqs. (2.135). Furthermore, for modes with zero magnetic dipole moment, the first imaginary contribution comes from the imaginary part of the (x^4)-term $\kappa_h^{(4)}$, that can be expressed as

$$\mathrm{Im}\left\{\kappa_h^{(4)}\right\} = -\frac{\left(\kappa_h^{\perp}\right)^2}{16}\left[\frac{3}{8}\sum_{i,j=1}^{2}\left(Q_{\mathrm{M}|h|ij}\right)^2 + 5|\mathbf{P}_{\mathrm{E2}|h}^{\perp}|^2\right] \tag{2.136}$$

where $Q_{\mathrm{M}|h|ij}$ are the components of the two-dimensional magnetic quadrupole tensor $\overleftrightarrow{\mathbf{Q}}_{\mathrm{M}|h}^{\perp}$, introduced in Eq. (A.10), and $\mathbf{P}_{\mathrm{E2}|h}^{\perp}$ is the two-dimensional toroidal dipole, defined in Eq. (A.9). In conclusion, the first imaginary correction for modes with zero magnetic dipole moment is determined by two contributions, accounting for the power radiated by the 2D magnetic quadrupole $\overleftrightarrow{\mathbf{Q}}_{\mathrm{M}|h}^{\perp}$ and by the 2D toroidal dipole $\mathbf{P}_{\mathrm{E2}|h}^{\perp}$.

As for the plasmonic corrections, on the basis of low-order correction calculations, we infer that a zero imaginary part of the (x^n)-correction implies a zero imaginary part of the $(x^n \log x)$-correction, as well.

2.3.4 Resonance frequency-shift and Q factor of dielectric modes

Assuming the object is made of nondispersive dielectric material with positive susceptibility χ, with $\mathrm{Im}\left\{\chi\right\} \ll \mathrm{Re}\left\{\chi\right\}$, the size parameter $x_h^{\perp}$ at the resonance of the h-th MQS mode $\mathbf{j}_h^{\perp}$ is defined as the value of x at which the real part of the susceptibility χ matches the eigenvalue $\kappa_h^{\perp}/x^2$, namely:

$$x_h^{\perp} = \frac{\omega_h^{\perp}}{c_0}\ell_c = \sqrt{\frac{\kappa_h^{\perp}}{\mathrm{Re}\left\{\chi\right\}}}, \tag{2.137}$$

and $\omega_h^{\perp}$ is the corresponding MQS resonance frequency.

In the full-wave regime, the resonance condition for the dielectric mode $\mathbf{v}_h$ is defined by zeroing the real part of the denominator of the h-th addend of the second summation of Eq. (2.112):

$$\mathrm{Re}\left\{\kappa_h\right\} = \mathrm{Re}\left\{\chi\right\} x_h^2, \tag{2.138}$$

being $x_h = \omega_h \ell_c / c_0$ the size parameter at the dielectric resonance.
For small particles $x_h \lessapprox 1$, by keeping only the real and imaginary nonzero corrections of the lowest order in Eq. (2.130), the dielectric eigenvalue $\kappa_h\left(x\right)$ is approximated as

$$\kappa_h\left(x\right) \approx \kappa_h^{\perp} + x^2\left(\mathrm{Re}\left\{\kappa_h^{(2)}\right\} + \kappa_h^{(2|L)}\log x\right) + i\left(\mathrm{Im}\left\{\kappa_h^{(n_i)}\right\}x^{n_i} + \mathrm{Im}\left\{\kappa_h^{(n_{iL}|L)}\right\}x^{n_{iL}}\log x\right), \tag{2.139}$$

where n_{iL} and n_i are the orders of the first nonzero imaginary corrections $\mathrm{Im}\left\{\kappa_h^{(n_{iL}|L)}\right\}$ and $\mathrm{Im}\left\{\kappa_h^{(n_i)}\right\}$. From the considerations made in the previous section, $n_{iL} > n_i$. By plugging the Eq. (2.139) into the Eq. (2.138), we find that the relative frequency shift of the dielectric resonance with respect to the MQS resonance $\Delta\omega_h/\omega_h^\perp = (\omega_h - \omega_h^\perp)/\omega_h^\perp$, or the relative shift in the resonance size parameter $\Delta x_h/x_h^\perp = (x_h - x_h^\perp)/x_h^\perp$, in the small cross-section limit $x_h^\perp \ll 1$, and for $\Delta\omega_h/\omega_h^\perp \ll 1$, can be approximated as

$$\frac{\Delta\omega_h}{\omega_h^\perp} = \frac{\Delta x_h}{x_h^\perp} \approx -\frac{1}{2\kappa_h^\perp}\left[\mathrm{Re}\left\{\kappa_h^{(2)}\right\}(x_h^\perp)^2 + \kappa_h^{(2|L)}(x_h^\perp)^2 \log x_h^\perp\right]. \tag{2.140}$$

Thus, as for the plasmonic counterpart, the relative frequency shift on any 2D dielectric mode is linked to the $(x^2 \log x)$-correction coefficient $\kappa_h^{(2|L)}$ and to the (x^2)-correction coefficient $\kappa_h^{(2)}$.

The radiation Q factor $\mathrm{Q}_h^\perp$ of the h-th MQS mode is obtained by considering the inverse of the FWHM fractional bandwidth of the h-th addend of the second summation in Eq. (2.112), assuming negligible nonradiative losses $\mathrm{Im}\{\chi\} \approx 0$, and using the expansion (2.139):

$$\mathrm{Q}_h^\perp = \frac{\kappa_h^\perp}{\mathrm{Im}\left\{\kappa_h^{(n_i)}\right\}}\left(\frac{1}{x_h}\right)^{n_i}. \tag{2.141}$$

If the mode $\mathbf{j}_h^\perp$ has nonvanishing magnetic dipole moment, its Q factor is obtained by combining Eqs. (2.135b) and (2.141):

$$\mathrm{Q}_h^\perp = \frac{4}{\kappa_h^\perp |\mathbf{M}_h|^2}\left(\frac{1}{x_h}\right)^2. \tag{2.142}$$

By expressing in Eq. (2.142) the EQS eigenvalue $\kappa_h^\perp$ in terms of the magnetostatic energy $\mathcal{W}_m\left\{\mathbf{j}_h^\perp\right\}$ of the mode $\mathbf{j}_h^\perp$ (using Eq. (2.32), adapted for TI objects), $Q_h^\perp$ is also found equal to 2π times the ratio of $\mathcal{W}_m\left\{\mathbf{j}_h^\perp\right\}$ to the energy radiated in a period by the 2D magnetic dipole $\mathbf{M}_h$ at the resonance frequency ω_h.

On the other hand, if the magnetic dipole vanishes, but at least one among the magnetic quadrupole moment $\overleftrightarrow{\mathbf{Q}}_{\mathrm{M}|h}^\perp$ and the “toroidal" dipole moment $\mathbf{P}_{\mathrm{E2}|h}^\perp$ is nonzero, the Q factor is obtained by using Eqs. (2.121) and (2.141):

$$\mathrm{Q}_h^\perp = \frac{16}{\kappa_h^\perp\left[\frac{3}{8}\sum_{i,j=1}^{2}\left(Q_{\mathrm{M}|h|ij}\right)^2 + 5|\mathbf{P}_{\mathrm{E2}|h}^\perp|^2\right]}\left(\frac{1}{x_h}\right)^4, \tag{2.143}$$

which is equal to 2π times the ratio of the magnetostatic energy of the h-th MQS mode to the sum of the energies radiated in a period by the magnetic quadrupole

$\overleftrightarrow{\mathbf{Q}}^{\perp}_{\mathrm{M}|h}$ and by the toroidal dipole moment $\mathbf{P}^{\perp}_{\mathrm{E2}|h}$, at the resonance frequency ω_h.

If they are all vanishing, the outlined process can be iterated by considering higher order magnetic multipoles.

In the opposite regime, dominated by material losses, the same considerations made for the 3D case in Sec. 2.2.4 apply. Specifically, the dissipation Q factor $Q_h^{\perp d}$ is obtained as the inverse of the factional bandwidth of the h-th addend of the second summation in (2.110), assuming dominating nonradiative losses, and has the same expression as in Eq. (2.91).

In an intermediate regime, the total Q factor, indicated with Q_h has the same expression as in Eq. (2.92).

2.3.5 Cylinder

As an example, we consider the plasmonic and dielectric resonances of an infinite cylinder with circular cross-section. The characteristic length ℓ_c of the object is assumed equal to the cylinder radius R, and the size parameter x is $x = \frac{\omega}{c_0}R$.

All the EQS eigenvalues have the same eigen-susceptibility [83], i.e.

$$\chi_n^{\parallel} = -2, \qquad \forall n \in \mathbb{N}. \tag{2.144}$$

Each eigenvalue is associated with 2 degenerate current modes $\mathbf{j}^{\parallel}_{pn}$, where $n \in \mathbb{N}$ is the multipolar order of the mode, and p distiguishes between even (e) and odd (o) modes with respect to the azimuthal variable. The expression of the EQS modes is given in Eq. (C.1) in Appendix C. The modes $\mathbf{j}^{\parallel}_{on}$ for $n = 1, 2, 3$ are shown in Fig. 2.5.

The MQS modes are divided into two sets. The first set is composed by the TE modes, whose vector field lies in the cross-sectional plane. Their eigenvalues $\kappa_{nl}^{\perp \mathtt{TE}}$ are

$$\kappa_{nl}^{\perp \mathtt{TE}} = Z_{n,l}^2, \tag{2.145}$$

where $n \in \mathbb{N}_0$, $l \in \mathbb{N}$, and Z_{nl} is the l-th zero of the n-th order Bessel function of the first kind J_n. Each eigenvalue is associated with a set of 2 degenerate current modes $\mathbf{j}_{pnl}^{\perp \mathtt{TE}}$, with even and odd parity $p \in \{e, o\}$, whose expression is given in Eq. (C.2) in Appendix C. The modes $\mathbf{j}_{enl}^{\perp \mathtt{TE}}$ for $n = 0, 1, 2, 3$ are shown in Fig. 2.5.

The second set is made of TM vector fields directed along the cylinder axis $\hat{\mathbf{z}}$. Their eigenvalues are $\kappa_{nl}^{\perp \mathtt{TM}}$ have the following expression

$$\kappa_{nl}^{\perp \mathtt{TM}} = Z_{n-1,l}^2, \tag{2.146}$$

where $n \in \mathbb{N}_0$, $l \in \mathbb{N}$. Each eigenvalue is associated with a set of 2 degenerate current modes $\mathbf{j}_{pnl}^{\perp \mathtt{TM}}$, $p \in \{e, o\}$, whose analytic expression is given in Eq. (C.3) in Appendix C. The modes $\mathbf{j}_{onl}^{\perp \mathtt{TM}}$ for $n = 0, 1, 2, 3$ are shown in Fig. 2.5.

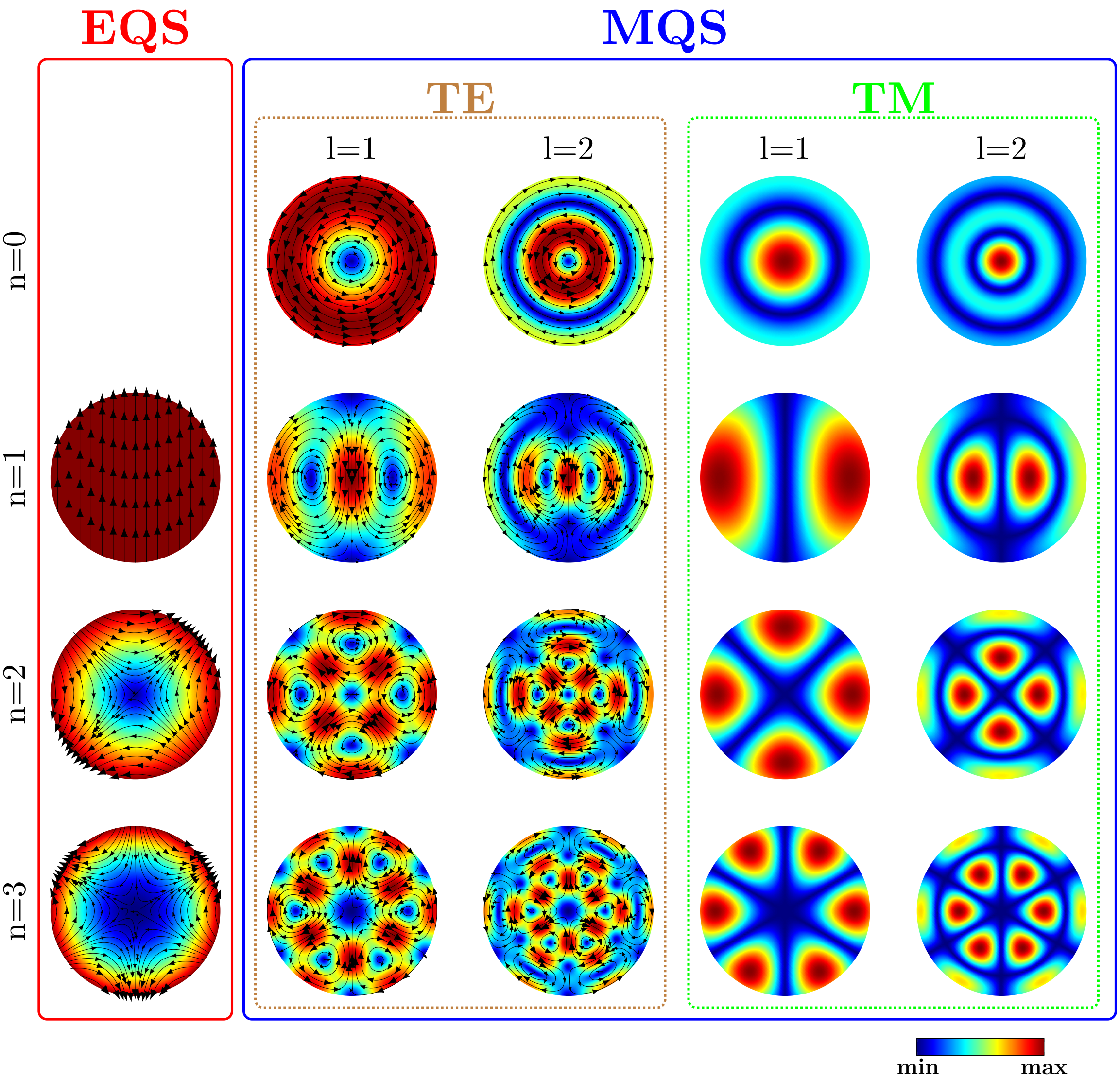

Figure 2.5 – Field lines of the quasistatic modes of an infinite cylinder with circular cross-section. Electroquasistatic modes $\mathbf{j}_{on}^{\parallel}$ with $n = 1, 2, 3$. The magnetoquasistatic modes are divided into two subsets: the TE MQS modes $\mathbf{j}_{enl}^{\perp \mathtt{TE}}$, and the TM modes $\mathbf{j}_{e1nl}^{\perp \mathtt{TM}}$, with $n = 0, 1, 2, 3$ and $l = 1, 2$. The MQS TM modes are vector fields oriented along the cylinder axis, and only their intensity over the cross-section is shown.

To the author's knowledge, a recurrence relation for the radiation corrections of the cylinder plasmonic and dielectric eigenvalues is not available in the literature. However, they can be calculated by applying the iterative method described in the previous sections. For instance, the $(x^2 \log x)$- and x^2-radiation corrections of the

EQS dipolar eigen-susceptibility $\chi_1^{\parallel} = -2$ is obtained by employing the expression of one of the uniform current modes, e.g., $\mathbf{j}_{o1}^{\parallel} = \hat{\mathbf{y}}/\sqrt{\pi}$ (see Sec. C.1) and the magnitude of its electric dipole moment $|\mathbf{P}_1^{\parallel}| = \sqrt{\pi}$ in Eqs. (2.117) and (2.120), leading to

$$\chi_1^{(2|L)} = 1, \tag{2.147}$$

$$\chi_1^{(2)} = 1 + \bar{\gamma} - \log 2 - i\,\frac{\pi}{2}. \tag{2.148}$$

From Eq. (2.127), its radiation Q is

$$\mathrm{Q}_1^{\parallel} = \frac{4}{\pi}\frac{1}{x_1^2}. \tag{2.149}$$

Similarly, the $(x^2 \log x)$- and x^2-radiation corrections of the MQS dipolar $\kappa_{0l}^{\perp} = Z_{0,l}^2$, $l \in \mathbb{N}$, is obtained by plugging the expression of one of the associated current modes, e.g., $\mathbf{j}_{e0l}^{\perp\mathtt{TE}} = \hat{\phi}\dfrac{J_1(Z_{0,l}r)}{\sqrt{\pi}|J_1(Z_{0,l}r)|}$, with (r, ϕ) the in-plane cylindrical coordinates (see Fig. C.1), and the magnitude of its magnetic dipole moment $|\mathbf{M}_0 l^{\perp}| = 2\sqrt{\pi}/Z_{0,l}$ in Eqs. (2.132) and (2.135), leading to

$$\kappa_{0l}^{(2|L)} = -2, \tag{2.150}$$

$$\kappa_{0l}^{(2)} = 2(\bar{\gamma} + \log 2) - i\,\pi. \tag{2.151}$$

From Eq. (2.142), their radiation Q is

$$\mathrm{Q}_{0l}^{\perp\mathtt{TE}} = \frac{Z_{0,1}^2}{\pi}\frac{1}{x_{0l}^2}. \tag{2.152}$$

On this basis, we now briefly investigate the resonances of an infinite cylinder with electrically small cross-section under excitation by an in-plane propagating and polarized plane wave. As for the sphere case in Sec. 2.2.5, we carry this analysis in two scenarios: in the first one, the cylinder is made of a Drude metal, while in the second one, of a high-index dielectric ($\mathrm{Re}\{\chi\} \gg 1$). In both cases, we assume low material losses ($\mathrm{Im}\{\chi\} \ll 1$) in order to compare the predicted radiation Q factor with the fractional bandwidth of the peaks. As physical observable, we choose absorption efficiency σ_{abs}, defined as $\sigma_{\text{abs}} = \dfrac{P_{\text{abs}}}{I_i 2R}$, where P_{abs} is the per-unit-length absorbed power, and I_i is the incident irradiance. Its expression is the same as in Eq. (2.100), where the integration is now performed over the cylinder cross-section Σ. It is calculated using the formulas in Eq. (8.37) in [87]. The radiative shift of the first peak of σ_{abs} and its Q factor are investigated as the object size increases. In particular, the plasmonic and dielectric resonance frequencies are compared against the frequency at which the curve has the peak, denoted as ω_{res}. Similarly, the Q factor of the plasmonic and dielectric modes are validated against the corresponding heuristic Q factors, given by the inverse of the full-width at half maximum `FWHM` [158].

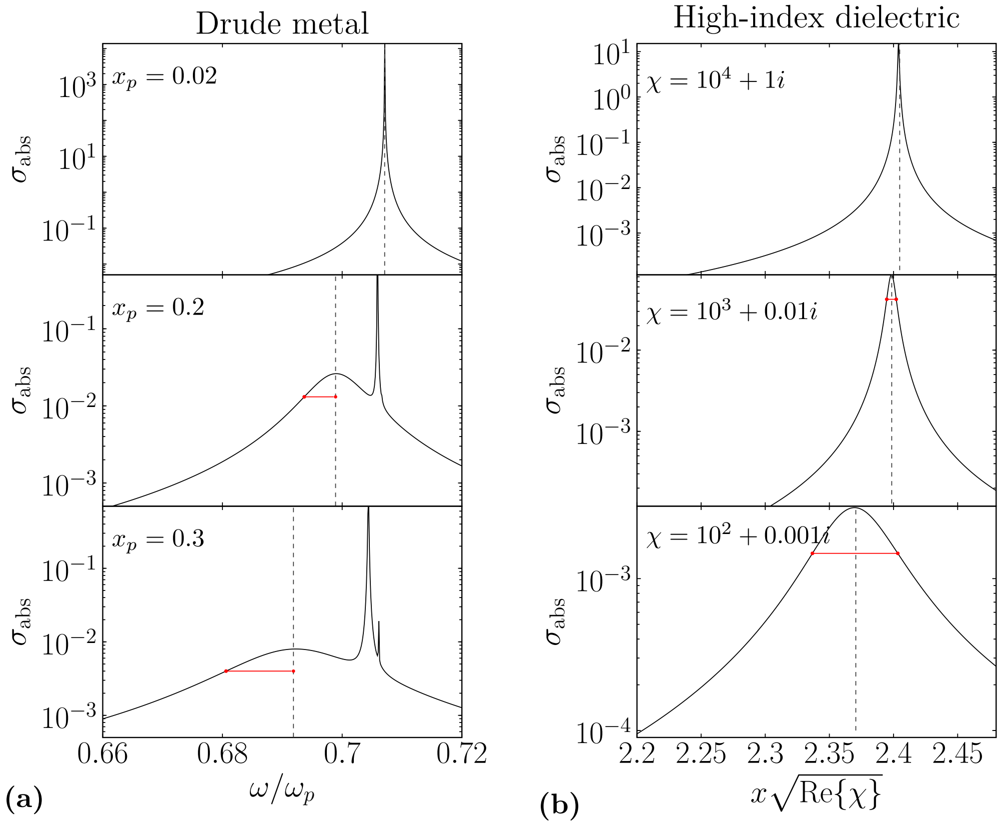

Figure 2.6 – (**a**) Absorption cross-section σ_{abs} of a Drude metal cylinder with circular cross section of radius $R = \ell_c$ as a function of $\omega/\omega_p = x/x_p$, for $x_p = 0.02$ (top panel), $x_p = 0.2$ (middle panel), $x_p = 0.3$ (bottom panel). (**b**) First peak of the σ_{abs} of a dielectric cylinder of circular cross-section, with susceptibility $\chi = 10^4 + i$ (top panel), $\chi = 10^3 + 0.1i$ (middle panel), $\chi = 10^2 + 0.01i$ (bottom panel), as a function of $x\sqrt{\text{Re}\{\chi\}}$. The resonance position obtained by Eq. (2.125) (case (**a**)) and Eq. (2.140) (case (**b**)) are shown with vertical dashed lines. Horizontal lines show the peak half-`FWHM` (**a**) and `FWHM` (**b**).

In Fig. 2.6a, we plot the σ_{abs} for a cylinder made of a low-loss Drude metal, with the dispersion relation given in Eq. (2.21), in which $\nu = 10^{-4}\omega_p$. We evaluate σ_{abs} for three different values of $x_p = 0.02,\, 0.2,\, 0.3$, which for a gold cylinder ($\omega_p = 6.79\,\text{Prad/s}$ [159]) correspond to $R \approx 1\,\text{nm},\, 9\,\text{nm},\, 13\,\text{nm}$. The resonance position of the first excited plasmonic mode, which in the quasistatic limit tends to the dipolar EQS mode $\mathbf{j}^{\|}_{e11}$ (if the impinging plane wave is $\hat{\mathbf{x}}$-polarized), is obtained using Eq.

(2.125), and is shown with a vertical dashed line. In Tab. 2.3, the resonance frequency ω_1 is compared against the corresponding peak position ω_{res}, and the resonant mode $\mathrm{Q}_1^{\|}$ against its heuristic counterpart `FWHM`$^{-1}$. Since other resonances occur very closely to the one under exam by increasing the size parameter, we calculate the `FWHM` as twice the relative half-bandwidth, obtained as the distance between ω_{res} and the smallest frequency at which the curve reaches half the maximum. In Fig. 2.6a, we mark this half-bandwidth with a red segment.

The dissipation $Q^{\|d}$ and the total Q_1 factors, calculated using Eqs. (2.64) and (2.65), respectively, are also shown.
For $x_p = 0.02$ (top panel), the radius R is much smaller than the plasma wavelength λ_p, and hence the EQS approximation well describes the resonance phenomenon: Eq. (2.122) exactly predicts the occurrence of the considered peak. In this case, the radiation and material losses are comparable, as confirmed by the values of the Q factors and the inverse of the `FWHM` in Tab. 2.3.
Increasing x_p to $x_p = 0.2$ (middle panel) and $x_p = 0.3$ (bottom panel), the peak undergoes a broadening and a shift from its quasistatic position. However, the resonance position obtained through Eq. (2.125), which incorporates the radiation corrections, accurately predicts the occurrence of the peak. This time, the resonance is dominated by radiation losses, as confirmed by the good agreement between the mode $\mathrm{Q}_1^{\|}$ and `FWHM`$^{-1}$ in Tab. 2.3. Furthermore, another sharp peak arises from the power spectrum, due to the coupling with the impinging radiation of the plasmonic mode that in the quasistatic limit tends to the EQS quadrupolar mode $\mathbf{j}_{e2}^{\|}$, with eigen-susceptibility also equal to $\chi_2^{\|} = -2$. Since this mode has zero dipole moment, according to Eq. (2.117), the $x^2 \log x$-correction of the EQS eigen-susceptibility vanishes, and the frequency-shift is dominated by the next order, which is the x^2-correction. Thus, as the size parameter increases, its resonance red shifts more slowly than the dipolar one.

x_p	ω_1/ω_p	$\omega_{\text{res}}/\omega_p$	$Q^{\|d}$	$\mathrm{Q}_1^{\|}$	Q_1	`FWHM`$^{-1}$
0.02	0.707	0.707	7071	6366	3350	4752
0.2	0.699	0.699	6990	64	63	64
0.3	0.692	0.692	6923	29	28	29

Table 2.3 – Resonance frequency ω_1 and Q factors $Q^{\|d}$, $\mathrm{Q}_1^{\|}$, Q_1 of the first plasmonic mode of a Drude metal ($\nu = 10^{-4}\omega_p$) cylinder with circular cross-section, for different values of x_p, and their heuristic estimates ω_{res} and `FWHM`$^{-1}$ at the peak of σ_{abs} in Fig. 2.6a

In Fig. 2.6b, we investigate the first peak of the σ_{abs} of a cylinder made of nondispersive high-index dielectric with low losses, as a function of the parameter $x\sqrt{\mathrm{Re}\left\{\chi\right\}}$. We consider three different values of susceptibility χ, namely $\chi = 10^4 + i$, $10^3 + 0.1i$, $10^2 + 0.01i$. In all cases, we have $\mathrm{Re}\left\{\chi\right\} = 10^4 \mathrm{Im}\left\{\chi\right\}$, and hence the dissipation Q, calculated using Eq. (2.91), is $Q^{\perp d} = 10^4$. The resonance position of the dielectric mode that tends to the MQS TE dipolar mode $\mathbf{j}_{e01}^{\perp \mathtt{TE}}$ (if the impinging plane wave is $\hat{\mathbf{x}}$-polarized) is obtained by Eq. (2.140), and highlighted with a vertical dashed line. A red segment joining the two ordinates at half maximum is also shown. In Tab. 2.4, the resonance parameter x_{01} is compared against the corresponding peak position x_{res}, and the resonant mode $\mathrm{Q}_{01}^{\perp}$ against its heuristic counterpart $\mathtt{FWHM}^{-1}$. The dissipation $Q^{\perp d}$ and the total Q_{01}, calculated using Eq. (2.92), are also shown.

For $\chi = 10^4 + i$ (top panel), the size parameter $x \in [0.022, 0.025]$ is very small, and the MQS approximation works well: Eq. (2.137) exactly predicts the occurrence of the σ_{abs} peak. Moreover, as for the examined plasmonic case, the radiation and material losses, as well as their Q factor, are comparable, as confirmed by the values of the dissipation $Q^{\perp d}$, radiation $\mathrm{Q}_{01}^{\perp}$, and the inverse of the `FWHM` in Tab. 2.4.

Decreasing $\mathrm{Re}\left\{\chi\right\}$ to the cases $\chi = 10^3 + 0.1i$ (middle panel) and $\chi = 10^2 + 0.01i$ (bottom panel), the size parameter is increased to $x \in [0.067, 0.078]$ and $x \in [0.220, 0.248]$, respectively, and the σ_{abs} peak experiences a broadening and a red shift with respect to its quasistatic position. As confirmed by the third and fourth columns of Tab. 2.4, Eq. (2.140), which takes into account the radiation corrections, correctly estimates the occurrence of the peak. In both cases, the resonance is dominated by radiation losses, and there is very good agreement between the mode $\mathrm{Q}_{01}^{\perp}$ and the $\mathtt{FWHM}^{-1}$.

χ	$x_{01}\sqrt{\mathrm{Re}\left\{\chi\right\}}$	$x_{\mathrm{res}}\sqrt{\mathrm{Re}\left\{\chi\right\}}$	$Q^{\perp d}$	$\mathrm{Q}_{01}^{\perp}$	Q_{01}	$\mathtt{FWHM}^{-1}$
$10^4 + i$	2.403	2.403	10^4	3183	2415	2683
$10^3 + 0.1i$	2.398	2.398	10^4	318	308	320
$10^2 + 0.01i$	3.094	3.097	10^4	32	32	35

Table 2.4 – Resonance position $x_{01}\sqrt{\mathrm{Re}\left\{\chi\right\}}$ and Q factors $Q^{\perp d}$, $\mathrm{Q}_{01}^{\perp}$, Q_{01} of the first dielectric mode of a high-index dielectric cylinder ($\mathrm{Re}\left\{\chi\right\} = 10^{-4}\mathrm{Im}\left\{\chi\right\}$) with circular cross-section, for different values of susceptibility χ, and their heuristic estimates $x_{\mathrm{res}}\sqrt{\mathrm{Re}\left\{\chi\right\}}$ and $\mathtt{FWHM}^{-1}$ at the peak of σ_{abs} in Fig. 2.6b

2.4 Two-dimensional objects (Surfaces)

We now consider the long-wavelength limit of the scattering problem for a thin body, namely an object whose thickness W is much smaller than its characteristic length ℓ_c and the operating wavelength λ. The complete full-wave analysis can be found in [102].

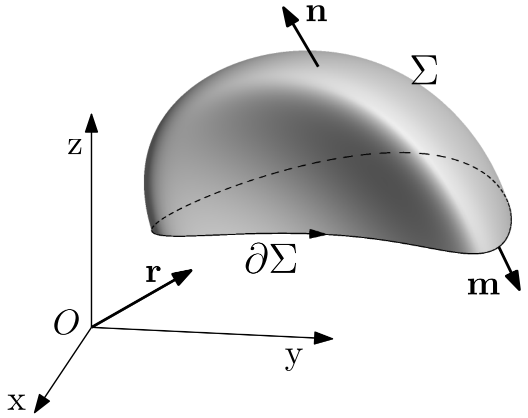

Figure 2.7 – An open surface Σ, with boundary $\partial\Sigma$ and normal $\hat{\mathbf{n}}$. $\hat{\mathbf{m}}$ is the outgoing normal to $\partial\Sigma$, tangent to Σ.

The object is illuminated by a time harmonic electric field $\mathrm{Re}\left\{\mathbf{E}_{\mathrm{inc}}(\mathbf{r})e^{-i\omega t}\right\}$. In this case, only the surface electromagnetic response of the material is relevant, and the body may be treated as it is two-dimensional (e.g., [161]). A two-dimensional (2D) material may be characterized in the frequency domain by either the susceptibility χ or, equivalently, the optical surface conductivity σ,

$$\sigma = -i\omega\varepsilon_0\chi W. \tag{2.153}$$

The surface of the 2D object and its boundary are denoted by Σ and $\partial\Sigma$, respectively, $\hat{\mathbf{n}}$ is the normal to Σ, and $\hat{\mathbf{m}}$ is the outgoing normal to $\partial\Sigma$, which is tangent to Σ, as sketched in Fig. 2.7.

The electromagnetic scattering by the 2D body is modeled by the integro-differential equation for the induced (free or polarization) surface current density $\mathbf{J}_s$ [102]. The constitutive relation of the 2D material is

$$\mathbf{J}_s(\mathbf{r}) = \sigma\overset{\leftrightarrow}{\mathbf{T}}\mathbf{E}(\mathbf{r}), \qquad \forall\mathbf{r} \in \Sigma, \tag{2.154}$$

where $\overset{\leftrightarrow}{\mathbf{T}}$ is the projector that extracts the tangential component of the electric field

$\mathbf{E}(\mathbf{r})$ to the oriented surface Σ,

$$\overset{\leftrightarrow}{\mathbf{T}}\mathbf{E}(\mathbf{r}) = -\hat{\mathbf{n}} \times \left[\hat{\mathbf{n}} \times \mathbf{E}(\mathbf{r})\right], \qquad \forall \mathbf{r} \in \Sigma. \tag{2.155}$$

The total electric field is expressed as $\mathbf{E} = \mathbf{E}_{\text{inc}} + \mathbf{E}_{\text{sca}}$, with $\mathbf{E}_{\text{sca}}$ being the electric field scattered by the object.

A surface charge density ρ_s arises on Σ, whose expression is $\rho_s = -\nabla_s \cdot \mathbf{J}_s / i\omega$, where ∇_s denotes the surface nabla operator on Σ. Eq. (2.154) expresses $\mathbf{J}_s$ in terms of the electric field $\mathbf{E}$ through the surface conductivity of the material. On the other hand, the scattered field can be expressed in terms of $\mathbf{J}_s$ by the electromagnetic potentials in the Lorenz gauge, as for the 3D case in Eq. (2.1) [146, 102],

$$\mathbf{E}_{\text{sca}}(\mathbf{r}) = \zeta_0 \left[\frac{1}{i\,x} \nabla \int_{\Sigma} \nabla_s \cdot \mathbf{W}\, g\left(\Delta r, x\right) dS' - i\,x \int_{\Sigma} \mathbf{W}\, g\left(\Delta r, x\right) dS'\right], \qquad \forall \mathbf{r} \in \mathbb{R}^3, \tag{2.156}$$

where the spatial coordinates have been normalized by ℓ_c, i.e., $\mathbf{r} \to \mathbf{r}/\ell_c$, ζ_0 is the vacuum impedance, and $g\left(\Delta r, x\right)$ is the dimensionless scalar Green's function in vacuum, given in Eq. (2.5). The first term on the right-hand side of Eq. (2.156) is the contribution of the electric scalar potential to the electric field, while the second term is the contribution of the magnetic vector potential.

By combining Eqs. (2.154) and (2.156), we obtain the integro-differential equation governing the induced surface current density field

$$\frac{\mathbf{J}_s(\mathbf{r})}{\sigma} - \zeta_0 \mathcal{L}^{\text{2D}}\left\{\mathbf{J}_s\right\}(\mathbf{r}) = \overset{\leftrightarrow}{\mathbf{T}}\mathbf{E}_{\text{inc}}(\mathbf{r}), \qquad \forall \mathbf{r} \in \Sigma, \tag{2.157}$$

where

$$\mathcal{L}^{\text{2D}}\left\{\mathbf{W}\right\} = \frac{1}{i\,x} \nabla_s \int_{\Sigma} \nabla_s \cdot \mathbf{W}\, g\left(\Delta r, x\right) dS' - i\,x \int_{\Sigma} \mathbf{W}\, g\left(\Delta r, x\right) dS', \qquad \mathbf{W} \in \Sigma, \forall \mathbf{r} \in \mathbb{R}^3, \tag{2.158}$$

which is solved with the boundary condition

$$\mathbf{J}_s \cdot \hat{\mathbf{m}}\big|_{\partial\Sigma} = 0, \tag{2.159}$$

which arises from the requirement that the average energy of the scattered electromagnetic field must be limited.

As for the 3D and TI cases, in order to represent the solution of Eq. (2.157) in the quasistatic limit $x \to 0$, we set up a complete basis joining two orthogonal sets.

The first set $\{\mathbf{j}_h^{\parallel}\}$ is given by the solution of the eigenvalue problem

$$\mathcal{L}_e^{\text{2D}}\left\{\mathbf{j}_h^{\parallel}\right\}(\mathbf{r}) = \frac{1}{\chi_h^{\parallel}}\mathbf{j}_h^{\parallel}(\mathbf{r}), \qquad \forall\mathbf{r}\in\Sigma, \tag{2.160}$$

where $\mathcal{L}_e^{\text{2D}}$ is the electrostatic integral operator that gives the electrostatic field as a function of the surface charge density:

$$\mathcal{L}_e^{\text{2D}}\left\{\mathbf{W}\right\}(\mathbf{r}) = \nabla_s \int_{\Sigma} \nabla_s\cdot\mathbf{W}\, g_0\left(\Delta r\right) dS', \qquad \mathbf{W}\in\Sigma,\, \forall\mathbf{r}\in\Sigma \tag{2.161}$$

where $g_0\left(\Delta r\right)$ is the dimensionless static Green's function in vacuum, given in Eq. (2.8). The spectrum of $\mathcal{L}_e^{\text{2D}}$ is countable infinite, and the eigenfunctions $\{\mathbf{j}_h^{\parallel}\}_{h\in\mathbb{N}}$ are nonsolenoidal ($\nabla_s\cdot\mathbf{j}_h^{\parallel}\neq 0$) and irrotational ($\nabla_s\times\mathbf{j}_h^{\parallel}=\mathbf{0}$). Moreover, $\mathcal{L}_e^{\text{2D}}$ is self-adjoint and definite negative, and hence the eigenvalues $\chi_h^{\parallel}$ are real and negative and the eigenfunctions are orthogonal according to the scalar product in Eq. (2.107). We then assume this set orthonormal, i.e., $\langle\mathbf{j}_h^{\parallel},\mathbf{j}_k^{\parallel}\rangle_\Sigma=\delta_{h,k}$. We label these eigenfunctions as the EQS modes of the surface Σ. The electric dipole moment $\mathbf{P}_h$ of the EQS mode $\mathbf{j}_h^{\parallel}$ can be obtained from Eq. (2.23), where the integration is now performed on the surface Σ, while the Q factor is given by Eq. (2.61).

The second set is composed by solenoidal ($\nabla_s\cdot\mathbf{j}_h^{\perp}=0$) and rotational ($\nabla_s\times\mathbf{j}_h^{\perp}\neq\mathbf{0}$) functions $\{\mathbf{j}_h^{\perp}\}_{h\in\mathbb{N}}$, orthogonal to the eigenfunctions $\{\mathbf{j}_h^{\parallel}\}$, and solutions of the eigenvalue problem

$$\mathcal{L}_m^{\text{2D}}\left\{\mathbf{j}_h^{\perp}\right\}(\mathbf{r}) = \frac{1}{\kappa_h^{\perp}}\mathbf{j}_h^{\perp}(\mathbf{r}), \qquad \forall\mathbf{r}\in\Sigma, \tag{2.162}$$

where $\mathcal{L}_m^{\text{2D}}$ is the magneostatic integral operator

$$\mathcal{L}_m^{\text{2D}}\left\{\mathbf{W}\right\}(\mathbf{r}) = \int_{\Sigma} \mathbf{W}\, g_0\left(\Delta r\right) dS', \qquad \mathbf{W}\in\Sigma,\, \forall\mathbf{r}\in\Sigma. \tag{2.163}$$

$\mathcal{L}_m^{\text{2D}}$ has a countable infinite spectrum, and is self-adjoint and definite positive, therefore the eigenvalues $\{\kappa_h^{\perp}\}_{h\in\mathrm{N}}$ are real and positive, and the eigenfunctions $\{\mathbf{j}_h^{\perp}\}_{h\in\mathbb{N}}$ are orthogonal according to the scalar product (2.107), and assumed normalized, namely $\langle\mathbf{j}_h^{\perp},\mathbf{j}_k^{\perp}\rangle_\Sigma=\delta_{h,k}$. We label these eigenfunctions as the MQS modes of the surface Σ. The magnetic dipole moment $\mathbf{M}_h$ of the MQS mode $\mathbf{j}_h^{\perp}$ is expressed as in Eq. (2.33), where the integration is now performed on the surface Σ, while the Q factor is given by Eq. (2.88).

Eventually, the surface current density induced on the surface Σ can be expressed as

$$\mathbf{J}_s = \sigma \sum_{h=1}^{\infty} \left[\frac{\sigma_h^{\|}}{\sigma_h^{\|} - \zeta_0 \sigma} \langle \mathbf{j}_h^{\|}, \overleftrightarrow{\mathbf{T}} \mathbf{E}_{\text{inc}} \rangle_\Sigma \, \mathbf{j}_h^{\|} + \frac{\sigma_h^{\perp}}{\sigma_h^{\perp} - \zeta_0 \sigma} \langle \mathbf{j}_h^{\perp}, \overleftrightarrow{\mathbf{T}} \mathbf{E}_{\text{inc}} \rangle_\Sigma \, \mathbf{j}_h^{\perp} \right], \tag{2.164}$$

where

$$\begin{aligned} \sigma_h^{\|} &= i\, x \chi_h^{\|}, \\ \sigma_h^{\perp} &= i \frac{\kappa_h^{\perp}}{x}, \end{aligned} \tag{2.165}$$

are the EQS and MQS *eigen-conductivities*, respectively. They are purely imaginary. Since $\chi_h^{\|} < 0$, the EQS eigen-conductivities $\sigma_h^{\|}$ has negative imaginary part. Moreover, they tend to 0 for $x \to 0$, but the EQS eigenvalue $\chi_h^{\|}$ remains finite. Conversely, since $\kappa_h^{\perp} > 0$, the MQS eigen-conductivities $\sigma_h^{\|}$ has positive imaginary part. Furthermore, they diverge for $x \to 0$, but the MQS eigenvalue $\kappa_h^{\perp}$ remains finite.

The expression of the surface current density $\mathbf{J}_s$ highlights two resonance conditions for σ. The first one is

$$\text{Im}\left\{\sigma(\omega_h)\right\} = \chi_h^{\|} \frac{\omega_h}{c_0} \ell_c, \tag{2.166}$$

with the resonant excitation of the EQS mode $\mathbf{j}_h^{\|}$. Eq. (2.166) suggests that in quasistatic limit, the EQS modes can be resonantly excited in conducting 2D materials, whose conductivity has negative and small imaginary part.

The second resonance condition is

$$\text{Im}\left\{\sigma(\omega_h)\right\} = \kappa_h^{\perp} \frac{c_0}{\omega_h \ell_c}, \tag{2.167}$$

with the resonant excitation of the MQS mode $\mathbf{j}_h^{\perp}$. Eq. (2.167) implies that the MQS modes can be resonantly excited in 2D dielectric objects of conductivity with positive and high imaginary part (unless active materials are used [102]).

As an example, in Fig. 2.8 we show the first three EQS and MQS modes of a spherical surface (sometimes called spherical inductor), whose expression is given in Eq. (B.8) and (B.9) in Appendix B. The EQS and MQS eigenvalues have the following expression [102]:

$$\chi_n^{\|} = -\frac{2n+1}{n(n+1)}, \tag{2.168}$$

$$\kappa_n^{\perp} = (2n+1), \qquad \forall n \in \mathbb{N}, \tag{2.169}$$

where n is the mode multipolar order, and the corresponding eigen-conductivities are

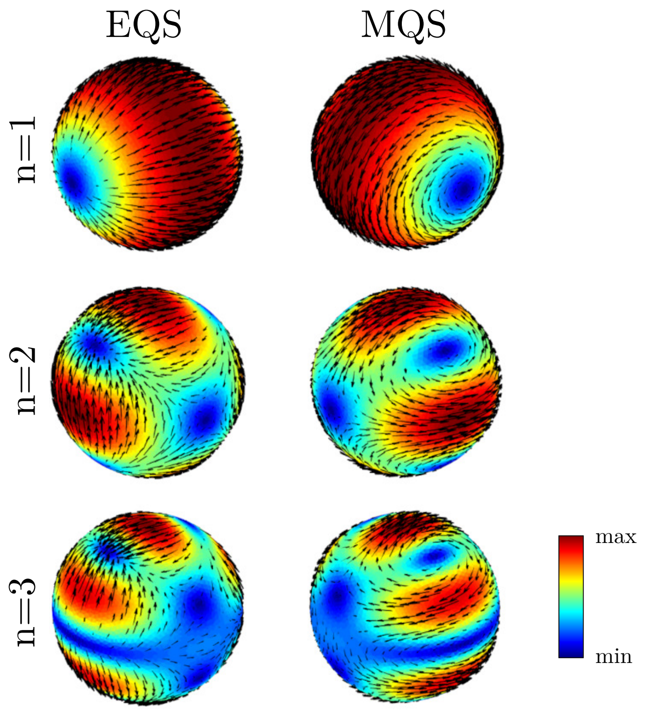

Figure 2.8 – Plots of the EQS $\mathbf{j}_n^{\parallel}$ and MQS $\mathbf{j}_n^{\perp}$ modes (n = 1, 2, 3) of a spherical surface [102]. The direction of each arrow represents the direction of the mode at the corresponding point on the spherical surface, while the length of the arrow and the color describe its amplitude.

obtained by applying Eq. (2.165).

2.5 Conclusions

The electromagnetic scattering response of an object is exhaustively characterized by the Maxwell's equations. When the object is much smaller than the vacuum wavelength, the complexity of the Maxwell's equations could be broken down into two more manageable units: the electro-quasistatic and magneto-quasistatic approximations, i.e., the ones behind the modelling of capacitors and inductors. The electroquasistatic approximation covers the resonances in small particles with negative dielectric permittivity, e.g., the plasmon resonances in metals at optical frequencies. The magneto-quasistatic one describes the resonace mechanism in small objects of high and positive permittivity, such as in AlGaAs and Si nanoparticles [36].

In this chapter, we built the mathematical apparatus needed to describe these two resonance mechanisms in the quasistatic regime, for homogeneous isotropic nonmagnetic objects. We considered three different geometries: three-dimensional, translational invariant, and two-dimensional (surfaces) objects. In each scenario, we linked the electro-quasistatic and magneto-quasistatic resonances to two linear eigenvalue problems involving compact and self-adjoint integral operators, in which the spectral parameter is the electric susceptibility χ. These eigenfunctions are the quasistatic current modes of the object, and the eigenvalues are related to its eigen-susceptibilities. The current modes and the eigen-susceptibilities only depend on the geometry of the body, and they are material independent.

Unfortunately, both approximations are unable to predict the resonance frequency shift and the radiation Q factor arising from the coupling with the radiation. For this purpose, we derived closed-form expressions for the radiation corrections to the quasistatic eigenvalues and modes. These corrections only depend on the quasistatic current mode distribution. On this basis, we provided closed-form expressions of the frequency shift and the radiation Q factor of both plasmonic modes (corrections of the EQS modes) and dielectric modes (corrections of the MQS modes), where the dependencies on the material and the size of the object are factorized.

For arbitrary shaped 3D objects and surfaces of dimension smaller than the operating wavelength, the relative frequency shift of any mode is a quadratic function of the size parameter x at the quasistatic resonance, whose prefactor depends on the ratio between the second-order correction coefficient of the quasistatic eigenvalue and the quasistatic eigenvalue.
The radiation Q factor is an inverse power function of x whose exponent is the order $n_i \geq 3$ of the first nonvanishing imaginary correction, and the prefactor only depends on the quasistatic eigenvalue and the multipolar components of the quasistatic modes.

For translational invariant structures with arbitrary shaped cross-section, the relative frequency shift $\dfrac{\Delta\omega_h}{\omega_h}$ of any mode is in the form $\dfrac{\Delta\omega_h}{\omega_h} = (Ax^2 + Bx^2 \log x)$, where A depends on the ratio between the real part of the second-order correction coefficient of the quasistatic eigenvalue and the quasistatic eigenvalue, and B on the ratio between the $(x^2 \log x)$-correction coefficient and the quasistatic eigenvalue.
The radiation Q factor for TI structures has the same form as for the 3D structures, but the order n_i of the first nonvanishing imaginary correction is now $n_i \geq 2$.

Chapter 3

Lower Bounds to Quality Factor of Small Radiators

The problem of finding the optimal current distribution supported by an electrically small radiator yielding the minimum Q factor is a classic problem in electromagnetism. In this chapter, a representation of the optimal current in terms of electroquasistatic and magnetoquasistatic scattering resonance modes, investigated in the previous chapter, is introduced. The provided representation leads to analytical and closed form expressions of the electric and magnetic polarizability tensors of arbitrary shaped objects, whose eigenvalues are known to be linked to the minimum Q. Hence, the minimum Q and the corresponding optimal current are determined from the sole knowledge of the eigenvalues and the dipole moments associated with the quasistatic scattering modes. It was found that when the radiator exhibits two orthogonal reflection symmetries, its minimum Q factor can be simply obtained from the Q factors of its quasistatic modes, through a simple parallel formula. If an electric-type radiator, which supports solenoidal and irrotational currents, admits a spatially uniform quasistatic resonance mode, then this mode is guaranteed to have the minimum Q factor. Analogously, a magnetic-type resonator, which supports solenoidal currents with vanishing normal component to the object, admitting a mode of the form $\hat{\mathbf{r}} \times \mathbf{c}$, where $\hat{\mathbf{r}}$ is the radial direction and $\mathbf{c}$ is a constant vector, has as minimum Q factor the one of the mode. Many examples are worked out, exemplifying the application of the introduced method to arbitrary shaped radiators, both three-dimensional and translational invariant, of both electric and magnetic type.

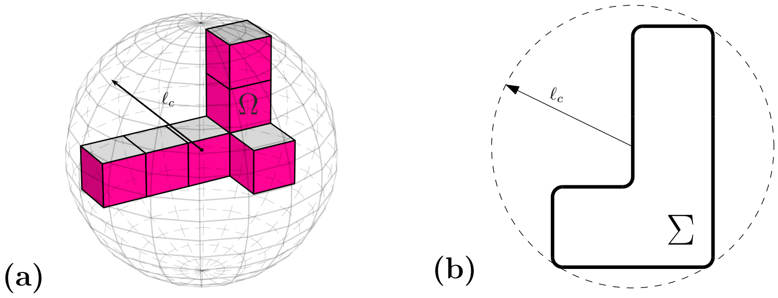

Figure 3.1 – ℓ_c is the radius of the minimum sphere circumscribing the 3D object (**a**), or the minimum circle enclosing the TI object cross-section (**b**). The search of the minimum current is constrained to the 3D radiator volume Ω (or surface Σ), and the TI radiator cross-section Σ.

3.1 Minimum Q factor of 3D radiators of the electric type

Let us consider a homogeneous, isotropic, non-magnetic, linear material occupying a domain, either a volume Ω or a surface Σ, of characteristic linear dimension ℓ_c. From now on, we choose ℓ_c to be the radius of the minimum sphere enclosing the three-dimensional object, as shown in Fig. 3.1a. The material has relative dielectric permittivity ε_R, electric susceptibility $\chi = \varepsilon_R - 1$, and it is surrounded by vacuum. The object is assumed electrically small, namely $x = \dfrac{\omega}{c_0}\ell_c < 1$.

3D radiators of the electric type support longitudinal current distributions, which belongs to the functional space $\mathbf{L}^2_{\parallel}(\Omega) = \{\mathbf{L}^2(\Omega) \,|\, \nabla \cdot \mathbf{j} = 0, \nabla \times \mathbf{j} = \mathbf{0} \text{ in } \Omega \setminus \partial\Omega\}$. Their Q factor can be expressed as 2π times the ratio of the electrostatic energy stored in the whole space to the energy radiated toward infinity in a period [118, 110, 108]:

$$Q = 3 \, \frac{\displaystyle\oint_{\partial\Omega} \sigma(\mathbf{r}) \oint_{\partial\Omega} \frac{\sigma(\mathbf{r}')}{|\mathbf{r} - \mathbf{r}'|} dS' dS}{\displaystyle\oint_{\partial\Omega} \sigma(\mathbf{r}) \oint_{\partial\Omega} \sigma(\mathbf{r}') \, |\mathbf{r} - \mathbf{r}'|^2 \, dS' dS} \, \frac{1}{x^3}, \tag{3.1}$$

where $\sigma = \mathbf{j} \cdot \hat{\mathbf{n}}$, and the spatial coordinates have been normalized by ℓ_c, i.e., $\mathbf{r} \to \mathbf{r}/\ell_c$. The problem of finding the minimum quality factor consists in the search of the *optimal* current density $\mathbf{j}$ which belongs to $\mathbf{L}^2_{\parallel}$, yielding the minimum value of the functional $x^3 Q$. The above expression for the radiation Q factor and the considerations we make in this section also hold for surface current densities supported on a two-dimensional domain Σ provided the quantity $\mathbf{j} \cdot \hat{\mathbf{n}}$ is replaced by $\nabla_s \cdot \mathbf{j}$, being ∇_s the surface nabla operator.

The minimization of the Q factor functional in Eq. (3.1) can be tackled by means of the Lagrange's multipliers method [108]: we fix the amplitude P of the electric dipole moment $\mathbf{P}$ of the optimal current, and search for the stationary points of the auxiliary Lagrangian

$$\mathcal{L}_E(\sigma,\lambda) = \oint_{\partial\Omega} \sigma(\mathbf{r}) \oint_{\partial\Omega} \frac{\sigma(\mathbf{r}')}{|\mathbf{r}-\mathbf{r}'|} dS' dS - \tau \left(\left| \oint_{\partial\Omega} \mathbf{r}\sigma(\mathbf{r}) dS \right|^2 - P^2 \right), \tag{3.2}$$

where τ is a Lagrange multiplier, and σ is subjected to the charge neutrality condition $\oint_{\partial\Omega} \sigma dS = 0.$. The variational problem (3.2) yields the critical equation [122]

$$\oint_{\partial\Omega} \frac{\sigma(\mathbf{r}')}{|\mathbf{r}-\mathbf{r}'|} dS' = \tau \mathbf{r} \cdot \oint_{\partial\Omega} \sigma(\mathbf{r}') \mathbf{r}' dS', \qquad \forall \mathbf{r} \in \partial\Omega. \tag{3.3}$$

Then, upon multiplying Eq. (3.3) with σ and integrating over $\partial\Omega$, we find that Q in Eq. (3.1) also satisfies [122]

$$x^3 Q = 6\pi \min_{\sigma} \tau. \tag{3.4}$$

Using the constraint $\left| \oint_{\partial\Omega} \mathbf{r}\sigma(\mathbf{r}) dS \right| = P > 0$, we recast Eq. 3.3 as

$$\oint_{\partial\Omega} \frac{\sigma(\mathbf{r}')}{|\mathbf{r}-\mathbf{r}'|} dS' = \tau P \hat{\mathbf{e}} \cdot \mathbf{r}, \qquad \forall \mathbf{r} \in \partial\Omega, \tag{3.5}$$

for some unknown unit vector $\hat{\mathbf{e}}$.

We now introduce the electric polarizability tensor: a linear correspondence between an homogeneous external displacement field $\varepsilon_0 E_0 \hat{\mathbf{e}}$ and the electric dipole moment $\mathbf{P}$, defined as

$$\mathbf{P} = \oint_{\partial\Omega} \sigma \mathbf{r} \, dS, \tag{3.6}$$

where σ is the solution of the surface integral equation

$$\oint_{\partial\Omega} \frac{\sigma(\mathbf{r}')}{4\pi |\boldsymbol{r}-\boldsymbol{r}'|} dS' = \varepsilon_0 E_0 \hat{\boldsymbol{e}} \cdot \mathbf{r} \qquad \forall \mathbf{r} \in \partial\Omega, \tag{3.7}$$

and it is subjected to the charge neutrality condition. Thus, the electric polarizability tensor γ_e is a 3×3 matrix, defined as the map $\gamma_e \cdot \hat{\boldsymbol{e}} \varepsilon_0 E_0 = \mathbf{P}$.[1]

Comparing Eq. (3.7) with Eq. (3.5), we identify the generic external displacement

---

[1] The electric and magnetic polarizability tensors have the dimension of volume. However, we will refer to a dimensionless polarizability tensor ($\boldsymbol{\gamma} \to \boldsymbol{\gamma}/\ell_c^3$) since the spatial coordinates normalization ($\mathbf{r} \to \mathbf{r}/\ell_c$).

field amplitude $\varepsilon_0 E_0$ with $\tau P \hat{\mathbf{e}}$, and the dipole moment defined in Eq. (3.6). Thus, we can further recast Eq. (3.5) as

$$\gamma_e \cdot \hat{\mathbf{e}} = \frac{1}{\tau}\hat{\mathbf{e}}, \tag{3.8}$$

which is an eigenvalue problem in $(\tau, \hat{\mathbf{e}})$ for γ_e. Finally, by combining Eq. (3.4) with Eq. (3.8), the minimum Q factor is [122]:

$$\left(x^3 Q\right)_{\min} = \frac{6\pi}{\gamma_{\mathrm{e,max}}}, \tag{3.9}$$

where $\gamma_{\mathrm{e,max}}$ is the maximum among the eigenvalues of the (dimensionless) electric polarizability tensor $\boldsymbol{\gamma}_e$ of the scaled object.

The surface integral operator in Eq. (3.7) is tightly related to the operator $\mathcal{L}_e\{\mathbf{w}\} = -\nabla \oint_{\partial\Omega} \frac{\mathbf{w}(\mathbf{r}') \cdot \hat{\mathbf{n}}'}{4\pi\left|\mathbf{r}-\mathbf{r}'\right|}\, dS'$, introduced in Sec. 2.1.1, describing the electrostatic (plasmon) resonances. We aim at determining the polarizability tensor through means of an EQS modes expansion.

The procedure consists in expanding the charge density σ solution of problem (3.7), in terms of the EQS current modes $\{\mathbf{j}_h^{\|}\}_{h\in\mathbb{N}}$, solutions of the EQS eigenvalue problem $\mathcal{L}_e\{\mathbf{j}_\mathbf{h}^{\|}\} = \mathbf{j}_h^{\|}/\chi_h^{\|}$, which constitute a complete basis for the search space $\mathbf{L}^2_{\|}(\Omega)$, namely:

$$\sigma(\mathbf{r}) = \sum_{h=1}^{\infty} a_h\, \mathbf{j}_h^{\|}(\mathbf{r}) \cdot \hat{\mathbf{n}}(\mathbf{r}) \qquad \text{on}\, \partial\Omega. \tag{3.10}$$

The charge density $\sigma(\mathbf{r})$ constructed in this way naturally satisfies the charge neutrality condition. By employing the above expansion in Eq. (3.7), multiplying both members by $\mathbf{j}_k^{\|} \cdot \hat{\mathbf{n}}$ and integrating over the surface boundary $\partial\Omega$, we obtain

$$\sum_{h=1}^{\infty} a_h \int_{\partial\Omega} \mathbf{j}_k^{\|}(\mathbf{r}) \cdot \hat{\mathbf{n}}(\mathbf{r}) \oint_{\partial\Omega} \frac{\mathbf{j}_h^{\|}(\mathbf{r}') \cdot \hat{\mathbf{n}}'}{4\pi\left|\mathbf{r}-\mathbf{r}'\right|} dS' dS = \left(\varepsilon_0 E_0 \hat{\mathbf{e}}\right) \cdot \int_{\Omega} \left(\mathbf{j}_k^{\|} \cdot \hat{\mathbf{n}}\right) \mathbf{r}\, dV. \tag{3.11}$$

By exploiting the EQS current modes and eigensusceptibilities $\{\chi_h^{\|}, \mathbf{j}_h^{\|}\}_{h\in\mathbb{N}}$ are solution of the EQS eigenvalue problem, and using the orthonormality condition $\langle \mathbf{j}_h^{\|}, \mathbf{j}_k^{\|}\rangle_\Omega = \delta_{h,k}$, we derive the expansion coefficients a_h of the charge density distribution

$$a_h = -\chi_h^{\|}\left(\varepsilon_0 E_0 \hat{\boldsymbol{e}}\right) \cdot \mathbf{P}_h, \tag{3.12}$$

and the corresponding dipole moment

$$\mathbf{P} = -\sum_{h=1}^{\infty} \chi_h^{\parallel} \left(\varepsilon_0 E_0 \hat{\boldsymbol{e}} \cdot \mathbf{P}_h\right) \mathbf{P}_h = \left[-\sum_{h=1}^{\infty} \chi_h^{\parallel} \mathbf{P}_h \otimes \mathbf{P}_h\right] \cdot \left(\varepsilon_0 E_0 \hat{\boldsymbol{e}}\right), \tag{3.13}$$

where $\mathbf{P}_h$ is the dipole moment of the EQS current mode $\mathbf{j}_h^{\parallel}$, given in Eq. (2.23), and $\mathbf{P}_h \otimes \mathbf{P}_h$ is the dyad resulting from the tensor (dyadic) product [162] of $\mathbf{P}_h$ with itself.

Therefore, the 3×3 electric polarizability tensor $\boldsymbol{\gamma}_e$ is [2]

$$\boldsymbol{\gamma}_e = -\sum_{h=1}^{\infty} \chi_h^{\parallel} \mathbf{P}_h \otimes \mathbf{P}_h. \tag{3.14}$$

The above closed-form identity is one of the main results of the spectral theory proposed in this work: it bridges the polarizability tensor with the EQS (plasmon) modes.

In the general case, the maximum eigenvalue $\gamma_{\text{e,max}}$ of the $\boldsymbol{\gamma}_e$ is associated with the minimum quality factor. The corresponding (normalized) eigenvector returns the direction of the dipole moment of the optimal current, which we call $\hat{\mathbf{p}}_{\text{opt}}$. The optimal current is readily obtained in terms of the EQS (plasmon) modes:

$$\mathbf{j}_{\text{opt}}(\mathbf{r}) = -\sum_{h=1}^{\infty} \chi_h^{\parallel} \left(\hat{\mathbf{p}}_{\text{opt}} \cdot \mathbf{P}_h\right) \mathbf{j}_h^{\parallel}(\mathbf{r}). \tag{3.15}$$

As we will see in the next sections, only few EQS modes have to be considered to have a good estimation of the minimum Q factor and the optimal current.

Symmetries in the shape of the radiator can markedly simplify the expression of the polarizability tensor, and the calculation of the optimal current and the minimum Q. Specifically, if the shape of the resonator has two orthogonal reflection symmetries, $\boldsymbol{\gamma}_e$ can be diagonalized by choosing a co-aligned coordinate system $(\mathbf{e}_1, \mathbf{e}_2, \mathbf{e}_3)$, (e.g., for an ellipsoid it is oriented along its principal axes). The dipole moments of the EQS mode are also aligned along these directions. In this case, the three occurrences of $\boldsymbol{\gamma}_e$ are given by:

$$\gamma_i = -\sum_{\substack{h \\ \mathbf{e}_i-\text{aligned}}} \chi_h^{\parallel} \left|\mathbf{P}_h\right|^2, \qquad i = 1, 2, 3 \tag{3.16}$$

where the summation only runs over the EQS modes exhibiting dipole moment directed along $\mathbf{e}_i$. In this case, the minimum Q along the axis $\mathbf{e}_i$ is obtained by the

---

[2] Since the EQS operator $\mathcal{L}_e$ is negative definite, the eigensusceptibilities $\{\chi_h^{\parallel}\}_{h\in\mathbb{N}}$ are negative valued, and the polarizability tensor is clearly semi-positive definite, as it should be [163].

parallel formula

$$\frac{1}{\left(x^3 Q\right)_{\min}} = \sum\nolimits_{\mathbf{e}_i-\text{aligned}}^{h} \frac{1}{x_h^3 Q_h^{\|}}, \tag{3.17}$$

where $Q_h^{\|}$ and x_h are the Q factor and the resonant size parameter [3] of the bright EQS mode $\mathbf{j}_h^{\|}$, respectively (see Sec. 2.2.2), i.e.

$$x_h^3 Q_h^{\|} = \frac{6\pi}{\left(-\chi_h^{\|}\right) |\mathbf{P}_h|^2}. \tag{3.18}$$

Then, the global minimum Q factor is taken among the Q for each axis.

In conclusion, if the shape of the resonator has two orthogonal reflection symmetries, the minimum Q factor along a particular direction $\mathbf{e}_i$ can be obtained as the parallel of the quality factor of the bright EQS (plasmon) modes aligned along that direction.

In addition, due to the orthonormality condition, when there exists a current mode which is spatially uniform along a given direction, there exists one and only one EQS mode with nonvanishing dipole moment along each symmetry axis (see Eq. (2.24)), which is guaranteed to exhibit the minimum quality factor.

The algorithm that we propose to determine the minimum Q factor of an electric type (alongside a magnetic type, see Sec. 3.2) radiator is summarized in Fig. 3.2. First, we preliminary calculate the EQS current modes associated with the assigned shape in which the search for the optimal current is performed. Then, if the object has two orthogonal reflection symmetry, the minimum Q along the principal axes is immediately obtained from the Q factor of the EQS mode oriented along that axis. If no such symmetries are present, then we analytically assembly the polarizability tensor by using the dipole moment and the eigenvalues of the modes, and eventually find its eigenvalues and eigenvectors. The minimum Q and optimal currents are then immediately obtained.

In the next three subsections, some examples are worked out, exemplifying the introduced method for the calculation of the minimum Q and the optimal current for radiators of the electric type. From a computational standpoint, the electrostatic eigenvalue problem (2.6) is solved by the surface integral method outlined in Refs. [70, 83].

---

[3] In Chapter 1 we used the symbol $x_h^{\|}$ or $x_h^{\perp}$ to indicate the resonant size parameter of the EQS $\mathbf{j}_h^{\|}$ or MQS $\mathbf{j}_h^{\perp}$ mode. Here we choose to use simply x_h to lighten the notation.

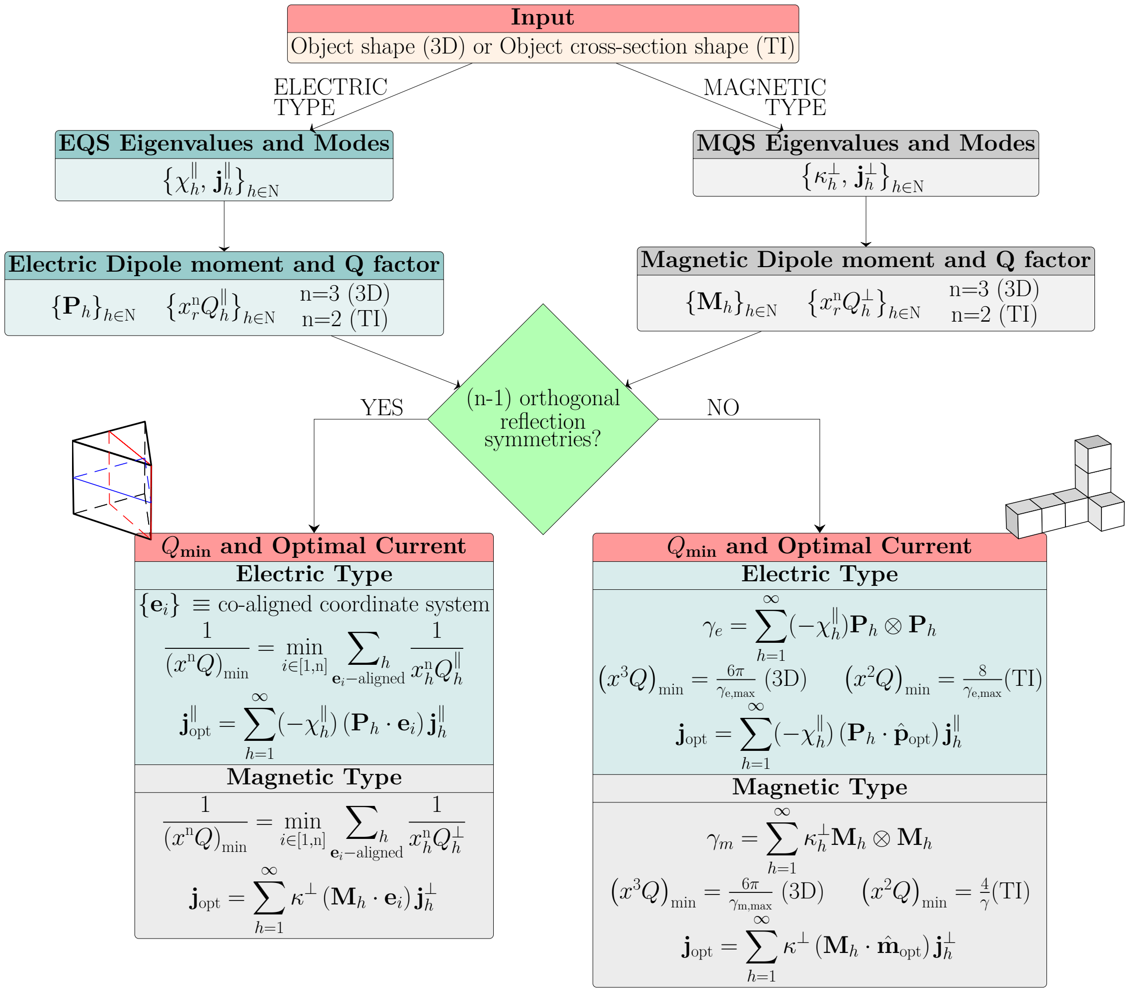

Figure 3.2 – Algorithm for the calculation of the minimum quality factor and optimal current of an arbitrary shaped 3D or TI radiator of the electric and magnetic types, using the quasistatic modes.

3.1.1 Shapes supporting uniform electrostatic mode

A homogeneous sphere supports three degenerate EQS bright modes, associated with the eigenvalue $\chi^{\parallel} = -3$ (Fröhlich condition [2]). The surface charge density of one of these modes is shown on the left of Fig. 3.3a, and is associated with the spatially uniform TM current mode $\mathbf{j}_1^{\parallel} = \sqrt{3/(4\pi)}\hat{\mathbf{z}}$, denoted in Sec. 2.2.5 and Sec. B.1.1 with $j_{e01}^{\parallel}$. For the considerations made in the previous section, they are the *only* three bright modes (one for each coordinate axis) exhibited by this shape. Thus, these modes correspond to the optimal current, and their Q factor coincides with the minimum allowed Q factor supported by longitudinal currents constrained within this shape:

$$\left(x^3 Q\right)_{\text{min}} = x_1^3 Q_1^{\parallel} = 1.5. \tag{3.19}$$

In conclusion, the plasmonic (EQS) dipole modes supported by a plasmonic sphere exhibit the minimum Q factor of radiatior of the electric type, in line with the results of Thal [107].

Similarly, a spheroid supports three uniform modes directed along the principal axes, and hence they are the only bright modes. We consider a prolate and an oblate spheroids with aspect ratio 2 : 1. On the right of Fig. 3.3a we show the surface charge density associated with the EQS current mode oriented along the major axes, and having eigenvalues $\chi^{\parallel} = -5.76$ (prolate) and $\chi^{\parallel} = -4.23$ (oblate) [164]. Thus, the modes' Q factor coincides with the minimum allowed Q factor supported by longitudinal currents constrained within this shape. Specifically, $(x^3Q)_{\text{min}} = 3.16$ and $(x^3Q)_{\text{min}} = 2.13$ for the considered prolate and oblate spheroids, respectively, in agreement with the closed-form expressions provided by Gustafsson at al. [106].

3.1.2 Shapes with two reflection symmetries

We now consider a rod with radius R, and height $H = 4R$, aligned along $\hat{\mathbf{z}}$. Following the algorithm outlined in Fig. 3.2, we compute the EQS modes by solving Eq. (2.6), and among them we select the bright ones. The surface mesh used for the mode calculation has 1885 nodes, and 3766 triangles. Their Q factor can be immediately calculated using their eigenvalues and electric dipole moment by Eq. (3.18). The four bright modes with the lowest Q are shown in Fig. 3.3b to the right of the " = " sign. The minimum Q supported by a longitudinal current confined in this volume is obtained by Eq. (3.17) from the parallel of the quality factors $x_h^3 Q_h^{\parallel}$ of the modes exhibiting nonvanishing dipole moment along $\hat{\mathbf{z}}$: it has value $(x^3\, Q)_{\text{min}} = 3.98$. We note that the Q factor of the first EQS mode is very close to the Q bound. This is because this particular mode is *almost* spatially constant, thus the dipole moment of the remaining modes is nearly vanishing. The relative error in the calculation of $(x^3\, Q)_{\text{min}}$ by considering only the first three modes is below 0.2%.

We then consider a sphere dimer of radius R, aligned along the $\hat{\mathbf{z}}$-axis with edge-edge gap $\delta = R/10$. On the left of the " = " sign in Fig. 3.3c we show the surface charge density associated with the optimal current distribution, on the right the three plasmon modes with lowest Q factors. The minimum Q factor is obtained by combining the quality factor of the bright modes, by using the parallel formula. Differently from the rod, where the fundamental plasmon mode exhibits a Q factor very close to the minimum Q, for a sphere dimer, the first mode exhibits a Q quite larger than the minimum. This is because the dimer of two nearly touching spheres support modes concentrated in the dimer gap, and hence strongly deviating from

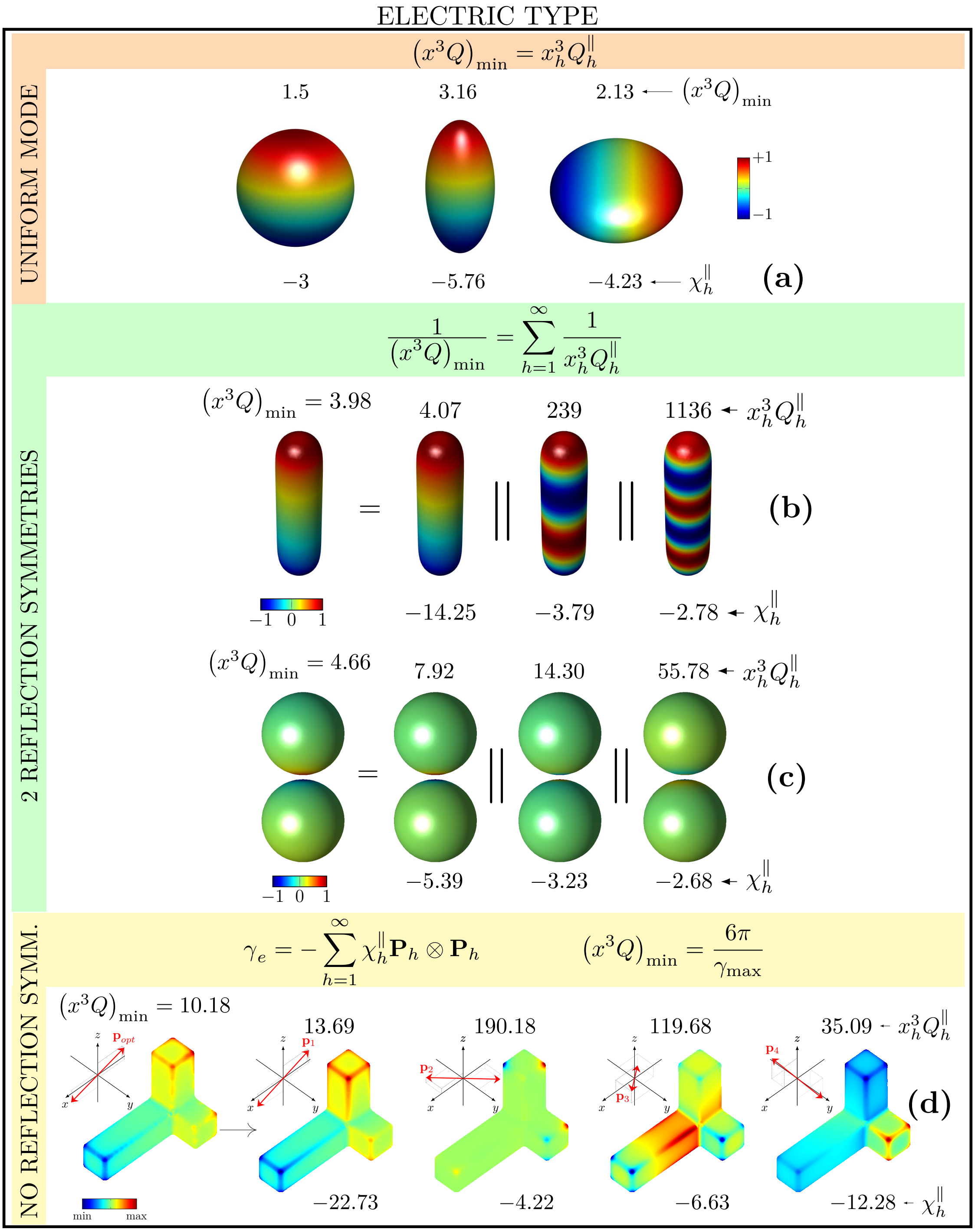

Figure 3.3 – Minimum Q and corresponding optimal charge density supported by radiators of the electric type of assigned shape: (**a**) a sphere, and prolate and oblate spheroids with aspect ratio 2 : 1, which have only one uniform bright EQS mode which coincides with the optimal charge density; geometries exhibiting two reflection symmetries, namely a rod with radius R and height $H = 4R$ (**b**) and a dimer of spheres with radius R and edge-edge gap $R/10$ (**c**); a shape with no symmetries (**d**). In (b-d), to the right of the " = " sign/arrow, plasmon modes with lowest Q factor, their individual Q factor (top) and eigenvalues (bottom).

uniform distributions.

3.1.3 Shapes with no symmetries

We now examine a tetris-like block with three orthogonal arms of different lengths and no reflection symmetries. We first compute the EQS resonances of this object, selecting the bright modes. The four bright modes with lowest Q factor are shown in Fig. 3.3 to the right of the " $=$ " sign. The direction of the dipole moment $\mathbf{P}_h$ of each mode is also shown in the insets. Aiming at determining the minimum Q factor achievable by currents confined within the object, and considering that there are no symmetries, we have to preliminary assembly the electric polarizability tensor $\boldsymbol{\gamma}_e$ using Eq. (3.14), using the dipole moments of the modes $\mathbf{P}_h$. The maximum eigenvalue of $\boldsymbol{\gamma}_e$ is associated with the minimum Q factor by Eq. (3.9). The optimal current is then obtained by using Eq. 3.15, and shown on the left of Fig. 3.3d. The relative error in the estimation of $(x^3\,Q)_{\min}$ by taking into account only the three modes shown in Fig. 3.3d is 26%. We have to consider at least 25 modes to have an error below 10%.

3.2 Minimum Q factor of 3D radiators of the magnetic type

We now consider three-dimensional radiators of the magnetic type, supporting transverse volume currents $\mathbf{j}$, which belong to the functional space $\mathbf{L}^2_\perp(\Omega) = \left\{\mathbf{L}^2(\Omega)\,|\,\nabla\cdot\mathbf{j}^{\parallel}=0, \text{ in } \Omega\setminus\partial\Omega \text{ and } \mathbf{j}^{\perp}\cdot\hat{\mathbf{n}}=\mathbf{0} \text{ on } \partial\Omega\right\}$. Their Q factor can be expressed as 2π times the ratio of the magnetostatic energy stored in the whole space to the energy radiated to infinity in a period [118, 110, 108]

$$Q = 6\frac{\displaystyle\int_\Omega \mathbf{j}(\mathbf{r})\cdot\int_\Omega \frac{\mathbf{j}(\mathbf{r}')}{|\mathbf{r}-\mathbf{r}'|}dV'dV}{\displaystyle\int_\Omega \mathbf{j}(\mathbf{r})\cdot\int_\Omega \mathbf{j}(\mathbf{r}')\,|\mathbf{r}-\mathbf{r}'|^2\,dV'dV}\,\frac{1}{x^3}. \tag{3.20}$$

This expression holds also in the case of the surface current density defined on the 2D object Σ provided that the volume integrals are replaced by surface integrals.

Following the same steps used for the radiators of the electric type, the minimization of the Q factor functional in Eq. (3.20) leads to [108]

$$\left(x^3 Q\right)_{\min} = \frac{6\pi}{\gamma_{\mathrm{m,max}}}, \tag{3.21}$$

where $\gamma_{\mathrm{m,max}}$ is the maximum eigenvalue of the 3×3 (dimensionless) magnetic polarizability tensor $\boldsymbol{\gamma}_m$ of the scaled object.

The polarizability tensor $\boldsymbol{\gamma}_m$ is a linear correspondence between an homogeneous external magnetic field $H_0\hat{\mathbf{e}}$ and the magnetic dipole moment of the volume current density distribution, defined as

$$\mathbf{M} = \frac{1}{2} \int_{\Omega} \mathbf{r} \times \mathbf{j} \, dV, \tag{3.22}$$

having zero-average over Ω (and therefore zero electric dipole moment) and solving the integral equation problem [122]:

$$\int_{\Omega} \frac{\mathbf{j}(\mathbf{r}')}{4\pi \left|\mathbf{r} - \mathbf{r}'\right|} dV' = \frac{1}{2} \left(H_0 \hat{\mathbf{e}}\right) \times \mathbf{r}, \quad \forall \mathbf{r} \in \Omega. \tag{3.23}$$

Thus, the magnetic polarizability tensor γ_m is a 3×3 matrix, defined as the map $\gamma_m \cdot \hat{\mathbf{e}} H_0 = \mathbf{M}$.

The volume integral operator in Eq. (3.23) is exactly the same operator $\mathcal{L}_m$ occurring in Eq. (2.12), which describes the magnetostatic (dielectric) resonance. One of the main contributions of the present work is the analytical closed-form calculation of the polarizability tensor by using the MQS modes set.

We expand the transverse current density solution of problem (3.23), in terms of the MQS current modes $\{\mathbf{j}_h^{\perp}\}_{h \in \mathbb{N}}$, solutions of the MQS eigenvalue problem $\mathcal{L}_m \left\{\mathbf{j}_h^{\perp}\right\} = \mathbf{j}_h^{\perp} / \kappa_h^{\perp}$ in weak form, which constitutes a complete basis for $\mathbf{L}_{\perp}^2(\Omega)$:

$$\mathbf{j}_{\mathrm{opt}}(\mathbf{r}) = \sum_{h=1}^{\infty} b_h \, \mathbf{j}_h^{\perp}(\mathbf{r}) \qquad \forall \mathbf{r} \in \Omega. \tag{3.24}$$

The resulting current $\mathbf{j}_{\mathrm{opt}}$ exhibits zero average (or zero electric dipole moment) over Ω by construction. By plugging the above expansion in Eq. (3.23), taking the scalar product of both members with $\mathbf{j}_k^{\perp}$, and using the orthonormality condition $\langle \mathbf{j}_h^{\perp}, \mathbf{j}_k^{\perp} \rangle_{\Omega} = \delta_{h,k}$, we obtain the expansion coefficients b_h of the current density distribution

$$b_h = \kappa_h^{\perp} \left(H_0 \hat{\mathbf{e}}\right) \cdot \mathbf{M}_h \tag{3.25}$$

and the corresponding magnetic dipole moment

$$\mathbf{M} = \sum_{h=1}^{\infty} \kappa_h^{\perp} \left(H_0 \hat{\mathbf{e}} \cdot \mathbf{M}_h\right) \mathbf{M}_h = \left[\sum_{h=1}^{\infty} \kappa_h^{\perp} \, \mathbf{M}_h \otimes \mathbf{M}_h\right] \cdot \left(H_0 \hat{\mathbf{e}}\right), \tag{3.26}$$

where $\mathbf{M}_h$ is the magnetic dipole moment of the MQS current mode $\mathbf{j}_h^{\perp}$, given in Eq.

(2.33).
Thus, the 3×3 magnetic polarizability tensor $\boldsymbol{\gamma}_m$ is

$$\boldsymbol{\gamma}_m = \sum_{h=1}^{\infty} \kappa_h^{\perp} \, \mathbf{M}_h \otimes \mathbf{M}_h. \tag{3.27}$$

Eq. (3.27) bridges the magnetic polarizability tensor with the MQS (dielectric) modes.

The maximum eigenvalue $\gamma_{\text{m,max}}$ of $\boldsymbol{\gamma}_m$ is associated with the minimum Q factor of a radiator of the magnetic-type by Eq. (3.21). The corresponding (normalized) eigenvector returns the direction of the dipole moment of the optimal current, which we call $\hat{\mathbf{m}}_{\text{opt}}$. The optimal current is readily obtained in terms of the MQS modes:

$$\mathbf{j}_{\text{opt}}(\mathbf{r}) = \sum_{h=1}^{\infty} \kappa_h^{\perp} \left(\hat{\mathbf{m}}_{\text{opt}} \cdot \mathbf{M}_h \right) \mathbf{j}_h^{\perp}(\mathbf{r}) \tag{3.28}$$

As we will see in the next sections, in many scenarios, only a few MQS modes have to be considered to have a good estimation of the minimum Q factor and the optimal current.

As in the electric type case, if the shape of the resonator has two orthogonal reflection symmetries, $\boldsymbol{\gamma}_m$ can be diagonalized by choosing a co-aligned coordinate system $(\mathbf{e}_1, \mathbf{e}_2, \mathbf{e}_3)$. In this case the dipole moments $\mathbf{M}_h$ are also aligned along either one of these directions. Thus, the three occurrences of $\boldsymbol{\gamma}_m$ are given by:

$$\gamma_i = \sum_{\substack{h \\ \mathbf{e}_i-\text{aligned}}} \kappa_h^{\perp} \left| \mathbf{M}_h \right|^2, \qquad i = 1, 2, 3 \tag{3.29}$$

where the summation only runs over the MQS modes exhibiting dipole moment directed along $\mathbf{e}_i$. In this case, the minimum Q for the axis $\mathbf{e}_i$ is obtained by the parallel formula

$$\frac{1}{\left(x^3 Q\right)_{\min}} = \sum_{\substack{h \\ \mathbf{e}_i-\text{aligned}}} \frac{1}{x_h^3 Q_h^{\perp}}, \tag{3.30}$$

where $Q_h^{\perp}$ and x_h are the Q factor and the resonant size parameter of the MQS mode $\mathbf{j}_h^{\perp}$ with nonvanishing magnetic dipole moment, respectively (see Sec. 2.2.4), i.e.

$$x_h^3 Q_h^{\perp} = \frac{6\pi}{\kappa_h^{\perp} |\mathbf{M}_h|^2}. \tag{3.31}$$

Eventually, the global minimum Q is taken among the Q for each axis.

In addition, due to the orthogonality of the MQS modes, if there exists a current mode of the form $\mathbf{r} \times \mathbf{c}$, with $\mathbf{c}$ a constant vector, this same mode is guaranteed to be the only one with non vanishing magnetic dipole moment along direction $\mathbf{c}$ (see Eq. (2.34)). Thus, it necessarily exhibits the minimum Q factor.

The algorithm that we propose to determine the minimum Q of a radiator of the magnetic type is summarized in Fig. 3.2.

As for the electric type case, we now illustrate some examples for the calculation of the minimum Q and the optimal current for 3D and 2D (surfaces) radiators of the magnetic type. In the cases in which the analytical solution is not available, the surface current modes have been evaluated by applying the Galerkin method and the Rao-Wilton-Glisson (RWG) functions have been used as basis functions to represent the surface current density (see Supplemental Material of [102]).

3.2.1 Shapes supporting a MQS mode of the form $\hat{\mathbf{r}} \times \mathbf{c}$

We now consider a radiator of the magnetic type having the form of a spherical shell. The MQS modes associated with this shape are given in Eq. (B.9) in Appendix B. Among them, three degenerate current modes have nonvanishing magnetic dipole moment, namely

$$\mathbf{j}_h^{\perp} = \sqrt{\frac{3}{8\pi}}\,\hat{\mathbf{r}} \times \mathbf{c}_h, \tag{3.32}$$

where $\mathbf{c}_h \in \{\hat{\mathbf{x}}, \hat{\mathbf{y}}, \hat{\mathbf{z}}\}$, with eigenvalue $\kappa_h^{\perp} = 3$, $h = 1, 2, 3$. In Sec. 2.4 and in Sec. B.1.2, they are denoted with $\mathbf{j}_{e11}^{\perp\mathtt{TE}}$, $\mathbf{j}_{o11}^{\perp\mathtt{TE}}$, and $\mathbf{j}_{e01}^{\perp\mathtt{TE}}$, respectively. Their magnetic dipole moment is oriented along the three orthogonal axes, namely

$$\mathbf{M}_h = \frac{2\pi}{3}\mathbf{c}_h. \tag{3.33}$$

Thus, according to the discussion in the previous section, there is one and only one mode with magnetic dipole moment along each coordinate axis. We show one of these current modes in Fig. 3.4a. Applying Eq. (3.30) this MQS mode also exhibits the minimum quality factor, namely

$$\left(x^3 Q\right)_{\min} = \left(x_h^3 Q_h^{\perp}\right) = 3 \tag{3.34}$$

This is in agreement with the seminal work of Thal [107].

3.2.2 Shapes with two reflection symmetries

We now consider a small radiator of the magnetic type having the shape of a solid sphere. The quasistatic modes and eigenvalues of this shape are investigated in Sec.

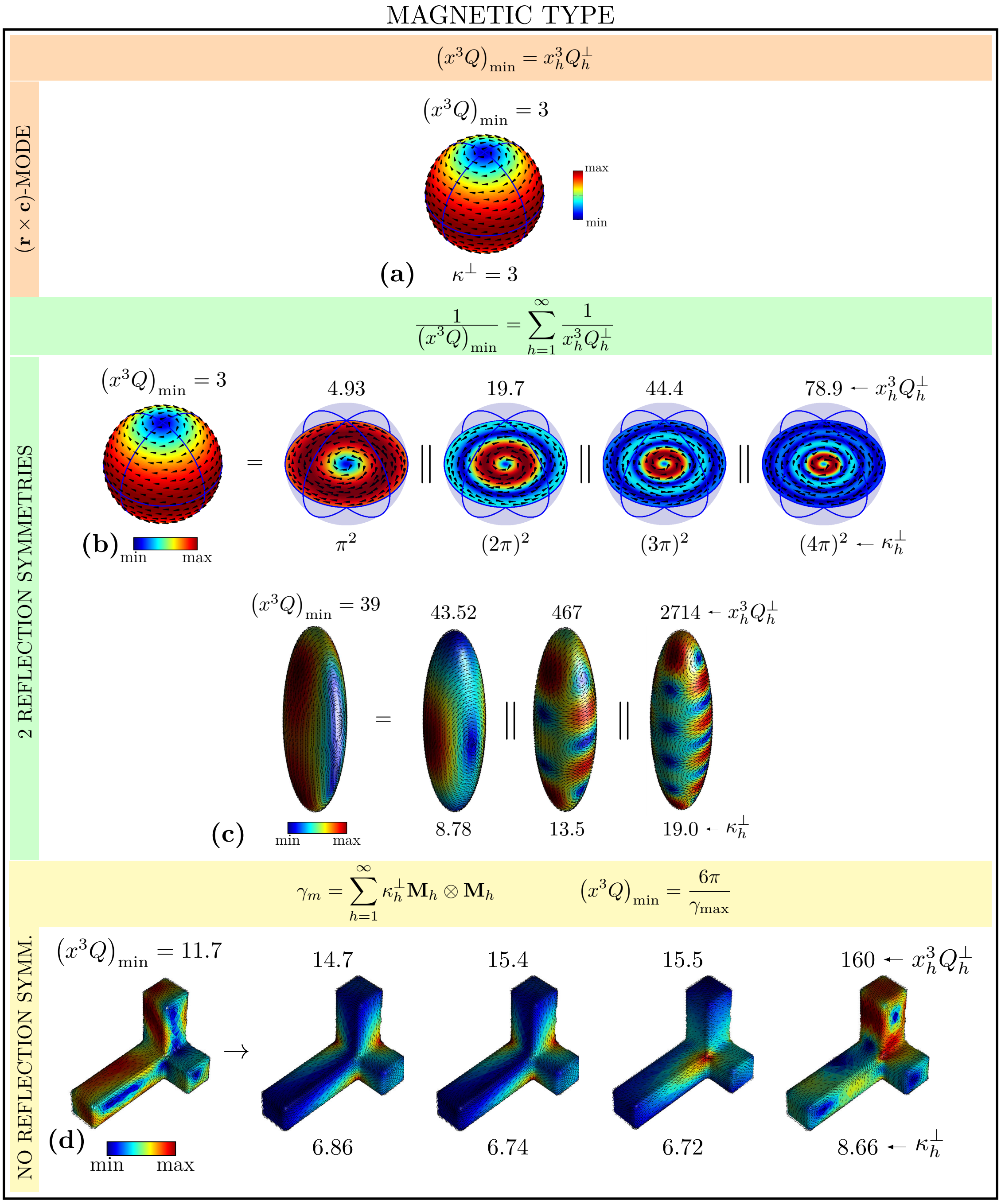

Figure 3.4 – Minimum Q and corresponding current distribution supported by radiators of the magnetic type of assigned shape: (**a**) a sphere shell which supports only one magnetoquasistatic mode of the form $\hat{\mathbf{r}} \times \mathbf{c}$ which coincides with the optimal current density; geometries exhibiting two reflection symmetries, namely a solid sphere (**b**) and a ellipsoid (**c**); a shape with no symmetries, namely a block with three arms of different lengths (**d**). In panel (b-d), to the right of the " = " sign, dielectric modes with lowest Q factor, their individual Q factor (top) and eigenvalues (bottom)

2.2.5. Unlike the sphere shell, this shape does not support a mode of the form $\hat{\mathbf{r}} \times \mathbf{c}$. Among the transverse current modes, we limit our analysis to the ones having nonvanishing magnetic dipole moment along $\hat{\mathbf{z}}$. These MQS current modes are

$$\mathbf{j}_h^{\perp}(r, \vartheta, \phi) = \frac{\sqrt{3\pi}}{2} j_1 \left(h \, \pi r\right) \, \hat{\mathbf{r}} \times \hat{\mathbf{z}} \tag{3.35}$$

where $\mathbf{r} = (r, \vartheta, \phi)$ is a spherical polar coordinate system centered in the sphere center, $h \in \mathbb{N}$, j_1 is the spherical Bessel function of the first kind and order 1. They are associated with the eigenvalues

$$\kappa_h^{\perp} = \left(h\pi\right)^2, \qquad h \in \mathbb{N}, \tag{3.36}$$

and have magnetic dipole moment

$$\mathbf{M}_h = \left(-1\right)^h 2 \frac{\sqrt{3\pi}}{\kappa_h^{\perp}} \hat{\mathbf{z}}. \tag{3.37}$$

In Sec. 2.2.5 and Sec. B.1.1, these MQS modes and eigenvalues are denoted with $\left\{\mathbf{j}_{e01l}^{\perp \mathtt{TE}}\right\}_{l \in \mathbb{N}}$ and $\left\{\kappa_{1l}^{\perp \, \mathtt{TE}}\right\}_{l \in \mathbb{N}}$, respectively.

Applying Eq. (3.31), we find their Q factor:

$$\left(x_h^3 Q_h^{\perp}\right) = \frac{\left(h\pi\right)^2}{2}. \tag{3.38}$$

The projection of the first four current modes on the equatorial section of the sphere is shown to the right of the " = " sign in Fig. 3.4b, with their Q factor. The minimum Q factor $\left(x^3 Q\right)_{\min}$ achievable by transverse currents confined to this volume is obtained by applying Eq. (3.30). This formula consists in the parallel of the quality factors of MQS modes exhibiting magnetic dipole moment along $\hat{\mathbf{z}}$:

$$\frac{1}{\left(x^3 Q\right)_{\min}} = \sum_{h=1}^{\infty} \frac{1}{\left(x_h Q_h^{\perp}\right)} = \frac{2}{\pi^2} \sum_{h=1}^{\infty} \frac{1}{h^2} = \frac{1}{3}. \tag{3.39}$$

In this parallel, by only considering the first 4 modes we obtain an estimation of $\left(x^3 Q\right)_{\min}$ of 3.44 (error of 15.4%). We have to consider at least 13 modes to have an error below 5%.

The optimal volume current $\mathbf{j}_{opt}$ is obtained applying (3.28). Interestingly, it is localized on the sphere's boundary

$$\mathbf{j}_{opt}(r, \vartheta, \phi) = \sqrt{\frac{3}{2\pi}} \, \delta\left(r - 1\right) \, \hat{\mathbf{r}} \times \hat{\mathbf{z}}, \tag{3.40}$$

where δ is the Dirac delta function. Thus, it corresponds to a surface current localized on the sphere's surface, which is the same optimal current found for a spherical shell. In conclusion, the minimum quality factor and the corresponding optimal current are in agreement with the results achieved by Thal [107] for a spherical inductor (see previous section). Therefore, in contrast with a plasmonic homogeneous sphere which supports a mode with minimum Q for electric type radiator, the first (fundamental) mode of homogeneous high-permittivity sphere does not exhibit the minimum Q for magnetic-type radiators.

We then consider a high-conductivity prolate spheroidal shell with aspect ratio $4 : 1$, with major axis aligned along $\hat{\mathbf{z}}$. Also this shape does not support a mode of the form $\hat{\mathbf{c}} \times \hat{\mathbf{r}}$. We preliminary compute the MQS resonances by solving the eigenvalue problem (2.162). We only consider the set of MQS modes exhibiting non-vanishing magnetic dipole moment along $\hat{\mathbf{z}}$. In Fig. 3.4c, we show the surface current, eigenvalue, and Q factor of the modes with the lowest Q factor. The minimum quality factor $(x^3\,Q)_{\mathrm{min}}$ of magnetic-type radiators supported by surface current density fields confined on this shape is obtained using the parallel formula in Eq. 3.30, and is $(x^3\,Q)_{\mathrm{min}} = 39$. If the parallel is only limited to the three modes shown in Fig. 3.4c, an error $< 1\%$ is achieved.

3.2.3 Shapes with no symmetries

We consider a shell with no reflection symmetries, defined as the surface of a tetris-like block with three orthogonal arms of different lengths. We preliminary compute its MQS resonances, selecting the modes with nonvanishing magnetic dipole moment. We then calculate their magnetic dipole moment $\mathbf{M}_h$, and Q factor by Eq. (3.31). The surface mesh used for the calculation has 1885 nodes, and 3766 triangles. The four modes with the lowest Q factor are shown in Fig. 3.4d to the right of the " = " sign, with their Q factor (above), and eigenvalue (below). Aiming at determining the minimum Q factor achievable by surface currents confined on this surface, and considering that there are no symmetries, we have to preliminary assembly the magnetic polarizability tensor $\boldsymbol{\gamma}_m$ using Eq. (3.27) from the dipole moments $\mathbf{M}_h$ of the modes. The maximum eigenvalue $\gamma_{m,max}$ of $\boldsymbol{\gamma}_m$ is associated with the minimum Q factor by Eq. (3.21). The optimal current is then obtained by using Eq. (3.28), and shown on the left of the " = " sign in Fig. 3.4d. By only considering the first 3 modes, we obtain an estimation of $(x^3 Q)_{\mathrm{min}}$ of 13.2 with an error of 12%.

3.3 Minimum Q factor of TI radiators of the electric type

In this section, we find the minimum quality factor of longitudinal current density distributions supported by translational invariant radiators having electrically small cross-section, i.e., $x = \frac{\omega}{c_0}\ell_c < 1$, being ℓ_c the radius of the minimm circle enclosing the object cross-section (see Fig. 3.1b).
The expression of the Q factor is

$$Q = -\frac{8}{\pi} \frac{\oint_{\partial\Sigma} \sigma(\mathbf{r}) \oint_{\partial\Sigma} \sigma(\mathbf{r}') \log|\mathbf{r}-\mathbf{r}'| dl' dl}{\oint_{\partial\Sigma} \sigma(\mathbf{r}) \oint_{\partial\Sigma} \sigma(\mathbf{r}') \left|\mathbf{r}-\mathbf{r}'\right|^2 dl dl'} \frac{1}{x^2}, \tag{3.41}$$

where the per unit length (p.u.l.) surface charge density $\sigma = \mathbf{j}\cdot\hat{\mathbf{n}}$, and $\hat{\mathbf{n}}$ lies in the cross-sectional plane. Once the shape of the cross-section Σ is assigned, the functional $x^2 Q$ can be minimized, yielding the minimum Q factor. For electric type radiators, the search space is constituted by the currents belonging to $\mathbf{L}^2_{\|}(\Sigma)$.

The same line of reasoning used for 3D radiators leads to the expression of the minimum Q factor:

$$\left(x^2 Q\right)_{\min} = \frac{8}{\gamma_{\text{e,max}}}, \tag{3.42}$$

where $\gamma_{\text{e,max}}$ is the maximum among the eigenvalues of the 2×2 electric polarizability tensor $\boldsymbol{\gamma}_e$. We then expand the charge density p.u.l. in terms of the EQS current modes solutions of the eigenvalue problem $\mathcal{L}_e^{2D}\{\mathbf{j}_h^{\|}\} = \mathbf{j}_h^{\|}/\chi_h^{\|}$, being $\mathcal{L}_e^{\mathtt{TI}}$ the 2D electrostatic operator (see 2.3), which constitute a complete basis for the funcitonal space $\mathbf{L}^2_{\|}(\Sigma)$. As a result, we arrive at the analytical expressions for $\boldsymbol{\gamma}_e$, identical to Eq. (3.14), and for the optimal current identical to Eq. (3.15).

If the shape of the object cross-section has a reflection symmetry, $\boldsymbol{\gamma}_e$ can be immediately put in the form of diagonal matrix by choosing a coordinate system $(\mathbf{e}_1, \mathbf{e}_2)$, in which one of the two basis vectors is oriented along the symmetry axis. In this case, the dipole moment of the EQS modes is also aligned along these directions, and the minimum Q for the axis $\mathbf{e}_i$ can be obtained through a parallel formula

$$\frac{1}{(x^2 Q)_{\min}} = \sum\nolimits_{\mathbf{e}_i-\text{aligned}}^{h} \frac{1}{x_h^2 Q_h^{\|}}, \tag{3.43}$$

where $Q_h^{\|}$ and x_h are the Q factor and the resonant size parameter of the bright EQS mode $\mathbf{j}_h^{\parallel}$, respectively (see Sec. 2.3.2), i.e.

$$x_h^2 Q_h^{\parallel} = \frac{8}{(-\chi_h^{\parallel})|\mathbf{P}_h|^2}. \tag{3.44}$$

Then, the global minimum Q factor is taken among the Q for each axis.

In addition, due to the orthogonality of EQS modes, if there exists a current mode spatially uniform along a given direction, this same mode is guaranteed to be the only one with nonvanishing dipole moment along that direction. Thus, it necessarily exhibits the minimum quality factor.

The algorithm that we propose to determine the minimum Q of a TI radiator of the electric type is summarized in Fig. 3.2.

In the next three subsections, some examples are worked out, exemplifying the introduced method for the calculation of the minimum Q and the optimal current for TI radiators of the electric type. The EQS current modes and eigenvalue solution of the problem (2.104) are found using the linear integral method outlined in Refs. [70, 83].

3.3.1 Shape supporting a uniform EQS mode

Let us consider a TI object of circular cross-section. It supports two degenerate EQS bright modes, associated with the eigen-susceptibility $\chi^{\parallel} = -2$. The linear charge density of one of this modes is shown in Fig. 3.5a, and is associated with the spatially uniform TE current mode $\mathbf{j}_1^{\parallel} = \hat{\mathbf{y}}/\pi$, denoted in Sec. 2.3.5 and Sec. C.1 with $\mathbf{j}_{o1}^{\parallel}$.

For the considerations made in the previous section, these current modes coincide with the optimal currents supported by the TI radiator of the electric type, and their Q factor is the minimum allowed Q supported by longitudinal currents constrained within this shape:

$$x^2 Q_{min}^{\parallel} = \frac{4}{\pi}. \tag{3.45}$$

To the author's best knowledge, this lower bound for the Q factor of translational invariant radiators of the electric type has not been reported before.

3.3.2 Shape with reflection symmetry

We now investigate a cylinder homo-dimer of radius R, with edge-edge gap δ. This system has reflection symmetries, but does not support any uniform current mode. The expression of the EQS modes is given in Eq. (C.6). In Sec. C.2 in Appendix C, we derive the Q factor of the bright ones with electric dipole moment directed along

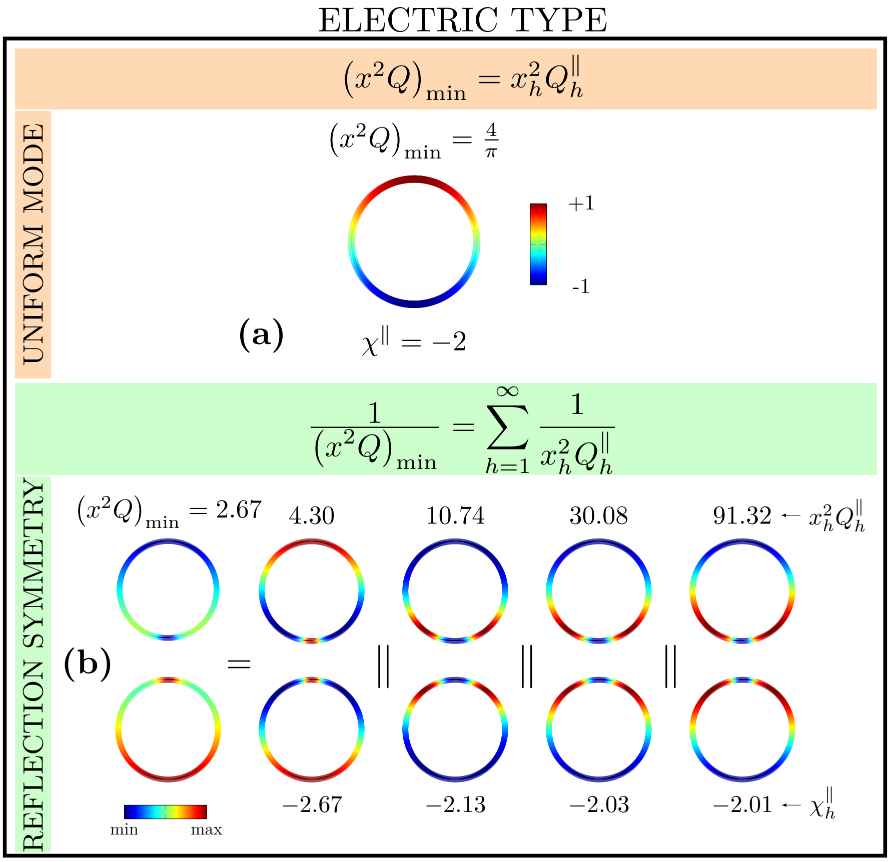

Figure 3.5 – Minimum Q and corresponding optimal charge density distribution supported by TI radiators of the electric. Optimal charge density supported by: (**a**) a cylinder of circular cross-section: this shape has only one uniform bright mode which coincides with the optimal charge density; (**b**) a geometry exhibiting two reflection symmetries, namely a dimer of cylinders with radius R and edge-edge gap $\delta = R/10$, and EQS modes with the lowest Q factor.

the dimer axis, and we display here their expression:

$$x_h^2 \mathrm{Q}_h^{\|} = \frac{4 + \delta/R}{2\pi h\, \delta/R} \left(\mathrm{e}^{2h\mu} - 1 \right), \tag{3.46}$$

where $\mu = \operatorname{arccosh}\left(1 + \frac{\delta}{2R}\right)$, being arccosh the inverse hyperbolic cosine.

In Fig. 3.5b, we show the linear charge density associated with the bright modes, with their individual Q , for a cylinder dimer with $\delta/R = 0.1$. The minimum Q factor $(x^2\, Q)_{\min}$ achievable by longitudinal currents supported by this structure is obtained by plugging the expression of the bright mode Q factor in Eq. (3.46) in the parallel formula in Eq. 3.43. In this parallel, by only considering the first 5 modes (shown in Fig. 3.5b), the relative error in the estimation of $(x^2Q)_{\min}$ is below 12%.

3.4 Minimum Q factor of TI radiators of the magnetic type

Here we find the minimum Q factor of TI radiators of magnetic type, which support transverse current density distributions $\mathbf{j}$ belonging to $\mathbf{L}^2_\perp(\Sigma)$. The expression of the Q factor is

$$Q = \frac{8}{\pi} \frac{\displaystyle\int_\Sigma \mathbf{j}(\mathbf{r}) \cdot \int_\Sigma \mathbf{j}(\mathbf{r}') \log|\mathbf{r}-\mathbf{r}'| dS dS'}{\displaystyle\int_\Sigma \mathbf{j}(\mathbf{r}) \cdot \int_\Sigma \mathbf{j}(\mathbf{r}') \left|\mathbf{r}-\mathbf{r}'\right|^2 dS dS'} \frac{1}{x^2}. \tag{3.47}$$

In this configuration, the magnetic polarizability tensor γ_m is a scalar, defined as the map $\gamma_m \hat{\mathbf{e}} H_0 = \mathbf{M}$. Thus, the minimization of the Q factor functional in Eq. (3.47) leads to:

$$\left(x^2 Q\right)_{\min} = \frac{4}{\gamma}. \tag{3.48}$$

We then expand the transverse current density $\mathbf{j}$ in terms of the MQS current modes $\{\mathbf{j}^\perp_h\}_{h\in\mathbb{N}}$, solutions of the MQS eigenvalue problem $\mathcal{L}^{\mathtt{TI}}_m \left\{\mathbf{j}^\perp_h\right\} = \mathbf{j}^\perp_h / \kappa^\perp_h$, being $\mathcal{L}^{\mathtt{TI}}_m$ the 2D magnetostatic operator (see Sec. 2.3), which constitutes a complete basis for $\mathbf{L}^2_\perp(\Sigma)$. As a result, we arrive at the closed form expressions of the magnetic polarizability tensor $\boldsymbol{\gamma}_m$, identical to Eq (3.27), and of the optimal current $\mathbf{j}_{\text{opt}}$ identical to Eq. (3.28).

In this case, the dipole moments $\mathbf{M}_h$ are always aligned along the structure axis the minimum Q is obtained by the parallel formula

$$\frac{1}{\left(x^2 Q\right)_{\min}} = \sum_{h=1}^{\infty} \frac{1}{x_h^2 Q_h^\perp} \tag{3.49}$$

where $Q^\perp_h$ and x_h are the Q factor and the resonant size parameter of the MQS mode $\mathbf{j}^\perp_h$ with nonvanishing magnetic dipole moment, respectively (see Sec. 2.3.4), i.e.

$$x_h^2 Q_h^\perp = \frac{4}{\kappa^\perp_h |\mathbf{M}_h|^2}. \tag{3.50}$$

The algorithm that we propose to determine the minimum Q of a TI radiator of the magnetic type is summarized in Fig. 3.2.

3.4.1 Shapes supporting a single MQS mode

We consider the shell of infinite cylinders with arbitrary cross-section. Since any linear current density supported by these structures is constrained on a closed line,

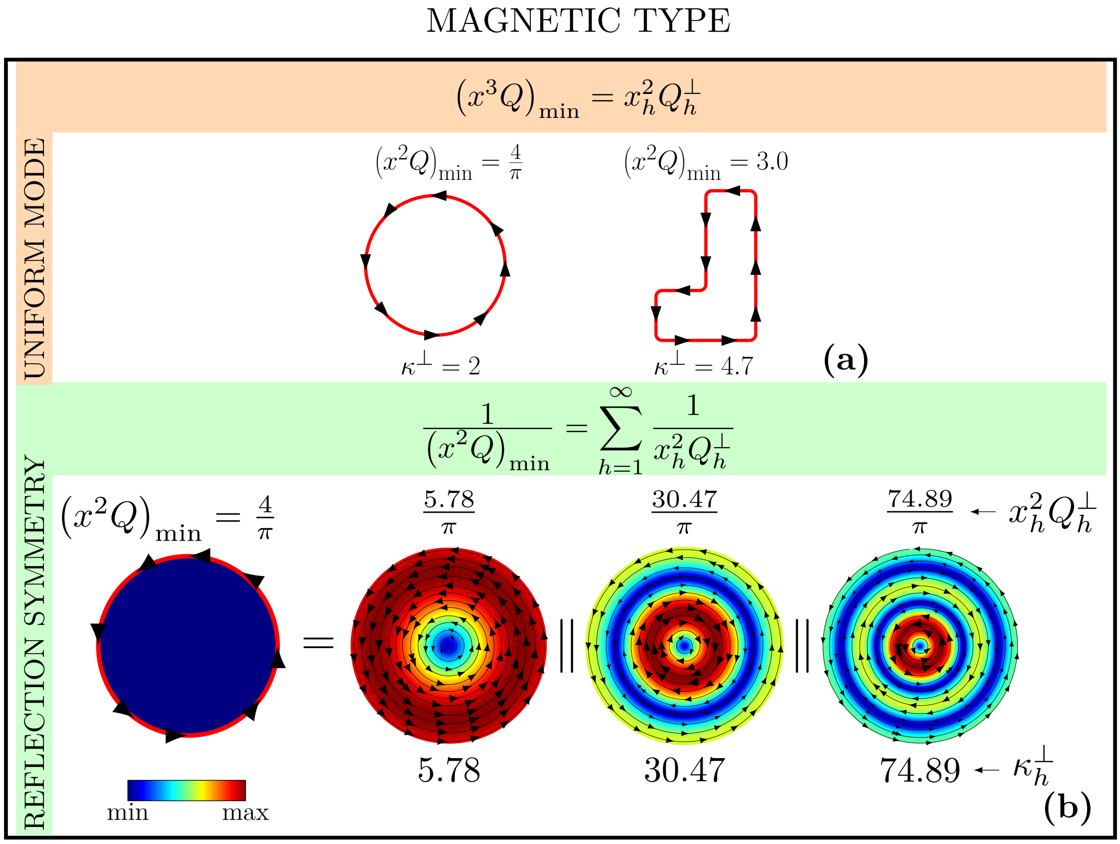

Figure 3.6 – Minimum Q factor and corresponding optimal current density distribution supported by TI radiators of the magnetic type of assigned shape: (**c**) a cylinder shell supporting only one uniform bright magnetoquasistatic mode of the form $\hat{\mathbf{r}} \times \mathbf{c}$, being $\hat{\mathbf{r}}$ the radial direction and $\mathbf{c}$ a constant vector, which coincides with the optimal current density; (**d**) a geometry exhibiting two reflection symmetries, namely a solid cylinder.

there exists one and only one MQS current mode with nonvanishing magnetic dipole moment. This mode is also uniform, and hence exhibits the minimum Q factor supported by the structure, whose expression is given in Eq. (3.50). In Fig. 3.6a we consider the shell of an infinite cylinder of circular cross-section. This shape supports a MQS mode with eigenvalue $\kappa^\perp = 2$ and magnetic dipole moment oriented along the cylinder axis. The resonant linear current density is

$$\mathbf{j}^\perp(r,\phi) = \frac{1}{\sqrt{2\pi}} \hat{\mathbf{z}} \times \hat{\mathbf{r}}, \tag{3.51}$$

where $\mathbf{r} = (r,\phi)$ are the in-plane cylindrical polar coordinates, and $\hat{\mathbf{z}}$ the cylinder axis direction. This MQS mode exhibits the minimum quality factor, namely

$$\left(x^2 Q\right)_{\min} = \left(x^2 Q^\perp\right) = \frac{4}{\pi}. \tag{3.52}$$

On the right of Fig. 3.6a we consider the shell of an infinite cylinder with an L-shaped cross-section and no reflection symmetries. This shape supports a uniform MQS current mode with eigenvalue $\kappa^{\perp} = 4.7$, and $x^2 Q^{\perp} = (x^2 Q)_{\min} = 3$.

3.4.2 Shape with reflection symmetry

We now examine a solid infinite cylinder with circular cross-section. The quasistatic modes and eigenvalues of this shape are investigated in Sec. 2.3.5. Despite the high symmetry, this shape does not support modes of the form $\hat{\mathbf{r}} \times \mathbf{c}$. The cylinder supports transverse current modes with nonvanishing magnetic dipole moment

$$\mathbf{j}_h^{\perp}(r, \phi) = \frac{J_1\left(Z_{0,h} r\right)}{\sqrt{\pi}\left|J_1\left(Z_{0,h}\right)\right|}\, \hat{\mathbf{z}} \times \hat{\mathbf{r}}, \qquad r \in [0,1],\, h \in \mathbb{N}, \tag{3.53}$$

shown in Fig. 3.6b to the right of the " = " sign. They are associated with the real and positive eigenvalues $\kappa_h^{\perp}$

$$\kappa_h^{\perp} = Z_{0,h}^2, \tag{3.54}$$

where $(\hat{\mathbf{r}}, \hat{\mathbf{z}})$ are the radial unit vector in the cross-section and the cylinder axis unit vector, respectively, J_1 is the Bessel function of the first kind with order 1, and $Z_{0,h}$ is the h-th zero of the Bessel function of the first kind with order 0. In Sec. 2.3.5 and Sec. C.1, these MQS modes and eigenvalues are denoted with $\{\mathbf{j}_{o0l}\}_{l \in \mathbb{N}}$ and $\left\{\kappa_{0l}^{\perp\mathtt{TE}}\right\}_{l \in \mathbb{N}}$, respectively.

Their magnetic dipole moment $\mathbf{M}_h$ has the expression

$$\mathbf{M}_h = (-1)^{h+1}\, \frac{2\sqrt{\pi}}{\kappa_h^{\perp}}\, \hat{\mathbf{z}}, \tag{3.55}$$

and, according to Eq. (2.152), their Q factor is given by $x_h^2 Q_h^{\perp} = \frac{Z_{0,h}^2}{\pi}$.

The optimal current is obtained applying Eq. (3.28), and is a current loop localized on the cylinder cross-section's boundary, i.e.

$$\mathbf{j}_{\text{opt}} = \sqrt{\pi}\delta(r-1)\, \hat{\mathbf{z}} \times \hat{\mathbf{r}}, \qquad \forall r, \tag{3.56}$$

where δ is the Dirac delta function. The optimal current $\mathbf{j}_{\text{opt}}$ is shown in Fig. 3.6b.

The minimum Q factor $\left(x^2 Q\right)_{\min}$ achievable by transverse currents confined to the cylinder cross-section is obtained through Eq. (3.49), which consists in the parallel of the quality factors of the infinite set of MQS modes exhibiting non-zero magnetic dipole moment along the cylinder axis $\hat{\mathbf{z}}$:

$$\left(x^2 Q\right)_{\min} = \left(\sum_{h=1}^{\infty} \frac{1}{x_h^2 Q_h^{\perp}}\right)^{-1} = \frac{4}{\pi}, \tag{3.57}$$

where we used the identity $\sum_{h=1}^{\infty} Z_{0,h}^{-2} = 1/4$ [165].
In this parallel, by considering only the first 4 modes we obtain an estimation of $(x^2 Q)_{\min}$ of $4.42/\pi$ (relative error of 9.4%). Using the first 8 modes leads to an error below 5%. The lower bound in Eq. (3.57), and its corresponding optimal current coincide with those of the shell of an infinite cylinder with circular cross-section.

To the author's best knowledge, the lower bound in Eq. (3.57) (or in Eq (3.52)) for the Q factor of translational invariant radiators of magnetic type has not been reported before.

3.5 Conclusions

Optimization problems defined on small radiators often consist in the search of the optimal current distribution which leads to the minimization of a chosen quantity. In these problems, the choice of a convenient basis for the description of the tentative optimal current density is a fundamental and unavoidable step. Upon this choice depends not only the efficacy of the numerical computation of the optimal solution, but also the attribution of meaningful physical insights to the results.

Since small electromagnetic radiators are considered, a convenient basis choice may be constituted by the quasistatic scattering modes supported by that shape, corresponding to source-free solution of the electrostatic and magnetoquasistatic limits of the Maxwell's equations. Specifically, electroquasistatic modes describe the resonances of small objects with negative permittivity (e.g., as in metals at optical frequencies). Magnetoquasistatic modes describe the resonances of small objects with very high and positive real part of the permittivity.

We demonstrated that an expansion of the current density in terms of quasistatic modes leads to analytical closed form expressions of the electric and magnetic polarizability tensors. Hence, the minimum Q and the corresponding optimal current is determined from the knowledge of the eigenvalues and dipole moments associated with the quasistatic scattering modes.

We found that when the radiator exhibits two orthogonal reflection symmetries, its minimum quality factor can then be simply obtained from the Q factors of the quasistatic modes associated with the radiator's shape, through a simple parallel formula.

Moreover, when an electric radiator supports a spatially uniform electroquasistatic resonance mode, this mode is guaranteed to have the minimum quality factor. Dually, when a magnetic radiator supports a magnetoquasistatic mode of the form $\hat{\mathbf{r}} \times \mathbf{c}$ where $\mathbf{c}$ is a constant vector and $\hat{\mathbf{r}}$ is the radial direction, this mode exhibits the minimum quality factor.

Eventually, we applied the proposed method to arbitrary shaped three-dimensional, two-dimensional, and translational invariant radiators, of both electric and magnetic type.

The introduced framework bridges a classic antenna problem with nano-antennas resonances, and may be especially appealing to researchers and engineers working in nano-optics, where a description in terms of modes is widely used.

Chapter 4

Material-independent modes

The approaches proposed so far well describe the resonances in the electromagnetic scattering from electrically small objects. However, they fail when the objects size is comparable to the incident wavelength.

In this chapter, we introduce a full-wave spectral theory for the description of the scattering from an arbitrary sized three-dimensional object. This technique is the natural extension of the quasistatic theory derived in Chap. 2. It is based on the representation of the scattered field in terms of eigenvalues and eigenfunctions (modes) of a full-retarded integral operator, which only depend on the object morphology, and are independent of the material of the object. For this reason they are denoted as *material-independent modes.* This representation has the merit of separating the role of the geometry of the object from the role played by its the material composition.

We apply this theory to investigate the modes and resonances a sphere, where most of the results are analytical or semi-analytical. The analysis of the sphere eigenvalues and modes allows a systematic classification of resonances and interference effects. In particular, the resonances and resonances modes are divided into plasmonic and dielectric modes, based on their long-wavelength behaviour. From the investigation of the loci spanned by the eigenvalues in the complex plane as a function of the sphere's size parameter, we classify the modes in terms of their bandwidth, separating them into narrow and broad modes, regardless of the excitation conditions. In this framework, we are able to explain the differences in the power spectrum scattered by dielectric and metal nanoparticles.

This paradigm has also been applied to the investigation of modes and resonances of other shapes with analytical solution, such as a coated sphere in [76], and a sphere dimer in [140], and shapes where the numerical approach is needed, such as a finite cylinder in [78], or two-dimensional triangles and rectangles in [102].

4.1 Full-wave modes and resonances

Let us consider a linear, isotropic, homogeneous material occupying a volume Ω, which is bounded by a closed surface $\partial\Omega$ with outward-pointing normal $\hat{\mathbf{n}}$. The medium is nonmagnetic, time-dispersive, with relative dielectric permittivity $\varepsilon_R(\omega)$, electric susceptibility $\chi = \varepsilon_R - 1$, and surrounded by vacuum. The object is excited by a time-harmonic electromagnetic field incoming from infinity $\operatorname{Re}\{\mathbf{E}_{\text{inc}}(\mathbf{r})e^{-i\omega t}\}$, where ω is the angular frequency. Let $\mathbf{E}^{-}_{\text{sca}}$ and $\mathbf{E}^{+}_{\text{sca}}$ be the scattered electric fields in the interior of Ω and in $\mathbb{R}^3 \setminus \bar{\Omega}$.

We have $\mathbf{J} = -i\omega\varepsilon_0\chi\mathbf{E}$, where $\mathbf{E} = \mathbf{E}^{+}_{\text{sca}} + \mathbf{E}_{\text{inc}}$ is the total electric field. Both the vector fields $\mathbf{E}$ and $\mathbf{J}$ are div-free in Ω due to the homogeneity and isotropy of the material. The current density $\mathbf{J}$ is governed by the full-wave volume integral equation [146, 147, 148]:

$$\frac{\mathbf{J}(\mathbf{r})}{\chi} - \mathcal{L}\left\{\mathbf{J}\right\}(\mathbf{r}) = -i\omega\varepsilon_0\,\mathbf{E}_{\text{inc}}(\mathbf{r}), \quad \forall \mathbf{r} \in \Omega, \tag{4.1}$$

where the operator $\mathcal{L}\{\cdot\}$ is

$$\mathcal{L}\left\{\mathbf{J}\right\}(\mathbf{r}) = -\nabla \oint_{\partial\Omega} \mathbf{J}(\mathbf{r}') \cdot \hat{\mathbf{n}}' \frac{e^{ix|\mathbf{r}-\mathbf{r}'|}}{4\pi|\mathbf{r}-\mathbf{r}'|}\,dS' + x^2 \int_{\Omega} \mathbf{J}(\mathbf{r}') \frac{e^{ix|\mathbf{r}-\mathbf{r}'|}}{4\pi|\mathbf{r}-\mathbf{r}'|}\,dV', \tag{4.2}$$

in which the spatial coordinates have been normalized by a characteristic linear length ℓ_c of the domain Ω, i.e., $\mathbf{r} \to \mathbf{r}/\ell_c$, and $x = \frac{\omega}{c_0}\ell_c$ is the object size parameter.

The spectrum of the operator $\mathcal{L}$ is countable infinite. Moreover $\mathcal{L}$ is symmetric [65]

$$\langle \mathbf{J}', \mathcal{L}\mathbf{J}'' \rangle_\Omega = \langle \mathcal{L}\mathbf{J}', \mathbf{J}'' \rangle_\Omega \tag{4.3}$$

where $\langle \mathbf{A}, \mathbf{B} \rangle_\Omega = \displaystyle\int_\Omega \mathbf{A} \cdot \mathbf{B}\,dV$, but not self-adjoint.

A spectral basis for representing the unknown $\mathbf{J}$ is given by the solutions of the auxiliary eigenvalue problem

$$\mathcal{L}\{\mathbf{w}_h\} = \frac{1}{\gamma_h}\mathbf{w}_h. \tag{4.4}$$

For any value of the size parameter x, its eigenvalues are complex, with $\operatorname{Im}\{\gamma_h\} < 0$. The eigenfunctions $\mathbf{w}_h$ and $\mathbf{w}_k$ corresponding to different γ_h and γ_k are not orthogonal in the usual sense, i.e., $\langle \mathbf{w}^*_h, \mathbf{w}_k \rangle_\Omega \neq 0$: they are biorthogonal [64, 65]

$$\langle \mathbf{w}_h, \mathbf{w}_k \rangle_\Omega = 0 \qquad \text{for} \quad \gamma_h \neq \gamma_k. \tag{4.5}$$

As anticipated in Chap. 2, in the quasistatic regime $x \to 0$, the eigenvalue problem in Eq. (4.4) splits in the electro-quasistatic (2.6) and magneto-quasistatic

(2.13) eigenvalue problems. In particular,

- The eigenfunctions of $\mathcal{L}$ that in the limit $x \to 0$ tend to the EQS modes are indicated with $\mathbf{u}_h$, and the corresponding eigenvalues are indicated with $1/\chi_h$. These eigenfunctions are called *plasmonic modes*.

- Dually, the set of eigenfunctions of $\mathcal{L}$ that in the limit $x \to 0$ tend to the MQS modes are indicated with $\mathbf{v}_h$, and the corresponding eigenvalues are indicated with x^2/κ_h. Although in the limit $x \to 0$, the eigen-susceptibilities κ_h/x^2 diverge, the quantities κ_h remain constant. These eigenfunctions are called *dielectric modes*.

The union of the two sets $\{\mathbf{u}_h\}$ and $\{\mathbf{v}_h\}$ is a basis for the unknown current density field in Eq. (4.1). Its solution is expressed as

$$\mathbf{J} = -i\omega\varepsilon_0\chi \sum_{h=1}^{\infty} \left[\frac{\chi_h}{\chi_h - \chi} \frac{\langle \mathbf{u}_h, \mathbf{E}_{\text{inc}} \rangle_\Omega}{\langle \mathbf{u}_h, \mathbf{u}_h \rangle_\Omega} \mathbf{u}_h + \frac{\kappa_h}{\kappa_h - \chi x^2} \frac{\langle \mathbf{v}_h, \mathbf{E}_{\text{inc}} \rangle_\Omega}{\langle \mathbf{v}_h, \mathbf{v}_h \rangle_\Omega} \mathbf{v}_h \right] \tag{4.6}$$

In the following, we denote these modes as *material independent modes* (MIMs), since they do not depend on the permittivity or susceptibility of the object, but only on its morphology.

We denote with $\mathbf{W}_h$ the electric field produced by the generic MIM $\mathbf{w}_h$. The fields $\mathbf{W}_h$ are extended in $\mathbb{R}^3$ by requiring that they satisfy the wave equation in $\mathbb{R}^3 \setminus \bar{\Omega}$, the boundary conditions on $\partial\Omega$, i.e.

$$\begin{aligned} \nabla^2 \mathbf{W}_h^- + x^2 \mathbf{W}_h^- &= \mathbf{0} \qquad \text{in } \mathbb{R}^3 \setminus \bar{\Omega}, && (4.7a) \\ \hat{\mathbf{n}} \times \left(\mathbf{W}_h^- - \mathbf{W}_h^+ \right) &= \mathbf{0} \qquad \text{on } \partial\Omega, && (4.7b) \\ \hat{\mathbf{n}} \times \left(\nabla \times \mathbf{W}_h^- - \nabla \times \mathbf{W}_h^+ \right) &= \mathbf{0} \qquad \text{on } \partial\Omega, && (4.7c) \end{aligned}$$

and the Silver-Müller conditions at infinity, namely

$$\begin{gathered} \mathbf{W}_h^- + \frac{1}{\mathrm{i}\, x} \hat{\mathbf{r}} \times \nabla \times \mathbf{W}_h^- = o\left(\frac{1}{r}\right), \\ \mathbf{W}_h^- = o\left(\frac{1}{r}\right), \quad \nabla \times \mathbf{W}_h^- = o\left(\frac{1}{r}\right), \end{gathered} \tag{4.8}$$

which constraint the scattered field $\mathbf{W}_h$ to be an outgoing wave.

By integrating the quantity $\nabla \cdot (\mathbf{W}_h \times \nabla \times \mathbf{W}_h^*)$ over $\mathbb{R}^3 \setminus \bar{\Omega}$, exploiting the divergence theorem and the properties of the eigenfunctions, we obtain

$$\operatorname{Re}\left\{\gamma_h\right\} = \frac{1}{\|\mathbf{W}_h\|^2_\Omega}\left[\frac{\|\nabla\times\mathbf{W}_h\|^2_{\mathbb{R}^3}}{x^2} - \|\mathbf{W}_h\|^2_{\mathbb{R}^3}\right], \tag{4.9a}$$

$$\operatorname{Im}\left\{\gamma_h\right\} = -\frac{1}{\|\mathbf{W}_h\|^2_\Omega}\oint_{S_\infty}\frac{\left|\mathbf{W}_r\right|^2}{x}dS, \tag{4.9b}$$

where $\|\mathbf{A}\|^2_V = \langle\mathbf{A}^*, \mathbf{A}\rangle_V$ and S_∞ is a far zone surface enclosing the object. Eq. (4.9a) suggests that $\operatorname{Re}\left\{\gamma_h\right\}$ does not have a definite sign, while Eq. (4.9b) implies that $\operatorname{Im}\left\{\gamma_h\right\}$ is non-positive. Specifically, $\operatorname{Im}\left\{\gamma_h\right\}$ is proportional to the contribution of the corresponding mode to the power radiated toward infinity, accounting for its radiating losses. This is in line with the expression of the quasi-static modes Q factor of an electrically small object, given in Eqs. (2.61) and (2.88), in which the imaginary part of the eigen-susceptibilities appears at the denominator.

In the limit of size parameter x tending to infinity, Eq. (4.7a) suggests that $\mathbf{W}_h^- \to \mathbf{0}$ in $\mathbb{R}^3 \setminus \bar{\Omega}$, therefore from Eqs. (4.9), we have

$$\lim_{x\to\infty}\gamma_h = -1, \qquad \forall h \in \mathbb{N}. \tag{4.10}$$

Accordingly, we have the following limits for the plasmonic and dielectric eigen-susceptibilities:

$$\lim_{x\to\infty}\chi_h = -1, \qquad \lim_{x\to\infty}\kappa_h = -\infty, \qquad \forall h \in \mathbb{N}. \tag{4.11}$$

Since all the quantities $\{\kappa_h\}_{h\in\mathbb{N}}$ related to the dielectric eigen-susceptibilities diverge for $x \to \infty$, from now on we switch from the eigen-susceptibilities $\{\gamma_h\}_{h\in\mathbb{N}}$ to the eigen-permittivities $\{\xi_h\}_{h\in\mathbb{N}}$, such that

$$\xi_h = \gamma_h + 1, \qquad \forall h \in \mathbb{N}. \tag{4.12}$$

We denote with ε_h the eigen-permittivity corresponding to the plasmonic eigen-susceptibility χ_h, and with η_h/x^2 the eigen-permittivity corresponding to the dielectric eigen-susceptibility κ_h/x^2, i.e.

$$\varepsilon_h = \chi_h + 1, \qquad \eta_h = \kappa_h + x^2, \qquad \forall h \in \mathbb{N}. \tag{4.13}$$

By doing so, the quantity η_h tends to the MQS eigenvalue $\kappa_h^\perp$ in the limit of x tending to 0, i.e.

$$\lim_{x\to 0}\eta_h = \kappa_h^\perp, \tag{4.14}$$

while, for finite $\kappa_h^{\perp}$ (they accumulate at infinity, see Sec. 2.1.2) it remains finite in the limit of x tending to infinity. Specifically, by using Eqs. (4.9) in the limit $x \to \infty$, we find that

$$\lim_{x\to\infty} \eta_h = \lim_{x\to\infty} \frac{\|\nabla \times \mathbf{W}_h\|_\Omega^2}{\|\mathbf{W}_h\|_\Omega^2} < +\infty \qquad \forall h \in \mathbb{N}. \tag{4.15}$$

Within this slightly different framework, from Eq. (4.6), the scattered electric field in $\mathbb{R}^3$ can be expressed as

$$\mathbf{E}_{\text{sca}} = (\varepsilon_R - 1) \sum_{h=1}^{\infty} \left[\frac{1}{\varepsilon_h - \varepsilon_R} \frac{\langle \mathbf{u}_h, \mathbf{E}_{\text{inc}} \rangle_\Omega}{\langle \mathbf{u}_h, \mathbf{u}_h \rangle_\Omega} \mathbf{U}_h + \frac{1}{\eta_h / x^2 - \varepsilon_R} \frac{\langle \mathbf{v}_h, \mathbf{E}_{\text{inc}} \rangle_\Omega}{\langle \mathbf{v}_h, \mathbf{v}_h \rangle_\Omega} \mathbf{V}_h \right], \tag{4.16}$$

where $\mathbf{U}_h$ and $\mathbf{V}_h$ are the extension of the modes $\mathbf{u}_h$ and $\mathbf{v}_h$ in $\mathbb{R}^3$, respectively.

The expansions in Eqs. (4.6) and (4.16) in terms of MIMs lead to a natural disjunction of the contribution of the material from the one of the geometry: the object permittivity appears only as rational functions in the expansion coefficients, while the object morphology is buried in the material independent eigenvalues and eigenfunctions. The terms $\langle \mathbf{u}_h, \mathbf{E}_{\text{inc}} \rangle_\Omega$ and $\langle \mathbf{v}_h, \mathbf{E}_{\text{inc}} \rangle_\Omega$ account for the coupling of the external excitation with the modes $\mathbf{u}_h$ and $\mathbf{v}_h$, respectively.

The simple functional dependence of $\mathbf{E}_{\text{sca}}$ on ε_R makes the MIM expansion particularly suitable for the design of a scatterer permittivity to achieve a prescribed tailoring of the scattered field, such as backscattering cancellation, maximization of the scattered field in a given point of space, or multipolar order suppression [65, 76, 141, 80].

4.1.1 Resonance condition. Broad and narrow resonances

Furthermore, the MIM expansion (4.16) effectively predicts the resonant behavior of 3D objects, as their shape, size, and permittivity vary. Since $\text{Im}\{\xi_h\} \leq 0$, the quantity $(\xi_h - \varepsilon_R)$ does not vanish in passive materials (where $\text{Im}\{\varepsilon_R\} > 0$) as ω or x varies. Nevertheless, for fixed geometry and material of the object, the amplitude of the generic mode $\mathbf{w}_h$ reaches its maximum in a neighbourhood of the frequency ω_h such that

$$\min_{\omega} \left| \frac{\xi_h(\omega) - \varepsilon_R(\omega)}{\varepsilon_R(\omega) - 1} \right| = \rho\{\mathbf{w}_h\} \tag{4.17}$$

This is the resonant condition for the mode $\mathbf{w}_h$: ω_h is its resonant frequency, $x_h = \frac{\omega_h}{c_0} \ell_c$ is its resonant size parameter, and $\rho\{\mathbf{w}_h\}$ is the corresponding residuum. They do not depend on the incident field.[1] The width of the corresponding resonance is related to

---

[1] The coupling coefficient $\langle \mathbf{w}_h, \mathbf{E}_{\text{inc}} \rangle_\Omega$ also depends on ω or x, but it varies very slowly if compared with $1/(\xi_h - \varepsilon_R)$.

the value of the residuum: a larger residuum is associated with a broader resonance. We denote a given mode $\mathbf{w}_h$ as *narrow* if its residuum $\rho\{\mathbf{w}_h\}$ is much smaller than 1, and as *broad* otherwise. Thus, we set a threshold equal to 0.2, beyond which the mode is considered broad, i.e.

$$\begin{aligned} \rho\{\mathbf{w}_h\} &< 0.2 \quad \rightarrow \text{ narrow mode,} \\ \rho\{\mathbf{w}_h\} &\geq 0.2 \quad \rightarrow \text{ broad mode.} \end{aligned} \tag{4.18}$$

It is particularly useful to analyze the modes resonance condition in a *material picture*, where the object geometry and the operating frequency are fixed, and the role of the spectral parameter is played by the permittivity. In this framework, the size parameter x is fixed, and the mode $\mathbf{w}_h$ undergoes a boost in the neighbourhood of the *optimal* permittivity ε_{R_h} such that

$$\min_{\varepsilon_R} \left| \frac{\xi_h(x) - \varepsilon_R}{\varepsilon_R - 1} \right| = \bar{\rho}\{\mathbf{w}_h\}(x). \tag{4.19}$$

The material picture allows us to characterize a mode resonance independently of the object permittivity. Specifically, for any size parameter x, the residuum $\bar{\rho}\{\mathbf{w}_h\}(x)$ from Eq. (4.19) is the lower bound of the residua $\rho\{\mathbf{w}_h\}$ at the resonant size parameter x, found by applying Eq. (4.17). In other words, if a mode $\mathbf{w}_h$ is resonantly excited in an object of permittivity ε_R, at the resonant size parameter x_h, and with residuum $\rho\{\mathbf{w}_h\}$, we will always have

$$\bar{\rho}\{\mathbf{w}_h\}(x_h) \leq \rho\{\mathbf{w}_h\}. \tag{4.20}$$

By solving Eq. (4.19), we find the optimal permittivity $\varepsilon_{R_h}(x)$

$$\varepsilon_{R_h}(x) = 1 + \frac{|\xi_h(x) - 1|^2}{\operatorname{Re}\{\xi_h(x)\} - 1}, \tag{4.21}$$

which is real valued, and the residua lower bound $\bar{\rho}\{\mathbf{w}_h\}(x)$

$$\bar{\rho}\{\mathbf{w}_h\}(x) = -\frac{\operatorname{Im}\{\xi_h(x)\}}{|\xi_h(x) - 1|}, \tag{4.22}$$

such that $0 \leq \bar{\rho}\{\mathbf{w}_h\}(x) \leq 1$, $\forall x$.

An immediate outcome of this method is that, at a specific size parameter x, according to the definition of narrow modes in Eq. (4.18), if $\bar{\rho}\{\mathbf{w}_h\}(x) \geq 0.2$ then the mode $\mathbf{w}_h$ can only generate a broad resonance, independently of the object material.

The real part of the eigen-permittivities ξ_h can be either negative or positive. If negative, the condition (4.21) can be satisfied (or approached) by metals in the visible spectral range ($\text{Re}\{\varepsilon_R\} < 0$), causing a plasmon resonance, hence the label "plasmon modes". If positive, the condition (4.21) is verified by dielectrics ($\text{Re}\{\varepsilon_R\} > 0$), causing a dielectric resonance, hence the label "dielectric modes". Furthermore, the eigen-permittivities ξ_h only depend on the size parameter x, therefore they can be exhaustively described by the loci they span in the complex plane as a function of x. The resulting diagrams, as well as the residua lower bounds, are universal, being applicable to every possible homogeneous object of given geometry, and constitute an invaluable tool to investigate its resonances.

4.2 Material-independent modes of a sphere

From now on, we assume that the region Ω is a sphere of radius R, which is chosen as the characteristic length $\ell_c = R$ of the object. Accordingly, the size parameter x is $x = \frac{\omega}{c_0} R$.

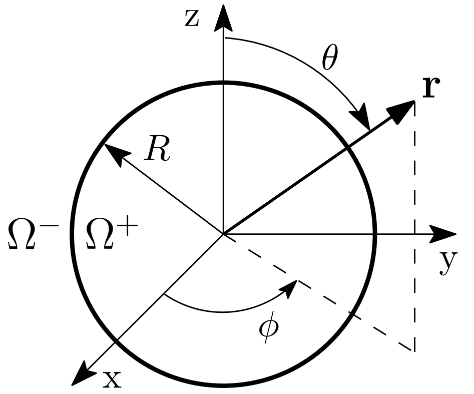

Figure 4.1 – Spherical polar coordinate system $\mathbf{r} = (r, \vartheta, \phi)$ centered on a sphere of radius R.

The MIMs of a sphere can be expressed analytically in terms of the vector spherical wave functions (VSWF) [65], using a spherical polar coordinate system $\mathbf{r} = (r, \vartheta, \phi)$ (Fig. 4.1). We indicate the plasmonic modes with $\mathbf{u}^{\texttt{TM}}_{pmn}$, which generate a magnetic field with vanishing radial component, so they are called transverse magnetic (TM) modes, tending to the TM EQS current modes $\mathbf{j}^{\parallel}_{pmn}$ for $x \to 0$. The dielectric modes are given by the union of two sets $\{\mathbf{v}^{\texttt{TM}}_{pmnl}, \mathbf{v}^{\texttt{TE}}_{pmnl}\}$: the current modes $\mathbf{v}^{\texttt{TM}}_{pmnl}$ of the first set tend to the TM MQS modes $\mathbf{j}^{\perp\texttt{TM}}_{pmnl}$ for $x \to 0$; the current modes $\mathbf{v}^{\texttt{TE}}_{pmnl}$ of the second set, and their corresponding electric field, have no radial component, so they are called transverse electric (TE) modes, and tend to the TE $\mathbb{A}^{\perp}$-modes $\mathbf{j}^{\perp\texttt{TE}}_{pmnl}$ for

$x \to 0$, which generate a magnetic vector potential with vanishing normal component to the object's boundary (see Sec. 2.1.2). Following Mie [166, 87], we also indicate the TM modes with *electric type* modes,[2] and the TE modes with *magnetic type* modes. The subscript p distinguishes between even (e) and odd (o) modes with respect to the azimuthal variable. The indices $n \in \mathbb{N}$ and $0 \leq m \leq n$ characterize the angular dependence of the modes: m is the number of oscillations along the azimuth and n is the multipolar order. The mode number $l \in \mathbb{N}$ is related to the number of maxima of the mode amplitude along the radial direction inside the sphere. Due to the spherical symmetry, the plasmonic eigen-permittivities depend only on the n index, while the dielectric eigen-permittivities depend on the indices $\{n, l\}$.

The expression of the sphere plasmonic and dielectric MIMs is

$$\mathbf{u}_{pmn}^{\mathtt{TM}}(\mathbf{r}) = \mathbf{N}_{pmn}^{(1)}\left(\sqrt{\varepsilon_n^{\mathtt{TM}}}\, x\mathbf{r}\right), \tag{4.23}$$

$$\mathbf{v}_{pmnl}^{\mathtt{TM}}(\mathbf{r}) = \mathbf{N}_{pmn}^{(1)}\left(\sqrt{\eta_{nl}^{\mathtt{TM}}}\, \mathbf{r}\right), \tag{4.24}$$

$$\mathbf{v}_{pmnl}^{\mathtt{TE}}(\mathbf{r}) = \mathbf{M}_{pmn}^{(1)}\left(\sqrt{\eta_{nl}^{\mathtt{TE}}}\, \mathbf{r}\right), \quad \forall \mathbf{r} \in \Omega \tag{4.25}$$

where $\{\varepsilon_n^{\mathtt{TM}}\}_{n \in \mathbb{N}}$ are the plasmonic eigen-permittivities, $\{\eta_{nl}^{\mathtt{TM}}/x^2, \eta_{nl}^{\mathtt{TE}}/x^2\}_{(n,l) \in \mathbb{N}^2}$ are the dielectric TM and TE eigen-permittivities, $\mathbf{N}_{pmn}^{(1)}$ and $\mathbf{M}_{pmn}^{(1)}$ are the VSWFs regular at the center of the sphere, whose expression is given in Eq. (B.17) in Appendix B. The MIMs are extended in $\mathbb{R}^3$ by requiring that they satisfy the wave equation in $\mathbb{R}^3 \setminus \bar{\Omega}$ and the boundary conditions on $\partial\Omega$ (4.7), and the Silver-Müller conditions at infinity (4.8). We denote the extension of the modes $\mathbf{u}_{pmn}^{\mathtt{TM}}$, $\mathbf{v}_{pmnl}^{\mathtt{TM}}$, $\mathbf{v}_{pmnl}^{\mathtt{TE}}$ in $\mathbb{R}^3$ with $\mathbf{U}_{pmn}^{\mathtt{TM}}$, $\mathbf{V}_{pmnl}^{\mathtt{TM}}$, $\mathbf{V}_{pmnl}^{\mathtt{TE}}$, respectively, and their expression is:

$$\mathbf{U}_{pmn}^{\mathtt{TM}}(\mathbf{r}) = \begin{cases} \mathbf{u}_{pmn}^{\mathtt{TM}}(\mathbf{r}) & \mathbf{r} \in \Omega \\ \tau_n^{\mathtt{TM}} \mathbf{N}_{pmn}^{(3)}(x\mathbf{r}) & \mathbf{r} \in \mathbb{R}^3 \setminus \bar{\Omega} \end{cases}, \tag{4.26}$$

$$\mathbf{V}_{pmn}^{\mathtt{TM}}(\mathbf{r}) = \begin{cases} \mathbf{v}_{pmn}^{\mathtt{TM}}(\mathbf{r}) & \mathbf{r} \in \Omega \\ \sigma_{nl}^{\mathtt{TM}} \mathbf{N}_{pmn}^{(3)}(x\mathbf{r}) & \mathbf{r} \in \mathbb{R}^3 \setminus \bar{\Omega} \end{cases}, \tag{4.27}$$

$$\mathbf{V}_{pmn}^{\mathtt{TE}}(\mathbf{r}) = \begin{cases} \mathbf{v}_{pmn}^{\mathtt{TE}}(\mathbf{r}) & \mathbf{r} \in \Omega \\ \sigma_{nl}^{\mathtt{TE}} \mathbf{M}_{pmn}^{(3)}(x\mathbf{r}) & \mathbf{r} \in \mathbb{R}^3 \setminus \bar{\Omega} \end{cases}, \tag{4.28}$$

where the superscript (3), appended to the VSWFs, denotes that the radial depen-

---

[2] Here, the label "electric type" has a different meaning than the one used in Chap. 3, in which it is used for electrically small radiators that support longitudinal current modes, which in this framework would only contain the TM plasmonic modes $\mathbf{u}_{pmn}^{\mathtt{TM}}$ for $x \to 0$, and not the TM dielectric modes $\mathbf{v}_{pmnl}^{\mathtt{TM}}$, supported by radiators of the magnetic type for $x \to 0$.

dence is given by the Hankel function of the first kind $h_n^{(1)}(\cdot)$, and

$$\begin{aligned}
\tau_n^{\mathtt{TM}} &= \frac{\sqrt{\varepsilon_n^{\mathtt{TM}}}\, j_n\!\left(\sqrt{\varepsilon_n^{\mathtt{TM}}}x\right)}{h_n^{(1)}(x)}, \\
\sigma_{nl}^{\mathtt{TM}} &= \frac{\sqrt{\eta_{nl}^{\mathtt{TM}}}\, j_n\!\left(\sqrt{\eta_{nl}^{\mathtt{TM}}}\right)}{x h_n^{(1)}(x)}, \\
\sigma_{nl}^{\mathtt{TE}} &= \frac{j_n\!\left(\sqrt{\eta_{nl}^{\mathtt{TE}}}\right)}{h_n^{(1)}(x)}.
\end{aligned} \tag{4.29}$$

The modes with $n = 1$ are dipolar modes, those with $n = 2$ are quadrupolar modes, and so on. We indicate the plasmonic modes $\mathbf{u}_{pmn}^{\mathtt{TM}}$ and the TE dielectric modes $\mathbf{v}_{pmnl}^{\mathtt{TE}}\Big|_{l=1}$ also as *fundamental* electric and magnetic type modes, respectively. Consistently, we denote the TM dielectric modes $\mathbf{v}_{pmnl}^{\mathtt{TM}}$ and the TE dielectric modes $\mathbf{v}_{pmnl}^{\mathtt{TE}}\Big|_{l>1}$ as *higher-order* electric and magnetic type modes, respectively.

The biorthogonality condition in Eq. (4.5) particularizes in

$$\begin{aligned}
&\langle \mathbf{u}_{pmn}^{\mathtt{TM}}, \mathbf{v}_{p'm'n'l'}^{\nu} \rangle_\Omega = 0, && \forall\,(p,\, m,\, n,\, p',\, m',\, n',\, \nu)\,, \\
&\langle \mathbf{v}_{pmnl}^{\nu}, \mathbf{v}_{p'm'n'l'}^{\nu'} \rangle_\Omega = 0, && \forall\,(\nu,\, p,\, m,\, n,\, l) \neq (\nu',\, p',\, m',\, n',\, l')\,,
\end{aligned} \tag{4.30}$$

where $\nu,\, \nu' \in \{\mathtt{TM}, \mathtt{TE}\}$. Moreover, due to the spherical symmetry, we also have that a subset of the modes is orthogonal in the usual sense, namely

$$\begin{aligned}
&\langle \left(\mathbf{u}_{pmn}^{\mathtt{TM}}\right)^*, \mathbf{v}_{p'm'n'l'}^{\mathtt{TE}} \rangle_\Omega = 0, && \forall\,(p,\, m,\, n,\, p',\, m',\, n')\,, \\
&\langle \left(\mathbf{u}_{pmn}^{\mathtt{TM}}\right)^*, \mathbf{v}_{p'm'n'l'}^{\mathtt{TM}} \rangle_\Omega = 0, && \forall\,(p,\, m,\, n) \neq (p',\, m',\, n')\,, \\
&\langle \left(\mathbf{v}_{pmnl}^{\nu}\right)^*, \mathbf{v}_{p'm'n'l'}^{\nu'} \rangle_\Omega = 0, && \forall\,(\nu,\, p,\, m,\, n) \neq (\nu',\, p',\, m',\, n')\,.
\end{aligned} \tag{4.31}$$

All the electric modes (TM) are orthogonal to the magnetic modes (TE), while, for instance, two dielectric modes sharing the values of the indices ν, p, m, n are not, even if they have different values of l. On the contrary, any two modes differing in at least one of the indices ν, p, m, n are orthogonal.

The sphere MIMs for $x \to 0$ are plotted in Fig. 2.2. Since they are weakly sensitive to changes of the size parameter x,[3] and since we will make extensive use of them in the following, we introduce a stylized version of them in Fig. 4.2. The TM mode $\mathbf{u}_{e11}^{\mathtt{TM}}$ shown in the top-left corner of Fig. 2.2 exhibits an electric dipole character. The TM mode $\mathbf{v}_{e111}^{\mathtt{TM}}$ has an electric “toroidal" dipole character [167],

---

[3] In [140], we plot the MIMs of a sphere of radius $R = \lambda/4$, and size parameter $x = \pi/2$, and they appear almost identical to their quasi-static version.

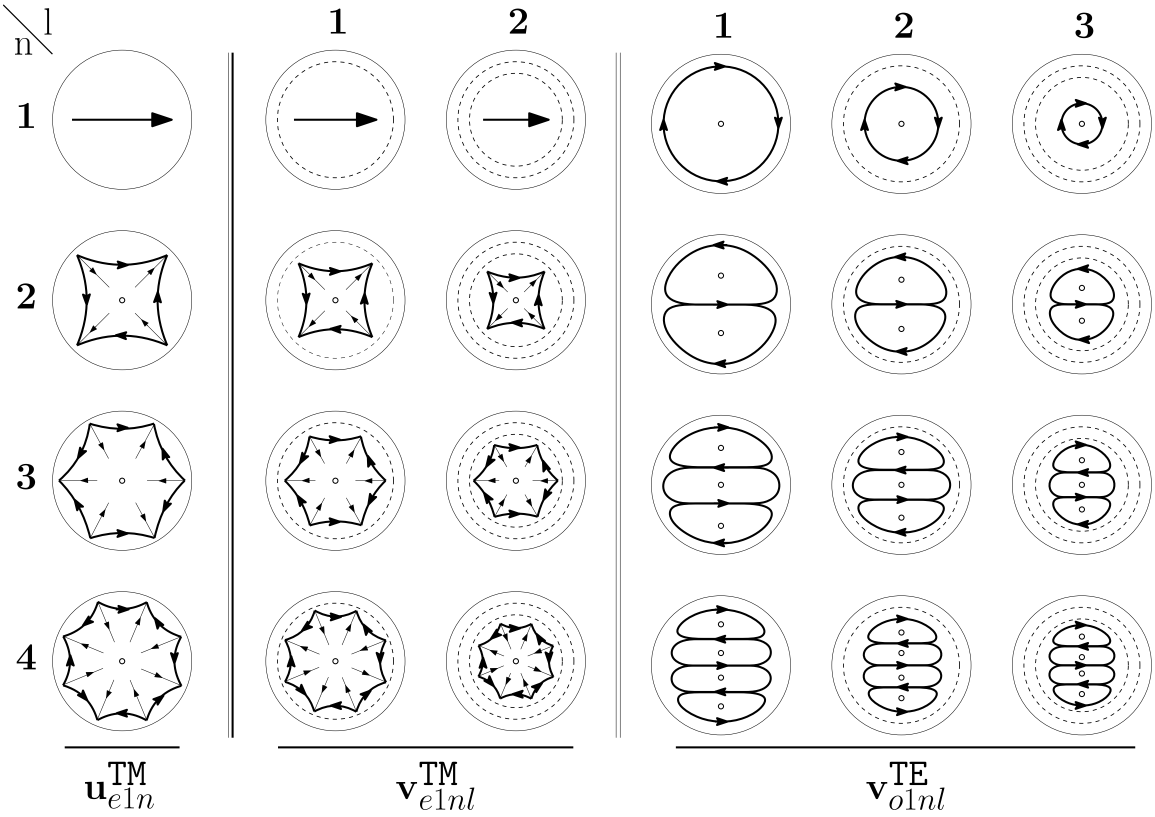

Figure 4.2 – Stylized version of the TM and TE modes of a sphere.

localized in an inner sphere region than the mode $\mathbf{u}_{e11}^{\texttt{TM}}$, and it is characterized by two oscillations along the (vertical) radial direction. Increasing the index l, while keeping fixed the order $n = 1$, we observe one more oscillation of the mode along the radial direction for $l = 2$. Furthermore, as l increases, the region where the field is localized is increasingly squeezed in proximity of the sphere center. For these reasons, the stylized representation of $\mathbf{u}_{e11}^{\texttt{TM}}$ is a single arrow, representing the electric dipole, enclosed by one circle, while the stylized version of $\mathbf{v}_{e11l}^{\texttt{TM}}$ is a single arrow enclosed by $l + 1$ circles, and squeezed as l increases. The mode $\mathbf{u}_{e12}^{\texttt{TM}}$ shows a quadrupolar character with two sources and two sinks of the field lines, whereas the mode $\mathbf{u}_{e13}^{\texttt{TM}}$ is of octupolar type with three sources and three sinks, and so on. In all cases, the higher-order modes $\mathbf{v}_{e12l}^{\texttt{TM}}$, $\mathbf{v}_{e13l}^{\texttt{TM}}$, $\mathbf{v}_{e14l}^{\texttt{TM}}$ exhibit a number of oscillations growing with l, and a region of maximum intensity increasingly squeezed in proximity of the sphere center. The stylized representations of $\mathbf{u}_{e1n}^{\texttt{TM}}$ and $\mathbf{v}_{e1nl}^{\texttt{TM}}$ visually highlight both the number of sources-sinks, and the number of oscillations along the radial direction.

The mode $\mathbf{v}_{o111}^{\texttt{TE}}$ has a magnetic dipole character: it exhibits one vortex, associated to a magnetic dipole moment directed orthogonally to the vortex plane. By increasing l, we note that one ($l = 2$) or two ($l = 3$) additional contra-rotating vortices arise. For this reason, the stylized representation of the mode $\mathbf{v}_{o11l}^{\mathtt{TE}}$ is a current loop, enclosed by l concentric circles. By increasing n to 2, the mode $\mathbf{v}_{o121}^{\mathtt{TE}}$ shows two identical vortices with antiparallel magnetic dipole moments. Also in this case, by increasing l, additional vortices appear. The number of oscillations of the mode along the radial (vertical) direction is l. The field lines of the magnetic octupole ($n = 3$, $l = 1$) and the magnetic hexadecapole ($n = 4$, $l = 1$) form three and four identical vortices, respectively. As we increase l, the number of oscillations of the mode along the radial (vertical) direction increases. The stylized representations of the TE modes highlight the number of vortices of the mode, and the number of oscillations along the radial direction.

The eigen-permittivities $\varepsilon_n^{\mathtt{TM}}$ and the quantities $\eta_{nl}^{\mathtt{TM}}$, $\eta_{nl}^{\mathtt{TE}}$ are obtained by zeroing the denominator of the Mie scattering coefficients [87] (see Eq. (B.11)), or are equivalently found as the roots of two power series [65], given in Eq. (B.12) of Appendix B.

4.3 Resonance properties of a sphere

We now investigate the behavior of the sphere plasmonic and dielectric eigen-permittivities by varying the size parameter x, deriving general properties of the electromagnetic scattering from the object.

4.3.1 Loci of the plasmonic modes

In Fig. 4.3 we show the loci spanned by the eigen-permittivities $\varepsilon_n^{\mathtt{TM}}$, for $n = 1, 2, 3, 4$, associated to the plasmonic electric dipole, quadrupole, octupole, and hexadecapole modes, respectively. As shown in Sec. 2.2.5, the loci start at the electrostatic values

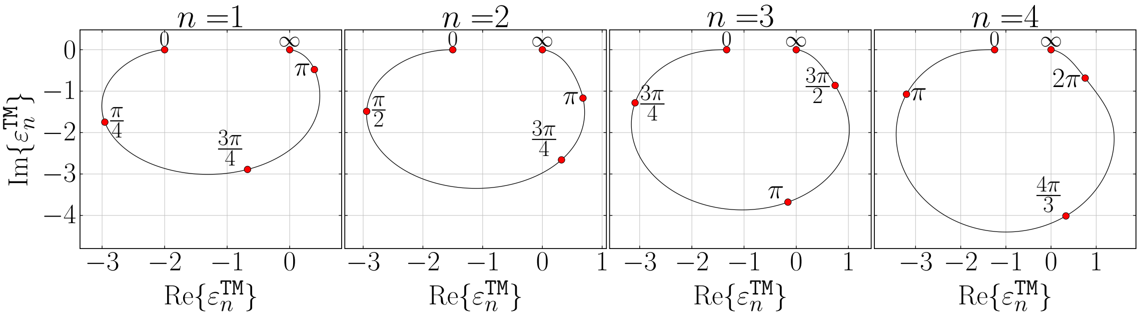

Figure 4.3 – Loci spanned in the complex plane by the plasmonic eigen-permittivities $\varepsilon_n^{\mathtt{TM}}$ of a homogeneous sphere by varying $x \in [0, \infty)$. We show the loci associated to the fundamental electric dipole ($n = 1$), quadrupole ($n = 2$), octupole ($n = 3$), hexadecapole ($n = 4$).

$$\lim_{x\to 0} \varepsilon_n^{\mathtt{TM}} = -\frac{n+1}{n}. \tag{4.32}$$

In particular, the eigen-permittivity $\varepsilon_1^{\mathtt{TM}}$, associated to the plasmonic dipole mode, approach -2 for $x \to 0$. According to the resonance condition for quasistatic modes in Eq. (2.58), or full-wave modes in Eqs. (4.19) and (4.21), the resonant permittivity is also $\varepsilon_R = -2$, in agreement with the Fröhlich condition [2]. Therefore for finite values of x, the condition (4.19) or (4.17) applied to the fundamental dipole represents the natural extension of the Fröhlich condition to the full retarded case. By increasing x, both the real and the imaginary part of $\varepsilon_1^{\mathtt{TM}}$ and all the other plasmonic eigenvalues $\varepsilon_n^{\mathtt{TM}}$ move toward more negative values. The decrease in the real part implies, for low losses Drude metals, a red shift of the corresponding resonant frequency [1], as shown in Sec. 2.2.2 with Eq. (2.60). When $x \approx 0.72$, the quantity $\mathrm{Re}\{\varepsilon_1^{\mathtt{TM}}\}$ reaches a minimum, and then starts increasing. For larger x, $\varepsilon_1^{\mathtt{TM}}$ lies in the fourth quadrant of the complex plane. Then, $\mathrm{Re}\{\varepsilon_1^{\mathtt{TM}}\}$ increases until $x \approx 2$ when it reaches the maximum value of 0.48, and eventually $\varepsilon_1^{\mathtt{TM}}$ asymptotically approaches the origin of the complex plane.

The eigen-permittivities $\varepsilon_2^{\mathtt{TM}}$, $\varepsilon_3^{\mathtt{TM}}$, $\varepsilon_4^{\mathtt{TM}}$ have a similar dynamic, with two main differences: as n increases, they trace a progressively wider trajectory, i.e., they reach increasingly negative imaginary part and large magnitude of the real part (see Fig. B.1, in which we show the loci of $\varepsilon_n^{\mathtt{TM}}$ for n up to $n = 25$); as n increases, the loci are swept with decreasing speed by the parameter x. This can be easily visualized in Fig. 4.3 by following the position of an eigen-permittivity for a fixed x as the order n varies: the eigen-permittivity at $x = \pi$, for instance, distinctly moves toward the beginning of the locus as n grows.

On the left of Fig. 4.4 we plot the lower bounds $\bar{\rho}\{\mathbf{u}_{pmn}^{\mathtt{TM}}\}$ for the residua associated with the resonances of the plasmonic modes under exam as a function of x, calculated by particularizing Eq. (4.22) to the plasmonic eigen-permittivities, namely

$$\bar{\rho}\{\mathbf{u}_{pmn}^{\mathtt{TM}}\}(x) = -\frac{\mathrm{Im}\{\varepsilon_n^{\mathtt{TM}}(x)\}}{|\varepsilon_n^{\mathtt{TM}}(x) - 1|}. \tag{4.33}$$

For the considerations made in Sec. 4.1, the residua lower bounds of a mode separate the size parameter axis into two intervals, viz. the size parameters at which the mode is intrinsically broad, and the size parameters at which the mode can generate a narrow resonance. The extremes x_n', x_n'' of the broad-resonances interval of a mode are found by solving the equation $\bar{\rho}\{\mathbf{u}_{pmn}^{\mathtt{TM}}\} = 0.2$. In the table on the right of Fig. 4.4, we list these extremes for the considered plasmonic modes. It tells us, for instance, that a narrow resonance of the dipole mode for $0.63 \le x \le 5$, or equivalently for a

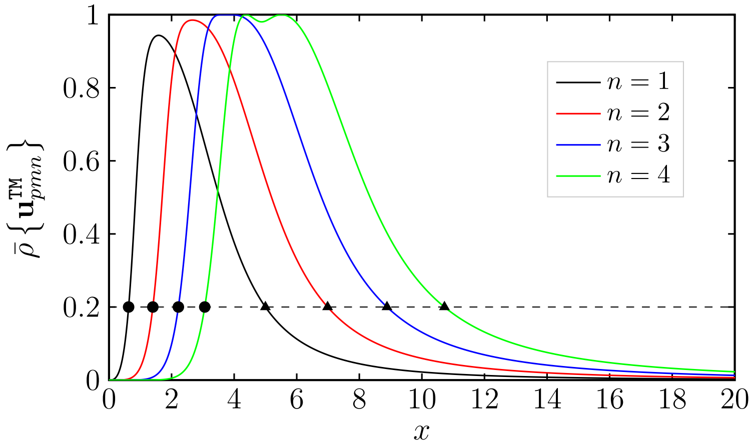

$\bar{\rho}(x'_n) = \bar{\rho}(x''_n) = 0.2$

n	x'_n (●)	x''_n (▲)
1	0.63	5.00
2	1.40	6.96
3	2.22	8.88
4	3.06	10.69

Figure 4.4 – Residua lower bounds of the plasmonic modes $\mathbf{u}^{\mathrm{TM}}_{pmn}$ for $n = 1, 2, 3, 4$, as a function of the size parameter x, calculated by using Eq. (4.33). On the right, the values x', x'' at which the residua lower bounds reach the value 0.2.

sphere with radius R such that $0.1\lambda \leq R \leq 0.8\lambda$, is inherently forbidden.

As a consequence of the decreasing speed of parametrization in the eigen-permittivity loci with the multipolar order n, the corresponding residua curves, and therefore the broad-resonances interval, shift toward larger x. Moreover, due to the widening of the loci, the interval length grows with n: for instance, the interval for the quadrupole mode starts at $x'_2 = 1.4$, and has length 5.56, while for the octupole mode, it starts at $x'_3 = 2.22$, and has lenght 7.63. Furthermore, all loci spanned by the eigen-permittivities under exam are confined in a limited region of the complex plane, in particular $-3 \leq \mathrm{Re}\{\varepsilon^{\mathrm{TM}}_1\} \leq 0.48$, $-2.94 \leq \mathrm{Re}\{\varepsilon^{\mathrm{TM}}_2\} \leq 0.71$, $-3.16 \leq \mathrm{Re}\{\varepsilon^{\mathrm{TM}}_3\} \leq 1.02$, $-3.43 \leq \mathrm{Re}\{\varepsilon^{\mathrm{TM}}_4\} \leq 1.4$, respectively. Consequently, as we will see in Sec. 4.6 these modes are broad in spheres with moderately positive permittivity, e.g., silicon (Si, $\varepsilon_R \approx 16$ [168]), since their residua $\rho\{\mathbf{u}^{\mathrm{TM}}_n\}$, defined in Eq. (4.17), exceed 1. On the contrary, for size parameters x at which the modes are not inherently broad, they may be narrow for metal spheres in the visible spectral range, whose permittivity lies in the second quadrant of the complex plane.

4.3.2 Loci of the dielectric modes

In Fig. 4.5 we show the loci spanned by the quantities η^{TM}_{nl} and η^{TE}_{nl}, which give the dielectric TM and TE eigen-permittivities if normalized by x^2. We display the loci associated to the higher order electric dipole modes ($n = 1$), for $l = 1$, 2, and to the fundamental ($l = 1$) and higher order ($l = 2$) magnetic dipole ($n = 1$) and quadrupole

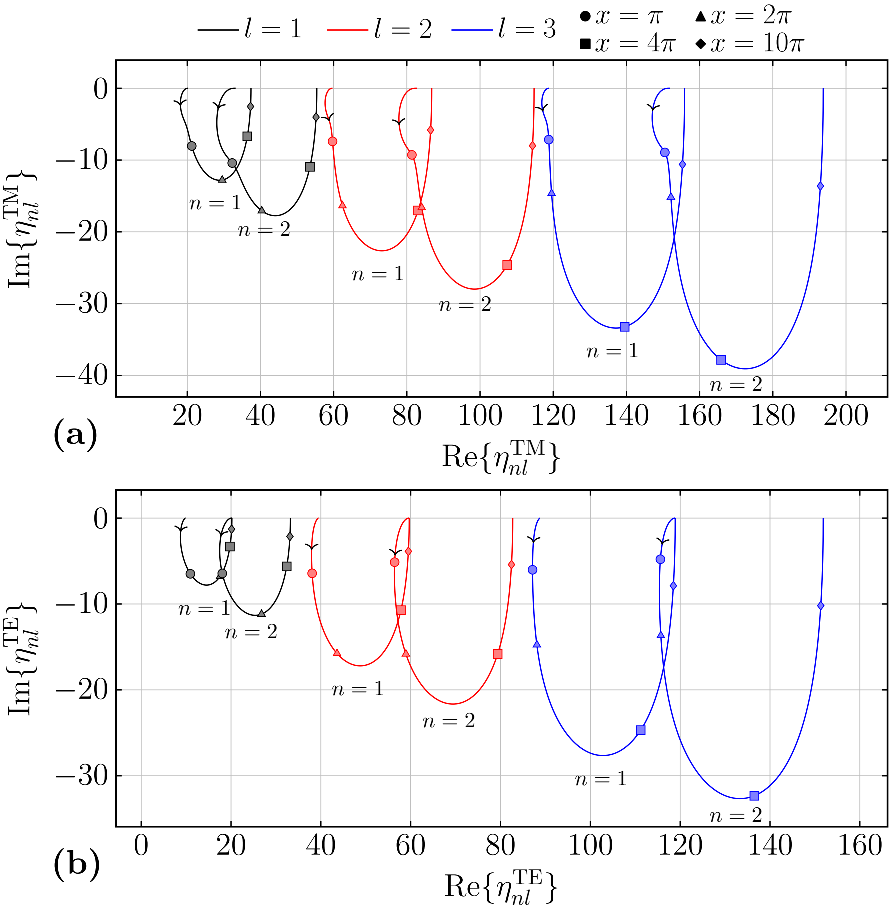

Figure 4.5 – Loci spanned in the complex plane by the sphere's $\eta_{nl}^{\texttt{TM}}$ (**a**) and $\eta_{nl}^{\texttt{TE}}$ (**b**) quantities, which, normalized by the squared size parameter x^2, give the dielectric TM and TE eigen-permittivities, respectively, by varying $x \in [0.\infty)$. We plot $\eta_{nl}^{\texttt{TM}}$ of the higher order electric dipole modes ($n = 1$), for $l = 1$, 2, and $\eta_{nl}^{\texttt{TE}}$ of the fundamental ($l = 1$) and higher order ($l = 2$) magnetic dipole ($n = 1$) and quadrupole ($n = 2$) modes.

($n = 2$) modes. The loci start at the values

$$\lim_{x\to 0} \eta_{nl}^{\texttt{TM}} = \kappa_{nl}^{\perp\texttt{TM}} = (z_{nl})^2 \qquad \lim_{x\to 0} \eta_{nl}^{\texttt{TE}} = \kappa_{nl}^{\perp\texttt{TE}} = (z_{n-1\,l})^2, \tag{4.34}$$

where z_{nl} is the l-th zero of the spherical Bessel function j_n, and end at the values

$$\lim_{x\to\infty} \eta_{nl}^{\texttt{TM}} = g_{nl}, \tag{4.35}$$

$$\lim_{x\to\infty} \eta_{nl}^{\texttt{TE}} = \kappa_{n+1\,l}^{\perp\texttt{TE}} = \kappa_{nl}^{\perp\texttt{TM}}, \tag{4.36}$$

where g_{nl} is the l-th zero of the derivative of the Riccati-Bessel function $\psi_n(y) = y\, j_n(y)$, i.e., $\psi_n'(g_{nl}) = 0$. Interestingly, for a fixed mode index l, the end of a locus for $\eta_{nl}^{\mathtt{TE}}$ at a multipolar order n, coincides with both the beginnings of the locus for $\eta_{n+1,l}^{\mathtt{TE}}$ at the next multipolar order $n+1$ and the locus for $\eta_{nl}^{\mathtt{TM}}$ at the same multipolar order n.

As discussed in Sec. 2.1.2, in the long-wavelength limit ($x \ll 1$), the eigen-permittivities associated to these modes diverge, and therefore they cannot be practically excited in electrically small metal particles, but only in spheres with positive and high permittivity.

As for the plasmonic eigen-permittivities, by increasing x, both the real and imaginary parts of $\eta_{nl}^{\mathtt{TM}}$ and $\eta_{nl}^{\mathtt{TE}}$ move toward more negative values. Moreover, from Eq. (2.87), the decrease in the real part lead to a red shift in the corresponding resonant frequency in high permittivity materials.

After reaching the minimum, both their real and imaginary parts start increasing until they asymptotically reach their maximum, which for the former is given in Eq. (4.35) while for the latter is 0. Thus, every locus covers a bounded region of the fourth quadrant of the complex plane. Furthermore, the normalized dielectric TM $\eta_{nl}^{\mathtt{TM}}$ and TE $\eta_{nl}^{\mathtt{TE}}$ eigen-permittivities share two properties with the plasmonic eigen-permittivities, viz. by increasing the multipolar order n and keeping fixed l (and vice versa), their loci have a progressively wider dynamics, and they are swept with growing speed by the parameter x.

At the top of Fig. 4.6, we plot the lower bounds $\bar{\rho}\{\mathbf{v}_{pmnl}^{\mathtt{TM}}\}$ and $\bar{\rho}\{\mathbf{v}_{pmnl}^{\mathtt{TE}}\}$, for the residua associated with the resonances of the considered dielectric modes, as a function of x, calculated by applying Eq. (4.22), namely

$$\bar{\rho}\{\mathbf{v}_{pmnl}^{\nu}\}(x) = -\frac{\operatorname{Im}\{\eta_{nl}^{\nu}(x)\}}{|\eta_{nl}^{\nu}(x) - x^2|}, \tag{4.37}$$

where $\nu \in \mathtt{TM,TE}$.

As for the plasmonic residua lower bounds, we calculate the extremes x'_{nl}, x''_{nl} of the size parameter intervals in which the modes are inherently broad, and we list them in the table at the bottom of Fig. 4.6. We notice, for instance, that a narrow resonance of the fundamental magnetic dipole mode $\mathbf{v}_{pm11}^{\mathtt{TE}}$ for $1.14 \leq x \leq 6.95$, or equivalently for a sphere with radius R such that $0.18\lambda \leq R \leq 1.12\lambda$, is inherently forbidden.

Due to the decreasing speed of parametrization in the dielectric loci with either the multipolar order n or the index l, the corresponding residua curves, and hence the intervals in which the modes are intrinsically broad, shift toward larger x. Moreover, the widening of the loci with the indices n and l produces an increase in the intervals' length: for instance, the interval for the second order ($l = 1$) electric dipole mode ($\mathbf{v}_{pm11}^{\mathtt{TM}}$) starts at $x'_{11} = 1.25$, and has length 7.83, while for the third ($l = 2$) order

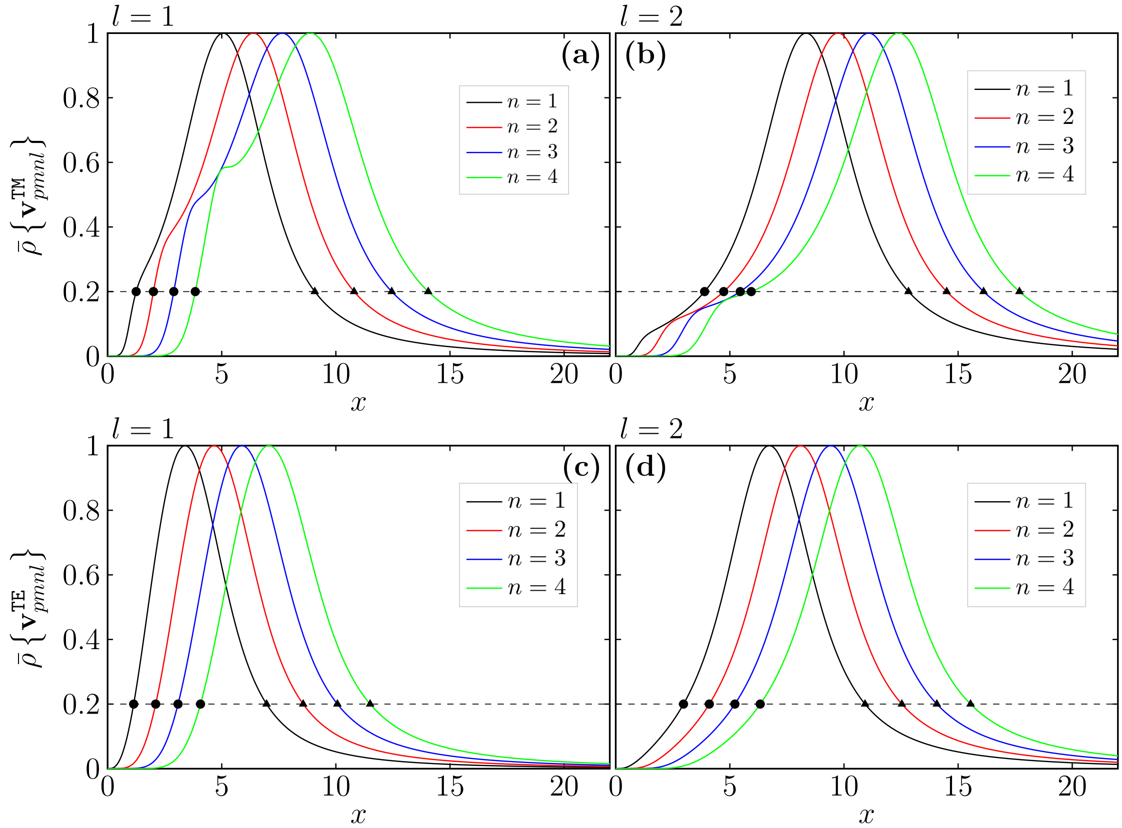

$\bar{\rho}\{\mathbf{v}^{\mathtt{TM}}_{pmnl}\}(x'_n) = \bar{\rho}\{\mathbf{v}^{\mathtt{TM}}_{pmnl}\}(x''_n) = 0.2$

	$l = 1$		$l = 2$	
n	x'_{nl} (●)	x''_{nl} (▲)	x'_{nl} (●)	x''_{nl} (▲)
1	1.25	9.08	3.88	12.83
2	2.01	10.79	4.74	14.51
3	2.90	12.44	5.45	16.11
4	3.85	14.04	5.95	17.70

$\bar{\rho}\{\mathbf{v}^{\mathtt{TE}}_{pmnl}\}(x'_n) = \bar{\rho}\{\mathbf{v}^{\mathtt{TE}}_{pmnl}\}(x''_n) = 0.2$

	$l = 1$		$l = 2$	
n	x'_{nl} (●)	x''_{nl} (▲)	x'_{nl} (●)	x''_{nl} (▲)
1	1.14	6.95	2.97	10.91
2	2.11	8.58	4.09	12.53
3	3.09	10.08	5.21	14.07
4	4.06	11.50	6.33	15.54

Figure 4.6 – Residua lower bounds of the dielectric TM modes $\mathbf{v}^{\mathtt{TM}}_{pmnl}$, for $l = 1$ (**a**) and $l = 2$ (**b**), and TE modes $\mathbf{v}^{\mathtt{TE}}_{pmnl}$, for $l = 1$ (**c**) and $l = 2$ (**d**), all for $n = 1, 2, 3, 4$, as a function of the size parameter x, calculated by using Eq. (4.33). Below, the values x', x'' at which the residua lower bounds reach the value 0.2.

electric dipole mode ($\mathbf{v}^{\mathtt{TM}}_{pm12}$), it starts at $x'_{12} = 3.88$, and has length 8.95.

As we will see in Sec. 4.5, these modes are broad in spheres with permittivity of negative real part, e.g., silver (Ag) or gold (Au) [169], since their residua, defined in Eq. (4.17), are greater than 1. Conversely, for size parameters x at which the modes are not intrinsically broad, they may be narrowly excited in spheres with permittivity of positive real part, e.g., Si.

4.4 Scattering efficiency

Let us now consider the scattering of an x-polarized plane wave propagating along z, i.e., $\mathbf{E}_{\text{inc}} = E_0 e^{ixz}\hat{\text{x}}$, by a sphere. By applying Eq. (4.16), we find the expression of the scattered electric field inside the sphere, in terms of its MIMs [65, 48]:

$$\mathbf{E}^{+}_{\text{sca}}(\mathbf{r}) = (\varepsilon_R - 1)\sum_{n=1}^{\infty} E_n \left\{ A_n^{\mathtt{TM}} \mathbf{u}^{\mathtt{TM}}_{e1n}(\mathbf{r}) + \sum_{l=1}^{\infty}\left[B^{\mathtt{TM}}_{nl}\mathbf{v}^{\mathtt{TM}}_{1enl}(\mathbf{r}) + B^{\mathtt{TE}}_{nl}\mathbf{v}^{\mathtt{TE}}_{1enl}(\mathbf{r})\right]\right\}, \quad \forall \mathbf{r} \in \Omega \tag{4.38}$$

where $E_n = \frac{i^n\sqrt{2(2n+1)}}{n(n+1)}$, and the scattering coefficients $A_n^{\mathtt{TM}}$, $B_{nl}^{\mathtt{TM}}$, $B_{nl}^{\mathtt{TE}}$ are given in Eqs. (B.18-B.20) of Appendix B. Due to the symmetry of $\mathbf{E}_{\text{inc}}$, only even electric modes and odd magnetic modes with $m = 1$ are excited.
The field outside the sphere is readily obtained by extending the MIMs in $\mathbb{R}^3$, using Eqs. (4.26-4.28):

$$\mathbf{E}^{-}_{\text{sca}}(\mathbf{r}) = (\varepsilon_R - 1)\sum_{n=1}^{\infty} E_n \left[\left(a_n^{\mathtt{TM}} + \sum_{l=1}^{\infty} b^{\mathtt{TM}}_{nl}\right)\mathbf{N}^{(3)}_{e1n}(x\mathbf{r}) + \left(\sum_{l=1}^{\infty} b^{\mathtt{TE}}_{nl}\right)\mathbf{M}^{(3)}_{o1n}(x\mathbf{r})\right], \quad \forall \mathbf{r} \in \mathbb{R}^3 \setminus \bar{\Omega}. \tag{4.39}$$

where the external scattering coefficients $a_n^{\mathtt{TM}} = \tau_n^{\mathtt{TM}} A_n^{\mathtt{TM}}$, $b_{nl}^{\mathtt{TM}} = \sigma_{nl}^{\mathtt{TM}} B_n^{\mathtt{TM}}$, $b_{nl}^{\mathtt{TE}} = \sigma_{nl}^{\mathtt{TE}} B_n^{\mathtt{TE}}$, with $\tau_n^{\mathtt{TM}}$, $\sigma_{nl}^{\mathtt{TM}}$, $\sigma_{nl}^{\mathtt{TE}}$ given in Eqs. (4.29).

The scattering cross-section for an arbitrary shaped object occupying a domain Ω of characteristic length ℓ_c, and size parameter $x = \frac{\omega}{c0}\ell_c$, can be defined as [87, 170]:

$$C_{\text{sca}} = \frac{\ell_c^2}{|E_0|^2 x}\oint_{S_c} \hat{\mathbf{r}} \cdot \text{Im}\left\{ (\nabla \times \mathbf{E}^{-}_{\text{sca}})^* \times \mathbf{E}^{-}_{\text{sca}} \right\} dS, \tag{4.40}$$

where S_c is an auxiliary surface enclosing Ω. We also define the scattering efficiency σ_{sca} as [87, 170]

$$\sigma_{\text{sca}} = \frac{C_{\text{sca}}}{G}, \tag{4.41}$$

where G is the particle cross-sectional area projected onto a plane perpendicular to the incident beam (e.g., $G = \pi R^2$ for a sphere of radius R). By combining Eqs. (4.39), (4.40), and (4.41), assuming the auxiliary surface S_c to be a spherical surface concentric with Ω, and exploiting the orthogonality of the VSWFs, we finally get for a sphere:

$$\sigma_{\text{sca}} = \frac{|\varepsilon_R - 1|}{x^2}\sum_{n=1}^{\infty}\left[\left| a_n^{\mathtt{TM}} + \sum_{l=1}^{\infty} b_{nl}^{\mathtt{TM}}\right|^2 + \left|\sum_{l=1}^{\infty} b_{nl}^{\mathtt{TE}}\right|^2\right]. \tag{4.42}$$

The expression of the scattering efficiency σ_{sca} in Eq. (4.42) shows that two electric (magnetic) modes sharing the multipolar order n, may interfere: for instance, a plasmonic mode $\mathbf{u}^{\mathtt{TM}}_{e1n}$ of index n may interfere with any TM dielectric mode $\mathbf{v}^{\mathtt{TM}}_{e1nl}$, $\forall l \in \mathbb{N}$. On the contrary, any two modes differing in the multipolar order n, or any electric and magnetic modes, cannot interfere.

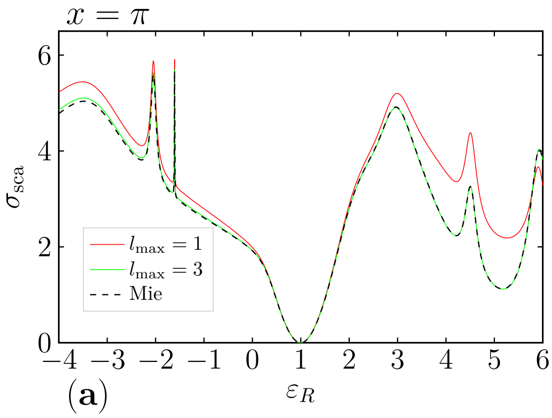

Figure 4.7 – Scattering efficiencies σ_{sca} of a dielectric sphere with size parameter $x = \pi$ (**a**) and $x = 2\pi$ (**b**) excited by a linearly polarized plane wave, as a function of $\varepsilon_R \in [-4, 6]$, calculated by applying Eq. (4.42) (solid lines), and by using the standard Mie theory (dashed line) [87]. In the calculations, we have truncated the external summation to $n_{\max} = 11$, and the internal summation to $l_{\max}$ shown in the panels' legend.

We define the partial scattering efficiency of a mode as the σ_{sca} that we would have if that only mode was excited, which is calculated using Eq. (4.42) by only considering the corresponding term in the summation: for instance, the partial σ_{sca} of the fundamental magnetic dipole mode $\mathbf{v}^{\mathtt{TM}}_{o111}$ is given by $\sigma_{\text{sca}} = \left|(\varepsilon_R - 1) b^{\mathtt{TE}}_{11}\right|^2 / x^2$. It is important to note that the total σ_{sca} is not the sum of the partial scattering efficiencies because the involved modes may interfere. Nevertheless, as we will see in the following, the partial scattering efficiencies enable us to identify the modes responsible for each peak of the total σ_{sca}.

In Fig. 4.7 we compare the scattering efficiency σ_{sca} of a sphere with $x = \pi$ (panel a) and $x = 2\pi$ (panel b), calculated by using Eq. (4.42), with the standard Mie theory [87]. We truncate the outer sum running over the multipolar orders n to $n_{\max} = 11$, and vary the index $l_{\max}$ at which the inner sums are truncated. In the case $x = \pi$, we truncate the inner sums to $l_{\max} = 1$ (red line), having agreement with the Mie theory only for small values of ε_R, and to $l_{\max} = 3$ (green line), for which the two results overlap almost perfectly. If we increase the size parameter to $x = 2\pi$, more modes are needed to reach convergence. Specifically, the MIMs expansion and the Mie theory give almost indistinguishable results for $l_{\max} = 6$.

4.5 Resonances and interferences in Ag spheres

Here we investigate the scattering efficiency σ_{sca} of a silver sphere as a function of x, under linearly polarized plane wave excitation.

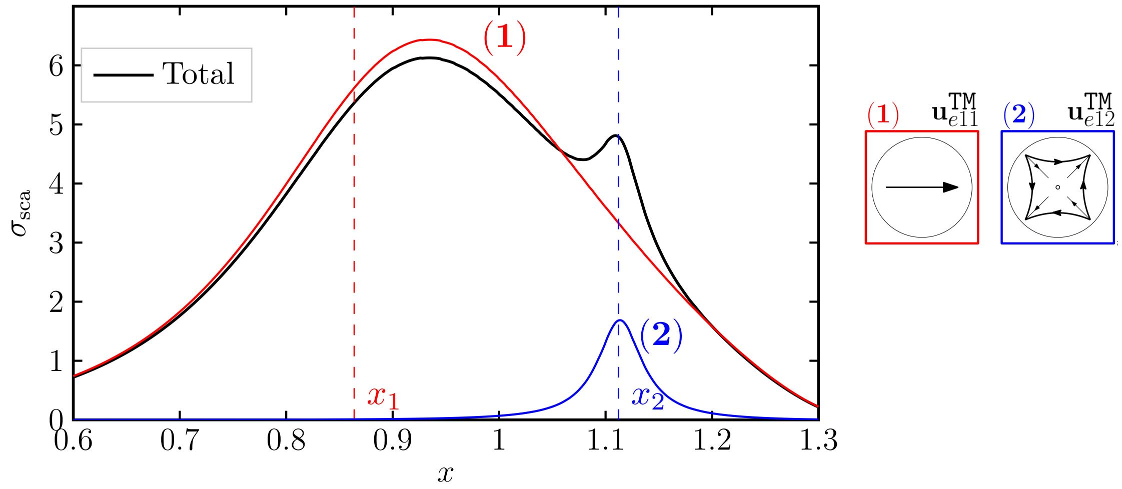

Figure 4.8 – Scattering efficiency σ_{sca} of an Ag sphere of radius $R = 67.5\,\text{nm}$, as a function of x. The partial scattering efficiencies (in color) of the two dominant modes $\mathbf{u}^{\mathtt{TM}}_{e11}$, $\mathbf{u}^{\mathtt{TM}}_{e12}$, the position of their resonant size parameters (dashed lines), and their stylized version (on the right), are also shown.

n	x_n	$\varepsilon_n^{\mathtt{TM}}(x_n)$	ω_n [Prad/s]	$\varepsilon_R(x_n)$	ρ	$\bar{\rho}(x_n)$	#peak	x_{peak}
1	0.86	-2.71 -2.28i	3.84	-7.39 + 0.25i	0.63	0.52	(1)	0.93
2	1.11	-2.20 -0.19i	4.94	-2.26 + 0.23i	0.13	0.06	(2)	1.11

Table 4.1 – Resonant size parameter x_n, eigen-permittivity $\varepsilon_n^{\mathtt{TM}}(x_n)$, Ag permittivity $\varepsilon_R(x_n)$, residuum ρ and residua lower bound $\bar{\rho}$ of the plasmonic sphere modes which dominate the scattering efficiency σ_{sca} of Fig. 4.8. The position of the peaks of the total σ_{sca} is also shown.

In Fig. 4.8, we plot σ_{sca} for a sphere of radius $R = 67.5\,\text{nm}$, with permittivity ε_R modeled by using experimental data [171]. We also show in color the partial scattering efficiencies of the two dominant plasmonic modes, viz. the fundamental electric dipole $\mathbf{u}^{\mathtt{TM}}_{\text{e}11}$ (red line) and quadrupole $\mathbf{u}^{\mathtt{TM}}_{112}$ (blue line) modes. Moreover, we list in Table 4.1 their resonant size parameters, calculated by using Eq. (4.17), the corresponding plasmonic eigen-permittivities, and the resonant frequencies, obtained from the size parameter definition $x = \frac{\omega}{c_0}R$. It is worth noting that these values do not depend on the excitation. The search interval for the resonance condition is the range

mode	x_{nl}	η_{nl}/x_{nl}^2	ω_{nl} [Prad/s]	ρ
$\mathbf{v}_{e111}^{\mathtt{TM}}$	0.21	439.90 -0.02i	0.95	3.27
$\mathbf{v}_{e121}^{\mathtt{TM}}$	0.21	726.16 -0.00i	0.95	4.75
$\mathbf{v}_{o111}^{\mathtt{TE}}$	1.41	4.39 -1.14i	6.27	1.63
$\mathbf{v}_{o121}^{\mathtt{TE}}$	0.21	441.32 -0.00i	0.95	3.28

Table 4.2 – Resonant size parameter, eigen-permittivity, and residuum ρ of the dielectric $\mathbf{v}_{e111}^{\mathtt{TM}}$, $\mathbf{v}_{e111}^{\mathtt{TM}}$, $\mathbf{v}_{o111}^{\mathtt{TE}}$, $\mathbf{v}_{o111}^{\mathtt{TE}}$ sphere modes, for an Ag sphere.

$x \in [0.21, 1.41]$, imposed by the available experimental data of the Ag permittivity in the frequency interval $[0.95, 6.26]\,$Prad/s. The table also highlights the residua $\rho\{\mathbf{u}_{e11}^{\mathtt{TM}}\}$, $\rho\{\mathbf{u}_{e12}^{\mathtt{TM}}\}$ associated to the modes' resonance, and the residua lower bound calculated at the resonant size parameters, using Eq. (4.33). The residuum assciated with the fundamental electric dipole mode exceeds 0.2: according to the definition of narrow and broad modes, given in Eq. (4.18), this mode is broad. Moreover, since the value of the residua lower bound at the resonant size parameter x_1 exceeds 0.2 itself, the mode $\mathbf{u}_{e11}^{\mathtt{TM}}$ is inherently broad, independently from the material filling the sphere. On the contrary, the fundamental electric quadrupole mode $\mathbf{u}_{e12}^{\mathtt{TM}}$ is narrow. In Table 4.1, we also show the values of the size parameters in correspondence of the two σ_{sca} peaks. The position of the first peak is slightely shifted with respect to the resonant size parameter of the first dominant mode $\mathbf{u}_{e11}^{\mathtt{TM}}$: this is due to both the coupling of the mode with the impinging plane wave, and the fact that the mode is broad. On the other hand, the position of the second peak coincides with the resonant size parameter of the second dominant mode $\mathbf{u}_{e12}^{\mathtt{TM}}$, because of its narrow resonance.

In Tables 4.2, we list the resonant size parameters, the associated eigen-permittivities, the resonant frequencies, and residua of some representative dielectric modes, viz. the fundamental $\mathbf{v}_{o111}^{\mathtt{TE}}$ and second order $\mathbf{v}_{o112}^{\mathtt{TE}}$ magnetic dipole modes, and the higher order electric dipole modes $\mathbf{v}_{e111}^{\mathtt{TM}}$, $\mathbf{v}_{e112}^{\mathtt{TM}}$. Their residua is one order of magnitude larger than the ones of the fundamental electric modes, and therefore they are all broad.

In conclusion, the power spectrum of the Ag nanospheres can be exhaustively described by considering only the fundamental electric dipole and quadrupole modes. For the considerations made in Sec. 4.4, there are no asymmetries in the σ_{sca} curve.

4.6 Resonances and interferences in Si spheres

Here we study the scattering efficiency σ_{sca} of a silicon sphere as a function of x. We employ permittivity $\varepsilon_R = 16$, non-dispersive in time. By doing so, the σ_{sca} does not depend on R and λ separately, but only on x.

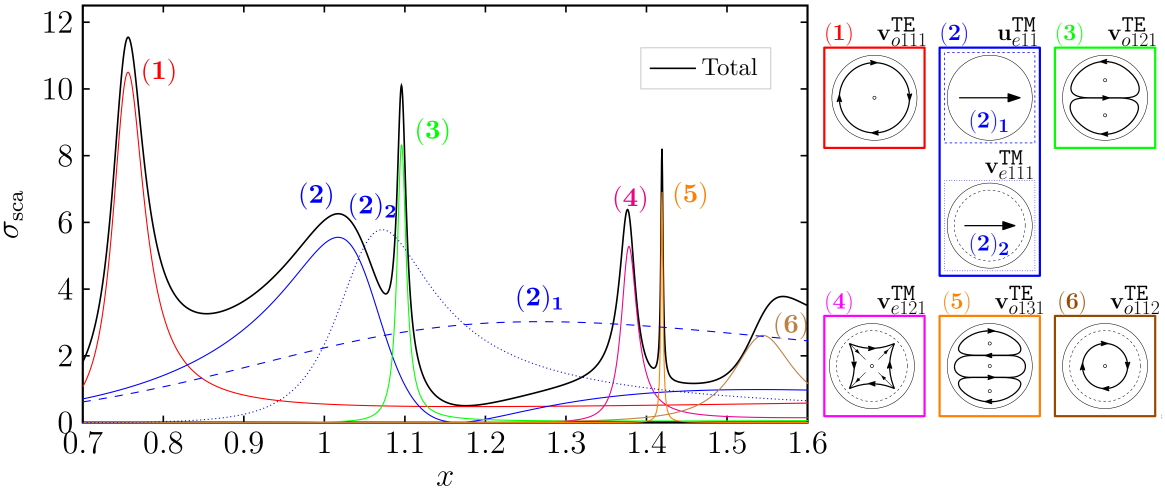

Figure 4.9 – Scattering efficiency σ_{sca} of a Si sphere, as a function of x. The partial scattering efficiencies (in color) of the seven dominant modes, and their stylized version (on the right), are also shown.

Mode	x_{res}	$\xi(x_{\mathrm{res}})$	ω_{res} [Prad/s]	ρ	$\bar{\rho}(x_{\mathrm{res}})$	#peak	x_{peak}
$\mathbf{v}^{\mathrm{TE}}_{o111}$	0.75	16.05 -1.07i	2.26	0.07	0.07	(1)	0.76
$\mathbf{u}^{\mathrm{TM}}_{e11}$	2.19	0.48 -0.97i	6.56	1.04	0.88	(2)	1.02
$\mathbf{v}^{\mathrm{TM}}_{e111}$	1.06	16.09 -2.16i	3.18	0.14	0.14	(2)	1.02
$\mathbf{v}^{\mathrm{TE}}_{o121}$	1.10	15.98 -0.21i	3.29	0.01	0.01	(3)	1.10
$\mathbf{v}^{\mathrm{TM}}_{e121}$	1.38	16.05 -0.31i	4.13	0.02	0.02	(4)	1.38
$\mathbf{v}^{\mathrm{TE}}_{o131}$	1.42	15.98 -0.04i	4.26	0.00	0.00	(5)	1.42
$\mathbf{v}^{\mathrm{TE}}_{0112}$	1.54	16.01 -0.96i	4.62	0.06	0.06	(6)	1.57

Table 4.3 – Resonant size parameter x_{res}, eigen-permittivity ξ, resonant frequency (when $R = 100\,\mathrm{nm}$), residuum ρ and residua lower bound $\bar{\rho}$ of the plasmonic sphere modes which dominate the scattering efficiency σ_{sca} of Fig. 4.9. If the mode is plasmonic, we have $\xi = \varepsilon^{\mathrm{TM}}_{n}$, while if it is dielectric $xi = \eta^{\mathrm{TM}}_{nl}/x^2$ or $\xi = \eta^{\mathrm{TE}}_{nl}/x^2$. The position of the peaks of the total σ_{sca} is also shown.

In Fig. 4.9 we plot the total σ_{sca} (black line), and the partial scattering efficiences (colored lines) of the dominant modes responsible for the σ_{sca} peaks. In Table 4.3, we list the resonant size parameters, the eigen-permittivities, the resonant frequencies (assuming $R = 100\,\mathrm{nm}$), the residua of the dominant modes, and the size parameters in correspondence of the σ_{sca} peaks. All σ_{sca} peaks but one can be attributed to the prevalent contribution of a single resonant mode. In particular, the first peak from the left occurs very closely to the resonant size parameter x_{res} of the fundamental magnetic dipole mode $\mathbf{v}_{o111}^{\mathtt{TE}}$, where its contribution is maximum. This fact is confirmed by Fig. 4.9, where the partial scattering efficiency of $\mathbf{v}_{o111}^{\mathtt{TE}}$ is also peaked in correspondence of x_{res} and it is dominant compared to the remaining partial efficiencies. Moreover, the value of the residuum associated with this resonance suggests that this mode is narrow.

Interestingly, no mode resonates in correspondence of the second peak. This peak occurs at $x = 1.02$ from the interplay between two off-resonance modes, namely the fundamental electric dipole $\mathbf{u}_{e11}^{\mathtt{TM}}$ and the second order electric dipole $\mathbf{v}_{e111}^{\mathtt{TM}}$, as demonstrated by the partial scattering efficiency of the two modes combined (solid blue line), calculated as $\sigma_{\mathrm{sca}} = |(\varepsilon_R - 1)\,(a_1^{\mathtt{TM}} + b_{11}^{\mathtt{TM}})|^2/x^2$, being $a_1^{\mathtt{TM}}$, $b_{11}^{\mathtt{TM}}$ the modes external scattering coefficients. We also plot their individual scattering efficiency, highlighting the broad and narrow characters of the fundamental and second-order dipole modes, respectively. It is worth noting that the fundamental electric dipole mode significantly contributes to the scattering efficiency along all the considered spectrum: this is due to its strong coupling with the exciting plane wave, and its strong radiation into the far field [79, 48].

In addition, the destructive interference of the fundamental and second order dipole modes according to Eq. 4.42 produces the scattering dip enclosed by the second and the third peaks at $x = 1.07$, and the corresponding Fano lineshape of σ_{sca}. In correspondence of this dip, the values of the scattering coefficients are $a_1^{\mathtt{TM}} = 1.103 - 1.343i$ and $b_{11}^{\mathtt{TM}} = 0.151 + 2.578i$.

The third peak is due to the resonance of the narrow fundamental magnetic quadrupole $\mathbf{v}_{o121}^{\mathtt{TE}}$ at its resonant size parameter $x_{\mathrm{res}} = 1.1$. Despite the close proximity of the resonance of $\mathbf{v}_{o121}^{\mathtt{TE}}$ to the preceding scattering dip, this mode cannot be held responsible for it, because of its orthogonality with the electric modes $\mathbf{u}_{e11}^{\mathtt{TM}}$ and $\mathbf{v}_{e111}^{\mathtt{TM}}$. Right after the third peak there is a dip, called *anapole* in the recent literature, which is also due the destructive interference of the fundamental and second order dipole modes.

The last three peaks are caused by the resonance of the narrow second order electric quadrupole $\mathbf{v}_{e121}^{\mathtt{TM}}$, fundamental magnetic octupole $\mathbf{v}_{o131}^{\mathtt{TE}}$, and second order magnetic dipole $\mathbf{v}_{o112}^{\mathtt{TE}}$, respectively.

It is possible to qualitatively compare the σ_{sca} of a Si nanoparticle, shown in Fig. 4.9, with the dark-field scattering spectrum measured by Kuznetsov et al. [37] for a

$R = 91\,\mathrm{nm}$ Si nanoparticle laying on a Si substrate. The experimental and theoretical peaks are found into one to one correspondence.

4.7 Conclusions

We introduced a representation of the scattered electromagnetic field from a linear, nonmagnetic, homogeneous, and isotropic object, in terms of a set of eigenfunctions of an auxiliary eigenvalue problem, which are independent of the object dielectric permittivity. We denoted them as material-independent modes.

These modes are divided into two sub-subsets, depending on their long-wavelength behaviour. They are denoted as plasmonic and dielectric modes, if in the quasistatic limit tend to the electro-quasistatic or magneto-quasistatic modes, respectively. Within this framework, we derived rigorous resonance conditions of the full-wave modes, independent from the excitation conditions. Through the resonance conditions, we defined the resonance residuum, i.e., a synthetic parameter that allows the classification of modes into broad and narrow ones, according to the resonance width. At a given resonance frequency, and hence a resonance size parameter, the lower bound for the modes residua is obtained from the sole knowledge of the corresponding eigenvalues, and thus is independent from both the material permittivity and the impinging field. This fact enables the identification of size parameter (or frequency) intervals in which the modes are inherently broad, and therefore their narrow resonance is forbidden in any material condition.

We carried out this analysis for a sphere, investigating its resonances through the material-independent mode expansion. We showed that, consistently with the quasistatic analysis in Chap. 2, the sphere plasmonic modes are the only ones resonantly excitable in a metal sphere with negative permittivity. Among them, only a subset is composed by narrow modes. Conversely, only the dielectric modes can be resonantly excited in a moderately high-index dielectric sphere, while the plasmonic modes are all broad. Therefore, since the excitable modes of metal and dielectric spheres constitute two disjoint sets, dielectric and metal nanoparticles of comparable size exhibit very different resonant behaviours.

On this basis, we were able to predict the resonance peaks in the scattering efficiency of a sphere made of either silver or silicon. In a silver sphere excited by a plane wave in the visible spectral range only the plasmonic dipolar and quadrupolar modes are resonantly excited. Among them, only the quadrupolar mode is narrow. Since they have different multipolar orders, their interference is inherently forbidden, and the scattering power spectrum has no asymmetry. On the contrary, in the case of a silicon sphere, excited by a plane wave in the visible / near-IR, the scattering power spectrum has multiple sharp peaks, most of them due to the resonant excitation of narrow dielectric modes. Interestingly, in this case, the interference between modes having the same multipolar order occurs. Specifically, the broad electric dipole plasmonic mode, which efficiently couples to the plane wave excitation, destructively interferes with the narrow higher order electric dipole (dielectric) mode, producing a Fano lineshape in the scattering power spectrum.

Chapter 5

Full-wave electromagnetic modes and hybridization in nanoparticle dimers

We investigate the resonances and modes of a sphere dimer by using the full-wave material-independent modes illustrated in the previous chapter. We describe the dimer modes in terms of the hybridization of the modes of the two constituent spheres: each dimer-mode is expressed in terms of a weighted linear combination of a set of isolated-sphere modes. The mathematical problem thus becomes a system of linear algebraic equations for the expansion coefficients. This scheme has been proposed by Bergman and Stroud [64] in 1980. However, they applied this method only in the long-wavelength limit when all radii, as well as the interparticle separations, are small compared to the wavelength outside the scatterers. The approach we propose applies to both plasmonic and dielectric dimers regardless of their size. This fact enables us to address, for the first time, the mode analysis and the hybridization in silicon dimers in the full-Maxwell regime, and to refine the understanding of plasmon-mode hybridization in a full-wave scenario.

5.1 Material-independent modes of a sphere dimer

We introduce the MIMs of a sphere dimer surrounded by vacuum. The spheres have radii R_1 and R_2, a gap size Δ, and a center-center separation D. They occupy the regions Ω_1 and Ω_2, while the surrounding space is denoted as Ω_3. We use two polar spherical reference frames centered in each sphere, and sharing the z-axis, which is also chosen as the dimer axis, as shown in Fig. 5.1. The two spheres are made of the same linear material, which is also nonmagnetic, isotropic, homogeneous in time and space, and time-dispersive. We define the dimensionless quantities

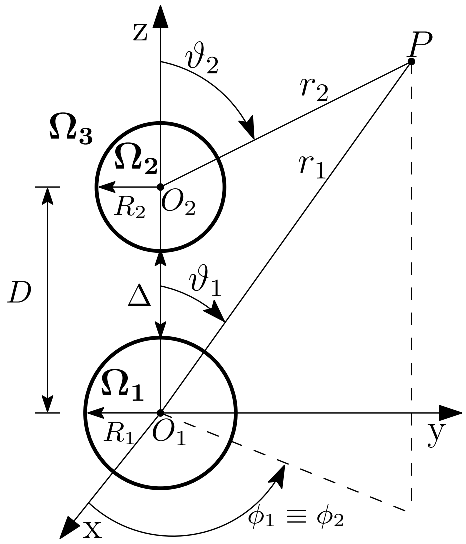

Figure 5.1 – Spherical polar coordinate systems centered on the spheres composing a dimer. The spheres have radii R_1 and R_2, edge-edge separation Δ, and center-center interparticle distance D.

$$\begin{aligned} x_1 &= \frac{\omega}{c_0} R_1, \\ x_2 &= \frac{\omega}{c_0} R_2, \\ d &= \frac{\omega}{c_0} D, \\ \delta &= \frac{\omega}{c_0} \Delta, \end{aligned} \tag{5.1}$$

and a general size parameter x

$$x = \frac{\omega}{c_0} \ell_c, \tag{5.2}$$

being ℓ_c a characteristic length of the sphere dimer, ω the operating radianfrequency.

As for the general case, introduced in Sec. 4.1, the dimer modes $\{\mathbf{w}_h\}_{h\in\mathbb{N}}$ can be subdivided into two subsets: the plasmonic subset $\{\mathbf{u}_h\}_{h\in\mathbb{N}}$ with eigen-permittivity $\{\varepsilon_h\}_{h\in\mathbb{N}}$ and the dielectric subset $\{\mathbf{v}_h\}_{h\in\mathbb{N}}$ with eigen-permittivity $\{\eta_h/x^2\}_{h\in\mathbb{N}}$.

Now we determine the modes of the dimer by using as basis functions the modes of the isolated spheres, introduced in Sec. 4.2. We denote the plasmonic modes of the j-th sphere as $\mathbf{u}_{pmn}^{\mathtt{TM}|j}$, and its dielectric modes as $\{\mathbf{v}_{pmnl}^{\mathtt{TM}|j}\}$ with $j \in \{1, 2\}$. Then, for the generic dimer mode we have (see Sec. D.1 in Appendix D):

$$\mathbf{w}_{pmq}(\mathbf{r}) = \sum_{\substack{n=\\ \max(1,m)}}^{\infty} \left\{ c^{\mathtt{TM}|j}_{pmq\,n}\, \mathbf{u}^{\mathtt{TM}|j}_{pmn}(\mathbf{r}) + \sum_{l=1}^{\infty} \left[d^{\mathtt{TM}|j}_{pmq\,nl}\, \mathbf{v}^{\mathtt{TM}|j}_{pmnl}(\mathbf{r}) + d^{\mathtt{TE}|j}_{\bar{p}mq\,nl}\, \mathbf{v}^{\mathtt{TE}|j}_{\bar{p}mnl}(\mathbf{r}) \right] \right\} \; \forall \mathbf{r} \in \Omega_j, \tag{5.3}$$

with $j = 1, 2$, $\mathbf{w}_{pmq} = \{\mathbf{u}_{pmq}, \mathbf{v}_{pmq}\}$, and $c^{\mathtt{TM}|j}_{pmq\,n}$, $d^{\mathtt{TM}|j}_{pmq\,nl}$, $d^{\mathtt{TE}|j}_{\bar{p}mq\,nl}$, are the projections of the dimer mode on the j-th single-sphere mode

$$\begin{aligned} c^{\mathtt{TM}|j}_{pmq\,n} &= \mathcal{P}_j \left\{ \mathbf{u}^{\mathtt{TM}|j}_{pmn}, \mathbf{w}_{pmq} \right\}, \\ d^{\mathtt{TM}|j}_{pmq\,nl} &= \mathcal{P}_j \left\{ \mathbf{v}^{\mathtt{TM}|j}_{pmnl}, \mathbf{w}_{pmq} \right\}, \\ d^{\mathtt{TE}|j}_{\bar{p}mq\,nl} &= \mathcal{P}_j \left\{ \mathbf{v}^{\mathtt{TE}|j}_{\bar{p}mnl}, \mathbf{w}_{pmq} \right\}, \end{aligned} \tag{5.4}$$

where,

$$\mathcal{P}_j \left\{ \mathbf{A}, \mathbf{B} \right\} = \frac{\langle \mathbf{A}, \mathbf{B} \rangle_{\Omega_1 \cup \Omega_2}}{\langle \mathbf{A}, \mathbf{A} \rangle_{\Omega_1 \cup \Omega_2}}, \tag{5.5}$$

with $\langle \mathbf{A}, \mathbf{B} \rangle_{\Omega_1 \cup \Omega_2} = \displaystyle\int_{\Omega_1 \cup \Omega_2} \mathbf{A} \cdot \mathbf{B} dV$. As shown in Sec. D.1 of Appendix D, the mathematical problem of determining such modes becomes a system of linear algebraic equations for the expansion coefficients $c^{\mathtt{TM}|j}_{pmq\,n}$, $d^{\mathtt{TM}|j}_{pmq\,nl}$, $d^{\mathtt{TE}|j}_{\bar{p}mq\,nl}$ [140, 64], whose explicit expression is given in Eq. D.16.

The dimer modes depend on three indices: $p \in \{e, o\}$ (in Eq. (5.3) the symbol $\bar{p}$ indicates the complement of p), $m \in \mathbb{N}_0$, and $q \in \mathbb{N}$. Due to the azimuthal symmetry, the dimer eigen-permittivities depend only on the indices $\{m, q\}$. In the limit $x \to 0$ the plasmonic eigen-permittivities ε_{mq} and the dielectric quantities η_{mq} are sorted in ascending order of magnitude, for any given m (e.g., $\lim_{x \to 0} \varepsilon_{m1} > \lim_{x \to 0} \varepsilon_{m2}$, or $\lim_{x \to 0} \eta_{m1} < \lim_{x \to 0} \eta_{m2}$). The same order is kept for finite values of x, by following the eigen-permittivities on the complex plane as x varies.

An intrinsic property of the structure is the splitting of the spectrum, independently from the dimension of the spheres: as the particles approach from a large distance ($d \gg \max\{x_1, x_2\}$), any single-sphere eigenvalue degenerates into two different eigenvalues. For instance, we will see in Sec. 5.2.1 that, for an homo-dimer, the fundamental electric dipole eigenvalue $\varepsilon_1^{\mathtt{TM}}$ turns into the ones related to the *bonding* and *antibonding* dipole modes [89].

In order to weight the contribution of the single-sphere modes $\mathbf{u}^{\mathtt{TM}|j}_{pmn}$, $\mathbf{v}^{\mathtt{TM}|j}_{pmnl}$, $\mathbf{v}^{\mathtt{TE}|j}_{pmnl}$ of the j-th sphere in the expansion (5.3) of the dimer mode $\mathbf{w}_{pmq}$, we introduce the following synthetic parameters:

$$
\begin{aligned}
\tilde{h}^{\mathtt{TM}|j}_{pmq\,n} &= \max_{\mathbf{r}\in\Omega_1\cup\Omega_2} \left|\mathrm{Re}\left\{c^{\mathtt{TM}|j}_{pmq\,n}\mathbf{u}^{\mathtt{TM}|j}_{pmn}\left(\mathbf{r}\right)\right\}\right|, \\
h^{\mathtt{TM}|j}_{pmq\,nl} &= \max_{\mathbf{r}\in\Omega_1\cup\Omega_2} \left|\mathrm{Re}\left\{d^{\mathtt{TM}|j}_{pmq\,nl}\mathbf{v}^{\mathtt{TM}|j}_{pmn}\left(\mathbf{r}\right)\right\}\right|, \\
h^{\mathtt{TE}|j}_{\bar{p}mq\,nl} &= \max_{\mathbf{r}\in\Omega_1\cup\Omega_2} \left|\mathrm{Re}\left\{d^{\mathtt{TE}|j}_{\bar{p}mq\,nl}\mathbf{v}^{\mathtt{TE}|j}_{\bar{p}mn}\left(\mathbf{r}\right)\right\}\right|.
\end{aligned}
\tag{5.6}
$$

The parameter $\tilde{h}^{\mathtt{TM}|j}_{pmq\,n}$, $h^{\mathtt{TM}|j}_{pmq\,nl}$, or $h^{\mathtt{TE}|j}_{\bar{p}mq\,nl}$ represents the maximum magnitude of the real part of the dimer mode within the j-th sphere (which corresponds to the amplitude at $t = 0$) that we would have if only the mode $\mathbf{u}^{\mathtt{TM}|j}_{pmn}$, $\mathbf{v}^{\mathtt{TM}|j}_{pmnl}$, or $\mathbf{v}^{\mathtt{TE}|j}_{\bar{p}mnl}$ in the expansion (5.3) were considered, respectively. In the following sections, for any given dimer mode $\mathbf{w}_{pmq}$ we normalize the parameters $\tilde{h}^{\mathtt{TM}|j}_{pmq\,n}$, $h^{\mathtt{TM}|j}_{pmq\,nl}$, $h^{\mathtt{TE}|j}_{\bar{p}mq\,nl}$ to the overall maximum, i.e., $\max\limits_{nl}\left\{\tilde{h}^{\mathtt{TM}|j}_{pmq\,n},\, h^{\mathtt{TM}|j}_{pmq\,nl},\, h^{\mathtt{TE}|j}_{\bar{p}mq\,nl}\right\}$. These normalized parameters will be denoted as

$$
\begin{aligned}
\tilde{H}^{\alpha|\mathtt{TM}|j}_{pmq\,nl} &= \frac{\tilde{h}^{\mathtt{TM}|j}_{pmq\,n}}{\max\limits_{nl}\left\{\tilde{h}^{\mathtt{TM}|j}_{pmq\,n},\, h^{\mathtt{TM}|j}_{pmq\,nl},\, h^{\mathtt{TE}|j}_{\bar{p}mq\,nl}\right\}}, \\
H^{\alpha|\mathtt{TM}|j}_{pmq\,nl} &= \frac{h^{\mathtt{TM}|j}_{pmq\,nl}}{\max\limits_{nl}\left\{\tilde{h}^{\mathtt{TM}|j}_{pmq\,n},\, h^{\mathtt{TM}|j}_{pmq\,nl},\, h^{\mathtt{TE}|j}_{\bar{p}mq\,nl}\right\}}, \\
H^{\alpha|\mathtt{TE}|j}_{\bar{p}mq\,nl} &= \frac{h^{\mathtt{TE}|j}_{\bar{p}mq\,nl}}{\max\limits_{nl}\left\{\tilde{h}^{\mathtt{TM}|j}_{pmq\,n},\, h^{\mathtt{TM}|j}_{pmq\,nl},\, h^{\mathtt{TE}|j}_{\bar{p}mq\,nl}\right\}},
\end{aligned}
\tag{5.7}
$$

with $\alpha \in \{\|, \perp\}$ according to whether the dimer mode is plasmonic ($\mathbf{w}_{pmq} \rightarrow \mathbf{u}_{pmq}$) or dielectric ($\mathbf{w}_{pmq} \rightarrow \mathbf{v}_{pmq}$), respectively. We call them *hybridization weights.*

From now on, for the sake of simplicity, we will only deal with homo-dimers, i.e., with the case $R_1 = R_2 = R$. In this configuration, due to the structure symmetry, we have that $\tilde{H}^{\alpha|\mathtt{TM}}_{pmq\,nl} = \tilde{H}^{\alpha|\mathtt{TM}|1}_{pmq\,nl} = \tilde{H}^{\alpha|\mathtt{TM}|2}_{pmq\,nl}$, $H^{\alpha|\mathtt{TM}}_{pmq\,nl} = H^{\alpha|\mathtt{TM}|1}_{pmq\,nl} = H^{\alpha|\mathtt{TM}|2}_{pmq\,nl}$, and $H^{\alpha|\mathtt{TE}}_{pmq\,nl} = H^{\alpha|\mathtt{TE}|1}_{pmq\,nl} = H^{\alpha|\mathtt{TE}|2}_{pmq\,nl}$. Furthermore, we choose as characteristic length ℓ_c, the spheres' radius R, i.e., $\ell_c = R$, and hence the structure size parameter x will be $x = \frac{\omega}{c_0}R$.

5.2 Modes hybridization

The sphere dimer MIMs in Eq. (5.3) are expressed in terms of a weighted linear combination of the single-sphere modes, namely in terms of the *hybridization* of the modes of the dimer's building blocks. By varying the arrangement of the constituent spheres, i.e., their distance, the single-sphere modes do not change: the only varying quantities are the expansion coefficients in Eq. (5.4), or equivalently the hybridization weights in Eq. (5.7). Thus, in order to monitor the behavior of the dimer modes by varying the constituent spheres' arrangement, we have to follow the expansion coefficients or the hybridization weights. On the other hand, if we fix the dimer geometry, i.e., the spheres radius R and the separation Δ, and vary the operation frequency ω, or, in other words, we keep fixed the ratio Δ/R and vary the size parameter x, both the expansion coefficients and the single-sphere modes vary and need to be recalculated.

As shown in Sec. 4.3 for a single sphere, the loci spanned by the structure's eigen-permittivities in the complex plane as a function of a parameter, constitute an invaluable tool to investigate the structure's resonances. In the specific case of a sphere homo-dimer, we have two scenarios: the first one consists in fixing the sphere radius and the operating frequency, and varying the interparticle separation; the second one consists in fixing the structure geometry, and varying the size parameter x (or the frequency).

In the following two sections, we consider the first scenario. Specifically, we investigate the hybridization of three representative sphere modes, viz. the fundamental electric dipole mode $\mathbf{u}^{\mathtt{TM}}_{pm1}$, the second ($l = 1$) order electric dipole mode $\mathbf{v}^{\mathtt{TM}}_{pm11}$, and the fundamental magnetic dipole mode $\mathbf{v}^{\mathtt{TE}}_{pm11}$, for two choices of size parameter x: $x = \pi/100$, and hence $R \ll \lambda$, and $x = 2\pi$, and hence $R = \lambda$. We investigate the dimer eigen-permittivity behavior moving the spheres from the configuration in which they are very far from each other ($\delta \gg x$) to the one in which they are relatively close ($\delta < x$). In the first configuration, the spheres interaction vanishes, and therefore the dimer eigen-permittivities simply degenerate into the single-sphere ones. In this way, we are able to identify the single-sphere eigen-permittivities and follow their transformation as the interparticle separation decreases.

5.2.1 Quasistatic hybridization

Here, we examine the case of a dimer of spheres of dimension much smaller than the wavelength λ, namely for $x = \pi/100$, that can be described by the quasistatic framework introduced in Chap. 2. In Fig. 5.2, we monitor the dimer eigenvalues by varying the dimensionless gap size δ from π to $\pi/200$. In particular, we start from the limit case $\delta \to \infty$, in which the dimer eigenvalues approach the quasi-static single-sphere eigenvalues $\varepsilon^{\mathtt{TM}}_{1}$, $\eta^{\mathtt{TM}}_{11}$, and $\eta^{\mathtt{TE}}_{11}$, for the azimuthal quantum numbers $m = 0, 1$. We then consider the shift of three selected dimer eigenvalues as the gap distance decreases with respect to the corresponding isolated sphere one. As δ decreases, two branches depart from all considered single-sphere eigenvalues, for both the azimuthal numbers $m = 0, 1$: one branch exhibits a negative shift, which we denote as the lower

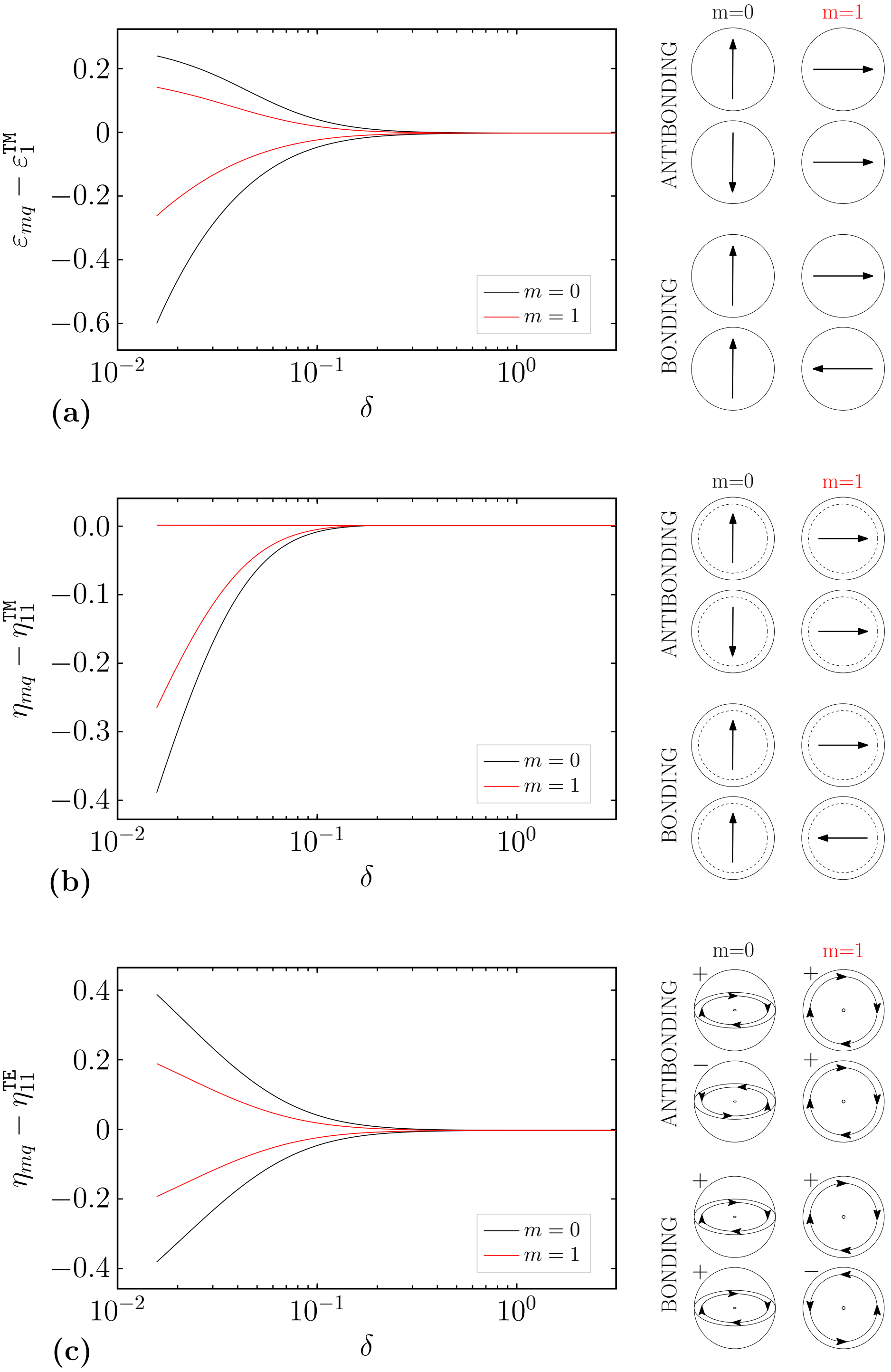

Figure 5.2 – Dimer eigenvalues as a function of the dimensionless edge-edge separation δ. Branches departing from the single-sphere plasmonic fundamental electric dipole eigen-permittivity $\varepsilon_1^{\mathtt{TM}}$ (**a**), dielectric second-order electric dipole quantity $\eta_{11}^{\mathtt{TM}}$ (**b**), dielectric fundamental magnetic dipole quantity $\eta_{11}^{\mathtt{TE}}$ (**c**). The quantity $\eta_{11}^{\mathtt{TM}}$ ($\eta_{11}^{\mathtt{TE}}$), normalized by the squared size parameter x^2, give the second-order electric (fundamental magnetic) dipole eigen-permittivity. On the right, the stylized version of the corresponding modes is also shown.

branch, and the other shifts in the opposite way, and we denote it as the upper branch. From the definition of the electrostatic energy of the EQS modes in Eq. (2.22), and of the magnetostatic energy of the MQS modes in Eq. (2.32), associated with the dimer eigenvalues, the lower branch corresponds to lower energy configurations, while the upper branch corresponds to higher energy configurations. Furthermore, it can be shown that the nature of the dimer modes corresponding to the branches does not change as δ decreases: the single-sphere modes remain almost unaltered in the dimer structure. Thus, on the right of Fig. 5.2, we represent the dimer modes using the stylized version of the single-sphere modes, depicted in Fig. 4.2.

In panel (a) we display the two branches departing from the fundamental electric dipole eigenvalue $\varepsilon_1^{\mathtt{TM}}$, which in the electro-quasistatic regime $x \to 0$ is $\varepsilon_1^{\mathtt{TM}} = \chi_1^{\parallel} + 1 = -2$. For $m = 0$, the dimer modes associated with the lower branch correspond to the interaction of two co-aligned electric dipoles, while the modes associated with the upper branch correspond to the counter-directed dipoles. Following Prodan and Nordlander [88, 89], we denote the former configuration (lower energy) as *bonding*, and the latter (higher energy) as *antibonding*. For $m = 1$, the coupling of the fundamental dipole modes has opposite sign with respect to the case $m = 0$: the antibonding dimer modes are the combination of two co-oriented fundamental dipole modes, while the bonding dimer modes correspond to the negative parity of the dipole modes. This is in agreement with Nordlander et al. [89].

In panel (b) we show the branches departing from a dielectric eigenvalue, namely, the second-order electric dipole quantity $\eta_{11}^{\mathtt{TM}}$ (also known as *toroidal* dipole), which if normalized by x^2 gives the corresponding eigen-permittivity. In the magnetoquasistatic regime $x \to 0$, it has the expression $\eta_{11}^{\mathtt{TM}} = \kappa_{11}^{\mathtt{TM}\perp} = z_{1,1}^2 = 20.19$, where $z_{n,l}$ is the l-th zero of the spherical bessel function j_n. Both the lower branches for $m = 0, 1$ shift downward much faster than the upper branches shift upward: the latters remain very close to the isolated sphere $\eta_{11}^{\mathtt{TM}}$. The assignment of the bonding and antibonding configuration follows the same rules of the fundamental electric dipole modes hybridization: for $m = 0$, the bonding configuration is constituted by co-oriented dipoles, while the antibonding one is constituted by the negative parity of the dipole modes; the opposite happens for $m = 1$.

In panel (c) we examine the case of the fundamental magnetic dipole quantity $\eta_{11}^{\mathtt{TE}}$, which has the expression $\eta_{11}^{\mathtt{TE}} = \kappa_{11}^{\mathtt{TE}\perp} = z_{0,1}^2 = 9.87$. For $m = 0$, the bonding mode is due to the combination of two in-phase fundamental magnetic dipole modes $\mathbf{v}_{e011}^{\mathtt{TE}}$, whose magnetic dipole is directed along the dimer axis, and therefore they are represented with current loops lying in the spheres' equatorial plane. Instead, the antibonding mode is the interaction of two fundamental magnetic dipole modes with negative parity. As in the aforementioned scenarios, for $m = 1$ the parity of the dipole moments of the bonding and antibonding modes is reversed with respect to the case $m = 0$.

5.2.2 Full-wave hybridization

We now investigate the case of a dimer of spheres of radius R equal to the wavelength, i.e., for $x = 2\pi$, for which a full-wave description is needed. When $\delta \to \infty$ the dimer eigenvalues approach the isolated sphere eigenvalues. In Fig. 5.3, we plot the loci spanned in the complex plane by the dimer eigenvalues originating from the single-sphere eigenvalues $\varepsilon_1^{\mathtt{TM}} = 0.17 - 0.08i$, $\eta_{11}^{\mathtt{TM}} = 29.55 - 12.78i$, and $\eta_{11}^{\mathtt{TE}} = 17.54 - 6.80i$, for the azimuthal quantum numbers $m = 0, 1$, by varying the dimensionless gap size δ from 18π to $\pi/100$.

As in the quasistatic case, because of the splitting property of the spectrum, two branches depart from all single-sphere eigenvalues as δ decreases. In this case, both branches' trajectories start as spiral curves, moving farther away as they revolve around the single-sphere eigenvalues. Similarly to the quasistatic scenario in Fig. 5.2, the dimer modes corresponding to the beginning of each branch are simply symmetric and antisymmetric combinations of the single-sphere modes. In Fig. 5.3, we plot the branches of the symmetric dimer modes with black curves, while the branches of the antisymmetric modes with red ones. Moreover, to better follow the dimer eigenvalues as δ varies, we add to the branches depicted in Fig. 5.3 dot marks in correspondence of selected values of gap size $\delta = k\pi$, for $k = 1, \ldots, 18$.

In Fig. 5.3(a-b) we plot the dimer plasmonic eigen-permittivity branches departing from the single-sphere eigen-permittivity $\varepsilon_1^{\mathtt{TM}}$, for $m = 0$, 1, respectively. In both cases, all branches' dynamics occur very closely to $\varepsilon_1^{\mathtt{TM}}$, and far from other single-sphere eigen-permittivities: as we will see for the branches emanating from $\eta_{11}^{\mathtt{TM}}$ and $\eta_{11}^{\mathtt{TE}}$ for $m = 1$, the proximity of the single-sphere eigenvalues in the complex plane to the dimer loci not only influences their trajectory, but also it has a key role in the hybridization process. In the case under exam, the absence of nearby single-sphere eigen-permittivities results in a negligible hybridization: the nature of the dimer modes corresponding to the two branches is preserved as δ decreases, and the single-sphere modes remain almost unaltered in the dimer configuration, as confirmed by Fig. 5.4, in which we display the considered dimer mode for $m = 0$ (panel a) and $m = 1$ (panel b) at $\delta = 18\pi$ (beginning of the branch), and $\delta = \pi/100$ (end of the branch). Thus, in both cases $m = 0, 1$, the dimer modes corresponding to the two whole branches can be simply represented as symmetric and antisimmetric combina-

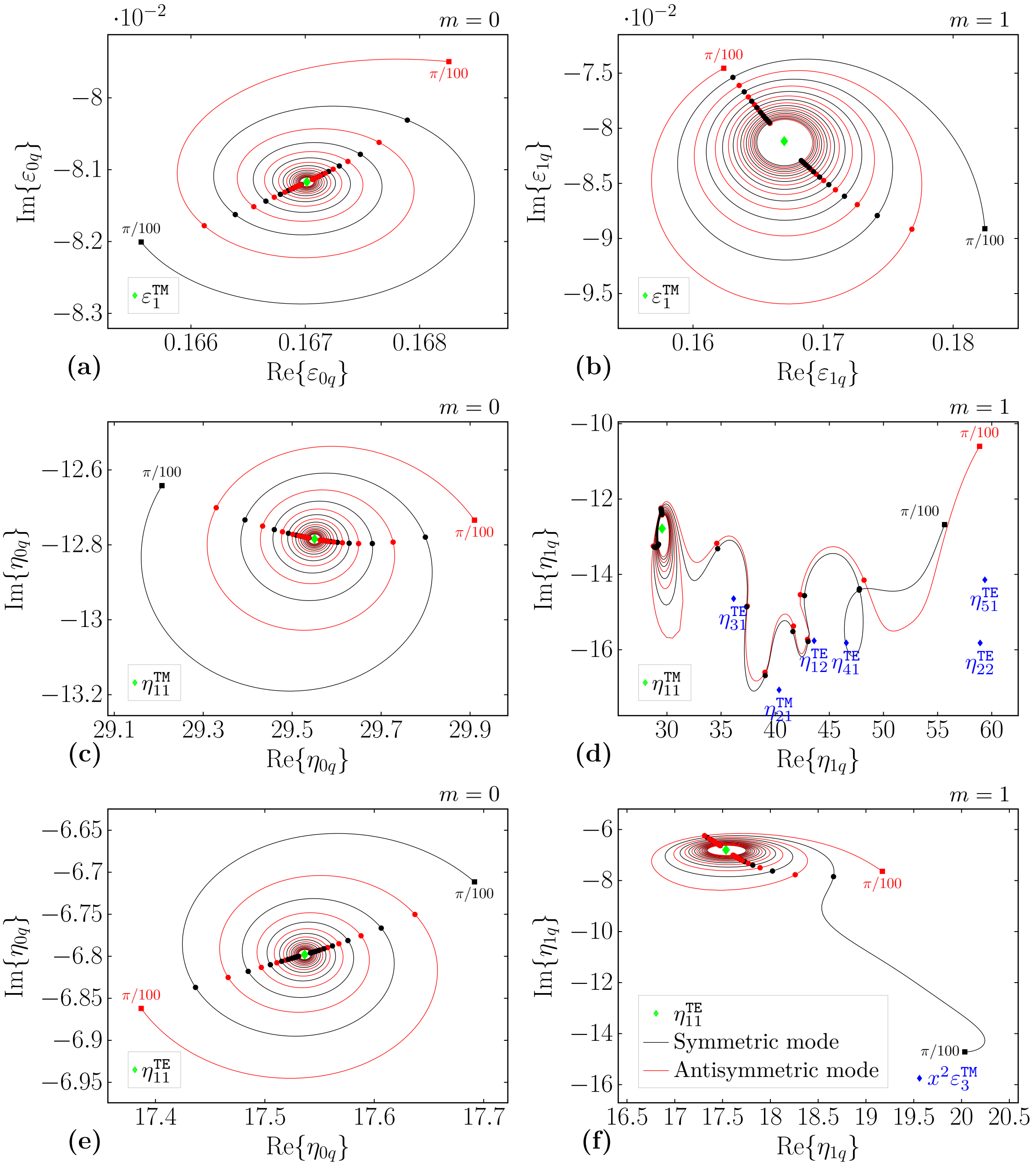

Figure 5.3 – Loci spanned in the complex plane by the eigenvalues of a sphere dimer with $x = 2\pi$ ($R = \lambda$), by varying the dimensionless gap size $\delta \in [\pi/100, 18\pi]$. The loci originate from the single-sphere fundamental electric dipole eigen-permittivity $\varepsilon_1^{\mathrm{TM}}$, for $m = 0$ (**a**) and $m = 1$ (**b**), second order electric dipole quantity η_{11}^{TM}, for $m = 0$ (**c**) and $m = 1$ (**d**), and fundamental magnetic dipole quantity η_{11}^{TE}, for $m = 0$ (**e**) and $m = 1$ (**f**). The dot marks are placed in correspondence of $\delta = k\pi$, for $k = 1, \ldots, 18$. The branch corresponding to the symmetric (antisymmetric) mode configuration is plotted with a black (red) line. The single-sphere eigenvalues, origin of the loci, are plotted with green marks, while the others with blue marks.

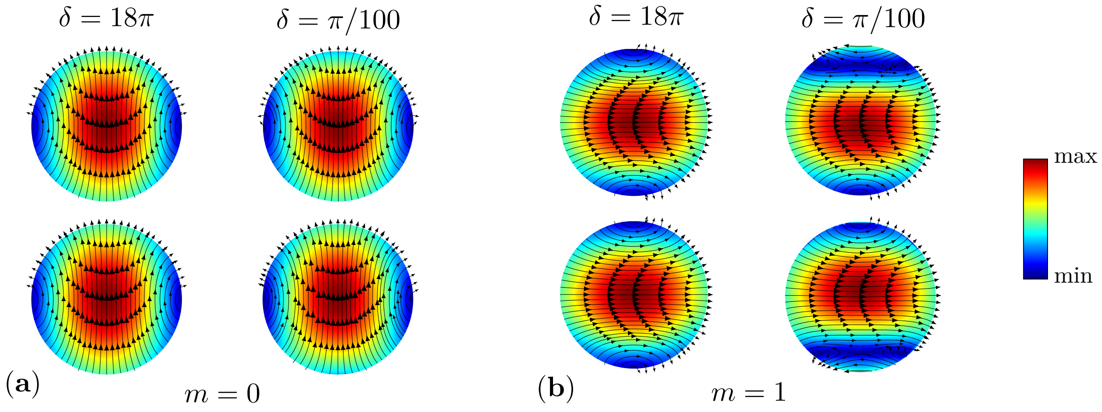

Figure 5.4 – Real part of the projection on the $y = 0$ plane of the dimer mode corresponding to the symmetric branch (black line) emanating from the single-sphere fundamental electric dipole eigen-permittivity $\varepsilon_1^{\mathtt{TM}}$ for $m = 0$ (**a**) and $m = 1$ (**b**), at $\delta = 18\pi$ and $\delta = \pi/100$.

tions of fundamental electric dipole modes $\mathbf{u}_{pm1}^{\mathtt{TM}}$, as in the quasistatic case sketched on the right of Fig. 5.2a.

For $m = 0$ (panel a), the minimum magnitude of the imaginary part is reached by the antisymmetric branch at the value $0.168 - 0.079i$, for the minimum considered distance, i.e., $\delta = \pi/100$. At the same δ, the symmetric branch reaches the value $0.166 - 0.082i$, with an higher magnitude of the imaginary part. From Eq. (4.9b), we recall that the imaginary part of a structure eigen-permittivity accounts for the radiating losses of the corresponding mode. This means that for the considered distance $\delta = \pi/100$, and hence very close spheres, the symmetric configuration has higher radiation losses than the antisymmetric one: this is due to the constructive interference of the fundamental dipole modes of the two spheres, which have a center-to-center distance D approximately equal to 2λ. Following the spiral trajectories, at $\delta = \pi$ (first dot on the branch trajectories), the assignment of the configuration of greater radiation losses is reversed: the dimer eigen-permittivity belonging to the antisymmetric branch has an imaginary part magnitude greater than the one belonging to the symmetric branch. From $\delta = \pi/100$ to this case $\delta = \pi$, the center-to-center distance has increased by $\lambda/2$: now the symmetric fundamental dipole modes interfere destructively, while the antisymmetric dipole modes interfere constructively. Then, every time the edge-edge distance δ is increased by π, the dimer eigen-permittivities will all make half a turn on the spirals until eventually they reach the single-sphere eigenvalue. It is important to point out that due to the modes spatial profile, different from the one of simple point dipoles placed at the spheres center, the minima and maxima for the imaginary part are not reached at δ equal to multiples of π, but are delayed by 0.32π, i.e., the maxima and minima for the imaginary part occur at approximately $\delta \approx (0.32 + k)\pi$, $k \in \mathbb{N}_0$.

The loci originating from $\varepsilon_1^{\mathtt{TM}}$ for $m = 1$ (panel b) follow a dynamics very similar to the case $m = 0$. This time, the antisymmetric configuration reaches the maximum for the imaginary part magnitude for $\delta = 0.82\pi$ at the value $0.167 - 0.096i$. Instead, the symmetric dimer mode reaches the minimum for $\delta = 0.66\pi$ at the value $0.169-0.074i$. Increasing the dimensionless gap size δ by multiples of π, the imaginary part of the dimer eigen-permittivities oscillates between its maximum and minimum until the branches degenerate into the single-sphere eigen-permittivities. From the same considerations made for $m = 0$, the minima and maxima for the imaginary part do not coincide with δ equal to multiples of π.

In Fig. 5.3(c-d) we plot the dimer dielectric branches departing from the single-sphere quantity $\eta_{11}^{\mathtt{TM}}$ (second order electric dipole or *toroidal* dipole), for $m = 0, 1$, respectively. The branches for $m = 0$ (panel c) are again spirals emanating from $\eta_{11}^{\mathtt{TM}}$, but they occupy a region in the complex plane wider than the aforementioned dimer plasmonic eigen-permittivities. Moreover, their trajectories are not influenced by any other single-sphere eigenvalue, and no other mode (different from the considered second order electric dipole) comes into play in the hybridization process. Thus, as for the plasmonic eigen-permittivities, the nature of the dimer modes corresponding to the two branches is preserved as δ decreases, and the single sphere modes remain unchanged in the dimer configuration. Hence, the dimer modes corresponding to the entire branches can be simply represented as symmetric and antisymmetric combinations of second-order electric dipole modes $\mathbf{v}_{p011}^{\mathtt{TM}}$, as on the right of Fig. 5.2b.

The symmetric branch reaches the maximum for the imaginary part magnitude at $29.494 - 13.186i$, for $\delta = 0.51\pi$. At the same distance, the antisymmetric branch achieves its minimum for the imaginary part magnitude, and therefore the corresponding mode has the minimum radiation losses. As for the examined plasmonic dielectric eigen-permittivities, every π added to the dimensionless gap size δ will let the dimer eigenvalues make half a turn on the spirals until they asymptotically approach the spirals center $\eta_{11}^{\mathtt{TM}}$.

The case $m = 1$ (panel b) is characterized by a very different dynamics. For $\delta \gtrapprox 8\pi$ both the branches remain close to $\eta_{11}^{\mathtt{TM}}$, while for smaller distances they move toward greater values for the real part, following paths unravelling among several single sphere eigenvalues. We now discuss the properties of the antisymmetric branch, with the aid of Fig. 5.5, where we show the corresponding dimer mode at four representative distances $\delta = 18\pi$, 6π, 2π, π. To the right of the dimer mode, we display the single-sphere modes involved in the hybridization, on top of their hybridization

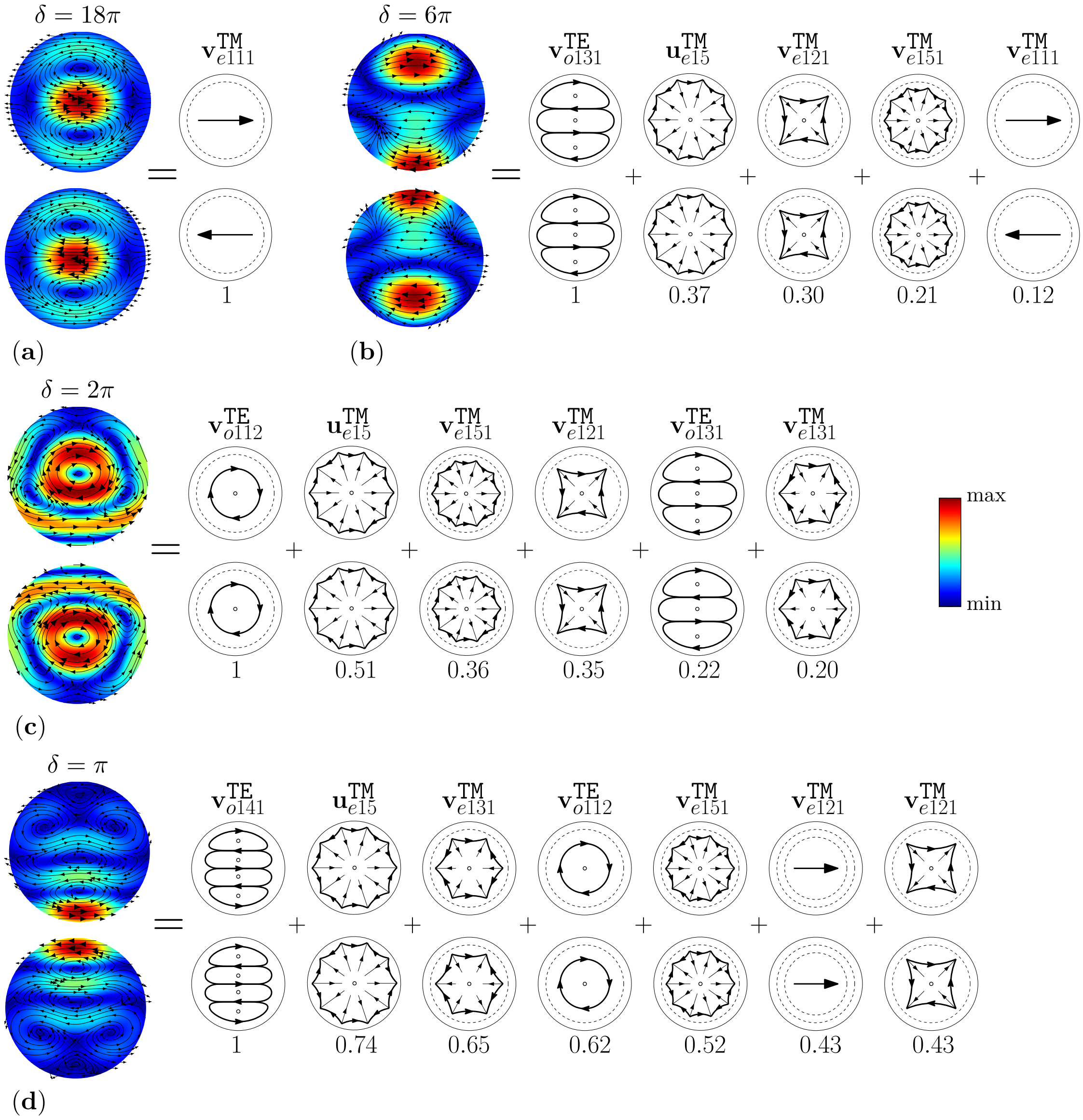

Figure 5.5 – Decomposition of the dimer mode corresponding to the antisymmetric branch (red line, Fig. 5.3d) emanating from the single-sphere second order electric dipole quantity $\eta_{11}^{\mathtt{TM}}$, in terms of hybridizing single-sphere modes, for the dimensionless gap sizes $\delta = 18\pi$ (**a**), $\delta = 6\pi$ (**b**), $\delta = 2\pi$ (**c**), and $\delta = \pi/100$ (**d**). The real part of the projection on the $y = 0$ plane of the dimer mode is shown. Below each stylized version of the single-sphere mode we also show its hybridization weight, defined in Eq. (5.7).

weights, defined in Eq. (5.7).

At $\delta = 18\pi$, the dimer eigenvalue is very close to $\eta_{11}^{\mathtt{TM}}$, and it corresponds to a dimer mode resulting from the simple antisymmetric combination of the spheres' second-order electric dipole modes $\mathbf{v}_{e111}^{\mathtt{TM}}$. In this case, no other modes are involved in the hybridization, as confirmed by Fig. 5.5a. After following a spiral trajectory around

$\eta^{\mathtt{TM}}_{11}$, the dimer locus passes very close to the single-sphere dielectric quantity $\eta^{\mathtt{TE}}_{31}$ at $\delta = 6\pi$. As shown in Fig. 5.5b, the corresponding dimer mode is significantly different from the one at $\delta = 18\pi$, and now the hybridization mechanism is relevant. In particular, the single-sphere mode $\mathbf{v}^{\mathtt{TE}}_{o131}$ corresponding to the encountered eigenvalue $\eta^{\mathtt{TE}}_{31}$ is dominant among all other single-sphere modes in the hybridization mechanism, as testified by their hybridization weights. A significant contribution comes also from the fundamental electric dotriacontapole $\mathbf{u}^{\mathtt{TM}}_{e15}$, second-order electric quadrupole $\mathbf{v}^{\mathtt{TM}}_{e121}$, second-order electric dotriacontapole $\mathbf{v}^{\mathtt{TM}}_{e151}$. Interestingly, the eigenvalues corresponding to these single-sphere modes are not close to the considered dimer eigenvalue. Furthermore, the second-order electric dipole mode $\mathbf{v}^{\mathtt{TM}}_{e111}$, from whose eigenvalue this locus has originated, has a very low hybridization weight, and therefore its effect in the dimer mode expansion is almost negligible.

Decreasing δ, the antisymmetric branch passes close to $\eta^{\mathtt{TM}}_{21}$ at $\delta \approx 5\pi$, and then to $\eta^{\mathtt{TE}}_{12}$ at $\delta \approx 3\pi$. At $\delta = 2\pi$, the dimer eigenvalue remains in proximity of $\eta^{\mathtt{TE}}_{12}$, and the corresponding dimer mode is shown in Fig. 5.5c. Also in this case, the dominant single-sphere mode in the dimer mode expansion is the mode corresponding to the closest single-sphere eigenvalue, i.e., the second order magnetic dipole mode $\mathbf{v}^{\mathtt{TE}}_{o112}$. The other modes involved in the hybridization are the fundamental and second order electric dotriacontapole $\mathbf{u}^{\mathtt{TM}}_{e15}$, $\mathbf{v}^{\mathtt{TM}}_{e151}$, second-order electric quadrupole $\mathbf{v}^{\mathtt{TM}}_{e121}$, fundamental magnetic octupole $\mathbf{v}^{\mathtt{TE}}_{o131}$, and second order electric octupole $\mathbf{v}^{\mathtt{TM}}_{e131}$.

Further decreasing δ to $\delta = \pi$, the branch is in proximity of $\eta^{\mathtt{TE}}_{41}$. At this dimensionless gap size, we show the corresponding dimer mode in Fig. 5.5d, for which the dominant single-sphere mode is the fundamental magnetic hexadecapole $\mathbf{v}^{\mathtt{TE}}_{o141}$, corresponding to the closest single-sphere eigenvalue. Unlike the other investigated scenarios, at this distance the dimer mode arises from the hybridization of many ($>$15) single-sphere modes, whose eigenvalues are relatively distant from the dimer branch. In particular, the most relevant modes are the fundamental and second order electric dotriacontapole $\mathbf{u}^{\mathtt{TM}}_{e15}$, $\mathbf{v}^{\mathtt{TM}}_{e151}$, second order electric octupole $\mathbf{v}^{\mathtt{TM}}_{e131}$ and quadrupole $\mathbf{v}^{\mathtt{TM}}_{e121}$, second order magnetic dipole $\mathbf{v}^{\mathtt{TE}}_{0112}$, and the third order electric dipole $\mathbf{v}^{\mathtt{TM}}_{e112}$.

For smaller δ, the branch passes near $\eta^{\mathtt{TE}}_{22}$, $\eta^{\mathtt{TE}}_{51}$ for $\delta \approx 0.67\pi$, 0.56π, respectively, and eventually, for $\delta = \pi/100$ it achieves the maximum for the imaginary part at the value $58.53 - 10.78i$.

The symmetric branch unwinds closely to the antisymmetric one, until $\delta \approx 2\pi$. On the other hand, its parametrization does not follow the one of the symmetric branch, but is delayed by exactly π: a point reached by the symmetric branch at δ is approached by the antisymmetric branch at $\delta + \pi$. At $\delta = 2\pi$, the symmetric branch assumes the value $23.90 - 7.20i$ and then follows a loop that closes at $\delta = 3\pi$:

there exist two distinct values of δ, namely $\delta = 2\pi$, 3π, which correspond to the same dimer eigen-permittivity. In other words, there exist two dimers of spheres of the same dimension, but at different distances, which share the same eigen-permittivity originating from the single-sphere $\eta_{11}^{\mathtt{TM}}$. As we will see in the next section, loops can also occur in the eigen-permittivity loci of a sphere dimer with fixed geometry by varying the size parameter x. Furthermore, this noose-like shape has been also observed in the plasmonic and dielectric eigen-permittivities of other structures, e.g., the coated sphere [76].

At $\delta < 2\pi$, the symmetric branch moves toward greater values for the imaginary part, until it assumes the value $55.58 - 12.72i$ at $\delta = \pi/100$.

In Fig. 5.3(e-f) we follow the two branches of dimer dielectric eigenvalues emanating from the single-sphere eigenvalue $\eta_{11}^{\mathtt{TE}}$, associated to the fundamental magnetic dipole mode, for $m = 0$, 1, respectively. Both the branches for $m = 0$ (panel c) are spirals departing from $\eta_{11}^{\mathtt{TE}}$, and their trajectories are not influenced by any other single-sphere eigenvalue, and no other mode is involved in the hybridization process. Thus, the dimer modes corresponding to the entire branches can be simply represented as symmetric and antisymmetric combinations of fundamental magnetic dipole modes $\mathbf{v}_{e011}^{\mathtt{TE}}$, as on the right of Fig. 5.2c. The antisymmetric branch achieves the maximum imaginary part magnitude at the value $17.5233 - 6.9458i$ for $\delta = 0.36\pi$. At the same distance, the symmetric branch reaches the minimum imaginary part magnitude at the value $17.53 - 6.66i$. As the other examined eigen-permittivities, by raising δ of multiples of π, the dimer eigenvalues will make half a turn on the spirals until they asymptotically approach $\eta_{11}^{\mathtt{TE}}$.

In the case $m = 1$ (panel d), the branches are still spirals, but for subwavelengths gaps $\delta \lessapprox \pi$ the two branches follow different trajectories. The antisymmetric branch remains close to the isolated sphere eigenvalue $\eta_{11}^{\mathtt{TE}}$, and far from other singles-sphere eigenvalues, and no other mode is involved in the hybridization process in this case. Conversely, the symmetric branch moves toward lower imaginary parts, and eventually achieves the value $20.07 - 14.66i$ at $\pi/100$, very close to the (normalized with x^2) eigen-permittivity $\varepsilon_3^{\mathtt{TM}}$. Thus, for very close spheres, the single-sphere fundamental electric octupole mode $\mathbf{u}_{p13}^{\mathtt{TM}}$ dominates the hybridization for the dimer mode originating from the fundamental magnetic dipole eigenvalue $\eta_{11}^{\mathtt{TE}}$.

5.3 Resonance properties

We now investigate the plasmonic and dielectric eigen-permittivities behavior of a sphere dimer of fixed relative gap size, by varying the size parameter x. In particular, we consider a dimer of spheres with radius R and gap size $\Delta = R/4$. As anticipated in Sec. 4.1 for the general case, all dimer plasmonic eigen-permittivities ε_{mq} tend to a negative finite value for $x \to 0$, while they tend to 0 for $x \to \infty$. Instead, the dielectric quantities η_{mq} tend to different finite real and positive values for $x \to 0$ and $x \to \infty$. As discussed in Sec.2.1.2, in the long-wavelength limit ($x \ll 1$), the eigen-permittivities associated to η_{mq} diverge, and therefore the associated modes cannot be practically excited in electrically small metal dimers, but only in dimers with positive and high permittivity.

Contrarily to the scenario examined in the previous sections, in which the size parameter x is fixed and the interparticle separation varies, in this case, the modes associated with the eigen-permittivity loci result from the hybridization of single-sphere modes that change with the parameter x.

In Fig. 5.6(a-b), we display the loci spanned by the first two plasmonic eigen-permittivities ε_{m1}, ε_{m2}, for $m = 0$ (panel a) and $m = 1$ (panel b). For $x \ll 1$, the eigen-permittivity ε_{01} approaches the real value -3.17 predicted by the electro-quasistatic approximation. The corresponding dimer mode is shown on the left of Fig. 5.7a. By increasing x, both the real and imaginary part of ε_{01} move toward more negative values. The decrease in the real part implies, for low loss Drude metals, a red shift of the corresponding resonant frequency [1], as shown in Sec. 2.2.2 with Eq. (2.60). When $x \approx 0.55$, the quantity $\operatorname{Re}\{\varepsilon_{01}\}$ reaches a minimum value of -4.66, and then starts increasing. For $x \gtrapprox \pi/3$, ε_{01} lies in the fourth quadrant of the complex plane. Then, $\operatorname{Re}\{\varepsilon_{01}\}$ increases until $x \approx 1.5$ when it reaches the maximum value of 0.49, and finally ε_{01} asymptotically reaches the origin of the complex plane.

The eigen-permittivity ε_{02} starts at the real value -1.82 (consistent with the electro-quasistatic prediction), and then features a similar dynamics to ε_{01}: it reaches a minimum value for the real part (-4.24) at $x = 1.48$, then a maximum (1.18) at $x = 2.13$, and eventually it asymptotically approaches the origin of the complex plane. The corresponding dimer mode in the limit $x \to 0$ is shown on the right of Fig. 5.7a. The main difference with the case $q = 1$ is that the locus of ε_{01} is swept with higher speed than the locus for ε_{02}, as the parameter x varies. This can be easily visualized in Fig. 5.6(a) by following the position of an eigen-permittivity for a fixed x as the order q varies: the eigen-permittivity at $x = \pi/5$, for instance, distinctly moves toward the beginning of the locus as q increases.

For $m = 1$, the eigen-permittivities ε_{11} and ε_{12} approach the values -2.48 and -1.76, respectively, for $x \ll 1$. Their corresponding dimer mode is plotted in Fig. 5.7b. By increasing x, they develop a dynamics of the same nature of the $m = 0$ counterpart. Moreover, as for the $m = 0$ case, the loci are swept with decreasing

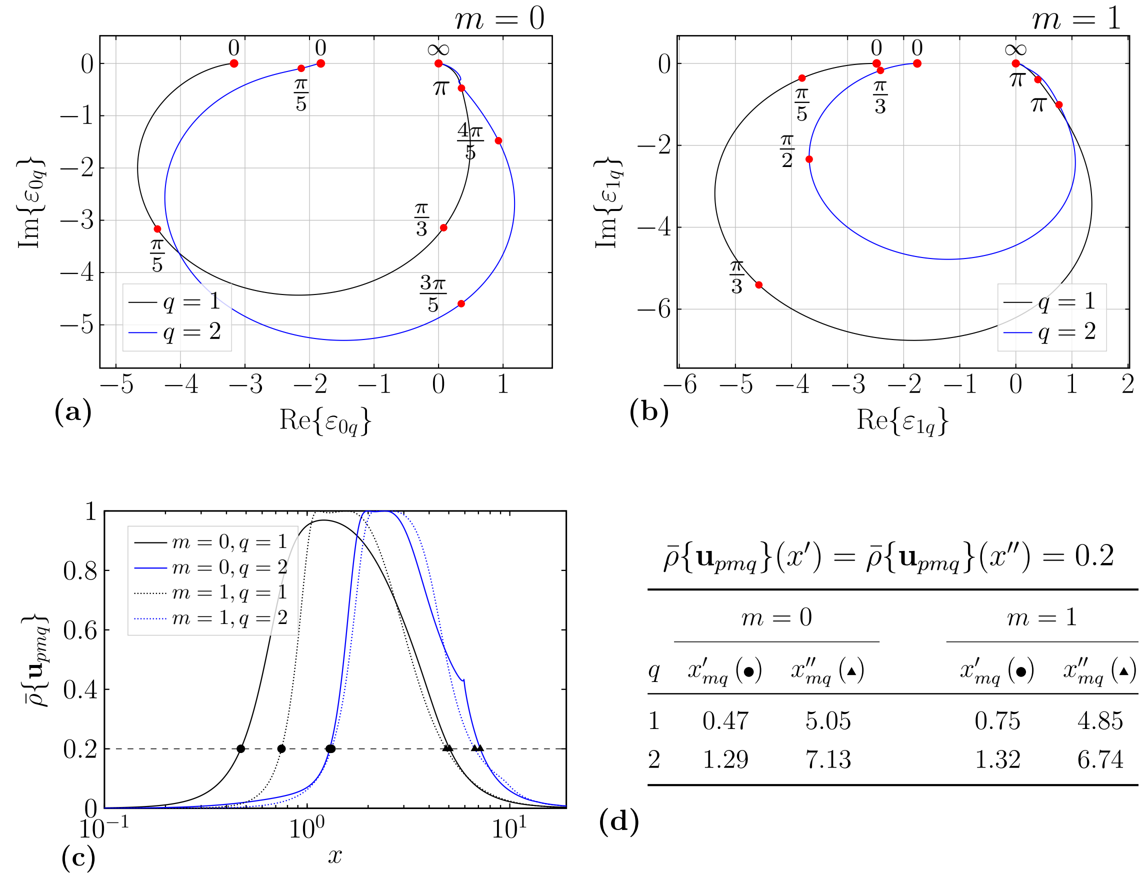

$\bar{\rho}\{\mathbf{u}_{pmq}\}(x') = \bar{\rho}\{\mathbf{u}_{pmq}\}(x'') = 0.2$

	$m = 0$		$m = 1$	
q	x'_{mq} (●)	x''_{mq} (▲)	x'_{mq} (●)	x''_{mq} (▲)
1	0.47	5.05	0.75	4.85
2	1.29	7.13	1.32	6.74

Figure 5.6 – Loci spanned in the complex plane by the plasmonic eigen-permittivities ε_{m1}, ε_{m2} of a dimer of spheres with radius R and gap $\Delta = R/4$, by varying $x \in [0, \infty)$, for $m = 0$ (**a**) and $m = 1$ (**b**). The corresponding modes in the limit $x \to 0$ are shown in Fig. 5.7. Residua lower bounds of the corresponding modes (**c**), and the values x'_{mq}, x''_{mq} at which the residua lower bounds reach the value 0.2 (**d**).

speed of parametrization with the order q. Interestingly, unlike the case of the single sphere, investigated in Sec. 4.3.1, the locus corresponding to the higher order ε_{12} is wider than the one for the lower order ε_{11}.

In Fig. 5.6c, we plot the lower bounds $\bar{\rho}\{\mathbf{u}_{pmq}\}$ for the residua associated with the resonances of the plasmonic modes under exam as a function of x. We recall that the mode residuum ρ, introduced in Sec. 4.1.1 in Eq. (4.17), is associated to the width of the corresponding resonance: if $\rho > 0.2$ the mode is broad, otherwise it is narrow. The lower bound $\bar{\rho}$ for the plasmonic modes has the same expression as for the sphere in Eq. (4.33), and it is independent of the dimer material. In the table in Fig. 5.6d, we list the values x'_{mq}, x''_{mq} at which $\bar{\rho} = 0.2$ for each considered mode. These values are the extremes of an interval of size parameters in which the modes

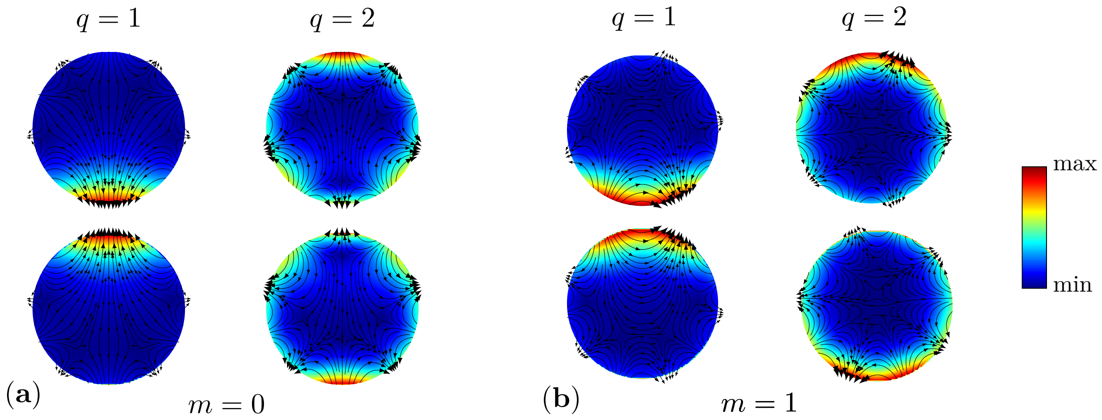

Figure 5.7 – Projection on the $y = 0$ plane of the dimer modes $\mathbf{u}_{emq}$, $q = 1, 2$, for $m = 0$ (**a**) and $m = 1$ (**a**) in the limit $x \to 0$, whose eigenvalue loci in the complex plane as a function of x are plotted in Fig. 5.6(a-b).

cannot be narrowly excited. For instance, in a sphere dimer with gap $\Delta = R/4$, a narrow resonance of the mode $\mathbf{u}_{p01}$ for $0.47 \leq x \leq 5.05$, or equivalently for a dimer of spheres with radius R such that $0.07\lambda \leq R \leq 0.80\lambda$, is inherently forbidden.

For any m, as a consequence of the decreasing speed of parametrization in the eigen-permittivity loci with the order q, the corresponding residua curves, and hence the broad-resonances interval, shift toward larger x.

All loci spanned by the eigen-permittivities under exam are confined in a limited region of the complex plane. From the same considerations made for the single sphere in Sec. 4.3.1, the considered modes are broad in sphere dimers with moderately positive permittivity, e.g., silicon, while they can be narrowly excited in metal dimers (e.g., silver or aluminium) in the visible spectral range.

In Fig. 5.8, we show the loci spanned in the complex plane by the first two dielectric quantities η_{m1}, η_{m2}, for $m = 0$ (panel a) and $m = 1$ (panel b). In the long wavelength limit $x \ll 1$, the quantities η_{01}, η_{02} approach the real values 9.35, 10.4, respectively, consistently with a magneto-quasistatic description. The corresponding dimer modes are shown in Fig. 5.9a. By increasing x, they feature a very similar dynamics. In fact, at first, both the real and imaginary parts of η_{01}, η_{02} move toward more negative values: from Eq. (2.87), this results in a red shift in the corresponding resonant frequency in high index materials. Then, their real part increases until both the eigenvalues asymptotically reach the real axis at the value 20.21. The speed of parametrization in the considered loci, this time, is comparable.

We now discuss the case $m = 1$. The dimer modes corresponding to η_{11} and η_{12} are shown in Fig. 5.9b. The quantity η_{11} starts at the value 9.61, reaches the

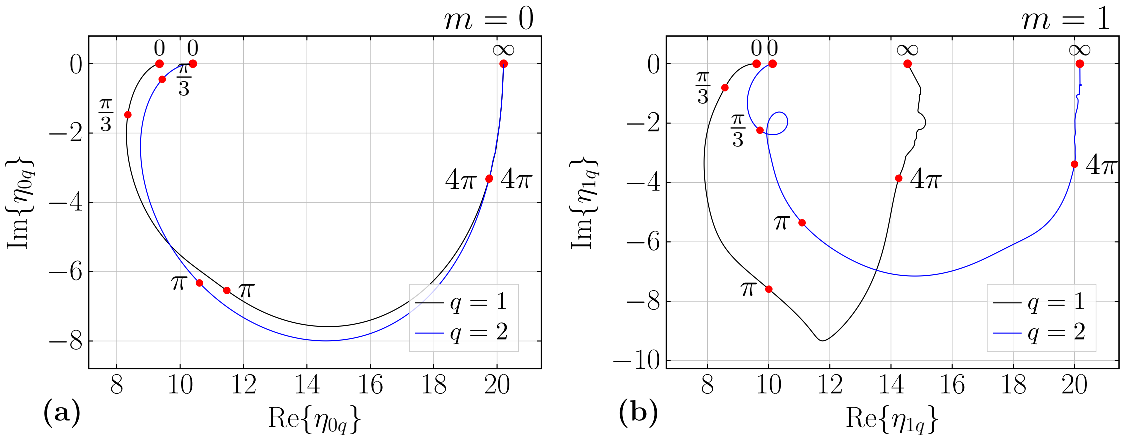

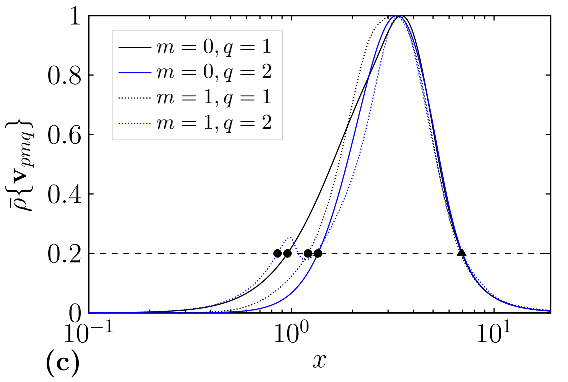

$\bar{\rho}\{\mathbf{v}_{pmq}\}(x') = \bar{\rho}\{\mathbf{v}_{pmq}\}(x'') = 0.2$

	$m = 0$		$m = 1$	
q	x'_{mq} (●)	x''_{mq} (▲)	x'_{mq} (●)	x''_{mq} (▲)
1	0.96	6.96	1.21	6.85
2	1.35	6.96	0.85	6.96

(d)

Figure 5.8 – Loci spanned in the complex plane by the dielectric quantities η_{m1}, η_{m2} of a dimer of spheres with radius R and gap $\Delta = R/4$, by varying $x \in [0, \infty)$, for $m = 0$ (**a**) and (**b**). η_{mq}, if normalized with the squared size parameter x^2 give the dimer dielectric eigen-permittivities. Residua lower bounds of the corresponding modes (**c**), and the values x'_{mq}, x''_{mq} at which the residua lower bounds reach the value 0.2 (**d**).

minimum for the real part at $x = 1.85$ for Re$\{\eta_{11}\} = 7.89$, and the minimum for the imaginary part at $x = 4.36$ for Im$\{\eta_{11}\} = -9.33$. Eventually, both the real and imaginary parts increase till η_{11} reaches the real axis at $\eta_{11} = 14.54$.

The quantity η_{12} approaches the value 10.13 in the long wavelength limit $x \ll 1$. After the usual decrease in the real and imaginary part, the locus follows a loop: there exist two distinct values of x, namely 0.67 and 1.62, which correspond to the same $\eta_{12} = 9.94 - 2.36i$. In other words, there exist two sphere dimers with gap $\Delta = R/4$, but with different radius (or operating frequency), which share the same value of η_{12}. Then, the locus reaches a minimum for the imaginary part at $x = 5.07$ for Im$\{\eta_{12}\} = -7.15$, and eventually, in the limit $x \to \infty$, it tends to the real value $\eta_{12} = 20.18$.

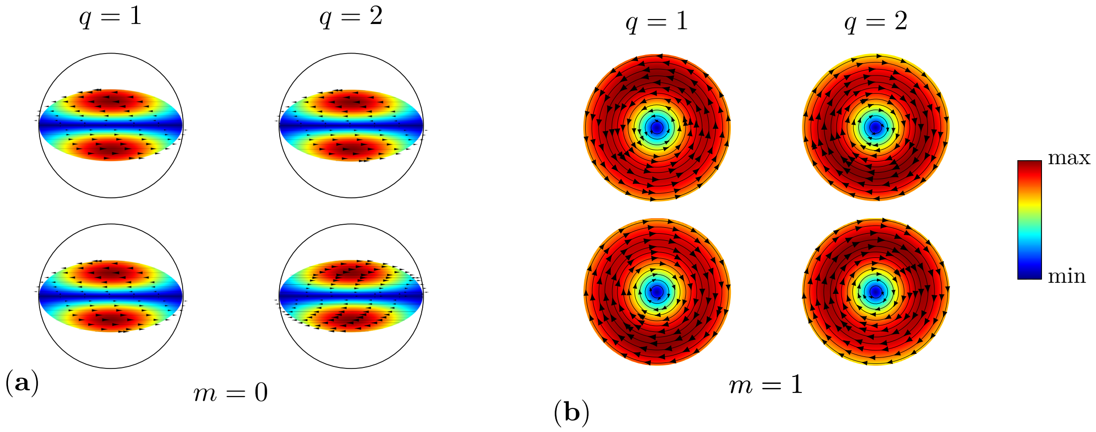

Figure 5.9 – (**a**) Projection on the spheres' equatorial plane of the dimer modes $\mathbf{v}o0q$, for $q = 1, 2$, in the limit $x \to 0$. (**b**) Projection on the $y = 0$ plane of the dimer modes $\mathbf{v}e1q$, for $q = 1, 2$, in the limit $x \to 0$. They correspond to the eigenvalues of the loci plotted in Figs. 5.8a and 5.8b, respectively, in the quasistatic limit $x \to 0$.

In Fig. 5.8c, we plot the lower bounds $\bar{\rho}\{\mathbf{v}_{pmq}\}$ for the residua associated with the resonances of the considered dielectric modes, as a function of x, calculated by applying Eq. (4.37). In the table in Fig. 5.8d, we list the extremes x'_{mq}, x''_{mq} of the size parameter intervals in which the modes are inherently broad. We notice, for instance, that a narrow resonance of the mode $\mathbf{v}_{p02}$ for $1.35 \leq x \leq 6.96$, or equivalently $0.21\lambda \leq R \leq 1.12\lambda$, is intrinsically forbidden. Since the dielectric loci under exam are similar, and the speed of parametrization is comparable, the residua lower bound curves are almost superimposed. Interestingly, the loop in the locus of η_{12} results in a small sub-interval $[1.08, 1.31]$ of size parameters (not shown in the table in Fig. 5.8d), in which the narrow resonance of the mode $\mathbf{v}_{p12}$ is allowed.

Contrarily to the plasmonic modes, the examined dielectric modes can be narrowly excited in sphere dimers of permittivity with positive real part, while they can only lead to broad resonances in materials with permittivity of negative real part, such as Ag or Au.

5.4 Full wave hybridization in Ag and Si dimers

We consider an homo-dimer with $R_1 = R_2 = R$ ($x = x_1 = x_2$), and two different edge-edge separations of $\Delta = R/4$ and $\Delta = R$, corresponding to a center-center separation of $D = 9/4R$ and $\Delta = 3R$, respectively. We vary the size parameter x in the interval $[0.6, 1.7]$. The total number of considered dimer modes is $N = 1600$, with $q = 1, \ldots, 320$, $m = 0, \ldots, 4$, $p = e$. Nevertheless, in each of the considered scenarios, the scattering is dominated by different subsets of dimer modes whose number is much smaller than N. The single-sphere modes used to represent the dimer modes are $\mathbf{u}^{\mathtt{TM}}_{emn}$, $\mathbf{v}^{\mathtt{TM}}_{emnl}$, $\mathbf{v}^{\mathtt{TE}}_{omnl}$ with $n = 1, \ldots, 8$, $l = 1, \ldots, 10$, and $m = 1, \ldots, 4$.

5.4.1 Transversely polarized Ag dimer

First, we study a silver homo-dimer with $R = 67.5\,\mathrm{nm}$, and edge-edge separation $\Delta = R/4 = 16.875\,\mathrm{nm}$. We model the silver permittivity $\varepsilon_{R,Ag}$ by using experimental data [169, 171], while we employ a constant non-dispersive in time permittivity $\varepsilon_{R,Si} = 16$ for the silicon [168]. We consider the modes that are excited by an incident field $\mathbf{E}_{\text{inc}}$ that is polarized along the dimer axis $\hat{\mathbf{z}}$, while it is propagating along the transverse direction $\hat{\mathbf{x}}$ (see Fig. 5.1), i.e., $\mathbf{E}_{\text{inc}} = E_0 e^{i\frac{\omega}{c_0}z}\hat{\mathbf{x}}$.

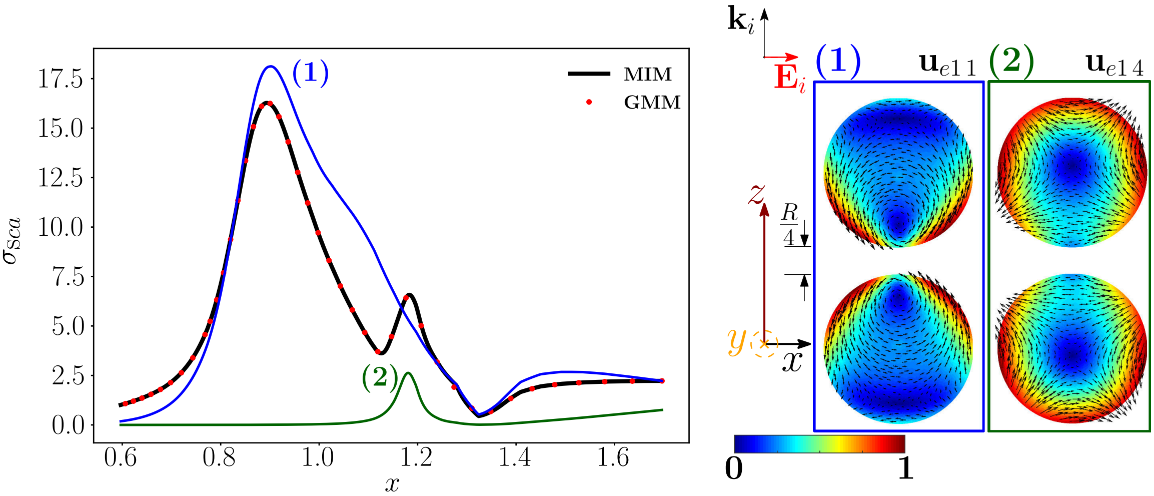

Figure 5.10 – Scattering efficiency σ_{sca} of an Ag homo-dimer as a function of the size parameter x, obtained via material-independent-mode expansion (black line) and by direct-calculation (red dots). The radius of each sphere is $R = 67.5\,\mathrm{nm}$, the edge-edge distance $\Delta = R/4 = 16.9\,\mathrm{nm}$. The dimer is excited by a plane wave propagating along the dimer's axis and polarized along the transverse direction. Partial scattering efficiency (in color) of two dominant dimer modes whose $y = 0$ plane projections are shown on the right.

In Fig. 5.10, we plot the scattering efficiency σ_{sca} obtained by using the material-independent-mode expansion (4.16) (black line), and by a direct calculation (red dots) as a function of the size parameter x. For the direct calculation, we use the code "Generalized Multiparticle Mie solution (GMM)" by Yu-lin Xu [172]. Specifically, we use in the GMM two VSWF sets centered in the two spheres, each of them described by Eq. (4) of Ref. [172] with $1 < n \leq 8$. The two results are in very good agreement. As expected, the scattering efficiency is significantly different from the one obtained in the quasi-electrostatic limit approximation [71] which is shown in Fig. D.1b in

Appendix D. We also show in color the partial scattering efficiencies of the dimer modes $\mathbf{u}_{e1\,1}$, $\mathbf{u}_{e1\,4}$ dominating the scattering response. Their projections (real part) on the $y = 0$ plane are represented on the right. The partial scattering efficiency is the scattering efficiency that we would have if only one dimer mode is excited at a time. It is important to note that the total scattering efficiency is not the sum of the partial scattering efficiencies because the modes with same index m may interfere. Nevertheless, the partial scattering efficiencies enable us to identify the dimer modes responsible for each peak of the total scattering efficiency.

mode	x_{emq}	ω_{emq} [Prad/s]	ε_{mq}	$\varepsilon_{R,Ag}$	ρ_{emq}	$\bar{\rho}_{emq}$	#peak	x_{peak}
$\mathbf{u}_{e1\,1}$	0.85	3.76	-5.35-2.80i	-9.88 + 0.31i	0.505	0.403	(1)	0.89
$\mathbf{u}_{e1\,4}$	1.17	5.22	-2.18-0.22i	-2.33 + 0.26i	0.15	0.07	(2)	1.18

Table 5.1 – Resonant size parameter x, corresponding value of the resonant frequency, eigen-permittivity, Ag permittivity, residuum and residua lower bounds of the dimer modes which dominate the scattering efficiency of Fig. 5.10. The positions of the peaks of the total scattering efficiency are also shown.

We list in Tab. 5.1 the values of the resonant size parameter x of the two dominant modes, together with the corresponding resonant frequency, eigen-permittivity, Ag permittivity, residuum, and residua lower bound. The resonant frequencies are obtained through the relation $\omega = \frac{c_0}{R} x$.

It is apparent that the two resonant frequencies are in very close proximity to the two σ_{sca} peaks, namely $x = 0.892$ and $x = 1.183$. The modes residua and their lower bounds tell us that the mode $\mathbf{u}_{e1\,1}$ is inherently broad, while $\mathbf{u}_{e1\,4}$ is narrow: this is consistent with the fact that the first partial scattering efficiency has a broader peak than the second one. As in the Ag single sphere (Fig. 4.8), and in the longitudinally polarized Ag dimer (see Fig. D.4 in Appendix D), the relevant dimer modes are all plasmonic.

In Fig. D.2 in Appendix D, we also plot within the two spheres the scattered electric field calculated at the two σ_{sca} peaks. The effects of the field propagation along the dimer axis are now important.

The dimer mode $\mathbf{u}_{e1\,1}$, responsible for the first σ_{sca} peak, originates from the hybridization of the single-sphere modes shown in Fig. 5.11. In particular, the fundamental electric dipole $\mathbf{u}_{e11}^{\text{TM}}$ and quadrupole $\mathbf{u}_{e12}^{\text{TM}}$ interact destructively in the close proximity of the gap. On the contrary, in the regions on the left and on the right of the dimer gap, the fundamental quadrupole $\mathbf{u}_{e12}^{\text{TM}}$, octupole $\mathbf{u}_{e13}^{\text{TM}}$, hexadecapole $\mathbf{u}_{e14}^{\text{TM}}$ interact constructively, determining a maximum in intensity.

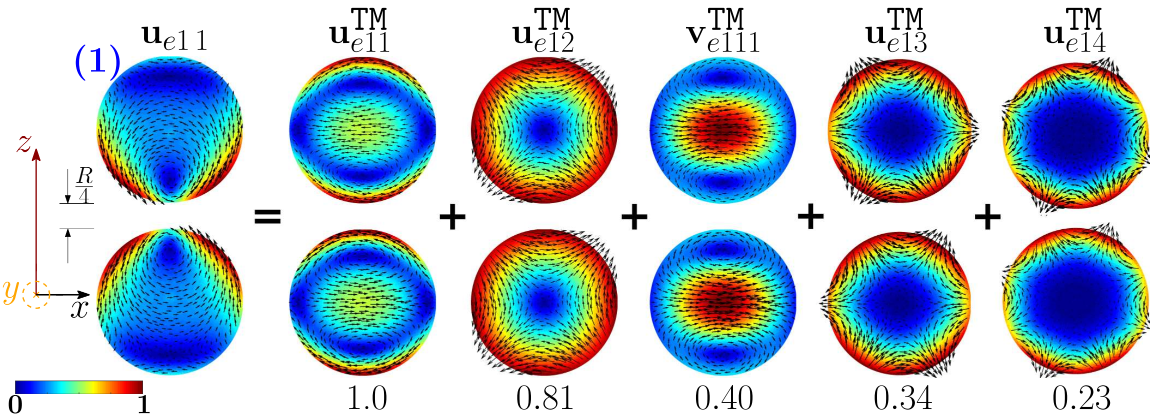

Figure 5.11 – Decomposition of the dimer mode $\mathbf{u}_{e1\,1}$ at $x = 0.892$ in terms of hybridizing single-sphere modes (real part of the projection on the $y = 0$ plane). Each single-sphere modes is multiplied by the expansion coefficients of Eq. (5.4). Below each single-sphere mode we also show its hybridization weight $\tilde{H}^{|||\mathtt{TM}}_{e11\,nl}$ ($H^{|||\mathtt{TM}}_{e11\,nl}$), defined in Eq. (5.7).

The mode $\mathbf{u}_{e1\,1}$ has a zero total dipole moment and it cannot be excited by a plane wave in the quasielectrostatic approximation. Nonetheless, in the presented full-Maxwell scenario its coupling to the plane-wave is different from zero. This is because the center-center distance between the two spheres is approximately one-third of the wavelength: thus the incident wavelength undergoes a phase inversion during its propagation within the dimer. The quasielectrostatic approximation also fails to predict the scattering efficiency (Fig. D.1b in Appendix D): the quasielectrostatic σ_{sca} features one peak which is due to the mode $\mathbf{u}_{e1\,2}$ characterized by field lines all oriented in the same direction.

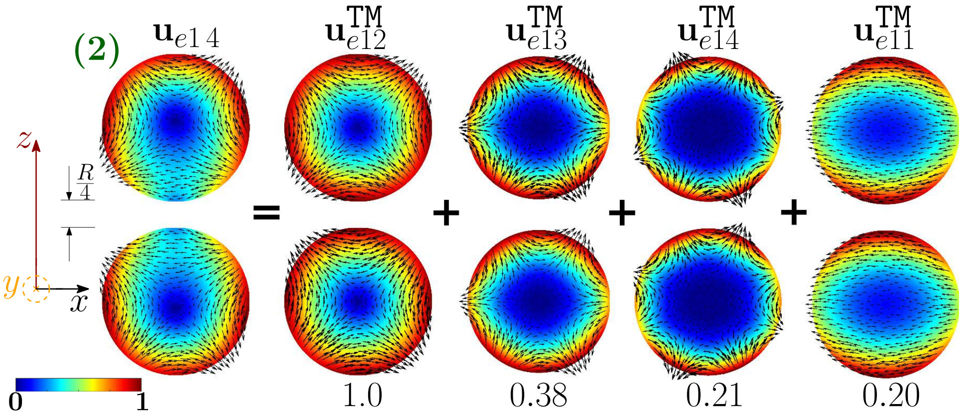

Figure 5.12 – Decomposition of the dimer mode $\mathbf{u}_{e1\,4}$ at $x = 1.183$, in terms of hybridizing single-sphere modes (real part of the projection on the $y = 0$ plane). Each single-sphere modes is multiplied by the expansion coefficients of Eq. (5.4). Below each single-sphere mode we also show its hybridization weight $\tilde{H}^{|||\mathtt{TM}}_{e14\,nl}$, defined in Eq. (5.7).

The dimer mode $\mathbf{u}_{e1\,4}$, which is behind the second σ_{sca} peak, arises from the interaction among the single-sphere modes shown in Fig. 5.12. The fundamental electric quadrupole $\mathbf{u}_{e12}^{\mathtt{TM}}$ and octupole $\mathbf{u}_{e13}^{\mathtt{TM}}$ interact destructively in the proximity of the gap and constructively within the region of each sphere opposite to the gap. A minor contribution to the hybridization process also comes from $\mathbf{u}_{e14}^{\mathtt{TM}}$ and $\mathbf{u}_{e11}^{\mathtt{TM}}$.

As the edge-edge distance between the two spheres increases to R the scattering efficiency changes (Fig. D.6 in Appendix D). The first σ_{sca} peak is even more dominated by the fundamental electric dipole (Fig. D.7 in Appendix D). The mode responsible for the second peak remains the fundamental electric quadrupole (Fig. D.8 in Appendix D).

5.4.2 Longitudinally polarized Si dimer

Now, we study the scattering from a homo-dimer of the same geometry but made of silicon, with permittivity $\varepsilon_R = 16$. We investigate the modes excited by a plane wave $\mathbf{E}_{\text{inc}}$ polarized along the dimer axis $\hat{\mathbf{z}}$, while it is propagating along the transverse direction $\hat{\mathbf{x}}$, i.e., $\mathbf{E}_{\text{inc}} = E_0 e^{i\frac{\omega}{c_0}x}\hat{\mathbf{z}}$.

In Fig. 5.13, we plot the scattering efficiency obtained by the material-independent-mode expansion (4.16) (black line) and by the direct GMM calculation [172] (red dots) as a function of the size parameter x. It is worth to note that σ_{sca} does not depend on R and λ separately, but only on x, because we have assumed that Si is nondispersive in time. We also show in color the partial scattering efficiencies of the eight dominant dimer modes, whose real projections on the $y = 0$ plane are represented on the right.

In Fig. 5.14, we show the σ_{sca} calculated by using only these 8 dimer modes, and the agreement with the GMM remains satisfactory.

We list in Tab. 5.2 the resonant size parameter of the eight dominant modes and the corresponding resonant frequency (assuming $R = 100\,\text{nm}$), eigen-permittivity, residuum, and residua lower bound. Looking at the residuum of the considered modes, we note that the plasmonic mode $\mathbf{u}_{e0\,1}$ is the only (inherently) broad mode, according to the definition in Eq. (4.18). Instead, all other dominant dielectric modes are narrow: for these modes, there always exists a value of x in correspondence of which $\text{Re}\left\{\eta_{mq}/x^2\right\} = \varepsilon_{R,Si}$, as it is also apparent from the fourth column of Tab. 5.2. As a consequence, the partial scattering efficiency of the mode $\mathbf{u}_{e0\,1}$ is very broad compared to the ones of dielectric modes. Nevertheless, as for the scattering from a single sphere analysed in Sec. 4.6, the mode $\mathbf{u}_{e0\,1}$ has to be considered because it strongly couples to the plane wave and it also has a stronger radiative strength [79].

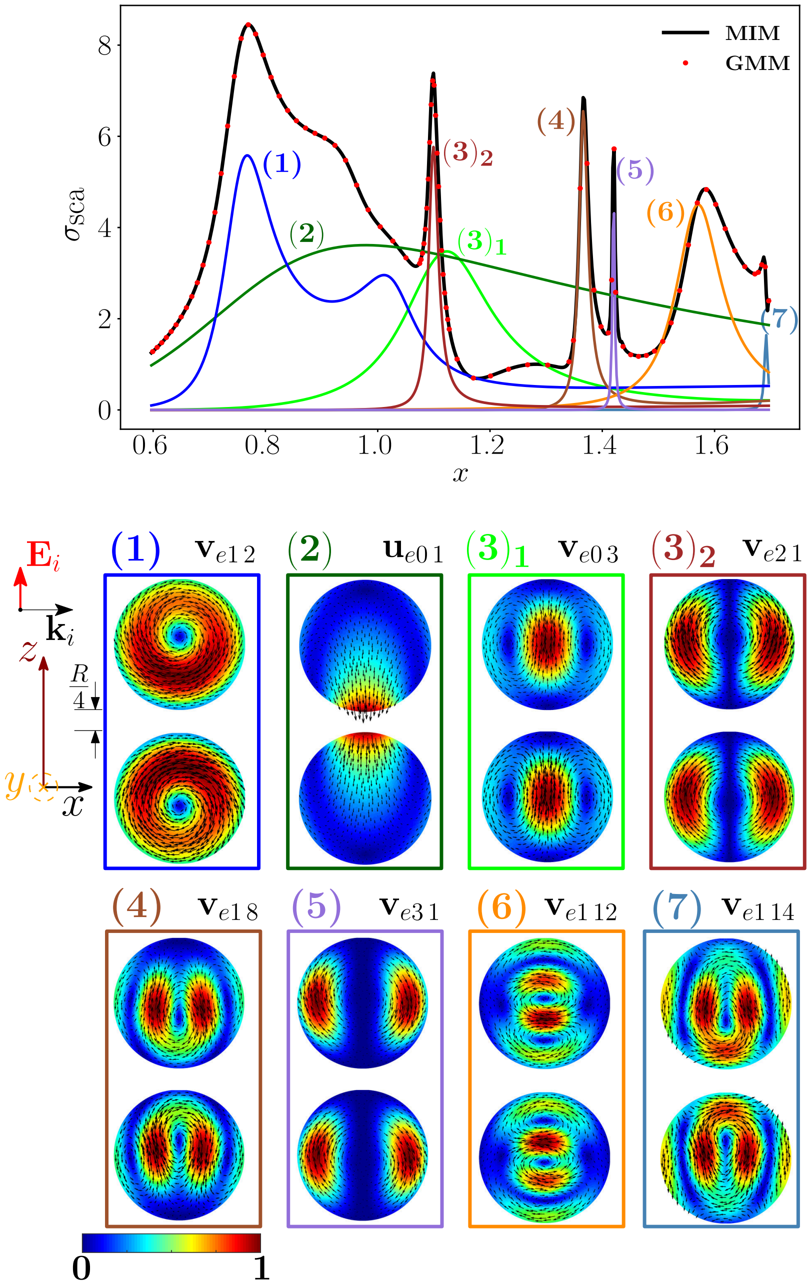

Figure 5.13 – Scattering efficiency σ_{sca} of a Si-spheres homo-dimer as a function of the size parameter x, obtained via material-independent-mode expansion (black line) and by direct-calculation (red dots). The radius of each sphere is R, the edge-edge distance $\Delta = R/4$. The dimer is excited by a plane wave polarized along the dimer's axis $\hat{\mathbf{z}}$ and propagating along the transverse direction $\hat{\mathbf{x}}$. Partial scattering efficiency (in color) of eight dominant dimer modes whose xz-plane projections (real part) are shown on the right.

Furthermore, only the dielectric modes and the fundamental electric dipole mode of the dimer are needed to correctly reproduce σ_{sca}: the plasmonic modes cannot be resonantly excited in homogeneous dielectric objects and, except for the fundamental

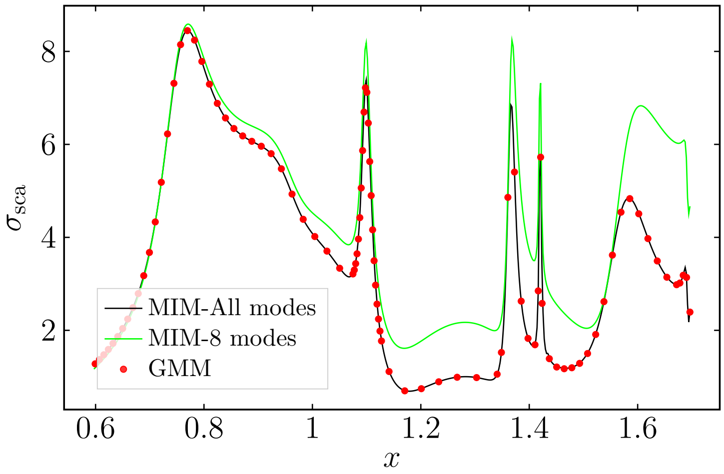

Figure 5.14 – Scattering efficiency $\sigma_{\rm sca}$ of a Si-spheres homo-dimer as a function of the size parameter x, obtained via the material-independent-mode expansion considering all the dimer modes (black line), only the eight dimer modes shown on the right of Fig. 5.13 (green line), and by the GMM direct-calculation (red dots). The radius of each sphere is R, the edge-edge distance $\Delta = R/4$. The dimer is excited by a plane wave polarized along the dimer axis and propagating orthogonally to it.

electric dipole, their coupling with a plane wave is weak [65, 48]. In Fig. D.3 in Appendix D, we display the scattered electric field in correspondence of the seven $\sigma_{\rm sca}$ peaks. It is apparent that at any $\sigma_{\rm sca}$ peak, the near-field distributions only roughly resemble the modes that dominate the scattering response.

As shown in Fig. 5.15, the dimer mode $\mathbf{v}_{e1\,2}$, which is responsible for the first peak of $\sigma_{\rm sca}$, arises from the hybridization of the fundamental magnetic dipole $\mathbf{v}^{\tt TE}_{o111}$ and the fundamental and second-order electric dipoles, i.e., $\mathbf{u}^{\tt TM}_{e11}$, $\mathbf{v}^{\tt TM}_{e111}$. The modes $\mathbf{u}^{\tt TM}_{e11}$ and $\mathbf{v}^{\tt TM}_{e111}$ constructively interact with $\mathbf{v}^{\tt TE}_{o111}$ within the region of each sphere located in between the gap and the center. The net effect is to move the vortex core away from the gap. We also introduce in Fig. 5.16 the *frequency hybridization diagram* for the dimer mode $\mathbf{v}_{e1\,2}$, where we show in the middle the dimer mode, on the left and on the right the TE and TM single-sphere modes that take part in the hybridization. The vertical position at which both the single-sphere and dimer modes are centred in the diagram is proportional to their resonant frequency obtained assuming $R = 100\,\mathrm{nm}$ (Tab. 5.2 and, for instance, Tabs. 4.1-4.3). We also show their hybridization weights.

Going back to the analysis of Fig. 5.13, the shoulder to the right of the first peak is due to the plasmonic mode $\mathbf{u}_{e0\,1}$. Then we found a dip of $\sigma_{\rm sca}$, which is due to the destructive interference between the dimer modes $\mathbf{v}_{e0\,3}$ and $\mathbf{u}_{e0\,1}$.

The next peak, labeled with (3), is mainly due to the mode $\mathbf{v}_{e2\,1}$, with minor

mode	x_{res}	ω_{res} [Prad/s]	ξ_{mq}	ρ	$\bar{\rho}$	# peak	x_{peak}
$\mathbf{v}_{e1\,2}$	0.760	2.29	16.11-2.23i	0.149	0.146	(1)	0.771
$\mathbf{u}_{e0\,1}$	1.696	5.08	-0.70 - 3.96i	1.038	0.919	(2)	0.901
$\mathbf{v}_{e0\,3}$	1.126	3.37	15.67-2.50i	0.168	0.168	(3)	1.099
$\mathbf{v}_{e2\,1}$	1.099	3.29	15.99-0.32i	0.021	0.021	(3)	1.099
$\mathbf{v}_{e1\,8}$	1.366	4.09	16.00-0.26i	0.017	0.017	(4)	1.336
$\mathbf{v}_{e3\,1}$	1.421	4.26	15.98-0.05i	0.004	0.003	(5)	1.423
$\mathbf{v}_{e1\,12}$	1.571	4.71	15.96-1.02i	0.068	0.068	(6)	1.584
$\mathbf{v}_{e1\,14}$	1.692	5.07	15.99-0.07i	0.005	0.005	(7)	1.688

Table 5.2 – Values of x minimizing the residua, corresponding value of the resonant frequency (when $R = 100\,\text{nm}$), eigen-permittivity ξ_{mq}, and residuum and residua lower bound of the dimer modes which dominate the scattering efficiency of Fig. 5.13. For a plasmonic mode, we have $\xi_{mq} = \varepsilon_{mq}$, while for a dielectric mode $\xi_{mq} = \eta_{mq}/x^2$. The positions of the peaks of the total scattering efficiency are also shown.

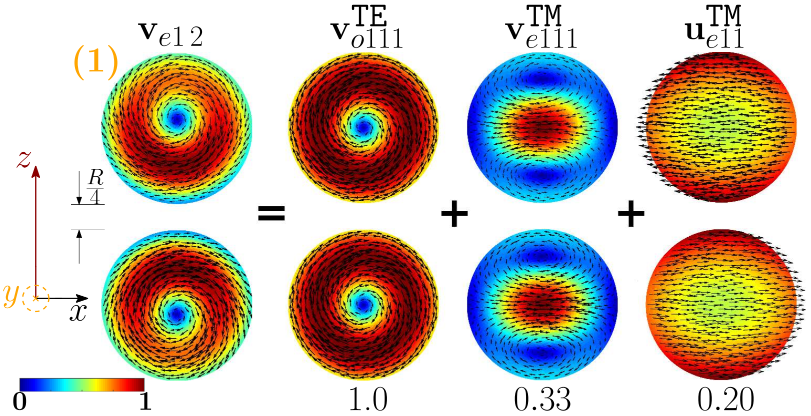

Figure 5.15 – Decomposition of the dimer mode $\mathbf{v}_{e1\,2}$ at $x = 0.771$ in terms of hybridizing single-sphere modes (real part of the projection on the $y = 0$ plane). Each single-sphere modes is multiplied by the expansion coefficients of Eq. (5.4). Below each single-sphere mode we also show its hybridization weight $\tilde{H}^{\perp|\mathtt{TM}}_{e11\,11}$, $H^{\perp|\mathtt{TM}}_{e11\,11}$, $H^{\perp|\mathtt{TE}}_{o11\,11}$, defined in Eq. (5.7).

contributions from the modes $\mathbf{v}_{e0\,3}$ and $\mathbf{u}_{e0\,1}$. The dimer modes $\mathbf{v}_{e2\,1}$ and $\mathbf{v}_{e0\,3}$ arise from the dominant contributions of the fundamental magnetic quadrupole $\mathbf{v}^{\mathtt{TE}}_{o121}$ and of the second-order electric dipole $\mathbf{v}^{\mathtt{TM}}_{e111}$, respectively. Then we found another low scattering region, which is once again due to the destructive interference between the dimer modes $\mathbf{v}_{e0\,3}$ and $\mathbf{u}_{e0\,1}$.

The dimer mode behind the σ_{sca} peak labelled with (4) is $\mathbf{v}_{e1\,8}$. As shown in Fig. 5.17, it arises from the hybridization among the second-order magnetic dipole $\mathbf{v}^{\mathtt{TE}}_{o112}$, the second-order electric quadrupole $\mathbf{v}^{\mathtt{TM}}_{e121}$, the third order electric dipole $\mathbf{v}^{\mathtt{TM}}_{e112}$,

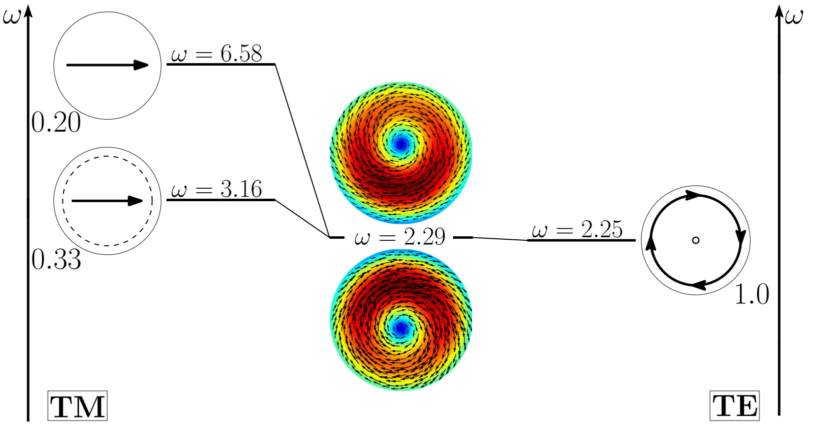

Figure 5.16 – Frequency levels describing the hybridization of the TE and TM modes of a 100 nm single-sphere into the dimer mode $\mathbf{v}_{e1\,2}$. The vertical axis represents the frequency (expressed in Prad/s). Next to each single-sphere mode we report its hybridization weight $\tilde{H}^{\perp|\mathtt{TM}}_{e11\,11}$, $H^{\perp|\mathtt{TM}}_{e11\,11}$, $H^{\perp|\mathtt{TE}}_{o11\,11}$, defined in Eq. (5.7).

and the fundamental magnetic quadrupole $\mathbf{v}^{\mathtt{TE}}_{o121}$. In particular, $\mathbf{v}^{\mathtt{TE}}_{o112}$ and $\mathbf{v}^{\mathtt{TM}}_{e121}$ constructively interact along the horizontal diameter of both spheres and destructively along the vertical diameter of both spheres. The "horseshoe" shape of this dimer

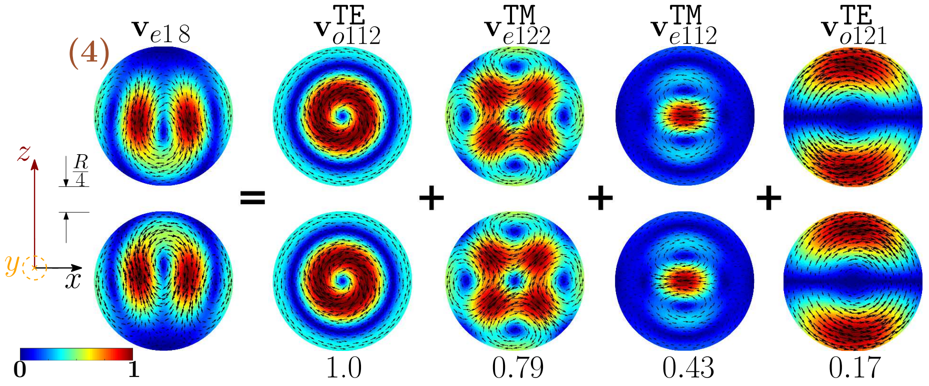

Figure 5.17 – Decomposition of the dimer mode $\mathbf{v}_{e1\,8}$ at $x = 1.366$ in terms of hybridizing single-sphere modes (real part of the projection on the $y = 0$ plane). Each single-sphere modes is multiplied by the expansion coefficients of Eq. (5.4). Below each single-sphere mode we also show its hybridization weight $H^{\perp|\mathtt{TM}}_{e18\,nl}$($H^{\perp|\mathtt{TE}}_{o18\,nl}$), defined in Eq. (5.7).

mode is determined by the action of the fundamental magnetic quadrupole $\mathbf{v}^{\mathtt{TE}}_{o121}$ that constructively interferes with the second-order magnetic quadrupole $\mathbf{v}^{\mathtt{TE}}_{o122}$ in the hemispheres of the two spheres closer to the gap, and destructively interferes in the remaining hemispheres. The contribution of the third order electric dipole $\mathbf{v}^{\mathtt{TM}}_{e112}$ pushes the vortex core within each sphere toward the gap, because it destructively interacts with $\mathbf{v}^{\mathtt{TE}}_{o112}$ in the semicircle closer to the gap, and constructively interacts in the opposite half. In Fig. 5.18 we also show the frequency hybridization diagram

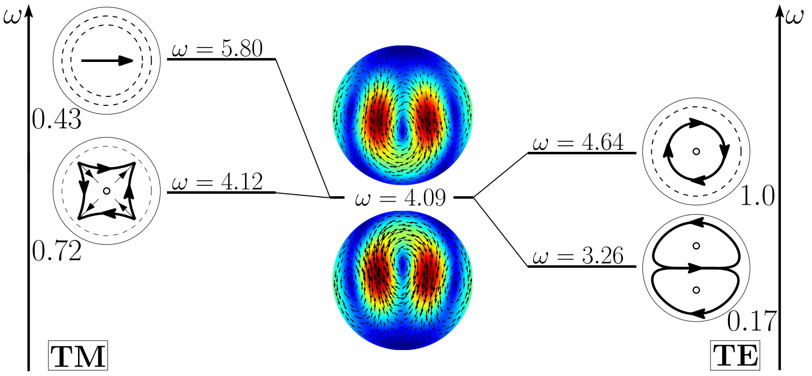

Figure 5.18 – Frequency levels describing the hybridization of the TE and TM modes of a 100 nm single-sphere into the dimer mode $\mathbf{v}_{e1\,8}$. The vertical axis represents the frequency (expressed in Prad/s). Next to each single-sphere mode we report its hybridization weight $H^{\perp|\mathtt{TM}}_{e18\,nl}$ ($H^{\perp|\mathtt{TE}}_{o18\,nl}$), defined in Eq. (5.7).

for the dimer mode $\mathbf{v}_{e1\,8}$.

In Fig. 5.19 we show the hybridization diagrams of the remaining modes of Fig. 5.13. Specifically, the dimer mode $\mathbf{u}_{e0\,1}$ (second peak) arises from the hybridization among the fundamental electric dipole $\mathbf{u}^{\mathtt{TM}}_{e01}$, quadrupole $\mathbf{u}^{\mathtt{TM}}_{e02}$, octupole $\mathbf{u}^{\mathtt{TM}}_{e03}$, hexadecapole $\mathbf{u}^{\mathtt{TM}}_{e04}$, and the second-order electric dipole $\mathbf{v}^{\mathtt{TM}}_{e011}$. The dimer mode $\mathbf{v}_{e0\,3}$ (third peak) is dominated by the second-order electric dipole $\mathbf{v}^{\mathtt{TM}}_{e011}$. The dimer mode $\mathbf{v}_{e2\,1}$ (third peak) is dominated by the fundamental magnetic quadrupole $\mathbf{v}^{\mathtt{TE}}_{o221}$. The dimer mode $\mathbf{v}_{e3\,1}$ (fifth peak) is dominated by the fundamental magnetic octupole $\mathbf{v}^{\mathtt{TE}}_{o331}$. No other mode besides the magnetic octupole is involved in the hybridization process, in these three cases. The mode $\mathbf{v}_{e1\,12}$ (sixth peak) arises from the hybridization of the second-order magnetic dipole $\mathbf{v}^{\mathtt{TE}}_{o112}$, second-order electric quadrupole $\mathbf{v}^{\mathtt{TM}}_{e121}$, second $\mathbf{v}^{\mathtt{TM}}_{e111}$ and third order $\mathbf{v}^{\mathtt{TM}}_{e112}$ electric dipoles, second-order magnetic quadrupole $\mathbf{v}^{\mathtt{TE}}_{o122}$, and fundamental magnetic octupole $\mathbf{v}^{\mathtt{TE}}_{o131}$. Finally, the mode $\mathbf{v}_{e1\,14}$ (seventh peak) results from the hybridization of second-order magnetic dipole $\mathbf{v}^{\mathtt{TE}}_{o122}$, third order electric dipole $\mathbf{v}^{\mathtt{TM}}_{e112}$, and second-order electric quadrupole $\mathbf{v}^{\mathtt{TM}}_{e121}$.

As for the Ag dimer, when we increase the edge-edge distance, the dimer modes change. Nevertheless, the single-sphere modes used as basis set remain the same, while the hybridization weights vary. For instance, when the edge-edge distance increases from $R/4$ to R the contribution of the fundamental magnetic dipole to the dimer mode that causes the first σ_{sca} peak increases compared to the remaining modes (Fig. D.10 in SI). This mode is the only one to survive when the distance goes to infinity (Fig. 4.9). Similarly, the dimer mode $\mathbf{v}_{e1\,7}$ associated to the peak (4) (Fig. D.11 in Appendix D), arises mainly from the second-order electric quadrupole $\mathbf{v}^{\mathtt{TM}}_{e121}$, while the second-order magnetic dipole $\mathbf{v}^{\mathtt{TE}}_{o112}$ that was dominant for edge-edge

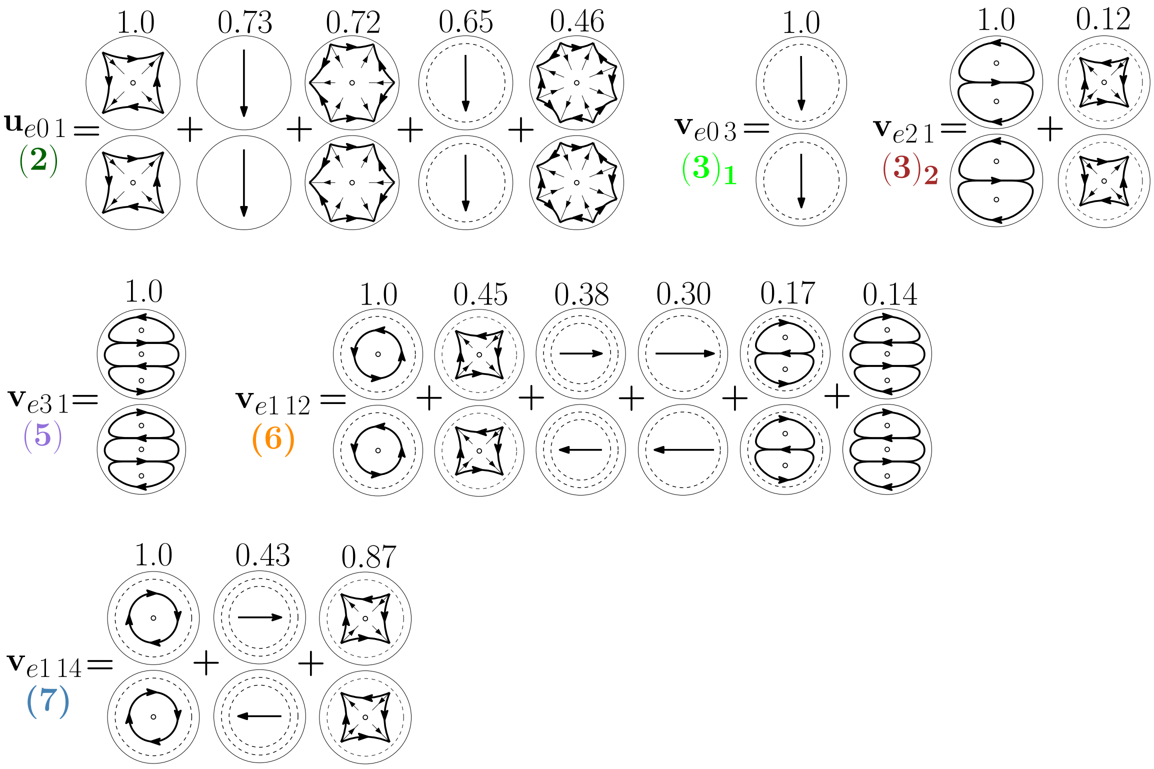

Figure 5.19 – Decomposition of the dimer modes $\mathbf{u}_{e0\,1}$, $\mathbf{v}_{e0\,3}$, $\mathbf{v}_{e2\,1}$, $\mathbf{v}_{e3\,1}$, $\mathbf{v}_{e1\,12}$, $\mathbf{v}_{e1\,14}$, at $x = 0.901, 1.099, 1.099, 1.423, 1.584, 1.688$, respectively, in terms of hybridizing single-sphere modes (real part of the projection on the $y = 0$ plane). Each single-sphere modes is multiplied by the expansion coefficients of Eq. (5.4). Above each single-sphere mode we also show its hybridization weight, defined in Eq. (5.7).

distance of $R/4$ (Fig. 5.17) now plays a minor role. The mode $\mathbf{v}^{\text{TM}}_{e121}$ is the only to survive when the distance goes to infinity (Fig. 4.9).

For the sake of completeness, in Fig. D.5 of Appendix D we show the scattering efficiency and the dominant modes for a transversely polarized Si homo-dimer.

5.5 Conclusions

We have investigated the resonances and the resonance modes in the electromagnetic scattering from a dimer of spheres by using the full-retarded material-independent modes. The electromagnetic scattering response of the dimer is described by a set of dimer modes. Each dimer mode is seen as the result of the hybridization of the modes of two constituent spheres, whose importance is quantified by hybridization weights. As we vary the gap size, although the dimer modes change, they are still represented in terms of the same set of single-sphere modes, but with different hybridization weights. This study represents the first full-Maxwell theory of hybridization in Si dimers, and it also constitutes an extension of the plasmon-mode hybridization theory to the full-retarded scenario. In the full-wave regime every dimer mode arises from the complex superposition of different single-sphere modes. Through the loci spanned by the dimer eigen-permittivities in the complex plane by varying the gap size, we provide a method to identify and justify the dominant single-sphere modes in the hybridization mechanism.

As for the full-wave modes of a sphere, investigated in the previous chapter, the modes are classified according to their behaviour in the long-wavelength limit, into plasmonic and dielectric modes. The dielectric modes cannot be resonantly excited in metal dimers, because their eigenpermittivities always have positive real part. In general, the plasmonic and dielectric modes of the dimer arise from the hybridization of both the plasmonic and dielectric modes of the isolated-sphere.

We parametrically investigate the eigenvalues associated to both plasmonic and dielectric modes as a function of the gap-size. In particular, starting from the very large gap size, we determine the shift of eigenvalue as the gap-size reduces. In the full-wave regime, we found that retardation effects play an important role, in particular the constructive (destructive) interference between the current densities induced within the two spheres determine a increase (decrease) of the amplitudes of the imaginary part of the eigenpermittivities. Thus the eigenvalues will describe spiral trajectories on the complex plane as a function of the gap-size.

By using this theoretical framework, we investigate the resonant scattering from metal and dielectric dimers with dimensions of the order of the incident wavelength under different plane-wave illuminations and different gap sizes. The scattering efficiency can be accurately described by a very limited number of dimer modes. Then, we quantitatively decompose these dimer modes into the modes of the constituent spheres, providing the corresponding hybridization weights. The plasmonic dimer modes are sufficient to describe the far-field scattering from metal dimers. On the contrary, the far field scattering from dielectric dimers involves resonant dielectric dimer modes and off-resonance plasmonic dimer modes. In dielectric dimers, interference effects between dielectric and plasmonic dimer modes may determine a suppression of the scattering cross section.

To offer an intuitive understanding we extend the hybridization diagrams introduced by Prodan et al. to the full-Maxwell analysis, showing the hybridization of the electric and magnetic modes of an isolated Si sphere into the dimer modes and the corresponding frequency levels.

Appendix A

Multipoles

A.1 Three-dimensional objects

The electric dipole moment $\mathbf{P}_h$ of the three-dimensional electro-quasistatic current mode $\mathbf{j}_h^{\|}$ of an object occupying a domain Ω with boundary $\partial\Omega$ is defined as

$$\mathbf{P}_h = \int_{\Omega} \mathbf{j}_h^{\|} dV = \oint_{\partial\Omega} \mathbf{r} \left(\mathbf{j}_h^{\|} \cdot \hat{\mathbf{n}} \right) dS, \tag{A.1}$$

where $\mathbf{r} \rightarrow \mathbf{r}/l_c$ and Ω are the coordinates and domain, respectively, scaled by the characteristic linear lenght l_c of the region Ω.
The electric quadrupole tensor $\overleftrightarrow{\mathbf{Q}}_{\mathrm{E}|h}^{\|}$ is defined as

$$\overleftrightarrow{\mathbf{Q}}_{\mathrm{E}|h}^{\|} = \int_{\Omega} \left(\mathbf{r}\, \mathbf{j}_h^{\|} + \mathbf{j}_h^{\|}\, \mathbf{r} \right)\, dV = \oint_{\partial\Omega} \left(\mathbf{j}_h^{\|} \cdot \hat{\mathbf{n}} \right) \mathbf{r}\mathbf{r}\, dS. \tag{A.2}$$

With respect to the standard definitions of surface charge density and electric multipoles [149], the prefactor $1/(-i\omega)$ is omitted.

The magnetic dipole moment $\mathbf{M}_h$ of the h-th magneto-quasistatic current mode $\mathbf{j}_h^{\perp}$ is defined as

$$\mathbf{M}_h = \frac{1}{2} \int_{\Omega} \mathbf{r} \times \mathbf{j}_h^{\perp}\, dV, \tag{A.3}$$

the toroidal dipole $\mathbf{P}_{\mathrm{E2}|h}^{\perp}$ is defined as

$$\mathbf{P}_{\mathrm{E2}|h}^{\perp} = \frac{1}{6} \int_{\Omega} \mathbf{r} \times \left(\mathbf{j}_h^{\perp} \times \mathbf{r} \right) dV, \tag{A.4}$$

and the magnetic quadrupole tensor $\overleftrightarrow{\mathbf{Q}}^{\perp}_{\mathrm{M}|h}$ as

$$\overleftrightarrow{\mathbf{Q}}^{\perp}_{\mathrm{M}|h} = \frac{1}{3}\int_{\Omega} [(\mathbf{r} \times \mathbf{j}^{\perp}_{h})\mathbf{r} + \mathbf{r}(\mathbf{r} \times \mathbf{j}^{\perp}_{h})]\, dV. \tag{A.5}$$

A.2 Translational invariant objects

The electric dipole moment $\mathbf{P}^{\|}_{h}$ of the two-dimensional electro-quasistatic current mode $\mathbf{j}^{\|}_{h}$ of a translational invariant object with cross-section Σ and linear boundary $\partial\Sigma$ is defined as

$$\mathbf{P}^{\|}_{h} = \int_{\Sigma} \mathbf{j}^{\|}_{h} dS = \oint_{\Sigma} \mathbf{r}\left(\mathbf{j}^{\|}_{h} \cdot \hat{\mathbf{n}}\right) dl, \tag{A.6}$$

where $\mathbf{r} \to \mathbf{r}/l_c$ and Σ are the coordinates and domain, respectively, scaled by the characteristic linear lenght l_c of the region Σ.
The electric quadrupole tensor $\overleftrightarrow{\mathbf{Q}}^{\|}_{\mathrm{E}|h}$ is defined as

$$\overleftrightarrow{\mathbf{Q}}^{\|}_{\mathrm{E}|h} = \int_{\Sigma} \left(\mathbf{r}\,\mathbf{j}^{\|}_{h} + \mathbf{j}^{\|}_{h}\,\mathbf{r}\right)\, dS = \oint_{\partial\Sigma} \left(\mathbf{j}^{\|}_{h} \cdot \hat{\mathbf{n}}\right)\, \mathbf{r}\mathbf{r}\, dl. \tag{A.7}$$

The magnetic dipole moment $\mathbf{M}^{\perp}_{h}$ of the h-th magneto-quasistatic current mode $\mathbf{j}^{\perp}_{h}$ is defined as

$$\mathbf{M}^{\perp}_{h} = \frac{1}{2}\int_{\Sigma} \mathbf{r} \times \mathbf{j}^{\perp}_{h}\, dS, \tag{A.8}$$

the toroidal dipole $\mathbf{p}^{\perp}_{\mathrm{E2}|h}$ is defines as

$$\mathbf{P}^{\perp}_{\mathrm{E2}|h} = \frac{1}{6}\int_{\Sigma} \mathbf{r} \times \mathbf{j}^{\perp}_{h} \times \mathbf{r}\, dS, \tag{A.9}$$

and the magnetic quadrupole tensor $\overleftrightarrow{\mathbf{Q}}^{\perp}_{\mathrm{M}|h}$ as

$$\overleftrightarrow{\mathbf{Q}}^{\perp}_{\mathrm{M}|h} = \frac{1}{3}\int_{\Sigma} [(\mathbf{r} \times \mathbf{j}^{\perp}_{h})\mathbf{r} + \mathbf{r}(\mathbf{r} \times \mathbf{j}^{\perp}_{h})]\, dS. \tag{A.10}$$

Appendix B

Sphere

B.1 Quasistatic regime

B.1.1 Solid sphere

We consider a sphere of radius R and a characteristic dimension ℓ_c equal to the radius $\ell_c = R$. We utilize a polar spherical reference frame (see Fig. 4.1), and we normalize the coordinates $\mathbf{r} = (r, \vartheta, \phi)$ by the chosen characteristic length ℓ_c, i.e. $\mathbf{r} \to \mathbf{r}/R$, and hence $r \in [0, 1]$.

The electro-quasistatic modes $\mathbf{j}^{\parallel}_{pmn}$ have the following expression

$$\begin{aligned}\mathbf{j}^{\parallel}_{\substack{e\\o}mn}(r, \vartheta, \phi) = \frac{1}{\sqrt{\alpha_{mn}}} \Bigg[&\begin{pmatrix} \cos m\phi \\ \sin m\phi \end{pmatrix} n P_n^m\left(\cos\vartheta\right) \hat{\boldsymbol{r}} + \begin{pmatrix} \cos m\phi \\ \sin m\phi \end{pmatrix} \frac{dP_n^m\left(\cos\vartheta\right)}{d\vartheta} \hat{\boldsymbol{\vartheta}} \\ &+ \begin{pmatrix} -\sin m\phi \\ +\cos m\phi \end{pmatrix} m \frac{P_n^m\left(\cos\vartheta\right)}{\sin\vartheta} \hat{\boldsymbol{\phi}} \Bigg] r^{n-1}, \qquad \text{(B.1)}\end{aligned}$$

where the subscripts $p = e$ and $p = o$ denote even and odd, P_n^m are the associated Legendre functions of the first kind of degree n and order m as defined and normalized in [173]. The prefactor α_{mn} guarantees that $\|\mathbf{j}^{\parallel}_{\substack{e\\o}mn}\|^2 = 1$, and has the expression

$$\alpha_{mn} = 2\pi n \left(\delta_m + 1\right) \frac{(m+n)!}{\left(2n+1\right)\left(n-m\right)!}, \qquad \text{(B.2)}$$

in which δ_m is the Kronecker delta.

The magneto-quasistatic modes are divided in two subsets. The first one is composed by the $\mathbb{A}^{\perp}$-modes $\mathbf{j}^{\perp\mathtt{TE}}_{pmnl}$, which have the form

$$\mathbf{j}^{\perp\mathtt{TE}}_{\substack{e\\o}mnl}(r,\vartheta,\phi)=\frac{1}{\sqrt{\beta_{mnl}}}\left[m\begin{pmatrix}-\sin m\phi\\+\cos m\phi\end{pmatrix}\frac{P_n^m\left(\cos\vartheta\right)}{\sin\vartheta}\hat{\boldsymbol{\vartheta}}\right.\\ \left.-\begin{pmatrix}\cos m\phi\\\sin m\phi\end{pmatrix}\frac{dP_n^m\left(\cos\vartheta\right)}{d\vartheta}\hat{\boldsymbol{\phi}}\right]j_n\left(z_{n-1,l}\,r\right), \tag{B.3}$$

where $z_{n,l}$ is the l-th zero of the n-th order spherical bessel function j_n, and the prefactor β_{mnl}, which guarantees that $\|\mathbf{j}^{\perp\mathtt{TE}}_{\substack{e\\o}mnl}\|^2=1$, is

$$\beta_{mnl}=\pi\left(\delta_m+1\right)\frac{n\left(n+1\right)\left(m+n\right)!}{\left(2n+1\right)\left(n-m\right)!}\,j_n^2\left(z_{n-1,l}\right). \tag{B.4}$$

The second one is made of the TM modes $\mathbf{j}^{\perp\mathtt{TM}}_{pmnl}$

$$\mathbf{j}^{\perp\mathtt{TM}}_{\substack{e\\o}mnl}(r,\vartheta,\phi)=\frac{1}{\sqrt{\gamma_{mnl}}}\left\{\begin{pmatrix}\cos m\phi\\\sin m\phi\end{pmatrix}n\left(n+1\right)P_n^m\left(\cos\vartheta\right)\frac{j_n\left(z_{nl}\,r\right)}{z_{nl}\,r}\hat{\boldsymbol{r}}\right.\\ +\begin{pmatrix}\cos m\phi\\\sin m\phi\end{pmatrix}\frac{dP_n^m\left(\cos\vartheta\right)}{d\vartheta}\frac{1}{z_{nl}\,r}\frac{d}{dr}\left[rj_n\left(z_{nl}r\right)\right]\hat{\boldsymbol{\vartheta}}\\ \left.+m\begin{pmatrix}-\sin m\phi\\+\cos m\phi\end{pmatrix}\frac{P_n^m\left(\cos\vartheta\right)}{\sin\vartheta}\frac{1}{z_{nl}\,r}\frac{d}{dr}\left[rj_n\left(z_{nl}r\right)\right]\hat{\boldsymbol{\phi}}\right\}, \tag{B.5}$$

where the prefactor γ_{mnl}, which guarantees that $\|\mathbf{j}^{\mathtt{TM}\perp}_{\substack{e\\o}mnl}\|^2=1$, is

$$\gamma_{mnl}=\pi\left(1+\delta_m\right)\frac{n\left(n+1\right)\left(n+m\right)!}{\left(2n+1\right)\left(n-m\right)!}j_{n-1}^2\left(z_{nl}\right). \tag{B.6}$$

The EQS and MQS eigenvalues have the following expression:

$$\begin{aligned}\chi_n^{\parallel}&=-\frac{2n+1}{n},\\ \kappa_{nl}^{\perp\,\mathrm{TE}}&=\left(z_{n-1,l}\right)^2,\\ \kappa_{nl}^{\perp\,\mathtt{TM}}&=\left(z_{n,l}\right)^2, \qquad \forall n\in\mathbb{N},\ l\in\mathbb{N}.\end{aligned} \tag{B.7}$$

B.1.2 Spherical shell

The EQS modes $\mathbf{j}^{\parallel}_{\substack{e\\o}mn}$ of a closed spherical surface have the following expression

$$\mathbf{j}^{\parallel}_{\substack{e\\o}mn}(\vartheta,\phi) = \frac{1}{\sqrt{\bar{\alpha}_{mn}}}\left[\begin{pmatrix}\cos m\phi\\ \sin m\phi\end{pmatrix}\frac{dP_n^m\left(\cos\vartheta\right)}{d\vartheta}\,\hat{\boldsymbol{\vartheta}} + \begin{pmatrix}-\sin m\phi\\ +\cos m\phi\end{pmatrix} m\frac{P_n^m\left(\cos\vartheta\right)}{\sin\vartheta}\,\hat{\boldsymbol{\phi}}\right], \tag{B.8}$$

The prefactor $\bar{\alpha}_{mn} = \alpha_{mn}(1+\delta_m)$, with α_{mn} given in Eq. (B.2), guarantees that $\|\mathbf{j}^{\parallel}_{\substack{e\\o}mn}\|^2_{\Sigma} = 1$. The plasmonic eigenvalues are $\chi^{\parallel}_n = -\dfrac{2n+1}{n(n+1)}$, $\forall n \in \mathbb{N}$.

The MQS modes $\mathbf{j}^{\perp}_{\substack{e\\o}mn}$ have the form

$$\mathbf{j}^{\perp\mathtt{TE}}_{\substack{e\\o}mn}(r,\vartheta,\phi) = \frac{1}{\sqrt{\bar{\beta}_{mn}}}\left[m\begin{pmatrix}-\sin m\phi\\ +\cos m\phi\end{pmatrix}\frac{P_n^m\left(\cos\vartheta\right)}{\sin\vartheta}\,\hat{\boldsymbol{\vartheta}} - \begin{pmatrix}\cos m\phi\\ \sin m\phi\end{pmatrix}\frac{dP_n^m\left(\cos\vartheta\right)}{d\vartheta}\,\hat{\boldsymbol{\phi}}\right], \tag{B.9}$$

the prefactor $\bar{\beta}_{mn}$, which guarantees that $\|\mathbf{j}^{\perp}_{\substack{e\\o}mnl}\|^2_{\Sigma} = 1$, has the following expression

$$\bar{\beta}_{mn} = 2\pi\left(\delta_m + 1\right)\frac{n\left(n+1\right)\left(m+n\right)!}{\left(2n+1\right)\left(n-m\right)!}. \tag{B.10}$$

The dielectric eigenvalues are $\kappa^{\perp}_n = (2n+1)$, $\forall n \in \mathbb{N}$.

B.2 Full-wave regime

B.2.1 Material-independent modes

The plasmonic $\varepsilon_n^{\mathtt{TM}}$ and the dielectric $\eta_{nl}^{\mathtt{TM}}$, $\eta_{nl}^{\mathtt{TE}}$ are found by solving the following equations

$$\begin{aligned}
\sqrt{\varepsilon_n^{\mathtt{TM}}}\frac{\psi_n\left(\sqrt{\varepsilon_n^{\mathtt{TM}}}x\right)}{\psi_n'\left(\sqrt{\varepsilon_n^{\mathtt{TM}}}x\right)} &= \frac{\xi_n(x)}{\xi_n'(x)},\\
\sqrt{\eta_{nl}^{\mathtt{TM}}}\frac{\psi_n\left(\sqrt{\eta_{nl}^{\mathtt{TM}}}\right)}{\psi_n'\left(\sqrt{\eta_{nl}^{\mathtt{TM}}}\right)} &= \frac{x\xi_n(x)}{\xi_n'(x)},\\
\frac{1}{\sqrt{\eta_{nl}^{\mathtt{TE}}}}\frac{\psi_n\left(\sqrt{\eta_{nl}^{\mathtt{TE}}}\right)}{\psi_n'\left(\sqrt{\eta_{nl}^{\mathtt{TE}}}\right)} &= \frac{\xi_n(x)}{x\xi_n'(x)},
\end{aligned} \tag{B.11}$$

which are obtained by zeroing the denominator of the standard Mie theory coefficients a_n (for $\varepsilon_n^{\mathtt{TM}}$ and $\eta_{nl}^{\mathtt{TM}}$) and b_n (for $\eta_{nl}^{\mathtt{TE}}$) for the scattering from a plane wave, given in Eqs. (4.56) and (4.57), respectively, in [87].

We recast the equations above in the following power series expansions:

$$\begin{aligned}
\mathcal{P}_n\left(\varepsilon_n^{\mathtt{TM}}\right) &= \sum_{h=0}^{\infty} p_{nh}(x)\,\left(\varepsilon_n^{\mathtt{TM}}-1\right)^h = 0,\\
\mathcal{Q}_n^{\mathtt{TM}}\left(\eta_{nl}^{\mathtt{TM}}\right) &= \sum_{h=0}^{\infty} q_{nh}^{\mathtt{TM}}(x)\,\left(\eta_{nl}^{\mathtt{TM}}-x^2\right)^h = 0,\\
\mathcal{Q}_n^{\mathtt{TE}}\left(\eta_{nl}^{\mathtt{TE}}\right) &= \sum_{h=0}^{\infty} q_{nh}^{\mathtt{TE}}(x)\,\left(\eta_{nl}^{\mathtt{TE}}-x^2\right)^h = 0,
\end{aligned} \tag{B.12}$$

where the coefficients p_{nh}, $q_{nh}^{\mathtt{TM}}$, and $q_{nh}^{\mathtt{TE}}$ are defined for any given n, x, and $h \geq 1$ as follows:

$$\begin{aligned}
p_{n0} = \, & q_{n0}^{\mathtt{TM}} = \, q_{n0}^{\mathtt{TE}} = h_{n+1}^{(1)}\left(x\right) j_n\left(x\right) - h_n^{(1)}\left(x\right) j_{n+1}\left(x\right),\\
q_{nh}^{\mathtt{TE}} = & -\frac{\left(-1\right)^{h-1}}{x^{h+1}\left(h-1\right)!}\frac{1}{\left(2\right)^{h-1}}\left[h_n^{(1)}\left(x\right) j_{n+h}\left(x\right)\right] +\\
& \frac{\left(-1\right)^h}{h!}\left(\frac{x}{2}\right)^h\left[h_{n+1}^{(1)}\left(x\right) j_{n+h}\left(x\right) - h_n^{(1)}\left(x\right) j_{n+h+1}\left(x\right)\right],\\
q_{nh}^{\mathtt{TM}} = \, & q_{nh}^{\mathtt{TE}} - \frac{\left(-1\right)^{h-1}}{x^{h+1}\left(h-1\right)!}\frac{1}{\left(2\right)^{h-1}}\frac{\left[xh_n^{(1)}\left(x\right)\right]'}{x} j_{n+h-1}\left(x\right),\\
p_{nh} = \, & x^{2h}\, q_{nh}^{\mathtt{TE}} - \frac{\left(-1\right)^{h-1}}{\left(h-1\right)!}\left(\frac{x}{2}\right)^{h-1}\frac{\left[xh_n^{(1)}\left(x\right)\right]'}{x} j_{n+h-1}\left(x\right),
\end{aligned} \tag{B.13}$$

j_n are the spherical Bessel functions of the first kind, h_n are the Hankel functions of the first kind.

In Fig. B.1, we plot the loci spanned in the complex plane by the plasmonic eigen-permittivities $\varepsilon_n^{\mathtt{TM}}$, for $n = 1, \ldots, 25$.

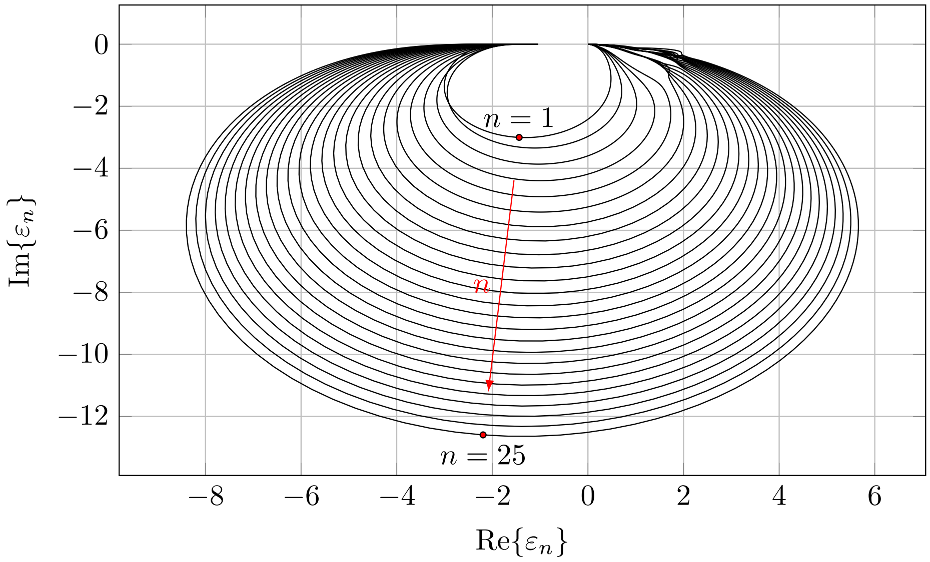

Figure B.1 – Loci spanned in the complex plane by the plasmonic eigen-permittivities $\varepsilon_n^{\mathtt{TM}}$ of a homogeneous sphere by varying $x \in [0, \infty)$, for $n = 1$, 2, ..., 25.

The expression of the full-wave material-independent modes $\mathbf{u}_{pmn}^{\mathtt{TM}}$, $\mathbf{v}_{pmnl}^{\mathtt{TM}}$, $\mathbf{v}_{pmnl}^{\mathtt{TE}}$ is

$$\mathbf{u}_{pmn}^{\mathtt{TM}}(\mathbf{r}) = \mathbf{N}_{pmn}^{(1)}\left(\sqrt{\varepsilon_n^{\mathtt{TM}}}\, x\mathbf{r}\right), \tag{B.14}$$

$$\mathbf{v}_{pmnl}^{\mathtt{TM}}(\mathbf{r}) = \mathbf{N}_{pmn}^{(1)}\left(\sqrt{\eta_{nl}^{\mathtt{TM}}}\, \mathbf{r}\right), \tag{B.15}$$

$$\mathbf{v}_{pmnl}^{\mathtt{TE}}(\mathbf{r}) = \mathbf{M}_{pmn}^{(1)}\left(\sqrt{\eta_{nl}^{\mathtt{TE}}}\, \mathbf{r}\right), \quad \forall \mathbf{r} \in \Omega \tag{B.16}$$

where $\mathbf{N}_{pmn}^{(1)}$ and $\mathbf{M}_{pmn}^{(1)}$ are the VSWFs regular at the center of the sphere. The general explicit expressions of the vector spherical wave functions (VSWF) are [87]:

$$\begin{aligned}
\mathbf{N}_{\substack{e\\o}mn}(\xi\,\mathbf{r}) &= n\,(n+1)\begin{pmatrix}\cos m\phi\\ \sin m\phi\end{pmatrix} P_n^m(\cos\vartheta)\,\frac{z_n(\xi\,r)}{\xi\,r}\hat{\mathbf{r}}\\
&+\begin{pmatrix}\cos m\phi\\ \sin m\phi\end{pmatrix}\frac{dP_n^m(\cos\vartheta)}{d\vartheta}\frac{1}{\xi\,r}\frac{d}{dr}\left[r z_n(\xi\,r)\right]\hat{\boldsymbol{\vartheta}}\\
&+m\begin{pmatrix}-\sin m\phi\\ \cos m\phi\end{pmatrix}\frac{P_n^m(\cos\vartheta)}{\sin\vartheta}\frac{1}{\xi\,r}\frac{d}{dr}\left[r z_n(\xi\,r)\right]\hat{\boldsymbol{\phi}}, \qquad \text{(B.17)}\\
\mathbf{M}_{\substack{e\\o}mn}(\xi\,\mathbf{r}) &= m\begin{pmatrix}-\sin m\phi\\ \cos m\phi\end{pmatrix}\frac{P_n^m(\cos\vartheta)}{\sin\vartheta}z_n(\xi\,r)\,\hat{\boldsymbol{\vartheta}}\\
&-\begin{pmatrix}\cos m\phi\\ \sin m\phi\end{pmatrix}\frac{dP_n^m(\cos\vartheta)}{d\vartheta}z_n(\xi\,r)\,\hat{\boldsymbol{\phi}},
\end{aligned}$$

where the subscripts e and o denote even and odd, and $P_n^m(\cdot)$ are the associated Legendre function of the first kind of degree n and order m. Moreover, the superscripts $^{(1)}$ and $^{(3)}$ are appended to the functions $\mathbf{M}_{\substack{e\\o}mn}$ and $\mathbf{N}_{\substack{e\\o}mn}$ to denote the function z_n, namely Bessel functions of the first kind j_n and Hankel functions of the first kind h_n, respectively.

B.2.2 Scattering coefficients

The expansion coefficients $A_n^{\mathtt{TM}}$, $B_{nl}^{\mathtt{TM}}$, $B_{nl}^{\mathtt{TE}}$ for the scattered electric field in Eq. (4.38) have the following expression

$$A_n^{\mathtt{TM}} = \frac{-2i}{E_n}\frac{\tilde{A}_n^{\mathtt{TM}}}{\left(\varepsilon_n^{\mathtt{TM}}-\varepsilon_R\right)}, \qquad \text{(B.18)}$$

$$B_{nl}^{\mathtt{TM}} = \frac{-2i}{E_n}\frac{\tilde{B}_{nl}^{\mathtt{TM}}}{\left(\eta_{nl}^{\mathtt{TM}}-x^2\varepsilon_R\right)}, \qquad \text{(B.19)}$$

$$B_{nl}^{\mathtt{TE}} = \frac{-2i}{E_n}\frac{\tilde{B}_{nl}^{\mathtt{TE}}}{\left(\eta_{nl}^{\mathtt{TE}}-x^2\varepsilon_R\right)}, \qquad \text{(B.20)}$$

where

$$\tilde{A}_n^{\mathtt{TM}} = \frac{\varepsilon_n^{3/2}}{(\varepsilon_n - 1)x\, h_n^{(1)}(x) j_n(\sqrt{\varepsilon_n^{\mathtt{TM}}}x)\left\{q_n^2(x)\varepsilon_n^2 + [q_n(x) + x^2]\varepsilon_n - n(n+1)\right\}}, \tag{B.21}$$

$$\tilde{B}_{nl}^{\mathtt{TM}} = \frac{x^4\left(\eta_{nl}^{\mathtt{TM}}\right)^{3/2}}{(\eta_{nl}^{\mathtt{TM}} - x^2) h_n^{(1)}(x) j_n(\sqrt{\eta_{nl}^{\mathtt{TM}}})\left\{q_n^2(x)\left(\eta_{nl}^{\mathtt{TM}}\right)^2 + [q_n(x) + x^2]\eta_{nl}^{\mathtt{TM}} - n(n+1)x^4\right\}}, \tag{B.22}$$

$$\tilde{B}_{nl}^{\mathtt{TE}} = \frac{x\eta_{nl}^{\mathtt{TE}}}{(\eta_{nl}^{\mathtt{TE}} - x^2) h_n^{(1)}(x) j_n(\sqrt{\eta_{nl}^{\mathtt{TE}}})\left\{\eta_{nl}^{\mathtt{TE}} + g_n(x)\left[x g_n(x) - (2n+1)\right] x\right\}}, \tag{B.23}$$

with

$$\begin{aligned} g_n(x) &= \frac{h_{n+1}^{(1)}(x)}{h_n^{(1)}(x)}, \\ q_n(x) &= n + 1 - x g_n(x). \end{aligned} \tag{B.24}$$

Appendix C

Quasistatic modes of some translational invariant structures

C.1 Circular cylinder

We consider an infinite cylinder with circular cross-section of radius R and a characteristic dimension ℓ_c equal to the radius $\ell_c = R$. We shall use a cylindrical polar reference frame (Fig. C.1), and we normalize the in-plane coordinates $\mathbf{r} = (r, \phi)$ by the chosen characteristic length ℓ_c, i.e. $\mathbf{r} \rightarrow \mathbf{r}/R$, and hence $r \in [0, 1]$. The electro-quasistatic normalized modes $\mathbf{j}^{\parallel}_{pn}$ have the following expression

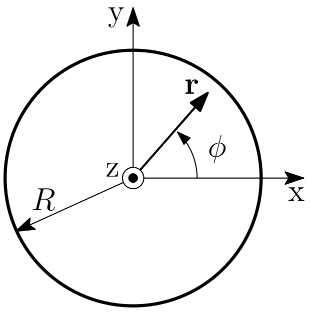

Figure C.1 – Cylindrical polar coordinate system. The z-axis is oriented along the cylinder axis.

$$\mathbf{j}^{\parallel}_{\substack{e\\o}n}(r,\phi) = \left[\begin{pmatrix} \cos n\phi \\ \sin n\phi \end{pmatrix} \hat{\boldsymbol{r}} + \begin{pmatrix} \sin n\phi \\ \cos n\phi \end{pmatrix} \hat{\boldsymbol{\phi}} \right] \sqrt{\frac{n}{\pi}} r^{n-1}, \tag{C.1}$$

where the subscripts $p = e$ and $p = o$ denote even and odd, and $n \in \mathbb{N}$ is the mode multipolar order. The EQS eigen-susceptibilities $\chi^{\parallel}_n$ are all equal to -2 [83].

The magneto-quasistatic modes are divided into two subsets. The first one is composed by modes whose vector field lies in the cross-sectional plane, and hence they are called TE modes. We denote them with $\mathbf{j}^{\perp\mathtt{TE}}_{pnl}$, and they are in the form

$$\mathbf{j}^{\perp\mathtt{TE}}_{\substack{e\\o}nl}(r,\phi) = \left[\begin{pmatrix} \cos n\phi \\ \sin n\phi \end{pmatrix} n \frac{J_n(Z_{n,l}r)}{r Z_{n,l}} \hat{\boldsymbol{r}} \right. \\ \left. + \begin{pmatrix} \sin n\phi \\ \cos n\phi \end{pmatrix} \left(J_{n-1}(Z_{n,l}r) - n\frac{J_n(Z_{n,l}r)}{r Z_{n,l}} \right) \hat{\boldsymbol{\phi}} \right] \frac{1}{\pi J_{n-1}(Z_{n,l})}, \tag{C.2}$$

where $n = \mathbb{N}_0$, $l \in \mathbb{N}$, J_n is the n-th order Bessel function of the first kind, and $Z_{n,l}$ is the l-th zero of J_n. They have unit norm over the cylinder cross-section. The MQS TE eigenvalues $\kappa_{nl}^{\perp\,\mathrm{TE}}$ are $\kappa_{nl}^{\perp\,\mathrm{TE}} = Z_{n,l}^2$.

The second set is made of normalized modes directed along the cylinder axis $\hat{\mathbf{z}}$. We denote them with $\mathbf{j}^{\perp\mathtt{TM}}_{pnl}$, and they have the following expression

$$\mathbf{j}^{\perp\mathtt{TM}}_{\substack{e\\o}nl}(r,\phi) = \sqrt{\frac{2}{\pi}} \begin{pmatrix} \cos n\phi \\ \sin n\phi \end{pmatrix} \frac{J_n(Z_{n-1,l}r)}{J_n(Z_{n-1,l})} \hat{\mathbf{z}}, \tag{C.3}$$

where $n = \mathbb{N}_0$, $l \in \mathbb{N}$. The MQS TM eigenvalues $\kappa_{nl}^{\perp\,\mathrm{TM}}$ are $\kappa_{nl}^{\perp\,\mathrm{TM}} = Z_{n-1,l}^2$.

The quasistatic eigenvalues can be obtained by zeroing the denominator of the a_n (for $\chi_n^{\parallel}$ and $\kappa_{nl}^{\mathrm{TE}\,\perp}$) and b_n (for $\kappa_{nl}^{\mathrm{TM}\,\perp}$) coefficients for the scattering from a plane wave, given in Eqs. (8.32) and (8.30), respectively, in [87], in the limit $x \to 0$. As for the sphere, the full-wave plasmonic and dielectric eigenvalues can be found by following these solutions as x varies.

C.2 Cylinder dimer

We now consider only the electroquasistatic modes of a cylinder homo-dimer with gap size δ and radius R, and total linear dimension D, as sketched in Fig. C.2. We choose the radius of the smallest circle enclosing the dimer cross-section as characteristic length ℓ_c of the object, i.e. $\ell_c = D/2$. Accordingly, the object size parameter x is $x = \frac{\omega}{c_0}\frac{D}{2}$. We shall use a bipolar coordinate system (u, v), which are related to the rectangular coordinates (x,y) by the formulas [174]:

$$\mathrm{x} = \frac{R \sinh u}{\sinh \mu (\cosh u - \cos v)}, \qquad \mathrm{y} = \frac{R \sin v}{\sinh \mu (\cosh u - \cos v)}, \tag{C.4}$$

where $-\infty \leq u \leq \infty$, $0 \leq v < 2\pi$, and

$$\mu = \operatorname{arccosh}\left(1 + \frac{\delta}{2R}\right), \tag{C.5}$$

being arccosh the inverse hyperbolic cosine. The circular boundaries of the cylinder dimer coincide with the lines at $u = \mu$ and $u = -\mu$. We then normalize the coordinates by the characteristic length ℓ_c, namely $\mathbf{r} \to \mathbf{r}/(0.5D)$.

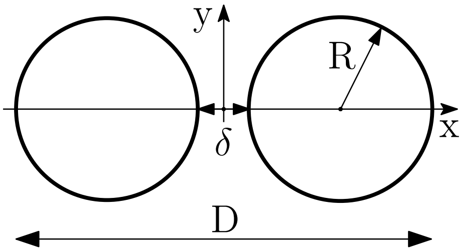

Figure C.2 – Cross-section of two infinite identical circular cylinders.

The structure normalized electroquasistatic modes $\mathbf{j}_n^{\parallel\pm}$ have the following expression [83]:

$$\mathbf{j}_n^{\parallel\pm}(u,v) = \sqrt{\frac{n}{8\pi}}\left(\cosh u - \cos v\right)$$
$$\begin{cases} e^{-n\,u}\left(e^{2n\mu}-1\right)\left[\hat{\mathbf{v}}\begin{pmatrix}\sin nv\\ \cos nv\end{pmatrix} + \hat{\mathbf{u}}\begin{pmatrix}\cos nv\\ -\sin nv\end{pmatrix}\right], & u \geq \mu \\ 2\left[\hat{\mathbf{v}}\begin{pmatrix}\sin nv\\ -\cos nv\end{pmatrix}\sinh nu - \hat{\mathbf{u}}\begin{pmatrix}\cos nv\\ -\sin nv\end{pmatrix}\cosh nu\right], & -\mu \leq u \leq \mu \\ e^{n\,u}\left(e^{2n\mu}-1\right)\left[-\hat{\mathbf{v}}\begin{pmatrix}-\sin nv\\ \cos nv\end{pmatrix}\sin nv + \hat{\mathbf{u}}\begin{pmatrix}\cos nv\\ \sin nv\end{pmatrix}\cos nv\right], & u \leq -\mu \end{cases} \tag{C.6}$$

where $n \in \mathbb{N}$. The corresponding EQS eigen-permittivities are mirror symmetric, i.e. $\varepsilon_n^{\parallel+}\varepsilon_n^{\parallel} = 1$, and have the following expression:

$$\varepsilon_n^{\parallel+} = -\coth n\mu, \tag{C.7}$$
$$\varepsilon_n^{\parallel-} = -\tanh n\mu. \tag{C.8}$$

The eigen-susceptibilities can be obtained as $\chi_n^{\parallel\pm} = \varepsilon_n^{\parallel\pm} - 1$. Both the modes and the eigenvalues depend only on the ratio between the gap size δ and the radius R. The modes $\mathbf{j}_n^{\parallel+}$ and $\mathbf{j}_n^{\parallel-}$ are bright and dark, respectively, as they exhibit non-zero and

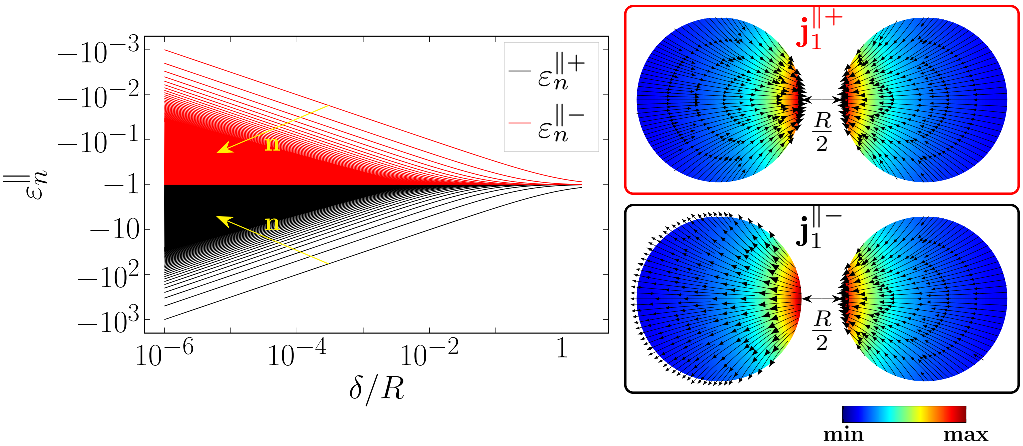

Figure C.3 – Bright ($\varepsilon_n^{\|+}$) and dark ($\varepsilon_n^{\|-}$) eigen-permittivities of a cylinder homo-dimer with radius R and gap-size δ, as a function of δ/R. On the right, field lines of the first EQS bright $\mathbf{j}_n^{\|+}$ and dark $\mathbf{j}_n^{\|-}$ current modes for $\delta/R = 1/2$.

zero electric dipole moment, defined in Eq. (A.6).

In Fig. C.3, we plot the eigen-permittivities $\varepsilon_n^{\|+}$ (black) and $\varepsilon_n^{\|-}$ (red) as a function of the relative gap size δ/R, parametrized by the mode index n, and an example of bright and dark modes for $\delta/R = 0.5$. For any relative gap size, as $n \to \infty$, all the eigen-permittivities tend to -1, which is the accumulation point of translational invariant plasmonic objects, regardless of their shape [71]. In the limit of well separated cylinders, i.e. $\delta/R \to \infty$, all the eigen-susceptibilities approach -1, and the scattering problem reduces to that of two non-interacting cylinders, whose eigen-susceptibilities are all located at -1. As δ decreases, the bright and dark eigen-susceptibilities shift toward more negative and positive values, respectively. Lower order eigen-susceptibilities shift more than high order eigen-susceptibilities.

The electric dipole moment $\mathbf{P}_n$ of the bright modes $\mathbf{j}_n^{\|+}$ has the following expression:

$$\mathbf{P}_n = \sqrt{8\pi \frac{\delta/R}{\delta/R + 4} k \, \mathrm{e}^{-n\mu}} \, \hat{\mathbf{x}}, \tag{C.9}$$

where $\hat{\mathbf{x}}$ is the unit vector directed along the structure axis (see Fig. C.2). Their radiation Q factor $\mathrm{Q}_n^{\|}$ is obtained by applying Eq. (2.127) of the main text:

$$x_n^2 \mathrm{Q}_n^{\|} = \frac{8}{|\chi_n^{\|+}|} \frac{1}{|\mathbf{P}_n|^2} = \frac{4 + \delta/R}{2\pi n \, \delta/R} \left(\mathrm{e}^{2n\mu} - 1 \right). \tag{C.10}$$

Appendix D

Sphere dimer

D.1 Methods

In this *methods* section, we show the derivation of the modes of a sphere dimer, by representing each dimer mode in terms of a weighted combination, i.e. hybridization of single-sphere modes. We also provide the explicit expressions for the corresponding hybridization coefficients given in Eq. 5.4.

At the very basis of any extension of the Mie theory to sphere dimers lies the vector spherical wave function (VSWF) addition theorem. This theorem enables the representation of the radiating VSWFs centred on one origin as an expansion of regular VSWFs centered on a different origin. The addition theorem was first derived in Refs. [175, 176], and it was later combined with the Mie theory in Refs. [177, 178]. Subsequently, it was significantly improved by many authors including Borghese et al. [179], Fuller et al. [180], and Mackowski [181, 182]. Very detailed introductions can be found in Refs. [183, 184].

Let us consider the problem of scattering by a dimer of spheres in free space. The geometry of the problem is sketched in Fig. 5.1. The spheres have radius R_1 and R_2, respectively, and they occupy the regions Ω_1 and Ω_2, while the surrounding space is denoted with Ω_3. The sphere Ω_1 is centred on the origin of a Cartesian coordinate system $O_1\mathbf{r}_1$, while the sphere Ω_2 is centred on the origin of a second Cartesian coordinate system $O_2\mathbf{r}_2$. The coordinate system $O_2\mathbf{r_2}$ is obtained by translating the coordinate system $O_1\mathbf{r_1}$ through a distance D along the z axis. The dimer is aligned along the direction of the z-axis in both coordinate systems. The size parameters x_1, x_2 of the spheres are defined in Eq. (5.1). The two spheres have the same material composition, which is assumed to be linear, nonmagnetic, isotropic, homogeneous in time and space, nondispersive in space, and time-dispersive with relative permittivity

$\varepsilon_R\,(\omega)$. The object is excited by a time harmonic electromagnetic field incoming from infinity $\mathrm{Re}\left\{\mathbf{E}_{\text{inc}} e^{-i\omega t}\right\}$. The expression of the scattered field $\mathbf{E}_{\text{sca}}$ in the whole space $\mathbb{R}^3$ is

$$\mathbf{E}_{\text{sca}} = (\varepsilon_R - 1) \sum_{q=1}^{\infty} \frac{1}{\xi_q - \varepsilon_R} \frac{\langle \mathbf{w}_q, \mathbf{E}_{\text{inc}} \rangle_{\Omega_1 \cup \Omega_2}}{\langle \mathbf{w}_q, \mathbf{w}_q \rangle_{\Omega_1 \cup \Omega_2}}\, \mathbf{W}_q, \tag{D.1}$$

where $\xi_q, \mathbf{w}_q$ are the q-th dimer material-independent mode and eigen-permittivity, solution of the homogeneous problem in Eq. (4.4), and $\mathbf{W}_q$ its extension to $\mathbb{R}^3$, satisfying Eqs. (4.7)-(4.8). Here, $\langle \mathbf{A}, \mathbf{B} \rangle_{\Omega_1 \cup \Omega_2} = \int_{\Omega_1 \cup \Omega_2} \mathbf{A} \cdot \mathbf{B}\, dV$.

Exploiting the symmetry of the problem, we can expand the vector field $\mathbf{W}$ in terms of the material-independent modes (extended in $\mathbb{R}^3$) of the two isolated spheres $\mathbf{U}^{\mathtt{TM}}_{pmn}$, $\mathbf{V}^{\mathtt{TM}}_{pmnl}$, $\mathbf{V}^{\mathtt{TE}}_{pmnl}$, given in Eq. (4.26-4.28), where $p \in \{e, o\}$ denote even and odd azimuthal dependence, $n \in \mathbb{N}$ is the mode multipolar order, $0 \leq m \leq n$ is the azimhutal quantum number, and $l \in \mathbb{N}$ is the mode order (see Sec. 4.2). Thus, the dimer modes will depend on the indices p, m, and have the following expansion:

$$\mathbf{W}_{pm} = \sum_{j=1}^{2} \mathbf{W}^{(j)}_{pm}, \tag{D.2}$$

where $\mathbf{W}^{(j)}_{pm}$ in the reference system $O_j \mathbf{r}_j$ assumes the following form:

$$\mathbf{W}^{(j)}_{pm}\,(\mathbf{r}_j) = \sum_{nl} \left\{ a^{\mathtt{TM}|j}_{pmn}\, \mathbf{U}^{\mathtt{TM}|j}_{pmn}(\mathbf{r}_j) + \sum_{l=1}^{\infty} \left[b^{\mathtt{TM}|j}_{pmnl}\, \mathbf{V}^{\mathtt{TM}|j}_{pmnl}(\mathbf{r}_j) + b^{\mathtt{TE}|j}_{\bar{p}mnl}\, \mathbf{V}^{\mathtt{TE}|j}_{\bar{p}mnl}(\mathbf{r}_j) \right] \right\}, \tag{D.3}$$

where $\sum\limits_{nl} = \sum\limits_{n=\max(1,m)}^{\infty} \sum\limits_{l=1}^{\infty}$, $\bar{(\cdot)}$ is the binary operator defined as $\bar{e} = o$ and $\bar{o} = e$. By using Eqs. (4.26-4.28) into D.3 we obtain:

$$\mathbf{W}^{(j)}_{pm}\,(\mathbf{r}_j) = \begin{cases} \sum\limits_{nl} \Big[a^{\mathtt{TM}|j}_{pmn} \mathbf{N}^{(1)}_{pmn} \left(\sqrt{\varepsilon^{\mathtt{TM}}_{n}}\, x_j \mathbf{r}_j \right) + b^{\mathtt{TM}|j}_{pmnl} \mathbf{N}^{(1)}_{pmn} \left(\sqrt{\eta^{\mathtt{TM}}_{nl}}\, \mathbf{r}_j \right) \\ \qquad + b^{\mathtt{TE}|j}_{\bar{p}mnl} \mathbf{M}^{(1)}_{\bar{p}mn} \left(\sqrt{\eta^{\mathtt{TE}}_{nl}}\, \mathbf{r}_j \right) \Big] \quad \mathbf{r}_j \in \Omega_j, \\ \\ \sum\limits_{nl} \Big[\left(a^{\mathtt{TM}|j}_{pmn} \tau^{\mathtt{TM}|j}_{n} + b^{\mathtt{TM}|j}_{pmnl} \sigma^{\mathtt{TM}|j}_{nl} \right) \mathbf{N}^{(3)}_{pmn}\,(x_j \mathbf{r}_j) \\ \qquad + b^{\mathtt{TE}|j}_{\bar{p}mnl} \sigma^{\mathtt{TE}|j}_{nl} \mathbf{M}^{(3)}_{\bar{p}mn}\,(x_j \mathbf{r}_j) \Big]\, \mathbf{r}_j \in \Omega_{\bar{j}} \bigcup \Omega_3. \end{cases} \tag{D.4}$$

where $\mathbf{M}^{(1)}_{pmn}, \mathbf{N}^{(1)}_{pmn}$ and $\mathbf{M}^{(3)}_{pmn}, \mathbf{N}^{(3)}_{pmn}$ are the regular and radiating VSWFs. given in Eq. (B.17). We have defined the following binary operator $\bar{(\cdot)}$: $\bar{1} = 2$ and $\bar{2} = 1$. Furthermore, we have implicitly normalized the coordinates in the j-th sphere by its radius ($\mathbf{r}_j \to \mathbf{r}_j / R_j$).

The field incident on the j-th sphere is only the field produced by the remaining $\bar{j}$-th sphere. Therefore, by applying Eq. (D.1) to the j-th sphere, we obtain:

$$\begin{aligned}
a^{\mathtt{TM}|j}_{pmn} &= \frac{\xi - 1}{\varepsilon^{\mathtt{TM}|j}_{n} - \xi}\, \mathcal{P}_j \left\{ \mathbf{u}^{\mathtt{TM}|j}_{pmn}, \mathbf{W}^{(\bar{j})}_{pm} \right\}, \\
b^{\mathtt{TM}|j}_{pmnl} &= \frac{\xi - 1}{\eta^{\mathtt{TM}|j}_{nl}/x_j^2 - \xi}\, \mathcal{P}_j \left\{ \mathbf{v}^{\mathtt{TM}|j}_{pmnl}, \mathbf{W}^{(\bar{j})}_{pm} \right\}, \\
b^{\mathtt{TE}|j}_{\bar{p}mnl} &= \frac{\xi - 1}{\eta^{\mathtt{TE}|j}_{nl}/x_j^2 - \xi}\, \mathcal{P}_j \left\{ \mathbf{v}^{\mathtt{TE}|j}_{\bar{p}mnl}, \mathbf{W}^{(\bar{j})}_{pm} \right\},
\end{aligned} \tag{D.5}$$

where the operator $\mathcal{P}_j\left\{\cdot\right\}$ is defined in Eq. (5.5) of the main text.

In order to apply D.5, and take full advantage of the orthogonality among VSWFs, we have to represent the field $\mathbf{W}^{(\bar{j})}_{pm}$ in the reference system $O_{\bar{j}}\mathbf{r}_{\bar{j}}$. We now use the VSWF translation-theorem, which enables us to represent the radiating VSWF centred at one origin, i.e. $\mathbf{r}_{\bar{j}}$, as an expansion of regular VSWF centered about another origin $\mathbf{r}_j$. It can be written as:

$$\begin{aligned}
\begin{pmatrix} \mathbf{M}^{(3)}_{pmn}\left(x_j \mathbf{r}_{\bar{j}}\right) \\ \mathbf{N}^{(3)}_{pmn}\left(x_j \mathbf{r}_{\bar{j}}\right) \end{pmatrix} = \sum_{\nu=\max(1,m)}^{\infty} \Bigg[& \begin{pmatrix} Q^{(j)}_{\mathtt{MM}_{mn\nu}}(d)\, \mathbf{M}^{(1)}_{pm\nu}\left(x_j \mathbf{r}_j\right) \\ Q^{(j)}_{\mathtt{NN}_{mn\nu}}(d)\, \mathbf{N}^{(1)}_{pm\nu}\left(x_j \mathbf{r}_j\right) \end{pmatrix} \\
& + \begin{pmatrix} Q^{(j)}_{\mathtt{MN}_{pmn\nu}}(d)\, \mathbf{N}^{(1)}_{\bar{p}m\nu}\left(x_j \mathbf{r}_j\right) \\ Q^{(j)}_{\mathtt{NM}_{pmn\nu}}(d)\, \mathbf{M}^{(1)}_{\bar{p}m\nu}\left(x_j \mathbf{r}_j\right) \end{pmatrix} \Bigg]
\end{aligned} \tag{D.6}$$

where the translation-addition coefficients are given by [172, 185]:

$$\begin{aligned}
Q^{(j)}_{\mathtt{MM}_{m\nu n}}(d) = Q^{(j)}_{\mathtt{NN}_{m\nu n}}(d) &= \frac{1}{2}\left[A^{mn}_{m\nu}(d, \bar{j} \to j) + \frac{\Gamma_{m\nu}}{\Gamma_{mn}} A^{-mn}_{-m\nu}(d, \bar{j} \to j) \right], \\
Q^{(j)}_{\mathtt{MN}_{\substack{o\\e}m\nu n}}(d) = Q^{(j)}_{\mathtt{NM}_{\substack{o\\e}m\nu n}}(d) &= \pm\frac{i}{2}\left[B^{mn}_{m\nu}(d, \bar{j} \to j) - \frac{\Gamma_{m\nu}}{\Gamma_{mn}} B^{-mn}_{-m\nu}(d, \bar{j} \to j) \right],
\end{aligned} \tag{D.7}$$

$$
\begin{aligned}
&\Gamma_{mn} = (-1)^m \frac{(n-m)!}{(n+m)!},\\
&A^{mn}_{m\nu}(d, \bar{j} \to j) = \begin{cases} (-1)^{n+\nu} \dfrac{E_{m\nu}}{E_{mn}} C_0 \displaystyle\sum_{q=0}^{\min(n,\nu)} i^p \, C_p \, a_{-mn\nu mq} \, h^{(1)}_p(d) & j = 1, \\ \dfrac{E_{m\nu}}{E_{mn}} C_0 \displaystyle\sum_{q=0}^{\min(n,\nu)} i^p \, C_p \, a_{-mn\nu mq} \, h^{(1)}_p(d) & j = 2, \end{cases}\\
&B^{mn}_{m\nu}(d, \bar{j} \to j) = \begin{cases} (-1)^{n+\nu} \dfrac{E_{m\nu}}{E_{mn}} C_0 \displaystyle\sum_{q=0}^{\min(n,\nu)} i^{p+1} \, C_p \, b_{mn\nu mq} \, h^{(1)}_{p+1}(d) & j = 1, \\ \dfrac{E_{m\nu}}{E_{mn}} C_0 \displaystyle\sum_{q=0}^{\min(n,\nu)} i^{p+1} \, C_p \, b_{mn\nu mq} \, h^{(1)}_{p+1}(d) & j = 2, \end{cases}\\
&p = n + \nu - 2q,\\
&E_{mn} = i^n \sqrt{\frac{(2n+1)(n-m)!}{n(n+1)(m+n)!}},\\
&C_0 = \frac{1}{2}(-1)^m \sqrt{\frac{(2\nu+1)(2n+1)(\nu-m)!(m+n)!}{\nu(\nu+1)n(n+1)(m+\nu)!(n-m)!}},\\
&C_p = (\nu+1)\nu + (n+1)n - p(p+1),
\end{aligned}
\tag{D.8}
$$

$a_{mn\nu mq}$ are the Gaunt coefficients and $b_{mn\nu mq}$ are combinations of the Gaunt coefficients, whose expression can be found in Refs. [172, 185].

By substituting Eq. D.4 into Eq. D.5 and by using the Eq. D.6-D.8, and truncating the summation indices n and l to the values $N_{\max}$ and $L_{\max}$, we obtain three coupled sets of homogeneous equations for any given pair of $m \in \mathbb{N}_0$ and $p = e, o$

$$
\begin{aligned}
\frac{1}{\varepsilon_n^{\mathtt{TM}|j} - 1} \Big\{ a^{\mathtt{TM}|j}_{pmn} + \mathcal{P}_j \left\{ \mathbf{u}^{\mathtt{TM}|j}_{pmn}, \mathbf{N}^{(1)}_{pmn}\left(x_j \mathbf{r}_j\right) \right\} \sum_{\substack{\nu= \\ \max(1,m)}}^{N_{\max}} \sum_{s=1}^{L_{\max}} \Big[b^{\mathtt{TE}|\bar{j}}_{\bar{p}m\nu s} \sigma^{\mathtt{TE}|\bar{j}}_{\nu s} Q^{(j)}_{\mathtt{MN}_{pm\nu n}} \\
+ \left(a^{\mathtt{TM}|j}_{pm\nu} \tau^{\mathtt{TM}|\bar{j}}_{\nu} + b^{\mathtt{TM}|\bar{j}}_{pm\nu s} \sigma^{\mathtt{TM}|\bar{j}}_{\nu s} \right) Q^{(j)}_{\mathtt{NN}_{m\nu n}} \Big] \Big\} = \frac{1}{\chi} a^{\mathtt{TM}|j}_{pmnl}
\end{aligned}
\tag{D.9}
$$

$$
\begin{aligned}
\frac{1}{\eta_{nl}^{\mathtt{TM}|j} / x_j^2 - 1} \Big\{ b^{\mathtt{TM}|j}_{pmn} + \mathcal{P}_j \left\{ \mathbf{v}^{\mathtt{TM}|j}_{pmnl}, \mathbf{N}^{(1)}_{pmn}\left(x_j \mathbf{r}_j\right) \right\} \sum_{\substack{\nu= \\ \max(1,m)}}^{N_{\max}} \sum_{s=1}^{L_{\max}} \Big[b^{\mathtt{TE}|\bar{j}}_{\bar{p}m\nu s} \sigma^{\mathtt{TE}|\bar{j}}_{\nu s} Q^{(j)}_{\mathtt{MN}_{pm\nu n}} \\
+ \left(a^{\mathtt{TM}|j}_{pm\nu} \tau^{\mathtt{TM}|\bar{j}}_{\nu} + b^{\mathtt{TM}|\bar{j}}_{pm\nu s} \sigma^{\mathtt{TM}|\bar{j}}_{\nu s} \right) Q^{(j)}_{\mathtt{NN}_{m\nu n}} \Big] \Big\} = \frac{1}{\chi} b^{\mathtt{TM}|j}_{pmnl}
\end{aligned}
\tag{D.10}
$$

$$\frac{1}{\eta_{nl}^{\mathtt{TE}|j}/x_j^2-1}\Big\{b_{\bar{p}mnl}^{\mathtt{TE}|j}+\mathcal{P}_j\left\{\mathbf{v}_{\bar{p}mn}^{\mathtt{TE}|j},\mathbf{M}_{\bar{p}mn}^{(1)}\left(x_j\mathbf{r}_j\right)\right\}\sum_{\substack{\nu=\\ \max(1,m)}}^{N_{\max}}\sum_{s=1}^{L_{\max}}\Big[b_{\bar{p}m\nu s}^{\mathtt{TE}|\bar{j}}\sigma_{\nu s}^{\mathtt{TE}|\bar{j}}Q_{\mathtt{MM}_{m\nu n}}^{(j)}$$

$$+\left(a_{pm\nu}^{\mathtt{TM}|\bar{j}}\tau_{\nu}^{\mathtt{TM}|\bar{j}}+b_{pm\nu s}^{\mathtt{TM}|\bar{j}}\sigma_{\nu s}^{\mathtt{TM}|\bar{j}}\right)Q_{\mathtt{NM}_{\bar{p}m\nu n}}^{(j)}\Big]\Big\}=\frac{1}{\chi}b_{\bar{p}mnl}^{\mathtt{TE}|j}$$

$$\text{with}\begin{pmatrix} n=\max\left(1,m\right),\ldots,N_{\max}\\ l=1,\ldots,L_{\max}\\ j=1,2\end{pmatrix}\qquad\text{(D.11)}$$

where $\chi=\xi-1$ is the eigen-susceptibility of the two sphere. For any given m and p indices, we have a system of $Q_{max}=\left[6L_{\max}\left(N_{\max}-\max\left(1,m\right)+1\right)\right]$ equations. It can be written in the matrix form:

$$\mathbf{T}^{(m,p)}\mathbf{y}^{(m,p)}=\frac{1}{\chi^{(m,p)}}\mathbf{y}^{(m,p)}\qquad\text{(D.12)}$$

where $\mathbf{y}_{pm}=\left[a_{pmn}^{\mathtt{TM}|j},\,b_{pmnl}^{\mathtt{TM}|j},\,b_{pmnl}^{\mathtt{TE}|j}\right]^T$ is the vector containing the expansion coefficients. We numerically evaluate the finite number of eigenvectors of the matrix $\mathbf{T}^{(m,p)}$.

For any pair of indices p,m, we have the eigenvalues $\chi_q^{(p,m)}$ for $q=1,\ldots,Q_{max}$. Starting from the eigenvalues $\chi_q^{(p,m)}$, it is possible to obtain the dimer eigenpermittivities ξ_{pmq} through the relation: $\xi_{pmq}=\chi_q^{(p,m)}+1$. The q-th eigenvector of the discrete problem is denoted as $\mathbf{y}_{pmq}$, and its coefficients are $[a_{pmq\,n}^{\mathtt{TM}|j},\,b_{pmq\,nl}^{\mathtt{TM}|j},\,b_{pmq\,nl}^{\mathtt{TM}|j}]$.

The electric-field modes can be obtained from the coefficient eigenvector $\mathbf{y}_{pmq}$ by using Eqs. D.2-D.4

$$\mathbf{W}_{pmq}^{(j)}=\sum_{j=1}^{2}\mathbf{W}_{pmq}^{(j)},\qquad\text{(D.13)}$$

$$\mathbf{W}_{pmq}^{(j)}\left(\mathbf{r}_j\right)=\sum_{nl}\left\{a_{pmq\,n}^{\mathtt{TM}|j}\,\mathbf{U}_{pmn}^{\mathtt{TM}|j}(\mathbf{r}_j)+\sum_{l=1}^{\infty}\left[b_{pmq\,nl}^{\mathtt{TM}|j}\,\mathbf{V}_{pmnl}^{\mathtt{TM}|j}(\mathbf{r}_j)+b_{\bar{p}mq\,nl}^{\mathtt{TE}|j}\,\mathbf{V}_{\bar{p}mnl}^{\mathtt{TE}|j}(\mathbf{r}_j)\right]\right\},\qquad\text{(D.14)}$$

In Eq. D.13 the mode $\mathbf{W}_{pmq}$ within each sphere is represented in terms of the superposition of two contributions $\mathbf{W}_{pmq}^{(1)}$ and $\mathbf{W}_{pmq}^{(2)}$ centered in different reference systems. In other words, the dimer mode within each sphere is represented in terms of the isolated sphere modes of the sphere 1 *and* of the sphere 2. Nevertheless, it is possible to overcome this problem by representing the dimer electric field mode $\mathbf{W}_{pmq}$ within the j-th sphere exclusively in terms of the isolated sphere modes $\mathbf{U}_{pmn}^{\mathtt{TM}}$, $\mathbf{V}_{pmnl}^{\mathtt{TM}}$, $\mathbf{V}_{pmnl}^{\mathtt{TE}}$ by using the translation-addition theorem for the VSWFs. Thus, we obtain the following representation of $\mathbf{W}_{pmq}$:

$$\mathbf{W}_{pmq}(\mathbf{r}_j) = \begin{cases} \displaystyle\sum_{nl} \Big[c^{\mathtt{TM}|j}_{pmq\,n}\, \mathbf{N}^{(1)}_{pmn} \left(\sqrt{\varepsilon^{\mathtt{TM}}_{n}} x_j \mathbf{r}_j\right) + d^{\mathtt{TM}|j}_{pmq\,nl}\, \mathbf{N}^{(1)}_{pmn} \left(\sqrt{\eta^{\mathtt{TM}}_{nl}} \mathbf{r}_j\right) \\ \qquad\qquad + d^{\mathtt{TE}|j}_{\bar{p}mq\,nl}\, \mathbf{M}^{(1)}_{\bar{p}mn} \left(\sqrt{\eta^{\mathtt{TE}}_{nl}} \mathbf{r}_j\right)\Big] \qquad \forall \mathbf{r}_j \in \Omega_j, \\ \\ \displaystyle\sum_{j=1}^{2} \sum_{nl} \Big[\Big(a^{\mathtt{TM}|j}_{pmq\,n} \tau^{\mathtt{TM}|j}_{n} + b^{\mathtt{TM}|j}_{pmq\,nl} \sigma^{\mathtt{TM}|j}_{nl} \Big]\, \mathbf{N}^{(3)}_{pmn} \left(x_j \mathbf{r}_j\right) \\ \qquad\qquad + b^{\mathtt{TE}|j}_{\bar{p}mq\,nl} \sigma^{\mathtt{TE}|j}_{nl} \mathbf{M}^{(3)}_{\bar{p}mn} \left(x_j \mathbf{r}_j\right)\Big], \qquad \forall \mathbf{r}_j \in \Omega_3, \end{cases} \tag{D.15}$$

where the coefficients $\{c^{\mathtt{TM}|j}_{pmq\,n},\, d^{\mathtt{TM}|j}_{pmq\,nl},\, d^{\mathtt{TE}|j}_{\bar{p}mq\,nl}\}$ are:

$$\begin{aligned} c^{\mathtt{TM}|j}_{pmq\,n} &= a^{\mathtt{TM}|j}_{pmq\,n} + \mathcal{P}_j \left\{ \mathbf{u}^{\mathtt{TM}|j}_{pmn}, \mathbf{N}^{(1)}_{pmn}\left(x_j \mathbf{r}_j\right)\right\} \sum_{\substack{\nu=\\ \max(1,m)}}^{N_{\max}} \sum_{s=1}^{L_{\max}} \Big[b^{\mathtt{TE}|\bar{j}}_{\bar{p}mq\,\nu s} \sigma^{\mathtt{TE}|\bar{j}}_{\nu s} Q^{(j)}_{\mathtt{MN}_{pm\nu n}} \\ &\qquad + \left(a^{\mathtt{TM}|j}_{pmq\,\nu} \tau^{\mathtt{TM}|\bar{j}}_{\nu} + b^{\mathtt{TM}|\bar{j}}_{pmq\,\nu s} \sigma^{\mathtt{TM}|\bar{j}}_{\nu s} \right) Q^{(j)}_{\mathtt{NN}_{m\nu n}} \Big] \Big\}, \\ d^{\mathtt{TM}|j}_{pmq\,nl} &= b^{\mathtt{TM}|j}_{pmq\,nl} + \mathcal{P}_j \left\{ \mathbf{v}^{\mathtt{TM}|j}_{pmn}, \mathbf{N}^{(1)}_{pmn}\left(x_j \mathbf{r}_j\right)\right\} \sum_{\substack{\nu=\\ \max(1,m)}}^{N_{\max}} \sum_{s=1}^{L_{\max}} \Big[b^{\mathtt{TE}|\bar{j}}_{\bar{p}mq\,\nu s} \sigma^{\mathtt{TE}|\bar{j}}_{\nu s} Q^{(j)}_{\mathtt{MN}_{pm\nu n}} \\ &\qquad + \left(a^{\mathtt{TM}|j}_{pmq\,\nu} \tau^{\mathtt{TM}|\bar{j}}_{\nu} + b^{\mathtt{TM}|\bar{j}}_{pmq\,\nu s} \sigma^{\mathtt{TM}|\bar{j}}_{\nu s} \right) Q^{(j)}_{\mathtt{NN}_{m\nu n}} \Big] \Big\}, \\ d^{\mathtt{TE}|j}_{\bar{p}mq\,nl} &= b^{\mathtt{TE}|j}_{\bar{p}mq\,nl} + \mathcal{P}_j \left\{ \mathbf{v}^{\mathtt{TE}|j}_{\bar{p}mn}, \mathbf{M}^{(1)}_{\bar{p}mn}\left(x_j \mathbf{r}_j\right)\right\} \sum_{\substack{\nu=\\ \max(1,m)}}^{N_{\max}} \sum_{s=1}^{L_{\max}} \Big[b^{\mathtt{TE}|\bar{j}}_{\bar{p}mq\,\nu s} \sigma^{\mathtt{TE}|\bar{j}}_{\nu s} Q^{(j)}_{\mathtt{MM}_{m\nu n}} \\ &\qquad + \left(a^{\mathtt{TM}|\bar{j}}_{pmq\,\nu} \tau^{\mathtt{TM}|\bar{j}}_{\nu} + b^{\mathtt{TM}|\bar{j}}_{pmq\,\nu s} \sigma^{\mathtt{TM}|\bar{j}}_{\nu s} \right) Q^{(j)}_{\mathtt{NM}_{\bar{p}m\nu n}} \Big] \Big\}. \end{aligned} \tag{D.16}$$

D.2 Scattering from an Ag dimer in the quasielectrostatic approximation

In this section, we investigate the scattering response of the Ag homo-dimer studied in Sec. 5.4.1, assuming this time the quasielectrostatic approximation. We use the formulation proposed in Chap. 2. The radius of each sphere is R and the edge-edge distance is $\Delta = R/4$. It is worth to remember that in the quasielectrostatic regime only the bright modes, i.e. modes that have a nonvanishing total dipole moment, contribute to the scattering efficiency.

Let us consider the scenario in which the dimer is excited by an electric field polarized along the dimer axis (z-axis). In Fig. D.1a we show the corresponding scattering efficiency. The two σ_{sca} peaks are caused by the modes $\mathbf{j}^{\parallel}_{e0\,1}$ and $\mathbf{j}^{\parallel}_{e0\,2}$. These modes exhibit nonvanishing total dipole moments along the z-axis. Their

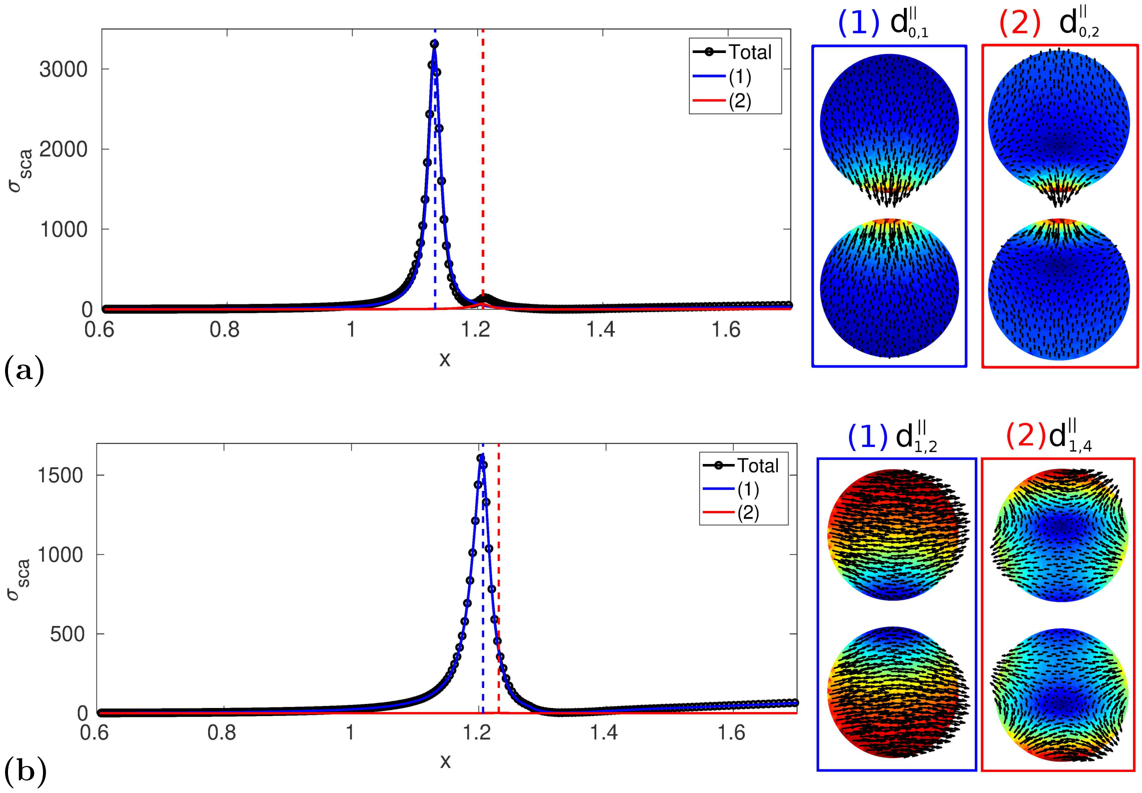

Figure D.1 – Scattering efficiency σ_{sca} of an Ag-spheres homo-dimer as a function of the spheres size parameter $x = \omega R/c_0$, obtained under the Q-ES approximation. The radius of each sphere is R, the edge-edge distance is $R/4$. The dimer is excited by an electric field polarized parallel to the dimer's axis (**a**), and orthogonally to the dimer axis (**b**). Partial scattering cross section (in color) of the two dominant dimer-modes whose projections on the $y = 0$ plane are shown on the right.

eigen-permittivities are $\varepsilon^{\|}_{e0\,1} = -3.16$ and $\varepsilon^{\|}_{e0\,2} = -1.82$. The corresponding resonant frequencies are $\omega = 5.01$ Prad/s and $\omega = 5.36$ Prad/s, respectively, while the resonant size parameters are $x = 1.13$ and $x = 1.21$, respectively which are highlighted in Fig. D.1a with vertical dashed lines.

In Fig. D.1b we show the scattering efficiency of the Ag dimer when it is excited by an electric field polarized transversely with respect to the dimer axis. The peak of σ_{sca} is due to the mode $\mathbf{j}^{\|}_{e1\,2}$. The mode $\mathbf{j}^{\|}_{e1\,4}$ gives a very small contribution. Their eigen-permittivities are $\varepsilon^{\|}_{e1\,2} = -1.83$, $\varepsilon^{\|}_{e1\,4} = -1.40$. The corresponding resonant frequencies are 5.35 Prad/s and 5.46 Prad/s and the corresponding resonant size parameters are $x = 1.20$ and $x = 1.23$, which are highlighted in Fig. D.1b with vertical dashed lines.

D.3 Additional results on the homo-dimer with gap size $\Delta = R/4$

D.3.1 Scattered electric field

We investigate the spatial distribution of the scattered electric field within the dimer in correspondence of the peaks of the scattering efficiency for the scenarios investigated in Sec. 5.4.

First, we consider the Ag homo-dimer with $R = 67.5\,\text{nm}$ and edge-edge distance $\Delta = R/4$. In Fig. D.2 we show the projection of the real part of the scattered electric field on the plane $y = 0$, for an Ag dimer, in correspondence of the σ_{sca} peaks of Fig. 5.10 at $x = 0.892$ (left) and at $x = 1.183$ (right). The homo-dimer is excited by a plane wave propagating parallel to the dimer axis and polarized orthogonally to it. It is apparent that the near field distribution at $x = 0.892$ consistently differs from the modes $\mathbf{u}_{e1\,1}$ which dominates the far-field response. On the contrary, at $x = 1.183$ (right) the near-field distribution closely resembles the mode $\mathbf{u}_{e1\,4}$, which is responsible for the second peak of σ_{sca}. Now, we investigate the scattering from a homo-dimer of the same geometry but made of a dielectric material, i.e. Silicon, with permittivity $\varepsilon_R = 16$. In Fig. D.3 we show the projection of the real part of the scattered electric field on the plane $y = 0$ in correspondence of the σ_{sca} peaks of Fig. 5.13, The homo-dimer is excited by a plane wave propagating orthogonally to the dimer axis and polarized along it. It is apparent from Fig. D.3 the effect of the propagation along the horizontal horizontal direction. Nevertheless, the electric field distributions in correspondence of the peaks only roughly resemble the modes shown in Fig. 5.13.

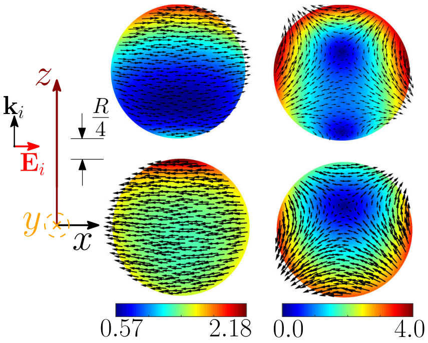

Figure D.2 – Real part of the projection on the $y = 0$ plane of the scattered electric field normalized by the incident magnitude E_0, at the first and second peak of the scattering spectrum of an Ag homo-dimer (shown in Fig. 5.10) when it is excited by a plane wave polarized orthogonally to the dimer axis.

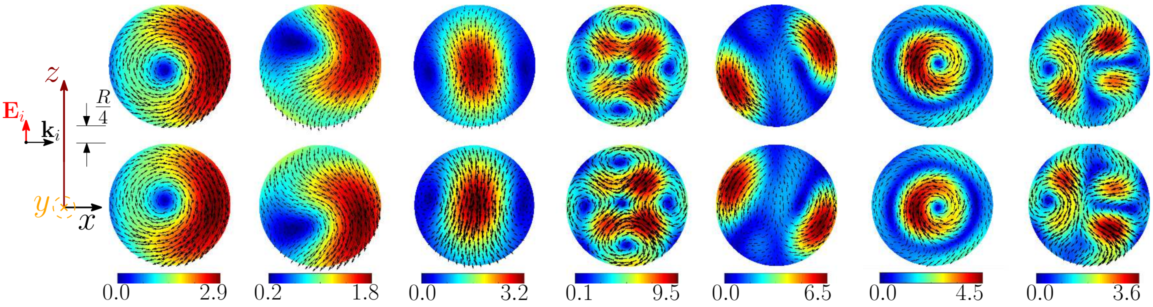

Figure D.3 – Real part of the projection on the $y = 0$ plane of the scattered electric field normalized by the incident magnitude E_0 at the peaks of the scattering spectrum of a Si homo-dimer (from left to right $x = 0.771$, $x = 0.901$ $x = 1.099$, $x = 1.366$, $x = 1.423$, $x = 1.584$, $x = 1.688$). The homo-dimer is excited by a plane wave polarized along to the dimer axis, and propagating orthogonally to it.

D.3.2 Scattering efficiencies

We consider the modes that are excited in an Ag homo-dimer by an incident field that is polarized along the dimer's axis $\hat{\mathbf{z}}$, while it is propagating along the transverse direction $\hat{\mathbf{x}}$. In Fig. D.4, we plot the scattering efficiency σ_{sca} obtained by using the material-independent-mode (MIM) expansion of Eq. 4.16 (black line), and by the direct GMM calculation (red dots) as a function of the size parameter x. The two results are in very good agreement. We also show in color the partial scattering efficiencies of three dominant dimer modes, whose real projections on the $y = 0$ plane are represented on the right. The analysis of the partial scattering efficiences reveals that the dimer mode $\mathbf{u}_{e0\,1}$ dominates the total scattering efficiency at its first peak, while the second peak is dominated by two different modes, viz. $\mathbf{u}_{e0\,3}$ and $\mathbf{u}_{e1\,3}$. Now, we investigate the scattering from a homo-dimer of the same geometry but made of a dielectric material, i.e. Silicon, with permittivity $\varepsilon_R = 16$.

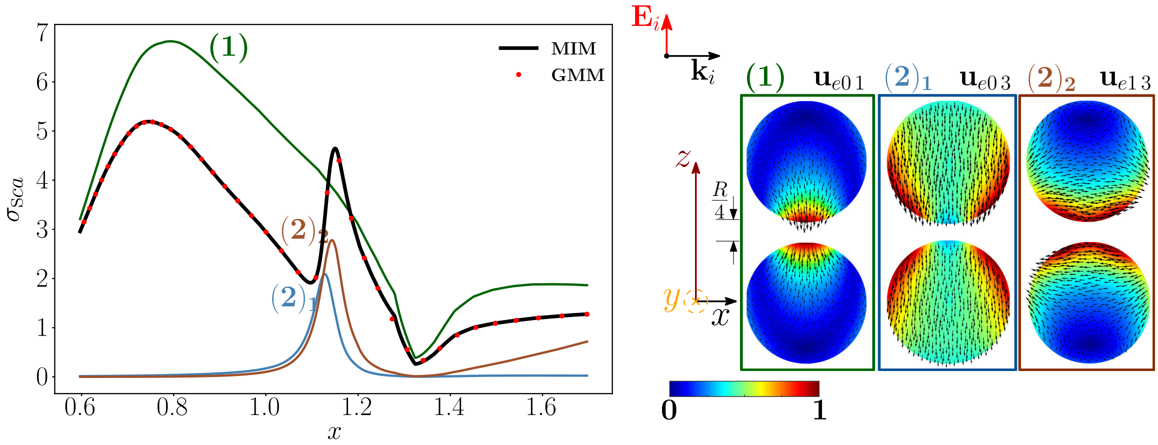

Figure D.4 – Scattering efficiency σ_{sca} of an Ag homo-dimer as a function of the spheres size parameter x, obtained via material-independent-mode expansion (black line) and by direct-calculation (red dots). The radius of each sphere is $R = 67.5\,\text{nm}$, the edge-edge distance $\Delta = R/4 = 16.875\,\text{nm}$. The dimer is excited by a plane wave polarized along the dimer axis $\hat{\mathbf{z}}$ and propagating along the transverse direction $\hat{\mathbf{x}}$. Partial scattering efficiencies (in color) of the three dominant dimer-modes whose $y = 0$-plane projections are shown on the right.

In Fig. D.5, we consider the scattering from a silicon homo-dimer. The incident plane wave is propagating along the dimer axis $\hat{\mathbf{z}}$, and polarized orthogonally to it. We plot the scattering efficiency obtained by the material-independent-mode expansion 4.16 (black line) and by direct GMM calculation [172] (red dots) as a function of the size parameter x. We also show in color the partial scattering efficiency of the eight dominant dimer modes, whose real projections on the $y = 0$ plane are represented on the right. The first and third peaks are dominated by the narrow dielectric modes $\mathbf{v}_{e1\,1}$ and $\mathbf{v}_{e1\,5}$, respectively. The peaks from four to seven are dominated by the narrow dielectric modes $\mathbf{v}_{e1\,6}$, $\mathbf{v}_{e1\,7}$, $\mathbf{v}_{e1\,9}$, $\mathbf{v}_{e1\,11}$, respectively. The second peak is due to the interference of the broad plasmonic mode $\mathbf{u}_{e1\,1}$ and the narrow dielectric mode $\mathbf{v}_{e1\,3}$, as confirmed by Tab. 4 in [140].

D.4 Scattering from an homo-dimer with gap size $\Delta = R$

In this section, we increase the gap size of the dimer from $R/4$ to R. Although, as we vary the distance between two spheres, the dimer modes change, we still denote, by an abuse of notation, the modes in this new configuration as $\mathbf{u}_{pm\,q}$ and $\mathbf{v}pm\,q$. The sorting of the dimer modes is induced by the corresponding eigen-permittivities. In the limit $x \to 0$, the eigen-permittivities are real and they are sorted in an ascending

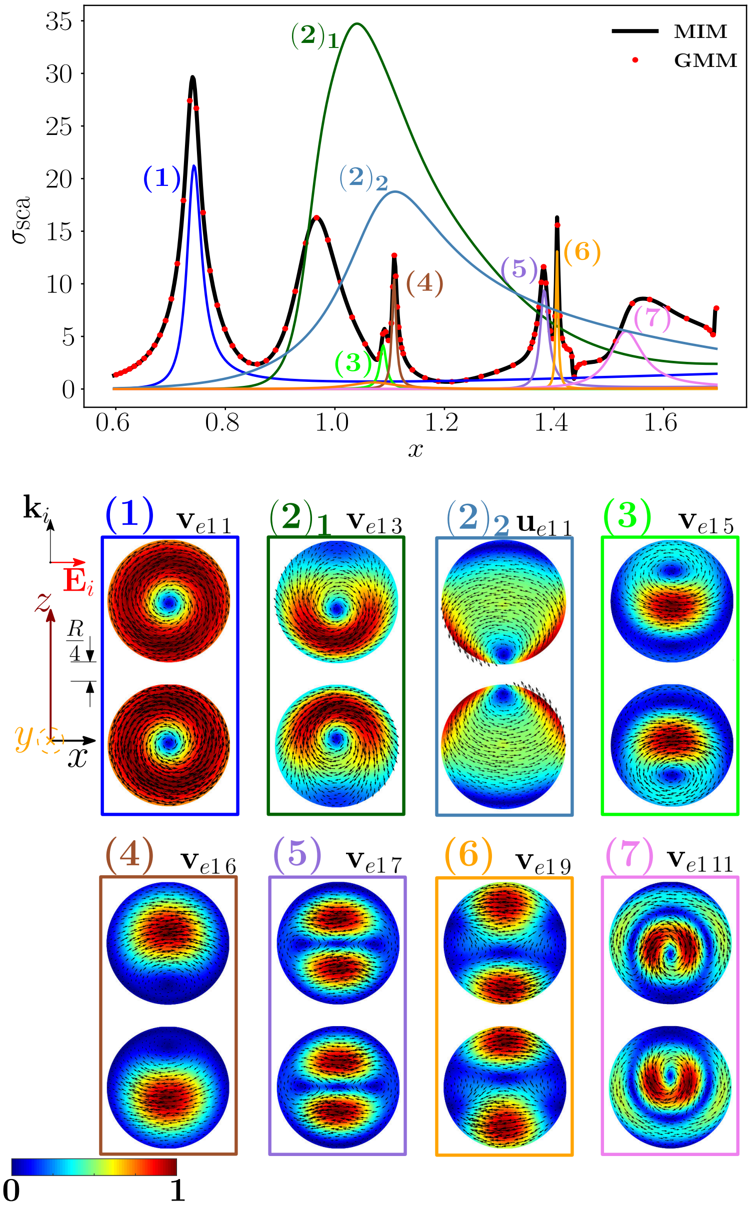

Figure D.5 – Scattering efficiency σ_{sca} of a Si-spheres homo-dimer as a function of the spheres size parameter x, obtained via the material-independent-mode expansion (black line) and by direct-calculation (red dots). The radius of each sphere is R, the edge-edge distance is $\Delta = R/4$. The dimer is excited by a plane wave propagating along the dimer's axis $\hat{\mathbf{z}}$ and polarized along the transverse direction $\hat{\mathbf{x}}$. Partial scattering efficiency (in color) of eight dominant dimer-modes whose real part projections on the $y = 0$ plane are shown on the right.

order. The same ordering is kept for finite values of x, by following each eigen-permittivity on the complex plane as x increases.

D.4.1 Transversely polarized Ag homo-dimer

We study a silver homo-dimer with $R = 67.5\,\mathrm{nm}$, and edge-edge separation $67.5nm$. We study a silver homo-dimer with $R = 67.5\,\mathrm{nm}$, and edge-edge separation $\Delta = 67.5\,\mathrm{nm}$. We consider the modes that are excited by an incident field polarized along the $\hat{\mathbf{x}}$-direction, and propagating along the direction $\hat{\mathbf{z}}$. In Fig. D.6, we plot the corresponding scattering efficiency obtained from both the mode expansion 4.16 (black line) and by direct GMM calculation (red dots). We also show in color the partial scattering efficiency of the dimer modes $\mathbf{u}_{e1\,1}$, $\mathbf{u}_{e1\,4}$ dominating the scattering response. Their projections on the $y = 0$ plane (real part) are shown on the right. The dimer mode $\mathbf{u}_{e1\,1}$, responsible for the first σ_{sca} peak originates from the hybridization of the single-sphere modes shown in Fig. D.7. In particular, the fundamental electric dipole $\mathbf{u}^{\mathtt{TM}}_{e11}$ and quadrupole $\mathbf{u}^{\mathtt{TM}}_{e12}$ and magnetic dipole $\mathbf{v}^{\mathtt{TE}}_{o111}$ interfere destructively in the close proximity of the gap, where the mode reaches a minimum.

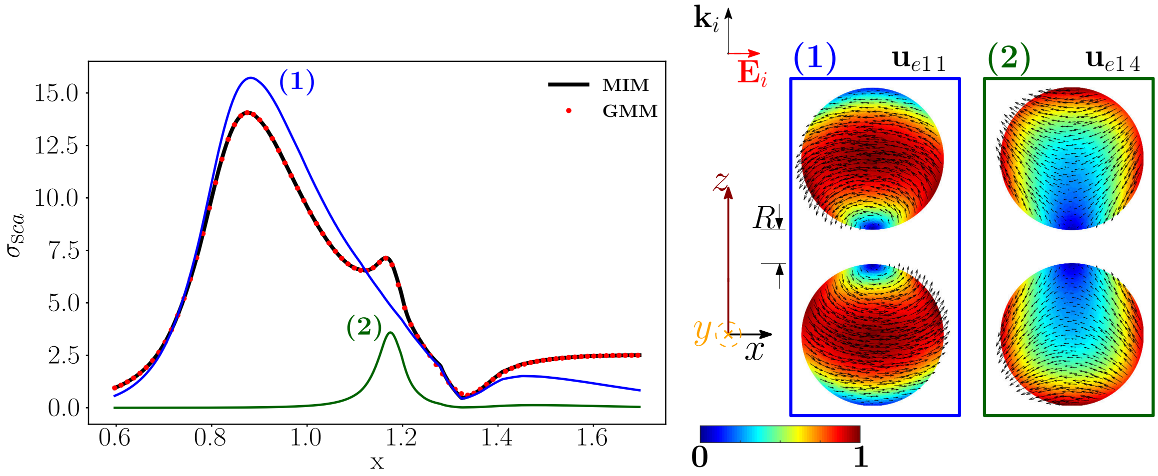

Figure D.6 – Scattering efficiency σ_{sca} of an Ag-spheres homo-dimer as a function of the spheres size parameter $x = \omega R/c_0$, obtained via the material-independent-mode expansion (black line) and by direct-calculation [172] (red dots). The radius of each sphere is $R = 67.5\,\mathrm{nm}$, the edge-edge distance is $\Delta = R = 67.5\,\mathrm{nm}$. The dimer is excited by a plane wave propagating along the dimer's axis and polarized orthogonally to it. Partial scattering cross section (in color) of two dominant dimer modes whose real part projections on the $y = 0$ plane are shown on the right.

The dimer mode $\mathbf{u}_{e1\,4}$ arises from the interaction of the single-sphere modes shown in Fig. D.8. The fundamental electric quadrupole $\mathbf{u}^{\mathtt{TM}}_{e121}$ and octupole $\mathbf{u}^{\mathtt{TM}}_{e13}$ interfere destructively in the proximity of the gap. The fundamental electric quadrupole and the electric dipole also interfere destructively in this region. The modes $\mathbf{u}^{\mathtt{TM}}_{e12}$ and $\mathbf{u}^{\mathtt{TM}}_{e13}$ interfere constructively in the region of each sphere opposite to the gap.

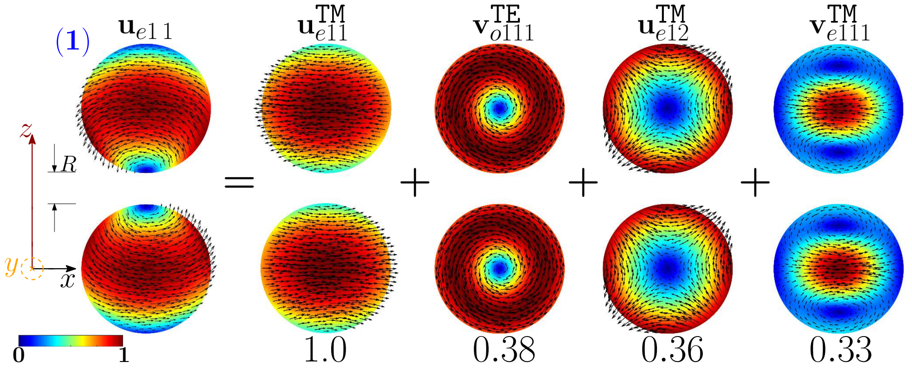

Figure D.7 – Decomposition of the dimer mode $\mathbf{u}_{e1\,1}$ at $x = 0.874$, in terms of hybridizing single-sphere modes (real part of the projection on the $y = 0$ plane). Each isolated sphere mode is multiplied by the corresponding expansion coefficient of Eq. (5.4). Below each single-sphere mode its hybridization weight $\tilde{H}^{|||\mathrm{TM}}_{e1\,1\,nl}$, $H^{|||\mathrm{TM}}_{e1\,1\,nl}$, or $H^{|||\mathrm{TE}}_{e1\,1\,nl}$ is shown. The nanoparticles distance is not to scale.

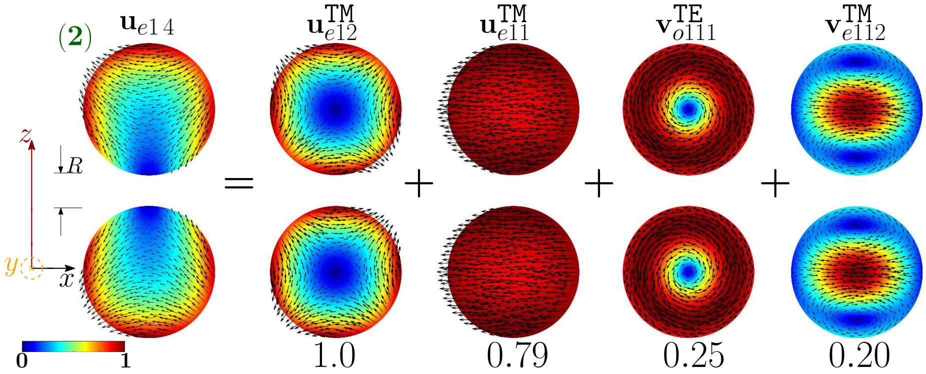

Figure D.8 – Decomposition of the dimer mode $\mathbf{u}_{e1\,4}$ at $x = 1.165$, in terms of hybridizing single-sphere modes (real part of the projection on the $y = 0$ plane). Each isolated sphere mode is multiplied by the corresponding expansion coefficient of Eq. (5.4). Below each single-sphere mode its hybridization weight $\tilde{H}^{|||\mathrm{TM}}_{e14\,nl}$, $H^{|||\mathrm{TM}}_{e14\,nl}$, or $H^{|||\mathrm{TE}}_{e114\,nl}$ is shown. The nanoparticles distance is not to scale.

D.4.2 Longitudinally polarized Si homo-dimer

Now, we investigate the scattering from a homo-dimer of the same geometry but made of silicon, with permittivity $\varepsilon_R = 16$. The incident plane wave is polarized along the dimer axis $\hat{\mathbf{z}}$, while it is propagating along the transverse direction $\hat{\mathbf{x}}$. In Fig. D.9, we plot the scattering efficiency obtained by the material-independent-mode expansion 4.16 (black line) and by direct GMM calculation [172] (red dots) as a function of the size parameter x. We also show in color the partial scattering efficiency of the seven dominant dimer modes, whose real projections on the $y = 0$ plane are represented on the right.

As shown in Fig. D.10, the dimer-mode $\mathbf{v}_{e1\,2}$, which is responsible for the first

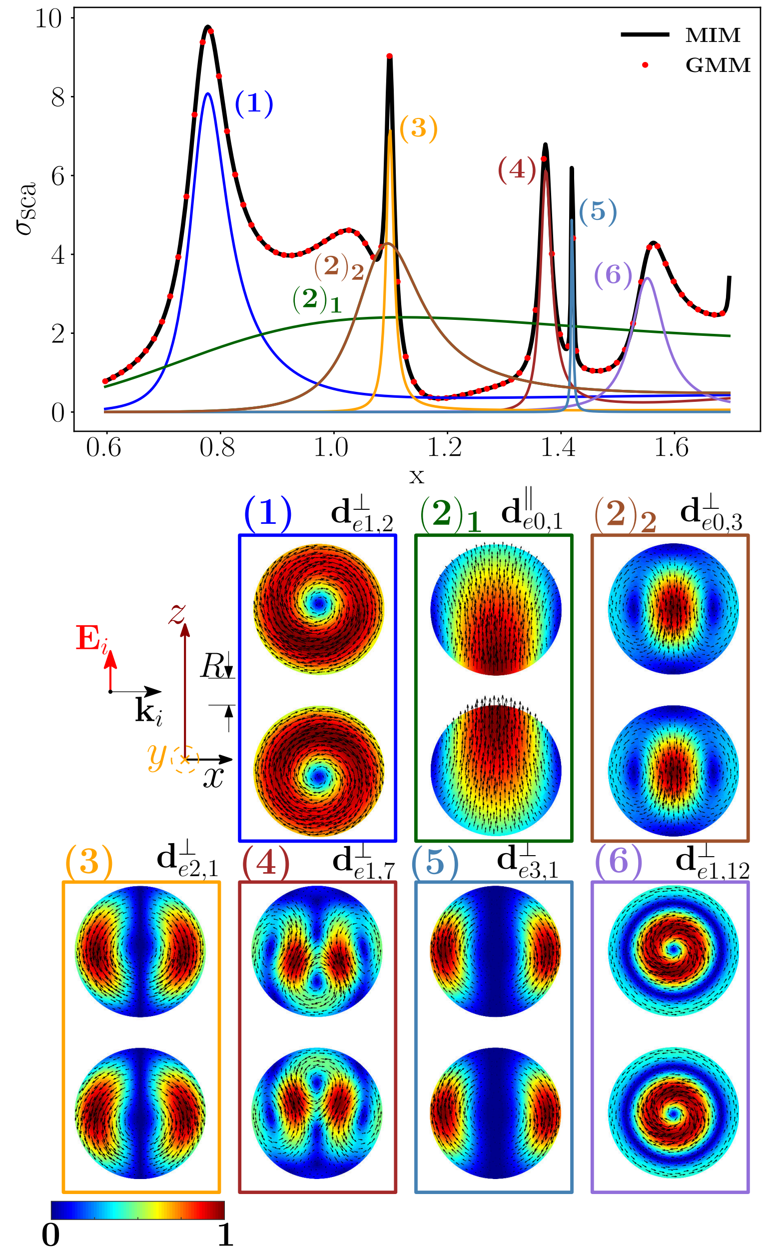

Figure D.9 – Scattering efficiency $\sigma_{\rm sca}$ of a Si-spheres homo-dimer as a function of the size parameter x, obtained via material-independent-mode expansion (black line) and by direct-calculation (red dots). The radius of each sphere is R, the edge-edge distance $\Delta = R$. The dimer is excited by a plane wave propagating orthogonally to the dimer and polarized along the dimer axis. Partial scattering efficiency (in color) of seven dominant dimer modes whose $y = 0$-plane projections are shown on the right.

peak of $\sigma_{\rm sca}$, arise from the hybridization of the fundamental magnetic dipole $\mathbf{v}^{\texttt{TE}}_{o111}$, and the fundamental and second order electric dipoles, i.e. $\mathbf{u}^{\texttt{TM}}_{e11}$, $\mathbf{v}^{\texttt{TM}}_{e111}$. The modes $\mathbf{u}^{\texttt{TM}}_{e11}$ and $\mathbf{v}^{\texttt{TM}}_{e111}$ constructively interact with $\mathbf{v}^{\texttt{TE}}_{o111}$ within the two hemispheres located closer to the gap and destructively in the remaining half-spheres. The net effect is to

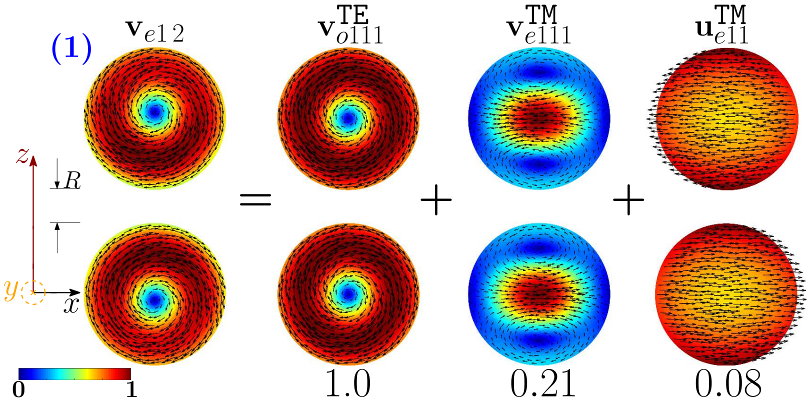

Figure D.10 – Decomposition of the dimer mode $\mathbf{v}_{e1\,2}$ at $x = 0.779$ in terms of hybridizing single-sphere modes (real part of the projection on the $y = 0$ plane). Each isolated sphere modes is multiplied by the expansion coefficients of Eq. (5.4). Below each single-sphere mode we also show its hybridization weight $\tilde{H}^{\perp|\mathtt{TM}}_{e12\,nl}$, $H^{\perp|\mathtt{TM}}_{e12\,nl}$, $H^{\perp|\mathtt{TE}}_{o12\,nl}$. The nanoparticles distance is not to scale.

move the vortex core away from the gap in each sphere.

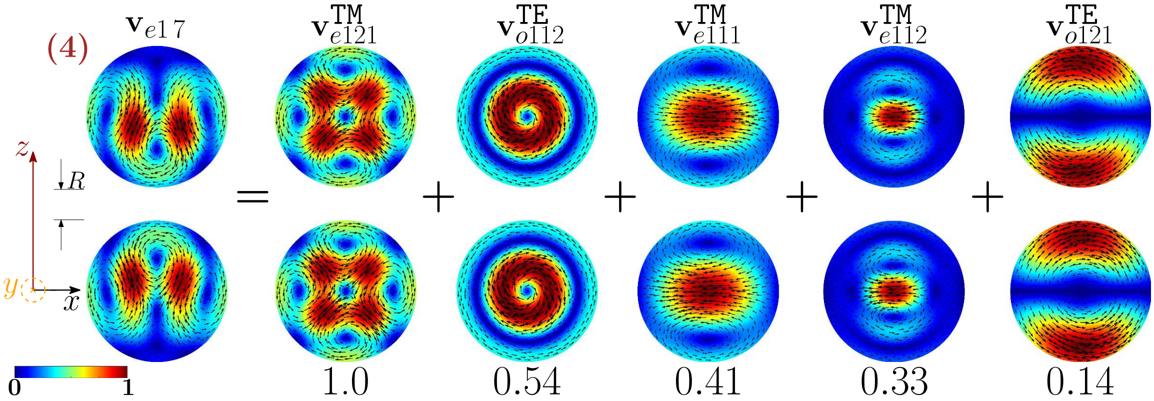

Figure D.11 – Decomposition of the dimer mode $\mathbf{v}_{e1\,7}$ at $x = 1.372$ in terms of hybridizing single-sphere modes (real part of the projection on the $y = 0$ plane). Each isolated sphere modes is multiplied by the expansion coefficients of Eq. (5.4). Below each single-sphere mode we also show its hybridization weight $H^{\perp|\mathtt{TM}}_{e17\,nl}$ ($H^{\perp|\mathtt{TE}}_{o17\,nl}$). The nanoparticles distance is not to scale.

The second σ_{sca} peak arise from the interference between the dimer-modes $\mathbf{u}_{e0\,1}$ and $\mathbf{v}_{e0\,3}$. The third peak is mainly due to the mode $\mathbf{v}_{e2\,1}$. In Fig. D.11 we show the dimer mode behind the fourth σ_{sca} peak, namely $\mathbf{v}_{e1\,7}$. It arises from the hybridization among the second order electric quadrupole $\mathbf{v}^{\mathtt{TM}}_{e121}$, which dominates the hybridization, and the second order magnetic dipole $\mathbf{v}^{\mathtt{TE}}_{o112}$, the third order electric dipole $\mathbf{v}^{\mathtt{TM}}_{e112}$, and the fundamental magnetic quadrupole $\mathbf{v}^{\mathtt{TE}}_{o121}$. We recall that for a gap size of $R/4$, the corresponding dimer-mode obtained shown in Fig. 5.17 of the main manuscript, the hybridization was dominated by the second order magnetic dipole.

Bibliography

[1] Stefan Alexander Maier. *Plasmonics: fundamentals and applications*. Springer Science & Business Media, 2007.

[2] Uwe Kreibig and Michael Vollmer. *Optical properties of metal clusters*. Vol. 25. Springer Science & Business Media, 2013.

[3] J. A. Schuller. “Plasmonics for extreme light concentration and manipulation.” In: *Nat. materials* 9 (2010).

[4] Jeffrey N Anker, W Paige Hall, Olga Lyandres, Nilam C Shah, Jing Zhao, and Richard P Van Duyne. “Biosensing with plasmonic nanosensors.” In: *Nature materials* 7.6 (2008), pp. 442–453.

[5] Martti Kauranen and Anatoly V Zayats. “Nonlinear plasmonics.” In: *Nature Photonics* 6.11 (2012), pp. 737–748.

[6] H. A. Atwater and A. Polman. “Plasmonics for improved photovoltaic devices.” In: *Nat. Mater.* 9 (2010), pp. 205–213.

[7] Alexandre Aubry, Dang Yuan Lei, Antonio I. Fernández-Domínguez, Yannick Sonnefraud, Stefan A. Maier, and J. B. Pendry. “Plasmonic Light-Harvesting Devices over the Whole Visible Spectrum.” In: *Nano Letters* 10.7 (July 14, 2010). Publisher: American Chemical Society, pp. 2574–2579. ISSN: 1530-6984.

[8] Nader Engheta and Richard W. Ziolkowski. *Metamaterials: Physics and Engineering Explorations*. Google-Books-ID: 51e0UkEuBP4C. John Wiley & Sons, June 23, 2006. 439 pp. ISBN: 978-0-471-78418-0.

[9] D. R. Smith, J. B. Pendry, and M. C. K. Wiltshire. “Metamaterials and Negative Refractive Index.” In: *Science* 305.5685 (Aug. 6, 2004). Publisher: American Association for the Advancement of Science Section: Review, pp. 788–792. ISSN: 0036-8075, 1095-9203.

[10] Ari Sihvola. “Metamaterials in electromagnetics.” In: *Metamaterials* 1.1 (Mar. 1, 2007), pp. 2–11. ISSN: 1873-1988.

[11] Andrea Alù and Nader Engheta. "Achieving transparency with plasmonic and metamaterial coatings." In: *Phys. Rev. E* 72.1 (July 2005), p. 016623.

[12] Andrea Alù and Nader Engheta. "Multifrequency Optical Invisibility Cloak with Layered Plasmonic Shells." In: *Physical Review Letters* 100.11 (Mar. 18, 2008). Publisher: American Physical Society, p. 113901.

[13] André Nicolet and Frédéric Zolla. "Cloaking with Curved Spaces." In: *Science* 323.5910 (Jan. 2, 2009). Publisher: American Association for the Advancement of Science Section: Perspective, pp. 46–47. ISSN: 0036-8075, 1095-9203.

[14] Ari Sihvola. "Enabling Optical Analog Computing with Metamaterials." In: *Science* 343.6167 (Jan. 10, 2014). Publisher: American Association for the Advancement of Science Section: Perspective, pp. 144–145. ISSN: 0036-8075, 1095-9203.

[15] Alexandre Silva, Francesco Monticone, Giuseppe Castaldi, Vincenzo Galdi, Andrea Alù, and Nader Engheta. "Performing Mathematical Operations with Metamaterials." In: *Science* 343.6167 (Jan. 10, 2014). Publisher: American Association for the Advancement of Science Section: Report, pp. 160–163. ISSN: 0036-8075, 1095-9203.

[16] Farzad Zangeneh-Nejad, Dimitrios L. Sounas, Andrea Alù, and Romain Fleury. "Analogue computing with metamaterials." In: *Nature Reviews Materials* 6.3 (Mar. 2021). Number: 3 Publisher: Nature Publishing Group, pp. 207–225. ISSN: 2058-8437.

[17] J. B. Pendry. "Negative Refraction Makes a Perfect Lens." In: *Physical Review Letters* 85.18 (Oct. 30, 2000). Publisher: American Physical Society, pp. 3966–3969.

[18] Satoshi Kawata, Yasushi Inouye, and Prabhat Verma. "Plasmonics for near-field nano-imaging and superlensing." In: *Nature Photonics* 3.7 (July 2009). Number: 7 Publisher: Nature Publishing Group, pp. 388–394. ISSN: 1749-4893.

[19] André Nicolet, Frédéric Zolla, and Christophe Geuzaine. "Transformation Optics, Generalized Cloaking and Superlenses." In: *IEEE Transactions on Magnetics* 46.8 (Aug. 2010). Conference Name: IEEE Transactions on Magnetics, pp. 2975–2981. ISSN: 1941-0069.

[20] A. Alu and Nader Engheta. “Physical insight into the "growing" evanescent fields of double-negative metamaterial lenses using their circuit equivalence.” In: *IEEE Transactions on Antennas and Propagation* 54.1 (Jan. 2006). Conference Name: IEEE Transactions on Antennas and Propagation, pp. 268–272. ISSN: 1558-2221.

[21] Jacob B Khurgin. “How to deal with the loss in plasmonics and metamaterials.” In: *Nature nanotechnology* 10.1 (2015), pp. 2–6.

[22] A. B. Evlyukhin, C. Reinhardt, A. Seidel, B. S. Luk’yanchuk, and B. N. Chichkov. “Optical response features of si-nanoparticle arrays.” In: *Phys. Rev. B* 82 (2010).

[23] A. B. Evlyukhin, C. Reinhardt, and B. N. Chichkov. “Multipole light scattering by nonspherical nanoparticles in the discrete dipole approximation.” In: *Phys. Rev. B* 84 (2011).

[24] A. Garcia-Etxarri. “Strong magnetic response of submicron silicon particles in the infrared.” In: *Opt. express* 19 (2011).

[25] Arseniy I. Kuznetsov, Andrey E. Miroshnichenko, Mark L. Brongersma, Yuri S. Kivshar, and Boris Luk’yanchuk. “Optically resonant dielectric nanostructures.” In: *Science* 354.6314 (Nov. 18, 2016). Publisher: American Association for the Advancement of Science Section: Review. ISSN: 0036-8075, 1095-9203.

[26] S. Kruk and Y. Kivshar. “Functional meta-optics and nanophotonics govern by mie resonances.” In: *ACS Photonics* 4 (2017).

[27] J. Van Bladel. “The Excitation of Dielectric Resonators of Very High Permittivity.” In: *IEEE Transactions on Microwave Theory and Techniques* 23.2 (Feb. 1975), pp. 208–217. ISSN: 0018-9480.

[28] H. C. van de Hulst. “Light scattering by small particles. New York (John Wiley and Sons), London (Chapman and Hall).” In: (1957).

[29] Gorden Videen and William S. Bickel. “Light-scattering resonances in small spheres.” In: *Phys. Rev. A* 45.8 (Apr. 1992), pp. 6008–6012.

[30] Robert Joseph Cava. “Dielectric materials for applications in microwave communicationsBasis of a presentation given at Materials Discussion No. 3, 26–29 September, 2000, University of Cambridge, UK.” In: *Journal of Materials Chemistry* 11.1 (2001), pp. 54–62.

[31] Rajesh K. Mongia and Prakash Bhartia. “Dielectric resonator antennas—a review and general design relations for resonant frequency and bandwidth.” In: *International Journal of Microwave and Millimeter-Wave Computer-Aided Engineering* 4.3 (1994), pp. 230–247.

[32] Ian M. Reaney and David Iddles. “Microwave Dielectric Ceramics for Resonators and Filters in Mobile Phone Networks.” In: *Journal of the American Ceramic Society* 89.7 (2006), pp. 2063–2072.

[33] HM Schlicke. “Quasi-Degenerated Modes in High-eps Dielectric Cavities.” In: *Journal of Applied Physics* 24.2 (1953), pp. 187–191.

[34] G. Rupprecht and R. O. Bell. “Dielectric Constant in Paraelectric Perovskites.” In: *Phys. Rev.* 135.3 (Aug. 1964), A748–A752.

[35] JC Sethares and SJ Naumann. “Design of microwave dielectric resonators.” In: *IEEE Transactions on Microwave Theory and Techniques* 14.1 (1966), pp. 2–7.

[36] A. B. Evlyukhin. “Demonstration of magnetic dipole resonances of dielectric nanospheres in the visible region.” In: *Nano letters* 12 (2012).

[37] A. I. Kuznetsov, A. E. Miroshnichenko, Y. H. Fu, J. Zhang, and B. Luk’Yanchuk. “Magnetic light.” In: *Sci. Reports* 2 (2012).

[38] Daria Smirnova and Yuri S. Kivshar. “Multipolar nonlinear nanophotonics.” In: *Optica* 3.11 (Nov. 2016), pp. 1241–1255.

[39] M. K. Schmidt, R. Esteban, J. J. Sáenz, I. Suárez-Lacalle, S. Mackowski, and J. Aizpurua. “Dielectric antennas - a suitable platform for controlling magnetic dipolar emission.” In: *Opt. Express* 20.13 (June 2012), pp. 13636–13650.

[40] Brice Rolly, Betina Bebey, Sebastien Bidault, Brian Stout, and Nicolas Bonod. “Promoting magnetic dipolar transition in trivalent lanthanide ions with lossless Mie resonances.” In: *Phys. Rev. B* 85.24 (June 2012), p. 245432.

[41] Tianhua Feng, Yi Xu, Zixian Liang, and Wei Zhang. “All-dielectric hollow nanodisk for tailoring magnetic dipole emission.” In: *Optics Letters* 41.21 (Nov. 2016), pp. 5011–5014. ISSN: 1539-4794.

[42] Jiaqi Li, Niels Verellen, and Pol Van Dorpe. “Enhancing Magnetic Dipole Emission by a Nano-Doughnut-Shaped Silicon Disk.” In: *ACS Photonics* 4.8 (2017), pp. 1893–1898.

[43] Denis G. Baranov, Roman S. Savelev, Sergey V. Li, Alexander E. Krasnok, and Andrea Alù. “Modifying magnetic dipole spontaneous emission with nanophotonic structures (Laser Photonics Rev. 11(3)/2017).” In: *Laser & Photonics Reviews* 11.3 (2017), 1770031–n/a. ISSN: 1863-8899.

[44] Isabelle Staude, Andrey E. Miroshnichenko, Manuel Decker, Nche T. Fofang, Sheng Liu, Edward Gonzales, Jason Dominguez, Ting Shan Luk, Dragomir N. Neshev, Igal Brener, and Yuri Kivshar. “Tailoring Directional Scattering through Magnetic and Electric Resonances in Subwavelength Silicon Nanodisks.” In: *ACS Nano* 7.9 (2013), pp. 7824–7832.

[45] J. Groep, T. Coenen, S. A. Mann, and A. Polman. “Direct imaging of hybridized eigenmodes in coupled silicon nanoparticles.” In: *Opt.* 3 (2016).

[46] P. Kapitanova. “Giant field enhancement in high-index dielectric subwavelength particles.” In: *Sci. Reports* 7 (2017).

[47] B. Luk’yanchuk. “The fano resonance in plasmonic nanostructures and metamaterials.” In: *Nat. materials* 9 (2010).

[48] Carlo Forestiere, Giovanni Miano, Mariano Pascale, and Roberto Tricarico. “A Full-Retarded Spectral Technique for the Analysis of Fano Resonances in a Dielectric Nanosphere.” In: *Fano Resonances in Optics and Microwaves: Physics and Applications.* Ed. by Eugene Kamenetskii, Almas Sadreev, and Andrey Miroshnichenko. Springer Series in Optical Sciences. Cham: Springer International Publishing, 2018, pp. 185–218. ISBN: 978-3-319-99731-5.

[49] George W. Hanson and Alexander B. Yakovlev. *Operator Theory for Electromagnetics: An Introduction.* Google-Books-ID: 2PfTBwAAQBAJ. Springer Science & Business Media, Mar. 9, 2013. 640 pp. ISBN: 978-1-4757-3679-3.

[50] E. Ching. “Quasinormal-mode expansion for waves in open systems.” In: *Rev. Mod. Phys.* 70 (1998).

[51] P. Lalanne, W. Yan, K. Vynck, C. Sauvan, and J. -. P. Hugonin. “Light interaction with photonic and plasmonic resonances.” In: *Laser & Photonics Rev.* 12 (2018).

[52] Frédéric Zolla, André Nicolet, and Guillaume Demésy. “Photonics in highly dispersive media: the exact modal expansion.” In: *Optics Letters* 43.23 (Dec. 1, 2018). Publisher: Optical Society of America, pp. 5813–5816. ISSN: 1539-4794.

[53] Benjamin Vial, Frédéric Zolla, André Nicolet, and Mireille Commandré. “Quasimodal expansion of electromagnetic fields in open two-dimensional structures.” In: *Physical Review A* 89.2 (Feb. 19, 2014). Publisher: American Physical Society, p. 023829.

[54] Philip Trøst Kristensen, Kathrin Herrmann, Francesco Intravaia, Kurt Busch, and Kurt Busch. “Modeling electromagnetic resonators using quasinormal modes.” In: *Advances in Optics and Photonics* 12.3 (Sept. 30, 2020). Publisher: Optical Society of America, pp. 612–708. ISSN: 1943-8206.

[55] E. A. Muljarov, W. Langbein, and R. Zimmermann. “Brillouin-Wigner perturbation theory in open electromagnetic systems.” In: *EPL (Europhysics Letters)* 92.5 (Dec. 2010). Publisher: IOP Publishing, p. 50010. ISSN: 0295-5075.

[56] P. T. Kristensen and S. Hughes. “Modes and mode volumes of leaky optical cavities and plasmonic nanoresonators.” In: *ACS Photonics* 1 (2013).

[57] P. T. Kristensen, C. Van Vlack, and S. Hughes. “Generalized effective mode volume for leaky optical cavities.” In: *Optics Letters* 37.10 (May 15, 2012). Publisher: Optical Society of America, pp. 1649–1651. ISSN: 1539-4794.

[58] C. Sauvan, J. -. P. Hugonin, I. Maksymov, and P. Lalanne. “Theory of the spontaneous optical emission of nanosize photonic and plasmon resonators.” In: *Phys. Rev. Lett.* 110 (2013).

[59] P. T. Kristensen, R. -. C. Ge, and S. Hughes. “Normalization of quasinormal modes in leaky optical cavities and plasmonic resonators.” In: *Phys. Rev. A* 92 (2015).

[60] R. J. Garbacz. “Modal expansions for resonance scattering phenomena.” In: *Proc. IEEE* 53 (1965).

[61] R. Harrington, J. Mautz, and Yu Chang. “Characteristic modes for dielectric and magnetic bodies.” In: *IEEE Transactions on Antennas and Propagation* 20.2 (Mar. 1972), pp. 194–198. ISSN: 0018-926X.

[62] J. Mäkitalo, M. Kauranen, and S. Suuriniemi. “Modes and resonances of plasmonic scatterers.” In: *Phys. Rev. B* 89 (2014).

[63] David A. Powell. “Resonant dynamics of arbitrarily shaped meta-atoms.” In: *Physical Review B* 90.7 (Aug. 6, 2014). Publisher: American Physical Society, p. 075108.

[64] D. J. Bergman and D. Stroud. “Theory of resonances in the electromagnetic scattering by macroscopic bodies.” In: *Phys. Rev. B* 22 (1980).

[65] C. Forestiere and G. Miano. “Material-independent modes for electromagnetic scattering.” In: *Phys. Rev. B* 94 (2016).

[66] R. Fuchs. “Theory of the optical properties of ionic crystal cubes.” In: *Phys. Rev. B* 11.4 (Feb. 1975), pp. 1732–1740.

[67] R. Rojas and F. Claro. “Electromagnetic response of an array of particles: Normal-mode theory.” In: *Phys. Rev. B* 34.6 (Sept. 1986), pp. 3730–3736.

[68] David J Bergman. “The dielectric constant of a composite material—a problem in classical physics.” In: *Physics Reports* 43.9 (1978), pp. 377–407.

[69] F. J. Garcia de Abajo and A. Howie. “Relativistic Electron Energy Loss and Electron-Induced Photon Emission in Inhomogeneous Dielectrics.” In: *Phys. Rev. Lett.* 80.23 (June 1998), pp. 5180–5183.

[70] D. R. Fredkin and I. D. Mayergoyz. “Resonant Behavior of Dielectric Objects (Electrostatic Resonances).” In: *Phys. Rev. Lett.* 91.25 (Dec. 2003), p. 253902.

[71] I. D. Mayergoyz, D. R. Fredkin, and Z. Zhang. “Electrostatic (plasmon) resonances in nanoparticles.” In: *Phys. Rev. B* 72 (2005).

[72] L. Dal Negro, G. Miano, G. Rubinacci, A. Tamburrino, and S. Ventre. “A Fast Computation Method for the Analysis of an Array of Metallic Nanoparticles.” In: *IEEE Trans. Magn.* 45.3 (2009), pp. 1618–1621.

[73] Vadim A Markel. “Pole expansion of the Lorenz-Mie coefficients.” In: *Journal of Nanophotonics* 4.1 (2010), p. 041555.

[74] C. Forestiere, G. Miano, S. V. Boriskina, and L. Dal Negro. “The role of nanoparticle shapes and deterministic aperiodicity for the design of nanoplasmonic arrays.” In: *Opt. Express* 17.12 (2009), pp. 9648–9661.

[75] Vadim A. Markel. “Antisymmetrical optical states.” In: *J. Opt. Soc. Am. B* 12.10 (Oct. 1995), pp. 1783–1791.

[76] M. Pascale, G. Miano, and C. Forestiere. “Spectral theory of electromagnetic scattering by a coated sphere.” In: *JOSA B* 34 (2017).

[77] Asaf Farhi and David J Bergman. “Electromagnetic eigenstates and the field of an oscillating point electric dipole in a flat-slab composite structure.” In: *Physical Review A* 93.6 (2016), p. 063844.

[78] C. Forestiere, G. Miano, G. Rubinacci, A. Tamburrino, R. Tricarico, and S. Ventre. “Volume Integral Formulation for the Calculation of Material Independent Modes of Dielectric Scatterers.” In: *IEEE Transactions on Antennas and Propagation* 66.5 (May 2018), pp. 2505–2514. ISSN: 1558-2221.

[79] C. Forestiere and G. Miano. “On the nanoparticle resonances in the full-retarded regime.” In: *J. Opt.* 19 (2017).

[80] Carlo Forestiere, Giovanni Miano, Mariano Pascale, and Roberto Tricarico. “Material-independent Modes for the Design of Electromagnetic Scattering.” In: *Compendium on Electromagnetic Analysis*. 5 vols. World Scientific, June 18, 2020, pp. 345–384. ISBN: 978-981-327-029-9.

[81] Hakan E. Türeci, A. Douglas Stone, and B. Collier. “Self-consistent multimode lasing theory for complex or random lasing media.” In: *Physical Review A* 74.4 (Oct. 31, 2006). Publisher: American Physical Society, p. 043822.

[82] Uwe Kreibig and Michael Vollmer. *Optical Properties of Metal Clusters*. Springer Series in Materials Science. Berlin Heidelberg: Springer-Verlag, 1995. ISBN: 978-3-540-57836-9.

[83] I. D. Mayergoyz, Z. Zhang, and G. Miano. “Analysis of Dynamics of Excitation and Dephasing of Plasmon Resonance Modes in Nanoparticles.” In: *Phys. Rev. Lett.* 98.14 (Apr. 2007), p. 147401.

[84] Feng Wang and Y. Ron Shen. “General Properties of Local Plasmons in Metal Nanostructures.” In: *Physical Review Letters* 97.20 (Nov. 17, 2006). Publisher: American Physical Society, p. 206806.

[85] Kuiru Li, Mark I. Stockman, and David J. Bergman. “Self-Similar Chain of Metal Nanospheres as an Efficient Nanolens.” In: *Physical Review Letters* 91.22 (Nov. 26, 2003). Publisher: American Physical Society, p. 227402.

[86] David J. Bergman and Mark I. Stockman. “Surface Plasmon Amplification by Stimulated Emission of Radiation: Quantum Generation of Coherent Surface Plasmons in Nanosystems.” In: *Physical Review Letters* 90.2 (Jan. 14, 2003). Publisher: American Physical Society, p. 027402.

[87] Craig F. Bohren and Donald R. Huffman. *Absorption and Scattering of Light by Small Particles*. Wiley, 1998.

[88] E. Prodan, C. Radloff, N. J. Halas, and P. Nordlander. “A hybridization model for the plasmon response of complex nanostructures.” In: *Sci.* 302 (2003).

[89] P. Nordlander, C. Oubre, E. Prodan, K. Li, and M. I. Stockman. “Plasmon Hybridization in Nanoparticle Dimers.” In: *Nano Letters* 4.5 (May 1, 2004). Publisher: American Chemical Society, pp. 899–903. ISSN: 1530-6984.

[90] Feng Hao, Colleen L. Nehl, Jason H. Hafner, and Peter Nordlander. "Plasmon Resonances of a Gold Nanostar." In: *Nano Letters* 7.3 (Mar. 1, 2007). Publisher: American Chemical Society, pp. 729–732. ISSN: 1530-6984.

[91] Mario Hentschel, Michael Saliba, Ralf Vogelgesang, Harald Giessen, A. Paul Alivisatos, and Na Liu. "Transition from Isolated to Collective Modes in Plasmonic Oligomers." In: *Nano Letters* 10.7 (July 14, 2010). Publisher: American Chemical Society, pp. 2721–2726. ISSN: 1530-6984.

[92] D. W. Brandl, C. Oubre, and P. Nordlander. "Plasmon hybridization in nanoshell dimers." In: *The J. chemical physics* 123 (2005).

[93] Darko Kajfez, Pierre Guillon, et al. *Dielectric resonators.* Noble Publishing Corporation Atlanta, 1998.

[94] Hung Yuet Yee. "Natural resonant frequencies of microwave dielectric resonators (correspondence)." In: *IEEE Transactions on Microwave Theory and Techniques* 13.2 (1965), pp. 256–256.

[95] P. Guillon and Y. Garault. "Accurate Resonant Frequencies of Dielectric Resonators." In: *IEEE Transactions on Microwave Theory and Techniques* 25.11 (Nov. 1977), pp. 916–922.

[96] Seymour B Cohn. "Microwave bandpass filters containing high-Q dielectric resonators." In: *IEEE Transactions on Microwave Theory and Techniques* 16.4 (1968), pp. 218–227.

[97] T. Itoh and R. S. Rudokas. "New Method for Computing the Resonant Frequencies of Dielectric Resonators (Short Papers)." In: *IEEE Transactions on Microwave Theory and Techniques* 25.1 (Jan. 1977), pp. 52–54.

[98] A. W. Glisson, D. Kajfez, and J. James. "Evaluation of Modes in Dielectric Resonators Using a Surface Integral Equation Formulation." In: *IEEE Transactions on Microwave Theory and Techniques* 31.12 (Dec. 1983), pp. 1023–1029.

[99] D. Kajfez, A. W. Glisson, and J. James. "Computed Modal Field Distributions for Isolated Dielectric Resonators." In: *IEEE Transactions on Microwave Theory and Techniques* 32.12 (Dec. 1984), pp. 1609–1616.

[100] Carlo Forestiere, Giovanni Miano, Guglielmo Rubinacci, Mariano Pascale, Antonello Tamburrino, Roberto Tricarico, and Salvatore Ventre. "Magnetoquasistatic resonances of small dielectric objects." In: *Phys. Rev. Research* 2.1 (Feb. 2020), p. 013158.

[101] Carlo Forestiere, Giovanni Miano, and Guglielmo Rubinacci. “Resonance frequency and radiative Q-factor of plasmonic and dieletric modes of small objects.” In: *Phys. Rev. Research* 2.4 (Nov. 2020), p. 043176.

[102] Carlo Forestiere, Giovanni Gravina, Giovanni Miano, Mariano Pascale, and Roberto Tricarico. “Electromagnetic modes and resonances of two-dimensional bodies.” In: *Phys. Rev. B* 99.15 (Apr. 2019). Publisher: American Physical Society, p. 155423.

[103] Holger Fischer and Olivier J. F. Martin. “Engineering the optical response of plasmonic nanoantennas.” In: *Optics Express* 16.12 (June 9, 2008). Publisher: Optical Society of America, pp. 9144–9154. ISSN: 1094-4087.

[104] Martin Kuttge, F. Javier García de Abajo, and Albert Polman. “Ultrasmall mode volume plasmonic nanodisk resonators.” In: *Nano Letters* 10.5 (May 12, 2010), pp. 1537–1541. ISSN: 1530-6992.

[105] A. Femius Koenderink, Andrea Alù, and Albert Polman. “Nanophotonics: Shrinking light-based technology.” In: *Science* 348.6234 (May 1, 2015). Publisher: American Association for the Advancement of Science Section: Review, pp. 516–521. ISSN: 0036-8075, 1095-9203.

[106] Mats Gustafsson, Christian Sohl, and Gerhard Kristensson. “Physical limitations on antennas of arbitrary shape.” In: *Proceedings of the Royal Society A: Mathematical, Physical and Engineering Sciences* 463.2086 (Oct. 2007), pp. 2589–2607.

[107] H. L. Thal. “New Radiation Q Limits for Spherical Wire Antennas.” In: *IEEE Transactions on Antennas and Propagation* 54.10 (2006), pp. 2757–2763.

[108] Mats Gustafsson, Doruk Tayli, and Marius Cismasu. *Physical bounds of antennas.* Vol. TEAT-7240. Technical Report LUTEDX/(TEAT-7240)/1-38/(2015). Electromagnetic Theory Department of Electrical and Information Technology Lund University Sweden, 2015.

[109] O. D. Miller, C. W. Hsu, M. T. H. Reid, W. Qiu, B. G. DeLacy, J. D. Joannopoulos, M. Soljačić, and S. G. Johnson. “Fundamental Limits to Extinction by Metallic Nanoparticles.” In: *Physical Review Letters* 112.12 (Mar. 26, 2014). Publisher: American Physical Society, p. 123903.

[110] G. A. E. Vandenbosch. “Simple Procedure to Derive Lower Bounds for Radiation Q of Electrically Small Devices of Arbitrary Topology.” In: *IEEE Transactions on Antennas and Propagation* 59.6 (June 2011), pp. 2217–2225. ISSN: 1558-2221.

[111] L. J. Chu. “Physical Limitations of Omni-Directional Antennas.” In: *Journal of Applied Physics* 19.12 (1948), pp. 1163–1175.

[112] H. Wheeler. “Small antennas.” In: *IEEE Transactions on Antennas and Propagation* 23.4 (July 1975). Conference Name: IEEE Transactions on Antennas and Propagation, pp. 462–469. ISSN: 1558-2221.

[113] H. A. Wheeler. “Fundamental Limitations of Small Antennas.” In: *Proceedings of the IRE* 35.12 (Dec. 1947), pp. 1479–1484. ISSN: 2162-6634.

[114] Roger F. Harrington. “Effect of antenna size on gain, bandwidth, and efficiency.” In: *Journal of Research of the National Bureau of Standards* 64 (1959).

[115] R Collin and S Rothschild. “Evaluation of antenna Q.” In: *IEEE Transactions on Antennas and Propagation* 12.1 (1964), pp. 23–27.

[116] J. S. McLean. “A re-examination of the fundamental limits on the radiation Q of electrically small antennas.” In: *IEEE Transactions on Antennas and Propagation* 44.5 (May 1996), pp. 672–. ISSN: 1558-2221.

[117] M. Gustafsson, M. Cismasu, and B. L. G. Jonsson. “Physical Bounds and Optimal Currents on Antennas.” In: *IEEE Transactions on Antennas and Propagation* 60.6 (June 2012), pp. 2672–2681. ISSN: 1558-2221.

[118] G. A. E. Vandenbosch. “Reactive Energies, Impedance, and Q Factor of Radiating Structures.” In: *IEEE Transactions on Antennas and Propagation* 58.4 (2010), pp. 1112–1127.

[119] J. Chalas, K. Sertel, and J. L. Volakis. “Computation of the Q Limits for Arbitrary-Shaped Antennas Using Characteristic Modes.” In: *IEEE Transactions on Antennas and Propagation* 64.7 (July 2016), pp. 2637–2647. ISSN: 1558-2221.

[120] M. Capek and L. Jelinek. “Optimal Composition of Modal Currents for Minimal Quality Factor.” In: *IEEE Transactions on Antennas and Propagation* 64.12 (Dec. 2016), pp. 5230–5242. ISSN: 1558-2221.

[121] L. Jelinek and M. Capek. “Optimal Currents on Arbitrarily Shaped Surfaces.” In: *IEEE Transactions on Antennas and Propagation* 65.1 (Jan. 2017), pp. 329–341. ISSN: 1558-2221.

[122] B. L. G. Jonsson and Mats Gustafsson. “Stored energies in electric and magnetic current densities for small antennas.” In: *Proceedings of the Royal Society A: Mathematical, Physical and Engineering Sciences* 471.2176 (Apr. 2015), p. 20140897. ISSN: 1364-5021, 1471-2946. arXiv: 1410.8704.

[123] N. J. Halas, S. Lal, W. -. S. Chang, S. Link, and P. Nordlander. “Plasmons in strongly coupled metallic nanostructures.” In: *Chem. reviews* 111 (2011).

[124] E. Prodan and P. Nordlander. “Structural tunability of the plasmon resonances in metallic nanoshells.” In: *Nano Lett.* 3 (2003).

[125] Eugene Kamenetskii, Almas Sadreev, and Andrey Miroshnichenko, eds. *Fano Resonances in Optics and Microwaves: Physics and Applications*. Springer Series in Optical Sciences. Springer International Publishing, 2018. ISBN: 978-3-319-99730-8.

[126] C. Forestiere, L. Dal Negro, and G. Miano. “Theory of coupled plasmon modes and fano-like resonances in subwavelength metal structures.” In: *Phys. Rev. B* 88 (2013).

[127] M. D. Turner, M. M. Hossain, and M. Gu. “The effects of retardation on plasmon hybridization within metallic nanostructures.” In: *New J. Phys.* 12 (2010).

[128] M. M. Sigalas, D. A. Fattal, R. S. Williams, S. Wang, and R. G. Beausoleil. “Electric field enhancement between two si microdisks.” In: *Opt. Express* 15 (2007).

[129] P. Albella. “Low-loss electric and magnetic field-enhanced spectroscopy with subwavelength silicon dimers.” In: *The J. Phys. Chem. C* 117 (2013).

[130] R. M. Bakker. “Magnetic and electric hotspots with silicon nanodimers.” In: *Nano Lett.* 15 (2015).

[131] Urs Zywietz, Mikolaj K Schmidt, Andrey B Evlyukhin, Carsten Reinhardt, Javier Aizpurua, and Boris N Chichkov. “Electromagnetic resonances of silicon nanoparticle dimers in the visible.” In: *ACS Photonics* 2.7 (2015), pp. 913–920.

[132] G. Boudarham, R. Abdeddaim, and N. Bonod. “Enhancing the magnetic field intensity with a dielectric gap antenna.” In: *Appl. Phys. Lett.* 104 (2014).

[133] A. Mirzaei and A. E. Miroshnichenko. “Electric and magnetic hotspots in dielectric nanowire dimers.” In: *Nanoscale* 7 (2015).

[134] P. Albella, R. Alcaraz de la Osa, F. Moreno, and S. A. Maier. “Electric and magnetic field enhancement with ultralow heat radiation dielectric nanoantennas: considerations for surface-enhanced spectroscopies.” In: *Acs Photonics* 1 (2014).

[135] M. Caldarola. “Non-plasmonic nanoantennas for surface enhanced spectroscopies with ultra-low heat conversion.” In: *Nat. communications* 6 (2015).

[136] J. Yan. “Directional fano resonance in a silicon nanosphere dimer.” In: *Acs Nano* 9 (2015).

[137] P. Albella, T. Shibanuma, and S. A. Maier. “Switchable directional scattering of electromagnetic radiation with subwavelength asymmetric silicon dimers.” In: *Sci. reports* 5 (2015).

[138] C. Wang. “Broadband optical scattering in coupled silicon nanocylinders.” In: *J. Appl. Phys.* 115 (2014).

[139] C. P. McPolin. “Imaging electric and magnetic modes and their hybridization in single and dimer algaas nanoantennas.” In: *Adv. Opt. Mater.* 6 (2018).

[140] Mariano Pascale, Giovanni Miano, Roberto Tricarico, and Carlo Forestiere. “Full-wave electromagnetic modes and hybridization in nanoparticle dimers.” In: *Scientific Reports* 9.1 (Oct. 10, 2019). Number: 1 Publisher: Nature Publishing Group, p. 14524. ISSN: 2045-2322.

[141] Carlo Forestiere, Giovanni Miano, Mariano Pascale, and Roberto Tricarico. “Directional scattering cancellation for an electrically large dielectric sphere.” In: *Optics Letters* 44.8 (Apr. 2019), pp. 1972–1975. ISSN: 1539-4794.

[142] Carlo Forestiere, Giovanni Miano, Mariano Pascale, and Roberto Tricarico. “Electromagneticc Scattering Resonances of Quasi-1-D Nanoribbons.” In: *IEEE Transactions on Antennas and Propagation* 67.8 (Aug. 2019). Conference Name: IEEE Transactions on Antennas and Propagation, pp. 5497–5506. ISSN: 1558-2221.

[143] Isaak D Mayergoyz. *Plasmon Resonances in Nanoparticles.* _eprint: https://www.worldscientific.com/doi/pdf/10.1142/8158. WORLD SCIENTIFIC, 2013.

[144] D. Kajfez and P. Guillon. *Dielectric resonators.* 1986.

[145] Mikhail V. Rybin, Kirill L. Koshelev, Zarina F. Sadrieva, Kirill B. Samusev, Andrey A. Bogdanov, Mikhail F. Limonov, and Yuri S. Kivshar. “High-Q Supercavity Modes in Subwavelength Dielectric Resonators.” In: *Phys. Rev. Lett.* 119.24 (Dec. 2017). Publisher: American Physical Society, p. 243901.

[146] J. G. Van Bladel. *Electromagnetic Fields.* Vol. 19. Series on Electromagnetic Wave Theory. John Wiley & Sons, New York, 2007.

[147] D. Schaubert, D. Wilton, and A. Glisson. “A tetrahedral modeling method for electromagnetic scattering by arbitrarily shaped inhomogeneous dielectric bodies.” In: *IEEE Transactions on Antennas and Propagation* 32.1 (Jan. 1984), pp. 77–85.

[148] Giovanni Miano, Guglielmo Rubinacci, and Antonello Tamburrino. “Numerical modeling for the analysis of plasmon oscillations in metallic nanoparticles.” In: *IEEE Transactions on Antennas and Propagation* 58.9 (2010), pp. 2920–2933.

[149] John David Jackson. *Classical electrodynamics.* John Wiley & Sons, 2007.

[150] Hermann A Haus and James R Melcher. *Electromagnetic fields and energy.* Vol. 107. Prentice Hall Englewood Cliffs, NJ, 1989.

[151] Harold Jeffreys, Bertha Jeffreys, and Bertha Swirles. *Methods of mathematical physics.* Cambridge University Press, 1999.

[152] Solomon Grigorievich Mikhlin. “Mathematical physics, an advanced course.” In: (1970). Publisher: North-Holland.

[153] L.V. Kantorovich and G.P. Akilov. *Functional Analysis.* Pergamon Press, 1982. ISBN: 978-0-08-023036-8.

[154] Kenneth Simonds Johnson. *Transmission circuits for telephonic communication.* D. Van Nostrand Company, 1939.

[155] Dimitrios C. Tzarouchis, Pasi Ylä-Oijala, and Ari Sihvola. “Unveiling the scattering behavior of small spheres.” In: *Physical Review B* 94.14 (Oct. 12, 2016). Publisher: American Physical Society, p. 140301.

[156] Dimitrios Tzarouchis and Ari Sihvola. “Light Scattering by a Dielectric Sphere: Perspectives on the Mie Resonances.” In: *Applied Sciences* 8.2 (Feb. 2018). Number: 2 Publisher: Multidisciplinary Digital Publishing Institute, p. 184.

[157] G. Colas des Francs, S. Derom, R. Vincent, A. Bouhelier, and A. Dereux. “Mie Plasmons: Modes Volumes, Quality Factors, and Coupling Strengths (Purcell Factor) to a Dipolar Emitter.” In: *International Journal of Optics* 2012 (Feb. 28, 2012). Publisher: Hindawi, e175162. ISSN: 1687-9384.

[158] Estill I. Green. “The Story of Q.” In: *American Scientist* 43.4 (1955). Publisher: Sigma Xi, The Scientific Research Society, pp. 584–594. ISSN: 0003-0996.

[159] Stefan A. Maier, Pieter G. Kik, and Harry A. Atwater. “Optical pulse propagation in metal nanoparticle chain waveguides.” In: *Physical Review B* 67.20 (May 6, 2003). Publisher: American Physical Society, p. 205402.

[160] Milton Abramowitz and Irene A Stegun. *Handbook of mathematical functions with formulas, graphs, and mathematical tables.* Vol. 55. US Government printing office, 1948.

[161] R. Harrington and J. Mautz. "An impedance sheet approximation for thin dielectric shells." In: *IEEE Transactions on Antennas and Propagation* 23.4 (July 1975), pp. 531–534. ISSN: 1558-2221.

[162] Anthony James Merrill Spencer. *Continuum Mechanics.* Dover Publications, 1992. ISBN: 0-486-43594-6.

[163] Daniel Sjöberg. "Variational principles for the static electric and magnetic polarizabilities of anisotropic media with perfect electric conductor inclusions." In: *Journal of Physics A: Mathematical and Theoretical* 42.33 (July 2009). Publisher: IOP Publishing, p. 335403. ISSN: 1751-8121.

[164] Isaak D Mayergoyz and Zhenyu Zhang. "Numerical analysis of plasmon resonances in metallic nanoshells." In: *IEEE transactions on magnetics* 43.4 (2007), pp. 1689–1692.

[165] Ian N. Sneddon. "On some infinite series involving the zeros of Bessel functions of the first kind." In: *Glasgow Mathematical Journal* 4.3 (Jan. 1960). Publisher: Cambridge University Press, pp. 144–156. ISSN: 2051-2104, 2040-6185.

[166] Gustav Mie. "Beiträge zur Optik trüber Medien, speziell kolloidaler Metallösungen." In: *Annalen der Physik* 330.3 (1908). _eprint: https://onlinelibrary.wiley.com/doi/pdf/10.1002/andp.19083300302, pp. 377–445. ISSN: 1521-3889.

[167] V. M. Dubovik and V. V. Tugushev. "Toroid moments in electrodynamics and solid-state physics." In: *Physics Reports* 187.4 (Mar. 1, 1990), pp. 145–202. ISSN: 0370-1573.

[168] Sadao Adachi. "Model dielectric constants of Si and Ge." In: *Physical Review B* 38.18 (Dec. 15, 1988). Publisher: American Physical Society, pp. 12966–12976.

[169] P. B. Johnson and R. W. Christy. "Optical Constants of the Noble Metals." In: *Phys. Rev. B* 6.12 (Dec. 1972), pp. 4370–4379.

[170] A. Doicu, T. Wriedt, and Y. A. Eremin. *Light Scattering by Systems of Particles.* Springer-Verlag, 2006.

[171] Yajie Jiang, Supriya Pillai, and Martin A Green. "Realistic Silver Optical Constants for Plasmonics." In: *Scientific Reports* 6 (2016), p. 30605.

[172] Yulin Xu. “Electromagnetic scattering by an aggregate of spheres.” In: *Appl. Opt.* 34.21 (1995), pp. 4573–4588.

[173] Craig F Bohren and Donald R Huffman. *Absorption and scattering of light by small particles.* John Wiley & Sons, 2008.

[174] Edward Harrington Lockwood. *A book of curves.* Cambridge University Press, 1967.

[175] S. Stein. “Addition theorems for spherical wave functions.” In: *Q. Appl. Math.* 19 (1961).

[176] O. R. Cruzan. “Translational addition theorems for spherical vector wave functions.” In: *Q. Appl. Math.* 20 (1962).

[177] C. Liang and Y. Lo. “Scattering by two spheres.” In: *Radio Sci.* 2 (1967).

[178] J. Bruning and Y. Lo. “Multiple scattering of em waves by spheres part i–multipole expansion and ray-optical solutions.” In: *IEEE Transactions on Antennas Propag.* 19 (1971).

[179] F. Borghese, P. Denti, G. Toscano, and O. Sindoni. “Electromagnetic scattering by a cluster of spheres.” In: *Appl. optics* 18 (1979).

[180] K. A. Fuller and G. W. Kattawar. “Consummate solution to the problem of classical electromagnetic scattering by an ensemble of spheres. i: Linear chains.” In: *Opt. letters* 13 (1988).

[181] D. W. Mackowski. “Analysis of radiative scattering for multiple sphere configurations.” In: *Proc. R. Soc. Lond. A* 433 (1991).

[182] D. W. Mackowski. “Calculation of total cross sections of multiple-sphere clusters.” In: *JOSA A* 11 (1994).

[183] M. I. Mishchenko, J. W. Hovenier, and L. D. Travis. *Light scattering by nonspherical particles.* San Diego: Academic Press, 2006.

[184] Ferdinando Borghese, Paolo Denti, and Rosalba Saija. *Scattering from Model Nonspherical Particles: Theory and Applications to Environmental Physics.* 2nd ed. Physics of Earth and Space Environments. Berlin Heidelberg: Springer-Verlag, 2007. ISBN: 978-3-540-37413-8.

[185] Y. -. L. Xu. “Calculation of the addition coefficients in electromagnetic multisphere-scattering theory.” In: *J. Comput. Phys.* 127 (1996).